THE UNIVERSITY OF ALBERTA

THE INDUCED DRAG REDUCTION MECHANISM OF WINGTIP SURFACES FROM STUDIES OF THE LIFT CURVE AND VORTEX WAKE

by

WILLIAM J. O'CALLAGHAN

A THESIS

SUBMITTED TO THE FACULTY OF GRADUATE STUDIES AND RESEARCH

IN PARTIAL FULFILMENT OF THE REQUIREMENTS FOR THE DEGREE

OF MASTER OF SCIENCE

IN

MECHANICAL ENGINEERING

DEPARTMENT OF MECHANICAL ENGINEERING

EDMONTON, ALBERTA

FALL 1988

Permission has been granted to the National Library of Canada to microfilm this thesis and to lend or sell copies of the film.

The author (copyright owner) has reserved other publication rights, and neither the thesis nor extensive extracts from it may be printed or otherwise reproduced without his/her written permission.

L'autorisation a été accordée à la Bibliothèque nationale du Canada de microfilmer cette thèse et de prêter ou de vendre des exemplaires du film.

L'auteur (titulaire du droit d'auteur) se réserve les autres droits de publication; ni la thèse ni de longs extraits de celle-ci ne doivent être imprimés ou autrement reproduits sans son autorisation écrite.

ISBN 0-315-45763-5

DO NOT USE THIS THESIS AS A FORMAT MODEL

PLEASE

consult the latest edition of

"REGULATIONS AND GUIDE FOR THE PREPARATION OF THESES"

or

the Faculty of Graduate Studies and Research

for format guidelines.

THE UNIVERSITY OF ALBERTA

RELEASE FORM

NAME OF AUTHOR William J. O'Callaghan

TITLE OF THESIS The Induced Drag Reduction Mechanism of Wingtip Surfaces from Studies of the Lift Curve and Vortex Wake

DEGREE FOR WHICH THIS THESIS WAS PRESENTED

Master of Science in Mechanical Engineering

YEAR THIS DEGREE GRANTED 1988

Permission is hereby granted to THE UNIVERSITY OF ALBERTA LIBRARY to reproduce single copies of this thesis and to lend or sell such copies for private, scholarly or scientific research purposes only.

The author reserves other publication rights, and neither the thesis nor extensive extracts from it may be printed or otherwise reproduced without the author's written permission.

(SIGNED) Bill O'Callaghan

PERMANENT ADDRESS:

#408A 6515-172 Street

Edmonton, Alberta

T5T 2E1

DATED OCTOBER 11 1988

THE UNIVERSITY OF ALBERTA

FACULTY OF GRADUATE STUDIES AND RESEARCH

The undersigned certify that they have read, and recommend to the Faculty of Graduate Studies and Research, for acceptance, a thesis entitled "The Induced Drag Reduction Mechanism of Wingtip Surfaces from Studies of the Lift Curve and Vortex Wake", submitted by William J. O'Callaghan in partial fulfilment of the requirements for the degree of Master of Science in Mechanical Engineering

David Marsden

Supervisor

Date 11 oct. 1988

Dedicated to Jackie, whose
love, patience, and concern
have sustained and
motivated me

ABSTRACT

The drag induced by the trailing vortex system of an aircraft wing was reduced by introducing auxiliary airfoil shaped surfaces, or fins, at the wingtip. Induced drag reduction, which is a result of reduced downwash due to a redistribution of vorticity in the wake, was improved by optimizing the number, positions, and orientations of the fins. An efficient wingtip modification redistributed vorticity by generating additional lift, particularly in the wingtip region. As a consequence, the spanwise centroid of the wake vorticity distribution was shifted outward and downwash on the wing was reduced.

The same reduction of downwash which reduces induced drag also causes an increase in the wing lift curve slope, $dC_L/d\alpha$. Because lift could be measured accurately by means of a set of chordwise pressure taps located at the mid-semispan of a rectangular wing, accurate evaluation of lift curve slope and, by inference, induced drag reduction could be performed. This procedure produced repeatable results that showed the influence of various wingtip configurations on effective aspect ratio and induced drag.

Redistribution of the wake vorticity was also investigated by traversing a five-hole flow angle probe through the vortex wake in cross-stream planes behind the wing. The probe provided the position and rotational velocity distribution of a trailing vortex.

The results suggested that a fin should have a span comparable to the wingtip chord and that its trailing edge should align with that of the wing. An untoed fin positioned in this manner and canted

outward through 45^{o} was shown to cause a considerable spread of vorticity: not only was the strength of the wingtip vortex reduced, the fin also shed from its tip a secondary vortex comparable in strength to the wingtip vortex. When a second fin, untoed and uncanted, was placed ahead of this fin, an induced drag reduction of 25.8% was measured. Supplementary tests indicated that little improvement in the induced efficiency of this combination could be had with the further introduction of additional fins.

ACKNOWLEDGEMENT

I wish to thank Dr. D.J. Marsden, my supervisor, without whose invaluable insights and advice this work might not have been possible.

I would also like to express my sincere appreciation to the workshop technicians of the Department of Mechanical Engineering. Special thanks are due to Bernie Faulkner, who constructed the wingtip devices and mounted the wing section, and to Tom Villett, whose knowledge of the wind tunnel proved to be invaluable. I also wish to acknowledge the combined efforts of Allan Muir, Max Schubert, and Terry Nord in fabricating the flow angle probe and its calibration mount.

TABLE OF CONTENTS

ABSTRACT.....v

ACKNOWLEDGEMENT.....vii

LIST OF TABLES.....xii

LIST OF FIGURES.....xiii

LIST OF PLATES.....xx

NOMENCLATURE.....xxi

1. INTRODUCTION..... 1

2. THEORETICAL BASIS AND EXPERIMENTAL TECHNIQUES..... 6

2.1 The Induced Drag of a Lifting Wing..... 6

2.2 Lift Curve Slope Comparisons..... 7

2.3 Foundations of Vortex Wake Analysis..... 11

3. EQUIPMENT..... 13

3.1 Wind Tunnel..... 13

3.2 Test Section Coordinate Convention..... 13

3.3 Wing Section..... 14

3.4 Wing Mounting..... 14

3.5 Wingtip Device Specifications..... 15

3.6 Tip Tank Numbering System..... 16

3.7 Five-Hole Flow Angle Probe..... 18

3.8 Measurement Apparatus..... 19

4. MEASUREMENT PROCEDURE..... 22

4.1 Wing Data Acquisition..... 22

4.2 Wake Data Acquisition..... 23

5. VALIDITY OF THE MEASUREMENT PROCEDURE..... 24

5.1 Lift Curve Measurements..... 24

5.1.1 Justification of Lift Measurement at Midspan.... 24

5.1.2 Calculation of the Lift Curve Slope..... 25

5.1.3 Sensitivity of the Calculations..... 26

5.1.4 Precision of the Lift Curve Results..... 28

5.2 Vortex Wake Analysis..... 28

5.2.1 Underlying Assumptions..... 28

a) Probe/Vortex Interaction..... 29

b) Completion of Roll-Up..... 29

c) Vortex Wake Decay..... 31

d) Axial Symmetry..... 32

e) Multiple-Vortex Wakes..... 32

5.2.2 Precision of the Wake Results..... 33

5.2.3 Distinction Between Vortex Strength and Intensity..... 34

6. DISCUSSION OF RESULTS..... 37

6.1 Lift Curve Results..... 37

6.1.1 Effects of Wingtip Geometry on Performance..... 38

a) Chordwise Position of a Fin..... 38

b) Cant Angle..... 40

c) Toe Angle..... 42

d) Fin Span..... 45

e) Mutual Interference Between Fins..... 47

f) Incremental Influence of an Additional Fin.. 47

6.2 Wake Analysis Results..... 50

6.2.1 Rotational Velocity Distributions..... 50

6.2.2 Core Width and Peak Rotational Velocity..... 55

6.2.3 Vortex Intensity..... 59

6.2.4 Vortex Positions..... 60

a) Spanwise Displacement due to Mutual Convection..... 62

b) Spanwise Displacement due to Vorticity Redistribution..... 64

c) Vortex Ascension due to the Experimental Setup..... 66

6.3 Flow Visualization..... 70

6.3.1 Observations of Surface Flow Patterns..... 70

6.3.2 Observations of the Trailing Vortices..... 71

6.4 Final Comments on the Results..... 72

7. CLOSING REMARKS..... 74

7.1 Conclusions..... 74

7.2 Recommendations for Future Research..... 76

BIBLIOGRAPHY..... 78

APPENDIX I: CALIBRATION AND USE OF THE FIVE-HOLE FLOW ANGLE PROBE.....166

I.1 Probe Coefficients.....166

I.2 Probe Calibration Procedure.....167

I.3 Use of the Probe in an Unknown Flow.....169

APPENDIX II: CALIBRATION OF VALIDYNE TRANSDUCERS.....177

APPENDIX III: WIND TUNNEL BOUNDARY CORRECTIONS.....179

APPENDIX IV: SOME COMMENTS ON VORTEX WAKE ANALYSIS.....183

IV.1 Laminar Vortex Equations.....183

IV.2 Turbulence.....184

IV.2.1 Causes and Mechanisms of Turbulence.....185

IV.2.2 Rate of Core Growth.....185

IV.2.3 Decay of Peak Rotational Volocities.....186

IV.2.4 Vortex Circulation Distribution.....186

IV.2.5 Effective Eddy Viscosity.....187

APPENDIX V: RELATION BETWEEN WING AND VORTEX CIRCULATION DISTRIBUTIONS.....188

V.1 The Method of Betz.....188

V.2 Central Rotational Velocity.....190

LIST OF TABLES

3-1 Wing surface coordinates of the static pressure taps..... 82

3-2 Possible placements and orientations of a fin on the tip tank..... 82

6-1 Induced drag reductions and effective aspect ratio increases as determined from the lift curve slopes..... 83

6-2 Influence of changes in the chordwise location of a fin on induced drag reduction..... 84

6-3 The effect of an additional fin in furthering induced drag reduction..... 84

6-4 Vortex core measurement results..... 85

III-1 Planform areas and volumes of the wingtip devices.....182

LIST OF FIGURES

1-1 Specifications of the Whitcomb winglet (from [4])..... 86

1-2 Definitions and conventions for the cant and toe angles of a winglet or fin..... 87

1-3 The mechanism through which a winglet behaves like a sail.. 87

1-4 The wingtip configurations of Spillman and Allen [12]..... 88

(a) Cascade arrangement..... 88

(b) Adjustable array of fins..... 89

1-5 The wingtip configurations of Zimmer [13]..... 90

(a) The optimal biplane arrangement of a set of wingtip fins..... 90

(b) Wingtip fins arranged with successively increasing incidences..... 90

1-6 Wingtip fins which combine the optimal biplane arrangement with a triangular tip extension (from [13])..... 91

2-1 Roll-up of the trailing vortex sheet behind a lifting rectangular wing..... 92

2-2 The relation between downwash and induced drag..... 93

(a) Typical circulation and downwash distributions for a lifting wing, with flow out of the page..... 93

(b) Mechanism of induced drag..... 93

2-3 The influence of a wingtip modification on the lift curve.. 94

2-4 Definitions and conventions for the rotational velocity and core width of a trailing vortex..... 95

(a) A cross section of a tip vortex showing the direction of rotation, with flow out of the page..... 95

(b) The rotational velocity distribution of a wingtip vortex, showing the peak rotational velocities and the core limits..... 95

3-1 Schematic diagram of the low speed wind tunnel showing locations of the fan and the main test section (not to scale)..... 96

3-2 Main test section dimensions and Cartesian coordinate convention..... 96

3-3 Placement and orientation of the wing model in the main test section..... 97

3-4 Dimensions and geometries of the wingtip modifications..... 98

(a) Specifications of the tip tank, including locations of fin supports..... 98

(b) Specifications of the tip tank fins..... 98

(c) Specifications of a truncated tip tank fin..... 99

(d) Specifications of the round tip..... 99

3-5 System of numbering tip tank fin supports.....100

3-6 Tip tank fin combinations with their corresponding three-digit codes.....101

3-7 Arrangement and specifications of the five-hole flow angle probe.....102

3-8 Local flow angle and velocity conventions for measurement with the five-hole flow angle probe.....103

3-9 Main test section showing arrangement of experimental apparatus.....104

3-10 Transmission of data from the wing and wake measurements to the computer.....105

4-1 Flowchart showing summary of lift curve measurement procedure.....106

4-2 Rotational velocity distribution measurement procedure.....107

(a) The radial coordinates of a trailing vortex including downwash conventions (flow is out of the page).....107

(b) Sample rotational velocity distribution of the vortex shed from the round tip with $C_L = 0.33$ and $(z/c)_t = 4.1$.....108

5-1 Changes in the wing load distribution due to a wingtip device.....109

(a) Overall lift increase due to displaced wingtip vortex.....109

(b) Redistribution of lift due to a redistribution of the downwash pattern.....109

5-2 The trajectory of a wingtip vortex during completion of roll-up.....110

5-3 Rotational velocity distribution of the vortex shed from the round tip with C_L = 0.16 and $(z/c)_t$ = 1.5.....111

5-4 Rotational velocity distribution of the vortex shed from the round tip with C_L = 0.33 and $(z/c)_t$ = 12.0.....112

5-5 Resolution of the rotational velocity distribution due to the measurement procedure.....113

5-6 The uncertainty in measured peak rotational velocity due to an uncentered traverse through a vortex.....113

(a) An uncentered traverse. Here the vertical traverse is centered, and the horizontal traverse is slightly offset.....113

(b) The measured rotational velocity distribution from the traverse in (a).....113

6-1 Influence of outward cant angle on induced drag reduction, measured at the foremost and middle chordwise positions.....114

6-2 Influence of toe angle on induced drag reduction, measured for tip tank configurations 001 and 020.....114

6-3 Results from Mangler [30] and Weber [31] for the theoretical induced drag factor of a wing with endplates on the upper surface at the wingtips.....115

6-4 Experimental results from Spillman and Allen [12] for the influence of fin span on lift-dependent drag factor.....115

6-5 Influence of fin span on induced drag reduction for configuration 020.....116

6-6 Influence of lateral separation between successive fins on induced drag reduction.....116

6-7 The effect an additional fin has in furthering induced drag reduction.....117

6-8 Rotational velocity distributions of the wingtip vortex due to the round tip with $(z/c)_t$ = 4.1.....118

(a) C_L = 0.33.....118

(b) C_L = 0.50.....119

(c) C_L = 0.66.....120

(d) C_L = 0.82.....121

6-9 Rotational velocity distributions of the wingtip vortex due to the unfinned tip tank with $(z/c)_t$ = 4.1.....122

(a) C_L = 0.34.....122

(b) C_L = 0.51.....123

(c) C_L = 0.68.....124

(d) C_L = 0.85.....125

6-10 Rotational velocity distributions of the wingtip vortex due to device 020 with $(z/c)_t$ = 4.1.....126

(a) C_L = 0.35.....126

(b) C_L = 0.54.....127

(c) C_L = 0.72.....128

(d) C_L = 0.89.....129

6-11 Rotational velocity distributions of the secondary vortex due to device 020 with $(z/c)_t$ = 4.1.....130

(a) C_L = 0.35.....130

(b) C_L = 0.54.....131

(c) C_L = 0.72.....132

(d) C_L = 0.89.....133

6-12 Rotational velocity distributions of the wingtip vortex due to device 300 3@ - 5 with $(z/c)_t$ = 4.1.....134

(a) C_L = 0.35.....134

(b) C_L = 0.53.....135

(c) C_L = 0.70.....136

(d) C_L = 0.87.....137

6-13 Rotational velocity distribution of the secondary vortex due to device 320 3@ - 5 with $(z/c)_t$ = 4.1 and C_L = 0.90.....138

6-14 Rotational velocity distributions of the wingtip vortex due to device 001 with $(z/c)_t$ = 4.1.....139

(a) C_L = 0.36.....139

(b) C_L = 0.54.....140

(c) C_L = 0.72.....141

(d) C_L = 0.89.....142

6-15 Rotational velocity distribution of the wingtip vortex due to device 020 with a fin span of 0.65 c_t , $(z/c)_t$ = 4.1, and C_L = 0.70.....143

6-16 Rotational velocity distribution of the secondary vortex due to device 020 with a fin span of 0.65 c_t , $(z/c)_t$ = 4.1, and C_L = 0.70.....144

6-17 Rotational velocity distribution of the wingtip vortex due to device 020 with a fin span of 0.43 c_t , $(z/c)_t$ = 4.1, and C_L = 0.69.....145

6-18 Rotational velocity distribution of the secondary vortex due to device 020 with a fin span of 0.43 c_t , $(z/c)_t$ = 4.1, and C_L = 0.69.....146

6-19 Local Cartesian coordinates relative to a wingtip or a fin tip from which a vortex is shed.....147

(a) Conventions for a vortex shed from the round tip.....147

(b) Conventions for a wingtip vortex shed from a tip tank configuration.....147

(c) Conventions for a secondary vortex shed from a tip tank configuration.....147

6-20 Core radii of various main and secondary vortices 4.1 chord lengths behind the wing trailing edge.....148

6-21 The effect of a wingtip modification on the redistributions of circulation and vorticity, and on the shedding of secondary vortices.....149

(a) Distributions due to the unfinned tip tank.....149

(b) Distributions due to the finned tip tank.....149

6-22 Peak rotational velocities of various main and secondary vortices 4.1 chord lengths behind the wing trailing edge.....150

6-23 Intensities of various main and secondary vortices 4.1 chord lengths behind wing trailing edge.....151

6-24 Vortex positions in a cross-stream plane 4.1 chord lengths behind the wing trailing edge.....152

(a) C_L = 0.35.....152

(b) C_L = 0.53.....153

(c) Vortices due to shortened fins included, C_L = 0.71....154

(d) C_L = 0.88.....155

6-25 Mutual rotation of the main and secondary vortices due to configuration 020.....156

(a) Convection due to increasing lift, with $(z/c)_t$ = 4.1...156

(b) Convection due to increasing downstream distance, with C_L = 0.71.....157

6-26 Spanwise displacements of various main and secondary vortices, including the centroid of the 020 vortices, 4.1 chord lengths behind wing trailing edge.....158

6-27 The outboard displacement of a wingtip vortex with increased loading near the tip.....159

6-28 Vortex image systems for a reflection plane model in a rectangular test section, with flow out of the page....160

(a) Wingtip vortex centered on test section centerline.....160

(b) Wingtip vortex displaced from test section centerline...161

(c) Wingtip vortex displaced from test section centerline and accompanied by a secondary vortex.....162

I-1 Numbering of probe orifices, with view directed downstream into the probe.....171

I-2 Flowchart showing summary of five-hole flow angle probe calibration procedure.....172

I-3 Local roll angle as determined from the calibration data.....173

I-4 Local pitch angle as determined from the calibration data....174

I-5 Influence of pitch and roll angles on the dynamic pressure parameter.....175

I-6 Influence of pitch and roll angles on the static pressure parameter.....176

II-1 Sample plot for calibration of a Validyne transducer.....178

V-1 The Betz [34] roll-up model for a simply loaded wing.....192

V-2 Rate of change of wingtip loading as determined from the central rotational velocities of various main and secondary vortices 4.1 chord lengths behind the wing trailing edge.....193

LIST OF PLATES

3-1 Orientation of wing section FX61-163/SF in the main test section with the view directed downstream.....163

3-2 The wing fitted with the round wingtip.....163

3-3 One possible tip tank configuration showing fins placed at all three chordwise positions.....164

3-4 XY portable traversing mechanism with the five-hole flow angle probe, viewed downstream.....164

3-5 Close-up view of the five-hole flow angle probe with its calibration mount.....165

NOMENCLATURE

A	aspect ratio, b/c
A_e	effective aspect ratio, $A/(1+\delta)$
b	wingspan
C_D	total drag coefficient, $D/(\rho U_\infty^2 s/2)$
C_{D_i}	total induced drag coefficient, $D_i/(\rho U_\infty^2 s/2)$
C_L	total lift coefficient, $L/(\rho U_\infty^2 s/2)$
$C_{M_{1/4}}$	total quarter-chord moment coefficient, $M_{1/4}/(\rho U_\infty^2 sc/2)$
C_p	probe orifice pressure coefficient, $(p-p_\infty)/(p_T-p_\infty)$
$\bar{C}_p$	average of the peripheral probe orifice pressure coefficients
C_{p_s}	local static pressure coefficient, Equation I-3
C_{p_T}	local total pressure coefficient, Equation I-2
c	wing mean chord
c_t	wingtip chord, equivalent to mean chord
D	total drag
D_i	total induced drag
E	uncertainty, the estimated error in an experimental variable normalized with respect to the measured value

e	distance downstream of wing required for completion of vortex sheet roll-up, Equation 5-2
h	span of a fin or winglet
h_{ep}	endplate height
I	vortex intensity, Equation 2-9
i	toe angle of a fin or winglet
j	cant angle of a fin or winglet
K	parameter of Equation 5-1 which relates e to the wing load distribution
k	lift-dependent drag factor
L	total lift
l	sectional lift
$M_{1/4}$	lift-induced pitching moment about the quarter-chord
m	lift curve slope, Equation 2-2
m_R	lift curve slope of a reference wing configuration
m_0	two dimensional lift curve slope, 1.863π/radian
P	local dynamic flow parameter, Equation I-1a
$P_{cal}(\theta,\phi)$	local dynamic flow parameter measured from the calibration, Figure I-5
p	probe orifice pressure

p_T	main test section total pressure
p_o	wall tap static pressure
Q	local sidewash flow parameter, Equation I-1b
q	local dynamic pressure
q_T	test section dynamic pressure
q_∞	effective freestream velocity relative to the wing
R	local upwash flow parameter, Equation I-1c
Re_{c_t}	Reynolds number based on wingtip chord
r	radial distance originating from the center of a vortex
r_{max}	core radius (radial distance at which $(v_\phi)_{max}$ occurs)
r_1	radial limit of Equation V-1
S	local static flow parameter, Equation I-1d
$S_{cal}(\theta,\phi)$	local static flow parameter measured from the calibration, Figure I-6
S_t	planform area of a wingtip device
s	wing planform area, bc
U_∞	freestream velocity
u	local longitudinal velocity component

V_R	local resultant velocity
V_t	volume of a wingtip device
v	local sidewash velocity component
v_r	radial velocity of a vortex
v_x	axial velocity of a vortex
$v_\theta(r)$	rotational velocity of a vortex
$(v_\theta)_{max}$	magnitude of the peak rotational velocity
w	local upwash velocity component
X, Y, Z	main test section coordinates, Figure 3-2
X_c, Y_c	coordinates of the centroid between a main and a secondary vortex, Equation 6-2
x, y, z	wing coordinates measured from the wing root
x_t, y_t, z_t	wing coordinates measured from a tip, Figure 6-19
x_{min}	spanwise location of a local minimum of the wing vorticity distribution
x_o	spanwise displacement of a vortex center, measured relative to the wing root
x_i	inboard limit of Equation V-1
$\bar{x}(x)$	centroidal location of the spanwise vorticity distribution

GREEK SYMBOLS

α	wing geometric incidence
α_e	effective incidence of wing due to downwash
β	downwash-induced incidence
Γ_v	circulation of a vortex
Γ_w	circulation on the wing
Γ_o	wing root circulation
ΔA_e	change in effective aspect ratio due to a wingtip device, Equation 2-8
ΔC_{D_i}	change in induced drag due to a wingtip device, Equation 2-6
Δj	lateral separation angle between successive fins
Δp	pressure difference between opposing peripheral orifices of the probe
δ	load distribution factor of Equation 2-1
ε	load distribution factor of Equation 2-2
θ	local pitch angle of the flow
κ	induced drag factor, $1+\delta$
λ	local pitch angle of the flow in a vertical plane
μ	local yaw angle of the flow in a horizontal plane

ν	fluid kinematic viscosity
ρ	fluid density
σ, τ	wing cross-sectional coordinates, Table 3-1
ϕ	local roll angle of the flow
ψ	polar angle in a vortex cross section

SUBSCRIPTS

A,B	labels of results from separate wingtip configurations, for purposes of comparison
m	of a wing with a modified wingtip
u	of a wing with an unmodified wingtip; also uncorrected for the wind tunnel boundaries

INTRODUCTION

The drag due to the influence of the trailing vortex system generated by the wing of a transport or general aviation aircraft can account for as much as 50% of the total aircraft drag during climbing flight and a substantial portion of drag, typically 20%, even during cruise. This drag is due to downwash at the wing caused by the trailing vortex system. Attempts to reduce induced drag by providing the wing with endplates are reported from as early as 1897 when Lanchester obtained a patent for vertical surfaces at the wingtips. More recently, Snyder and Zumwalt [1] report the use of wingtip-mounted propellers to actively alter the downwash distribution along the wing. Other researchers [2]-[3] have diffused the wingtip vortex by introducing spanwise blowing at the tip, thereby reducing both induced drag and the vortex wake hazard encountered by following aircraft.

In 1976, Whitcomb [4] introduced small nearly vertical winglike surfaces, or winglets, mounted at the wingtips. These reduced the induced drag of a representative first-generation narrow-body jet transport by 20% at a design lift coefficient of 0.44 and a cruise Mach number of 0.78. Winglets also caused a 9% increase in the lift-to-drag ratio, more than twice the value obtained with a spanwise wingtip extension for the same bending moment penalty. Figure 1-1 shows the Whitcomb winglet, as it is now called, to be composed of two parts: a large aft-positioned upper winglet, canted outward 15^{o}, and a smaller winglet, placed ahead of and below the upper winglet, canted outward 36^{o}. Figure 1-2 provides conventions for both the cant angle

and the winglet incidence, or toe angle.

The Whitcomb winglet works in part like an endplate: it spreads the wake vorticity, with a subsequent vertical diffusion of the wingtip vortex and a consequent reduction in downwash. However, unlike an endplate, the winglet is also an efficient lifting surface. The significance of this may readily be seen in Figure 1-3, where the winglet utilizes the local flow around the wingtip to generate both a lift and a drag. These forces may be recombined into two components: an inwardly directly spanwise force, and a chordwise force, which provides a component of thrust in the direction of motion. The winglet thus tends to behave like a sail, over and above the mechanism of vorticity redistribution. In this manner the winglet is superior to an endplate, which is not an efficient lifting surface. In addition, Asai [5] has noted that a winglet is also superior to a spanwise wingtip extension, in that the winglet has a narrower chord and thus incurs a lower parasite drag penalty.

Whitcomb designed the winglet in an attempt to obtain the wing load distribution that would in theory provide minimum induced drag in subcritical flow. He admitted, however that his model was not optimum. More recently, other investigators [5] - [10] have altered the original geometry in order to further improve efficiency. Ishimitsu and Zanton [8], for example, changed the airfoil shape so that the winglet would work satisfactorily at low speeds yet not develop flow separation at high speeds. Some researchers have even done away with the lower winglet altogether. (Whitcomb proved its benefit to be marginal.)

The Whitcomb winglet and its descendants have seen use on jet transports such as the KC-135A [8], the L-1011 and DC-10 [9], the Canadair Challenger, as well as the Gates Learjet Model 28 Longhorn and Model 55 [10], and Model 28/29 [11]. Lighter aircraft such as sailplanes and general aviation aircraft might be better suited to the low speed wingtip devices discussed by Spillman and Allen [12]. These employ an array of inclined auxiliary winglike surfaces, or fins, each of which implements the sail mechanism of Figure 1-3. Spillman and Allen reasoned that because flow angles at the wingtip are highly dependent on the wing incidence, a single fin placed at the tip may experience upper surface flow separation at high incidences, or undersurface separation at low incidences. But, several fins arranged in a spiral cascade about the tip would reduce the tip flow angles to less severe values, and would thus reduce the likelihood of separation. The array should be cascaded in a direction opposite to that of the tip flow so that each fin but the foremost benefits from the downwash of the fin ahead. Of course, no fin should cross the wake of another - an angular separation of 15^{o} or more was suggested.

Spillman and Allen found the cascade of Figure 1-4a to increase the lift-to-drag ratio by 21% at a lift coefficient of 0.35, with a corresponding effective aspect ratio increase of over 40%. Here, three identical fins are mounted on the surface of a tip tank. An extensive set of wind tunnel measurements was conducted on the adjustable device of Figure 1-4b, where the number of fins, their position, and their angular spacing could be varied. The lift-dependent drag factor was reduced by 9% with one horizontal fin and by 29% with three fins. Because each additional fin contributed a

progressively smaller amount toward drag reduction, three or four fins were found to be adequate. It was also found that an array in which the fins were essentially horizontal gave the lowest lift-dependent drag for a given lift coefficient, and an array for which the fins were essentially vertical gave the lowest lift-dependent drag for a given wing root bending moment. Of these, the horizontal array had the lower lift-dependent drag.

Some other wingtip devices that are intended for low speed flight are those of Zimmer [13]. One of his wingtip configurations is illustrated in Figure 1-5a, where four fins are arranged in two inclined pairs. Within each pair, the fin incidences are set apart by 6^{o}. This placement forms an optimal biplane arrangement, so named because the aerodynamic performance of a biplane is maximized if the upper and lower wing incidences differ by about 6^{o}. Zimmer found this device to be more effective than a similar device, shown in Figure 1-5b, for which the fin incidences were set apart in equal increments. The configuration of Figure 1-6, which combines the optimal biplane arrangement with a triangular wingtip extension, was found to be superior when gains in aerodynamic performance were compromised with penalties in weight and drag. Water tunnel tests showed it to reduce total drag by 13% at a lift coefficient of 0.3.

The danger of the optimal biplane arrangement is that one fin may lie within the wake of another at low wing incidences. Also, if flow separation develops on the leading fin, the trailing fin may not benefit from the downwash. In addition, Zimmer's devices are essentially spanwise wingtip extensions and therefore may contribute a substantial amount to the bending moments along the wingspan,

especially at the wing root.

Asai [5] has noted that wingtip devices such as winglets have not seen widespread use on major new aircraft because designers are not fully convinced that a wing/winglet combination is more feasible than a planar wing. This is partly because there is no good theoretical explanation for the drag reduction mechanism. The intent of this work is to explore the mechanism through which auxiliary wingtip surfaces reduce induced drag and to provide criteria for optimizing the placement and geometry of these surfaces. This research is also concerned with the development of induced drag measurement techniques. Induced drag reduction is calculated from the measured change in the lift curve slope of a wing as it is fitted with different wingtip configurations. The effectiveness of a wingtip device may also be inferred from the extent to which the device redistributes vorticity on the wing and within the wingtip vortex. A five-hole flow angle probe, when traversed through the wingtip vortices behind different devices, affords comparisons of these vortices on the basis of their relative strengths and positions. Low speed wind tunnel experiments form the basis of the investigations.

2. THEORETICAL BASIS AND EXPERIMENTAL TECHNIQUES

2.1 THE INDUCED DRAG OF A LIFTING WING

A conventional planar wing generates a series of streamwise vortices distributed along its entire span. The vortices are shed from the wing trailing edge as a continuous sheet of vorticity which subsequently rolls up into two wingtip vortices some distance downstream of the wing, as shown in Figure 2-1. The wake vorticity is most intense near the wingtips, where the rate of change of the circulation distribution is greatest.

The streamwise vortices induce downwash along the wingspan. A typical downwash distribution is displayed in Figure 2-2a, along with the corresponding circulation distribution. The mechanism which relates downwash to lift is depicted schematically in Figure 2-2b, which shows a cross section of the wing. The downwash, w, and freestream, U_∞, velocities combine to produce a resultant effective freestream velocity, q_∞, which is displaced from the undisturbed freestream direction by an induced angle of incidence, β. As a result, the wing section lies at an effective incidence, α_∞, which is lower than the geometric incidence, α.

When the wing is placed in a stream of velocity q_∞, it experiences a force perpendicular to the direction of q_∞. The Kutta-Zhukovsky theorem expresses this force (per unit length in a spanwise direction) in terms of the bound vorticity on the wing: $\rho q_\infty \Gamma_0$. This force is the vector sum of the sectional lift $\rho U_\infty \Gamma_0$ and the sectional induced drag $\rho w \Gamma_0$, which are perpendicular to the

directions of U_∞ and w respectively. It can be seen that an increase in downwash reduces the magnitude of the effective incidence, and corresponds to an increase in induced drag.

As the downwash varies across the span so must the sectional induced drag, and a spanwise integration of the sectional induced drags produces the total induced drag. (Note that the downwash remains constant only along the span of a wing which has an elliptical lift distribution, and the total induced drag is a minimum.)

It follows that for the same geometric incidence, a three-dimensional wing lifts less strongly than a two-dimensional wing, which has no trailing vortices and no downwash. This is illustrated in Figure 2-3, which presents the linear portions of the lift curves for three configurations: a conventional planar wing, the same wing with a suitably modified wingtip, and a two-dimensional wing. Their respective lift curve slopes are labeled m_w, m_m, and m_o. A properly designed wingtip device reduces downwash and increases loading near the wingtips, thus making the wing more two-dimensional. This effect is reflected as an increase in the lift curve slope. Once modified, the wing can fly at a lower angle of attack for the same lift coefficient.

2.2 LIFT CURVE SLOPE COMPARISONS

The induced drag of a wing and the slope of its lift curve are related through their dependence on the downwash distribution from the trailing vortex system. One experimental technique of this work is to determine the reduction in induced drag due to a wingtip device by

measuring the corresponding increase in the lift curve slope. This method, although indirect, provides a fundamental measure of induced drag because both lift curve slope and induced drag rely on the same mechanism. This method also excludes the masking effects of viscous drag and form drag that would otherwise be present had the drag been measured directly.

Consider expressions for the induced drag and lift curve slope of a conventional wing:

$$C_{D_i} = \frac{C_L^2 (1+\delta)}{\pi A} , \tag{2-1}$$

$$m = \frac{m_0}{1+\frac{m_0(1+\varepsilon)}{\pi A}} . \tag{2-2}$$

The factors δ and ε are small numbers that account for the shape of the lift distribution and are both zero for a wing with an elliptical lift distribution. The lift curve slope for a two-dimensional wing is m_0 and its theoretical value is 2π per radian. If Equation 2-2 is solved for the geometric aspect ratio and substituted into Equation 2-1, a relation between induced drag and the slope of the lift curve is obtained:

$$C_{D_i} = C_L^2 \frac{(1+\delta)}{(1+\varepsilon)} \left[\frac{1}{m} - \frac{1}{m_0} \right] . \tag{2-3}$$

If a wing is fitted with a wingtip device, the resulting change

in induced drag may be calculated as a nondimensional percentage change where the unmodified wing is used as a baseline:

$$\Delta C_{D_i} = \frac{C_{D_{i_m}} - C_{D_{i_u}}}{C_{D_{i_u}}} \quad . \tag{2-4}$$

The unmodified and modified cases are represented by the subscripts u and m respectively. The change in induced drag as indicated by the measured lift curve slopes is obtained by substituting Equation 2-3 into Equation 2-4:

$$\Delta C_{D_i} = \left[\frac{1+\delta_m}{1+\varepsilon_m}\right]\left[\frac{1+\varepsilon_u}{1+\delta_u}\right]\left[\frac{m_o/m_m - 1}{m_o/m_u - 1}\right] - 1 \tag{2-5}$$

where the modified and unmodified cases are compared at the same lift coefficient. Although a wingtip device can be expected to alter the values of δ and ε for the wing, it appears reasonable to assume that the ratio of $1+\delta$ to $1+\varepsilon$ does not change appreciably when the wingtip is modified. With this assumption, Equation 2-5 reduces to:

$$-\Delta C_{D_i} = \left[\frac{1-m_u/m_m}{1-m_u/m_o}\right] \tag{2-6}$$

where $-\Delta C_{D_i}$ denotes induced drag reduction.

Equation 2-6 is the desired expression which relates changes in the lift curve slope to changes in induced drag. It can be seen that if a wingtip device causes the slope of the lift curve to rise, it also causes induced drag to be reduced.

An increase in the lift curve slope can also be shown to correspond with an increase in effective aspect ratio. If the effective aspect ratio of a wing is established as

$$A_e = \frac{A}{1+\varepsilon},$$

then Equation 2-2 may be rewritten as

$$m = \frac{m_0}{1+\frac{m_0}{\pi A_e}}$$

and solved for the effective aspect ratio in terms of the lift curve slope:

$$A_e = \frac{1}{\pi}\left[\frac{1}{m} - \frac{1}{m_0}\right]^{-1}.$$

This may be substituted into Equation 2-7, which is similar in form and function to Equation 2-4:

$$\Delta A_e = \frac{A_{em} - A_{eu}}{A_{eu}}, \tag{2-7}$$

so that the change in effective aspect ratio may be expressed as

$$\Delta A_e = -\left[\frac{1-m_m/m_u}{1-m_m/m_0}\right]. \tag{2-8}$$

It can be seen from Equation 2-8 that a wingtip device which increases the lift curve slope of a wing increases its effective aspect ratio as well. Note that this derivation is without simplifying assumptions. In contrast, the derivation for induced drag reduction required an estimate of the behaviour of the lift distribution in order to reduce Equation 2-5 to Equation 2-6.

2.3 FOUNDATIONS OF VORTEX WAKE ANALYSIS

A rolled-up vortex may be modelled as a rotating viscous core surrounded by a potential field. A cross section of a typical vortex in Figure 2-4a shows the rotational velocity, v_ϕ, to be tangent to the direction of swirl at any radial distance, r, from the center. The wing enters from the left side, and flow is out of the page. The velocities are radially distributed in the manner shown in Figure 2-4b. The velocities on the inboard side of the vortex follow a negative convention because they induce downwash on the wing. The core is seen to be bordered by the two rotational velocity peaks that flank the vortex center. These peaks are separated by a distance of $2r_{max}$ where r_{max} is the core radius.

The characteristics of a wingtip vortex are governed by the wing loading and tip geometry. A wingtip modification such as a winglet or an array of fins can alter the vortex wake considerably, including dispersion of the wake vorticity as well as changes in the number, strengths, and positions of the trailing vortices. A useful parameter for comparing the vortices shed from different wing geometries is the vortex intensity I. This may be defined as

$$I = 2\pi(rv_\theta)_{max} \quad . \tag{2-9}$$

The intensity of a vortex differs from its strength in that strength must be calculated using rotational velocities from the outer field of the vortex in order to avoid the turbulent and viscous actions which reduce velocities near the core. Because the measurements of this work are conducted in and near the core region, vortex comparisons based on intensity, though approximate, are more convenient and give a good indication of the relative strengths between different vortices. The differences between strength and intensity are treated fully in Section 5.2.3.

3. EQUIPMENT

3.1 WIND TUNNEL

All experiments were conducted in the University of Alberta low speed wind tunnel which is depicted schematically in Figure 3-1. It encloses two test sections within an unslotted closed-return channel. The upper portion houses a 200 HP fan and a test section that was not used for this work. A settling chamber and the rectangular main test section (8.0 x 4.0 x 36 ft) make up the lower portion. Filters and flow straighteners situated throughout the upper channel and just before the settling chamber reduce the air turbulence level in the main test section to a very low value, about 0.01%.

A maximum airspeed of 130 ft/sec can be achieved in the main test section, with a velocity profile uniform to within 1% when the test section is free of experimental apparatus.

3.2 TEST SECTION COORDINATE CONVENTION

The right-handed coordinate convention depicted in Figure 3-2 is used for the main test section. The origin is placed at the entrance to the test section on the centerline. The X-axis points horizontally toward the wall against which the wing is mounted and the Y-axis points vertically downward. The Z-axis coincides with the test section centerline.

3.3 WING SECTION

A wing section of 3.91 ft semispan was used as a reflection plane model to which wingtip devices could be attached. The section is described by Marsden [14] as FX61-163/SF, a slotted flapped version of a sailplane wing. It has a constant chord of 1.53 ft and the aspect ratio is 5.10. The wing is untwisted and untapered with 2.2% camber and 16.3% maximum thickness. Every test was performed with the flap completely retracted.

As noted in [14], the aerodynamic characteristics of the wing and its good performance at low Reynolds numbers make it suitable for light powered aircraft. It is thus well suited for the low speed measurements undertaken in this work.

A set of chordwise static pressure taps on the wing enabled measurement of the surface pressure distribution. The taps are located along the mid-semispan on the upper and lower surfaces, as well as on the flap. Table 3-1 lists the measured tap coordinates.

3.4 WING MOUNTING

The wing section was mounted horizontally with its spanwise axis normal to the test section walls. This is illustrated in Figure 3-3 and pictured in Plate 3-1. The wing was positioned approximately five chord lengths downstream from the test section mouth, with its tip near the test section centerline. Its base was held against a wooden platform with a steel rod. One end of the rod extended longitudinally into the wing at its quarter-chord point and the other end protruded

through the platform and a test section wall. A handle on this end allowed the wing incidence to be adjusted manually.

3.5 WINGTIP DEVICE SPECIFICATIONS

A variety of wingtip devices were created by affixing different combinations of airfoil shaped fins to a wingtip-mounted tip tank. The specifications of the tip tank and fins are provided in Figure 3-4.

Figure 3-4a describes the tip tank, which had a length of 1.64 c_t and a maximum thickness of 14% of its length. Its rear half retained seven fin supports that were distributed amongst three chordwise positions, one for each of three fins. Different wingtip configurations could be created by securing combinations of up to three fins to the tip tank, with no more than one fin per chordwise position.

Figure 3-4b specifies the fin dimensions. The fin airfoil shapes were modelled after that of the wing section UA(2)-180, which is known to have good characteristics at low Reynolds numbers. Every fin had a sharp unswept trailing edge, a mean chord of approximately 0.22 c_t, and a root chord limited to 0.33 c_t so that fins mounted at adjacent chordwise positions do not overlap. The fins were each twisted 5^{o}, enough to account for the variation in crossflow with radial distance from the wingtip, but not so much as to promote flow separation. Their spans vary slightly so that when they are mounted on the tip tank, their tips remain equally distant from the tip tank centerline. Each fin retained in its base a threaded rod and a pin at the one-third and three-quarter chord points respectively. The rod allowed the fin to be

bolted securely to the tip tank and the pin prevented fin rotation. The pin could be inserted into one of three pinholes provided with a fin support, thus allowing the fin root chordline to be fixed at a toe angle of -5^{o}, 0^{o} or $+5^{o}$. Fins are mounted such that their lift vectors point upward and/or toward the wing root. Plasticene, applied around the base of a fin, ensured a smooth cont ous fairing between tip tank and fin.

The leading edge of a fin placed at the foremost chordwise position lay just ahead of the crest of the main wing, $0.23\,c_t$ behind the wing leading edge. A distance of $0.054\,c_t$ separated the trailing edges of the wing and a fin placed at the middle position. A fin placed at the aftmost position extended horizontally in a spanwise direction with its trailing edge situated flush with the rearward tip of the tip tank.

The main set of tip tank measurements was complemented with a supplementary study in which the span of the fin for the middle chordwise position was varied. The fin was truncated from its tip to spans of $0.65\,c_t$ and $0.43\,c_t$, from an original span of $0.87\,c_t$. Figure 3-4c shows the dimensions of the shortened fin.

Finally, a rounded tip represented a standard of reference. The tip is specified in Figure 3-4d and is pictured with the wing section in Plate 3-2.

3.6 TIP TANK NUMBERING SYSTEM

The tip tank is illustrated once more in Figure 3-5. The order in which the fin supports are numbered is included as well. Each

numbered support allows a fin to be placed at a particular cant angle. The correspondence is listed in Table 3-2. Different fin combinations on the tip tank are identified by the three digit code

$$abc\ ,$$

where a, b, and c correspond to chordwise positions A, B, and C respectively, also shown in Figure 3-5. Each digit of the code contains the number of the support to which a fin is attached. If no fin is mounted at a given chordwise position, the corresponding digit is zero. For example, the tip tank configuration 301 signifies one fin placed at chordwise position A in hole number 3, no fin at chordwise position B, and one fin in hole number 1 at chordwise position C. The code 000 indicates an unfinned tip tank.

Toe angles are zero degrees unless otherwise indicated, as shown below:

026 6@ - 5,

for instance, indicates fins in the holes numbered 2 and 6, with the fin in hole 6 being toed out by five degrees. The fin in hole 2 is at a toe angle of zero degrees.

The truncated fin of Figure 3-4c was used exclusively on configuration 020. The variable fin spans are identified as follows:

020 - fin span at $0.87\,c_t$,

020 L1 - fin span of $0.65\,c_t$,

020 L2 - fin span of $0.43\,c_t$.

One possible tip tank configuration is pictured in Plate 3-3.

Here all three fins are employed: the foremost is uncanted, the middlemost is canted outward 45^{o}, and the rearmost is canted 90^{o}. The toe angles of all three fins are 0^{o}. This particular configuration, incidentally, has a form similar to that of the Spillman and Allen [12] cascade. Figure 3-6 provides an easy reference through which to identify different fin combinations: the tip tank configurations that are discussed in the results are pictured with their corresponding codes.

3.7 FIVE-HOLE FLOW ANGLE PROBE

The five-hole probe is modelled after one described by Wickens and Williams [15]. It may be used in an unknown flow field to determine the local flow angles, the local resultant velocity and its components, and the local total and static pressure coefficients. When placed in a vortex wake, the probe provides the local rotational velocity as well.

The probe is constructed from four stainless steel tubes arranged symmetrically about a fifth as shown in Figure 3-7. The outer tubes lie in pairs along two orthogonal planes centered on the axial tube. The faces of each pair are ground to an included angle of 90^{o}. That of the axial tube is ground normal to the probe axis.

Pressure differences between opposing outer tubes furnish the local flow angles when the probe is faced upstream in a nonaxial flow field. As Figure 3-8 shows, the local resultant flow velocity vector, V_R, forms a pitch angle, θ, with the probe axis in a combined pitch plane. A roll angle, ϕ, describes the orientation of

this plane with the vertical. The orientation of the local resultant velocity vector may also be described in terms of a pitch angle, λ, in the vertical plane and a yaw angle, μ, in a horizontal plane. These angles are also shown in Figure 3-8.

The resultant velocity vector at the tip of the probe may be separated into three mutually perpendicular components that lie parallel with the test section coordinate axes. Sidewash, v, and longitudinal, u, components point in the positive X and Z directions respectively, and an upwash, w, component points in the negative Y direction.

The tip design of the probe limits its application to impinging flows for which the local pitch angle does not exceed 45^{o}. The procedures for calibration and use of the probe are based on those provided in [15] and are outlined in Appendix I.

3.8 MEASUREMENT APPARATUS

The experimental arrangement, which is depicted schematically in Figure 3-9, enabled measurements of the wing surface pressure distribution, flow angles within the trailing vortex wake, and the test section airspeed.

The five-hole probe was mounted on a portable XY traversing mechanism, or traverse, which is pictured in Plate 3-4. A close-up view of the probe and its mount is provided in Plate 3-5. The traverse was always placed so that the probe tip lay in the same cross-stream plane as one of six wall taps, or stations, situated downstream of the wing. For example, Figure 3-9 shows the probe positioned at Station 4.

The wall taps, which were spaced every 4.0 ft along the test section wall at its mid-height, provided baseline pressures for wake analysis.

A pitot-static tube positioned about three chord lengths downstream of the wing and outside of the wake furnished the test section airspeed. The airspeed upstream of the wing was obtained from another pitot-static tube positioned near the entrance to the test section.

A mercury-in-glass thermometer inside the test section supplied the working air temperature and a mercury barometer provided the barometric pressure.

Figure 3-10 is a schematic diagram of the data acquisition system which is semi-automated, being run for the most part by a HP 85 minicomputer.

Validyne transducers receive pressure differences from the measurement apparatus and convert them to electronic signals through a variable reluctance principle. The responses are linearized by a set of carrier demodulators, one for each transducer. (The transducer calibration procedure is provided in Appendix II.)

Multiple lines from the wing pressure taps feed into ports of a scanivalve which in turn feeds into the wing Validyne. On command from the computer, the scanivalve is cycled through the lines, connecting each in turn to the transducer. The reference side of the Validyne is left open to the atmosphere, as is the zero port of the scanivalve. When the scanivalve is homed at its zero port, equal pressures are felt on either side of the wing Validyne, and the transducer may be zeroed.

Lines from the five-hole probe and the total pressure from the

test section pitot feed into another scanivalve in a similar manner. Here, a wall tap provides the reference pressure.

A scanner selects a particular transducer on cue from the computer, which in turn accepts the response through a digital multimeter. The data are then stored on magnetic tape for later use. The wing pressure distributions may be plotted as they are obtained by using a pen plotter.

An indexer steps the traverse in the horizontal and vertical directions in a cross-stream plane behind the wing. The sizes and number of steps may be specified by the operator.

The measurement system is powered by a 24 volt supply.

4. MEASUREMENT PROCEDURE

4.1 WING DATA ACQUISITION

This section outlines the procedure used to obtain the lift curve for the wing. The flowchart in Figure 4-1 accompanies the discussion.

The wing incidence is set to a desired angle after system start-up and with the wind at full speed. (The incidence must be set while the wind is at full speed because otherwise, as the wind accelerates, the lift-generated moment will cause the wing to slip by a few tenths of a degree.) The wing scanivalve is then cycled through the surface pressure taps until a pressure distribution has been obtained. At this point the wind is shut off.

Surface pressure taps are absent at the leading and trailing edges of the wing, so the pressures at these points must be estimated. The leading edge pressure is calculated from an average of two linear extrapolations, one from each of the upper and lower surface pressure distributions. The trailing edge pressure is found in like manner. An integration of the complete pressure distribution provides a sectional lift coefficient and hence one point on the lift curve. A complete lift curve is generated by repeating the measurements for different angles of attack.

The measurements are corrected for the test section walls; wind tunnel boundary corrections are summarized in Appendix III.

The wing operates at a Reynolds number of 1.0×10^6 based on the mean chord when the wind is at full speed. The Reynolds number based on the root chord of a fin is 0.33×10^6.

4.2 WAKE DATA ACQUISITION

Before the vortex wake behind a wingtip device was measured, the five-hole flow angle probe was positioned with its long axis parallel to the test section centerline and with its tip in line with a wall tap station. Then, with the wind at full speed, the vortex center was located by traversing the probe in a cross-stream plane until its central tube registered a minimum pressure. Rotational velocities were gathered by stepping the probe in 0.05 inch increments through the innermost two inches of the vortex. Two velocity distributions were measured, one along a horizontal radial axis and the other along a vertical axis. Radial coordinates originate from the vortex center, with positive directions as shown in Figure 4-2a. Also shown are the downwash sides of the vortex: these are taken to be the inboard and bottom sides.

The sample plot of Figure 4-2b was measured 4.1 chord lengths behind the wing fitted with the round tip for a lift coefficient of 0.33. Circle and square symbols enclose data from the horizontal and vertical traverses respectively. Rotational velocities are normalized with respect to the freestream velocity. The core limits are seen to be defined by the rotational velocity peaks on either side of the vortex center. Variations in the positions and magnitudes of these peaks due to vortex asymmetry or experimental uncertainties could be reduced by averaging the results from both distributions.

Apart from the initial survey in which the vortex center was located, the entire measurement procedure was automated.

5. VALIDITY OF THE MEASUREMENT PROCEDURE

5.1 LIFT CURVE MEASUREMENTS

5.1.1 Justification of Lift Measurement at Midspan

A total lift coefficient for the wing section could not be measured due to the nature of the experimental arrangement: either a force balance or a spanwise integration of the lift distribution is required to find total lift. Instead, the measured midspan sectional lift coefficient is used to generate the lift curve. This lift is assumed to be a reasonable approximation of the total lift for reasons that follow.

A wingtip device is suspected to affect the wing loading in two ways. These are illustrated schematically in Figure 5-1. First, a device increases the wing aspect ratio. It also displaces the wingtip vortex outward, resulting in reduced downwash across the wingspan. Thus, a wingtip device increases sectional lift at all spanwise stations, as shown in Figure 5-1a. A set of chordwise pressure taps will sense a lift increase no matter their spanwise location. Second, a wingtip device redistributes vorticity with a subsequent redistribution of downwash. Because vortex laws require that no vorticity is lost or dissipated in the near wake, reduced downwash near the wingtip must be associated with increased downwash across the rest of the wing. This causes the lift distribution to increase toward the wingtip and to decrease near the wing root, as shown in Figure 5-1b. Lift remains unchanged near the middle of the wing.

Both of these mechanisms occur simultaneously with the introduction of a wingtip device. Of the two the first is believed to

be more dominant: although minimal to immeasureable changes in midspan sectional lift are possible with the second mechanism, the results of Section 6.1 will show that substantial induced drag reductions (up to 26%) can be measured using pressure taps located at midspan.

5.1.2 Calculation of the Lift Curve Slope

The lift curve of the wing model is highly linear for lift coefficients between about 0.2 and 0.8, corresponding to uncorrected wing incidences of about -2^{o} and 5^{o}. This is the normal operating range of the wing. As the wing incidence is increased beyond this range, flow separation begins to develop on the wing upper surface, leading to a loss of lift. This is manifested in the lift curve as a departure from linearity. Likewise, reduction of wing incidence below the operating range leads to loss of lift due to undersurface separation. It was found that the location and extent of the linear range for the wing model depended slightly on the wingtip geometry. Before the lift curve slope could be measured, the endpoints of the linear range had to be determined.

Lift coefficients were always measured for a specific set of wing incidences which encompassed the linear range. This set contained uncorrected wing incidences between -4^{o} and 8^{o}, spaced 1^{o} apart. Additional half-degree steps were included at -3.5^{o}, -2.5^{o}, and 8.5^{o}, in order to better define the regions where the lift curve becomes nonlinear. In all, sixteen points make up the lift curve.

The lift curve data were grouped into a series of twenty-five intervals, each with different endpoints. The endpoints were taken

from the first five and last five data points. Each interval thus enclosed points corresponding to uncorrected wing incidences between -2^{o} and 5^{o}. Linear regressions were performed on the intervals, and the lift curve slope was obtained from the interval which had the highest correlation coefficient. Linearity was found to be excellent for the lift curves of all wingtip configurations: a typical value for the correlation coefficient was about 0.9999.

The advantage of this method is that it uses as many data points as possible while avoiding departures from linearity. As well, it is automated and runs quickly. It is thus more flexible than a procedure where the slope is found for a fixed, prespecified domain of wing incidences.

5.1.3 Sensitivity of the Calculations

One can differentiate Equation 2-6 to find the sensitivity of calculated induced drag reduction to changes in lift curve slope. Equation 2-6 in functional form is

$$-\Delta C_{D_i} = f(m_w) . \qquad (2\text{-}6)$$

Differentiating,

$$d(-\Delta C_{D_i}) = \frac{\partial f(m_w)}{\partial m_w} dm_w .$$

where the sensitivity is given by the partial derivative. This results in

$$d(-\Delta C_{D_i}) = \frac{m_w / m_w^2}{1 - m_w / m_0} \, dm_w$$

Dividing through by Equation 2-6 and rearranging,

$$\frac{d(-\Delta C_{D_i})}{-\Delta C_{D_i}} = \frac{1}{m_m/m_u - 1} \frac{dm_m}{m_m} .$$

This may be rewritten in terms of the uncertainty, E :

$$E(-\Delta C_{D_i}) = \frac{1}{m_m/m_u - 1} E(m_m) .$$

Note that if the uncertainty of lift curve slope measurement is the same for all tests, then uncertainties in calculated induced drag reduction decrease with increasing lift curve slope.

Some results from Section 6 (Table 6-1) will be borrowed at this point in order to demonstrate the sensitivity of the relation given above. For example, if the unmodified tip tank is used as a reference, then m_u is 1.358 π/radian. If one uses the lift curve results for configuration 300, which performed marginally well with an induced drag reduction of 6.1%, then m_m is 1.381 π/radian and the sensitivity takes on a value of 59.0. That is, if the uncertainty in m_m is, say, 0.1% then the corresponding uncertainty in induced drag reduction is 5.9%. The sensitivity is seen to improve remarkably as the performance of a wingtip device improves. For example, configuration 321 was the best overall configuration with a lift curve slope of 1.463π/radian and an induced drag reduction of 26.0%. Here, the sensitivity works out to a value of 12.9. Although an exact numerical value for $E(m_m)$ (and hence for $E(-\Delta C_{D_i})$) was not found, the measured lift curve slopes are believed to be very precise for reasons

which may be found in the next subsection.

5.1.4 Precision of the Lift Curve Results

Two sources of error may be associated with lift measurement. One is associated with experimental inaccuracies and leads to scatter in the lift curve data. Because the lift curve slope is a derivative, it is highly sensitive to this type of error. Yet, as was discussed in Section 5.1.2, the data had extremely high correlations, indicating very little scatter over the linear range. The other error source is associated with the lift measurement technique. That is, even though a lift coefficient can be measured with high precision, it may not match the true total lift coefficient. Here, there are two causes for error: the test section walls impose constraints on the airflow; and the total lift is approximated with the midspan sectional lift. A supporting discussion for the latter was provided in Section 5.1.2. As well, wind tunnel boundary corrections were applied in order to counter the influence of the test section walls. The measured lift is therefore believed to be representative of the true lift.

5.2 VORTEX WAKE ANALYSIS

5.2.1 Underlying Assumptions

Five basic assumptions are implied in the analysis of a vortex wake:

1. Interference between the five-hole flow angle probe and a trailing vortex is minimal.

2. The trailing vortex sheet has rolled up in a complete and orderly fashion.
3. The wake has not decayed appreciably.
4. The rolled-up vortex is axially symmetric.
5. Constituents of a multiple-vortex wake may be treated separately.

These assumptions are justified in the subsections that follow.

a) **Probe/Vortex Interaction**

The trajectory of a trailing vortex tends to approach the freestream direction asymptotically as the vortex rolls up, as shown in Figure 5-2. It is thus reasonable to assume that the axis of an essentially completely rolled-up vortex is parallel with the free-stream direction.

As noted by Uzel and Marchman [16] and by Mason and Marchman [17], a measurement probe placed in a vortex core disturbs it least if the probe and core axes are coincident. It is therefore assumed that the five-hole probe may be faced directly upstream so as to minimize vortex disturbance.

b) **Completion of Roll-up**

The trailing vortex sheet is assumed to wrap around itself in an orderly fashion such that vorticity shed from the wingtip winds up in the center of the completely rolled-up vortex. The outer layers of the vortex are made up of vorticity shed from near the wing root. Figure 5-2, which includes a cross-sectional view of the trailing vortex sheet, illustrates the manner of roll-up.

The rate of roll-up and the degree to which it is complete at a particular point downstream depend in part on the wing loading. Spreiter and Sacks [18] have noted that with higher loading near the wingtip, the shed vorticity is more intense and rolls up at a faster rate. In fact, Corsiglia et al [19] mention that a rectangular wing with rectangular loading precipitates an extremely rapid rate of roll-up. With more conventional wings, Rossow [20] states that roll-up is generally practically complete within three to five span lengths behind an aircraft.

Spreiter and Sacks found that the downstream distance, e, at which roll-up is complete for a lifting wing may be expressed as

$$\frac{e}{c} = \frac{K A b}{C_L c}, \tag{5-1}$$

where c is the mean chord of the wing. For a wing with elliptical loading, $K = 0.28$. Specifically, the equation for the wing section that was used in this work, a flat rectangular wing with an aspect ratio of 5, is

$$\frac{e}{c} \simeq \frac{2.5}{C_L}, \tag{5-2}$$

where data from Figure 9 of [18] have been used. For the range of lift coefficients that were used in this work, Equation 5-2 implies that roll-up is complete between about three and seven chord lengths behind the wing section.

These results may be applied to the measured rotational velocity distributions for the wingtip vortex at several points downstream of

the wing section. The wing is fitted with the round tip. Figure 5-3 shows the distribution about 1.5 chord lengths behind the wing trailing edge for a lift coefficient of 0.16. The breaks in the velocity distribution indicate that the vortex sheet is still in the early stages of wrap-up. Figure 4-2b (the sample plot of Section 4.2) shows roll-up to be much closer to completion 4.1 chord lengths behind the wing trailing edge for a lift coefficient of 0.33. There is little change between this distribution and that of Figure 5-4, which was measured at the same lift coefficient and a downstream distance of 12.0 chord lengths.

Most wake analyses were performed 4.1 chord lengths behind the wing. Strictly speaking, roll-up is not always fully complete at this point. Nevertheless, on the basis of the data presented in the preceding discussion, roll-up has proceeded to a degree that it may be deemed essentially complete.

c) **Vortex Wake Decay**

Viscosity does not take on significance until much later stages in wake evolution. Long after the entire vortex sheet has rolled up into trailing vortices, they begin to decay through viscous interactions and sometimes through internal fluctuations of turbulence and axial velocity.

It is assumed that decay processes have not been initiated at points where wake measurements are conducted. This assumption is based once again upon a comparison of Figures 4-2b and 5-4, which shows little change in the cross-sectional characteristics of the wingtip vortex as it is carried to the end of the test section. A

rotating vortex is usually stable enough that the time scale required for decay is much greater than those used in this work.

d) **Axial Symmetry**

In order to simplify the wake analysis, a rolled-up vortex is assumed to be axially symmetric. Although downwash in the region of the wing can tend to increase the rotational velocities on the inboard side of the vortex, this will be noted in Section 5.2.2 to be slight and therefore negligible. Also, Westwater [21] and Moore [22] mention in their numerical studies of wake evolution that the vortex can take on a distinctly elliptical shape, but this occurs at time scales comparable to those of decay and is not considered to present a problem.

e) **Multiple-Vortex Wakes**

Some wingtip devices may cause multiple-vortex wakes to be shed from either side of a wing. This phenomenon is not a new or unusual one, endplates and flaps also cause secondary vortices to be shed.

The number, positions, and strengths of the shed vortices are determined by the shape of the load distribution on the wing. The mechanism of multiple vortex shedding is treated fully in Section 6.2.4.

Closely spaced vortices may interact and/or merge with each other. Turbulent transport and the subsequent diffusion of vorticity are caused by the straining interactions between vortices. However, merging is not always a necessary consequence of a multiple-vortex

wake. Its occurrence depends on the signs and strengths of the vortices, as well as their separation distance. According to Bilanin et al [23], vortices of like sign and equal strength will merge if close enough, and it was found in [24] that a weak vortex will convect around a strong vortex without significantly altering the strong vortex.

Given enough time, the constituents of a multiple-vortex wake may interact so as to destroy axial symmetry and complicate the wake analysis severely. However the time scales required for interaction are generally very large, and the very weak secondary vortices that were encountered in this work are believed to have a minimal effect on the wingtip vortex. It is assumed, then, that each vortex in a multiple-vortex wake may be viewed as distinct from the rest.

5.2.2 PRECISION OF THE WAKE RESULTS

Figure 5-5 demonstrates that even with a fine point spacing the peak of the rotational velocity distribution may not be accurately defined. In order to increase resolution and reduce errors in both the measured magnitutude of the peak velocity and its radial position, a very fine point spacing (0.05") was used. The core radius is therefore resolvable to within one half of this spacing, or 0.025".

The measured core position was found to be repeatable to within 0.13". Thus, the flow angle probe could not always be passed precisely through the vortex center as desired. An example of this problem is illustrated in Figure 5-6a which shows a cross section of the vortex. The horizontal traverse is shown to be offset slightly

from the center, whereas the vertical traverse remains on an axis of symmetry. The resulting measured velocity distributions are depicted in Figure 5-6b. It can be seen that the horizontal traverse measures velocities that are lower than the true values. As well, the measured core radius is smaller.

Other factors contribute to uncertainty in measured peak rotational velocity. For one, the flow angle probe becomes increasingly less accurate in regions with high flow angles (near 45^{o}), particularly within the core. As well, most of the measured rotational velocity distributions were found to be slightly asymmetric: velocities on the inboard side of a vortex were up to about 5% higher than those on the outboard side. This might be caused by downwash from the wing bound vortex which tends to increase velocities on the inboard side of a trailing vortex. Asymmetry may also be due to incomplete vortex roll-up.

In order to reduce the margin of error, the peak rotational velocities and core radii as measured from both the horizontal and vertical traverses were averaged.

5.2.3 Distinction Between Vortex Strength and Intensity

A wingtip device redistributes vorticity on the wing and in the wake with a consequent change in strength of the wingtip vortex. Vortex strength is best calculated with rotational velocities measured in the irrotational outer field, where the measurements are least susceptible to viscous interactions and turbulent fluctuations near the core region. As well, some researchers [25]-[27] have noted

that most vorticity is diffused into the wake, so that unless measurements are conducted across much of the outer regions of the vortex, the calculated strength will be much less than that indicated by the Kutta-Zhukovsky theorem:

$$l = \rho U_{\infty} \Gamma_{o} .$$

For example, Donaldson and Bilanin [26] discovered that only 54% of the total circulation of a vortex may be found within a vortex radius of $r/(b/2) < 0.10$. The measurements of this investigation, however, are made within a radius of $r/(b/2) < 0.021$ in order to accurately define the core limits. Here it is more convenient to use the peak rotational velocity to estimate vortex strength.

A measure of vortex strength is the intensity, I, which was defined as

$$I = 2\pi (r v_{\theta})_{max} . \qquad (2\text{-}9)$$

A distinction between strength and intensity must be made because the extent to which viscosity affects the velocities near the core edge is unknown. Turbulence can also affect these velocities but it is not known if the vortices of this work are laminar or turbulent. For a laminar vortex, the intensity takes on a theoretical value of 0.716. This result is presented in Appendix IV along with an extended discussion on turbulent vortices. As well, other uncertainties in the measured peak rotational velocity were discussed in the previous

subsection. Nevertheless, it is desired only to compare different wingtip vortices on a qualitative basis. Here, then, intensity is a sufficient indication of strength.

6. DISCUSSION OF RESULTS

6.1 LIFT CURVE RESULTS

In order to redistribute the wake vorticity, a wingtip device must generate circulation (lift) so as to draw off some of the bound vorticity from the wingtip vortex. The effectiveness of the device is determined by geometrical details such as the span and twist of each fin, as well as their placement and orientation with respect to the wingtip. A technique to measure the overall effectiveness would allow experimental evaluation of the effect of changes in the device geometry. In this investigation an indirect determination of induced drag is derived from a measurement of changes in the lift curve slope as was discussed in Section 2.2.

Table 6-1 lists the measured lift curve slope, induced drag reduction, and effective aspect ratio increase due to each wingtip configuration. Equations 2-6 and 2-8 are reproduced below for the reader's convenience.

$$-\Delta C_{D_i} = \left[\frac{1-m_w/m_m}{1-m_w/m_e}\right] , \tag{2-6}$$

$$\Delta A_e = -\left[\frac{1-m_m/m_w}{1-m_m/m_e}\right] . \tag{2-8}$$

The unmodified wingtip here is taken to be the unfinned tip tank. Thus, $m_w = 1.358\,\pi$/radian, which is an average of two repeatability

runs (labelled #1 and #2) that were measured for this configuration. As well, Marsden [14] has found the two dimensional lift curve slope for wing section FX61-163/SF to be 1.863π/radian. This value is used for m_o rather than the theoretical value of 2π /radian for a thin wing.

The induced drag reduction (5.8%) and effective aspect ratio increase (6.1%) due to the unfinned tip tank are obtained from a comparison with the round tip. For this case only, m_o = 1.336π per radian, which again is an average of two repeatability measurements. The unfinned tip tank improves performance for two reasons: it extends the wing farther in a spanwise direction than does the round tip and thus carries the load distribution outward to a greater extent; and it has more surface area than the round tip, so the local flow angles round the wingtip are reduced. The latter of these was noted by Spillman and Allen [12] for their tip tank.

Finally, it should be noted that the measured induced drag reductions of Table 6-1 are highly repeatable. However, because the repeatability measurements for a given wingtip configuration are composed of only two runs, there are not enough data to accurately estimate a value for the repeatability.

6.1.1 Effects of Wingtip Geometry on Performance

a) Chordwise Position of a Fin

The importance of the chordwise location of an auxiliary fin is determined by the extent of flow interference between the fin and

wing. Flow separation on the wing might occur if the fin were located near the position of the wing pressure peak, so the fin should be placed either ahead of or behind this peak. Whitcomb's results [4] support this conjecture: as long as the winglet leading edge did not exceed the wing crest, the flow interference between wing and winglet that could promote separation was minimized. Although these results were obtained under supercritical conditions, none of the low speed devices of Spillman and Allen [12] had fins which exceeded the wing crest either.

The tip tank was constructed in accordance with these considerations: all fins were placed aft of the wing crest. As a result, no tests were performed to determine the consequences of a fin placed ahead of the crest. Perhaps it should be noted at this point that other researchers at the University of Alberta have since performed a supplementary set of winglet tests, after the measurements of this work were completed. An induced drag reduction of 26% was obtained for one particular winglet whose leading edge lay flush with the wing leading edge. Unfortunately, time limitations permit no more than this brief note.

Several tip tank configurations are compared in Table 6-2 on the basis of improvement in induced drag reduction due to changes in the chordwise location of a fin while the cant angle and toe angle are held constant. The reader may find the diagrams of Figure 3-6 to be a helpful visual aid in the discussion that follows.

A comparison of the results for configurations 300 and 050 shows induced drag reduction to improve by 5.2% when a fin with 90^{o} cant is moved from the rearmost chordwise position to the middle chordwise

position. This trend is once again evident upon comparison of configurations 301 and 051: induced drag reduction improves by 3.8%. The improvement is due to the fact that a fin at the rearmost position lies entirely behind the wing in a region where downwash patterns have already been established and flow angles are high, and is therefore susceptible to flow separation. In fact, flow visualization (Section 6.3.1) showed extensive flow separation to exist on this fin. By toeing the fin outward through 5^{o}, the separation regions could be reduced in size somewhat. Nevertheless, because flow separation prevents the fin from generating lift to its full potential, the result is poor induced drag reduction (6.1%).

Apart from these results, Table 6-2 provides no conclusive evidence through which to optimize fin placement. If a fin is canted 45^{o}, it would appear to be better placed at the middle chordwise position, whereas if it were uncanted, it should be placed at the foremost chordwise position. According to the results of other investigators, an optimal chordwise placement appears to be one for which the trailing edges of fin and wing are flush. Whitcomb [4], for example, recommended that this be the case on the basis of some exploratory investigations, but he gave no physical explanation. As well, the arrays of Spillman and Allen [12] were arranged so that the trailing edges of the aftmost fin and the wing were aligned.

b) **Cant Angle**

The result of canting a vertical fin outward is to allow easier fairing of the tip tank/fin intersection and thus reduce the

possibility of flow separation. According to Heyson et al [29] the benefit of a single winglet over a spanwise wingtip extension is best for small cant angles. In fact, studies of the Whitcomb winglet and its variations indicate a cant angle of 15^{o} to be near optimum [11]. As well, Spillman and Allen [12] noted that canting vertical endplates outward by only 5^{o} can reduce induced drag considerably.

Although a small outward cant may be best for a single near vertical fin or winglet, larger cant angles are required for multiple-fin arrays. Each following fin must be canted further outward than the fin directly ahead so as to allow beneficial mutual interference between the fins. As a consequence, the cant angles of the foremost and aftmost fins can differ by as much as 90^{o}. For these arrays, highly canted fins tend to behave as tip extensions and fins with little or no cant behave more like endplates.

The role of large cant angles in induced drag reduction was tested by using a single fin attached to the tip tank at a specific chordwise position. The fin was given successively increasing degrees of cant, with the lift curve of the wing measured at each step. The resulting induced drag reductions are displayed in Figure 6-1, along with the corresponding tip tank configuration codes. Results are presented for the foremost and middle chordwise positions only; there was no provision at the aftmost chordwise position for any cant angles other than 90^{o}.

The effect of outward cant at the middle chordwise position is quite pronounced. Figure 6-1 shows a cant angle of 45^{o} to improve induced drag reduction by approximately 4.5% over cant angles of 0^{o} or 90^{o}. Induced drag reduction appears to be nearly independent of cant

angle at the foremost chordwise position, at least for cants of up to 45^{o}. It is not known if this trend continues for higher cant angles.

It should be noted that the results of Figure 6-1 contain some inconsistencies. For example, note the difference in toe angle for the two chordwise positions: at the foremost position, a fin is toed out 5^{o} whereas it is untoed at the middle position. Note also the difference in cant angle domains. It follows that a direct comparison of the cant angle results from both positions cannot be made because of these differences. Unfortunately, time limitations and the tip tank geometry did not allow for circumstances other than these.

Configuration 020 reduces induced drag by 17.0%, more than any other configuration of Figure 6-1. This configuration was also observed to shed a strong fin vortex secondary to the wingtip vortex. Evidently, vorticity redistribution in the wingtip region contributes to the superior induced drag reduction. It appears that the fin has an ideal orientation relative to the tip flow so as to induce secondary vortex shedding. For now, it will suffice to say that no fin at any other cant angle or chordwise position shed as strong or as noticeable a vortex. Section 6.2 examines this result in detail.

c) **Toe Angle**

As Conley [10] pointed out, an untwisted winglet must necessarily be toed outward because the variation in crossflow away from the wingtip may otherwise promote flow separation on the winglet upper surface. Also, in light of the sail mechanism shown in Figure 1-3, a toed-out winglet can increase the magnitude of thrust in the direction

of motion.

Parasite drag and bending moments increase with toe-out to the point where they nullify reductions in induced drag, so an optimum toe-out angle will depend on the wing load limits and the flight conditions. According to Conley, toe-out need not be more than a few degrees.

The influence of toe angle on induced drag reduction was studied for two tip tank configurations: one configuration (001) retained a single vertical fin at the foremost chordwise position, and the other (020) retained a single fin, canted outward 45^{o}, at the middle chordwise position. These are the two single-fin configurations that were found to reduce induced drag the most when the fins were untoed. The toe angle results are presented in Figure 6-2.

Both configurations show a noticeable drop in effectiveness when a fin is toed from 0^{o} to -5^{o}. The losses in induced drag reduction are 3.7% and 7.1% for the 020 and 001 configurations respectively. These results appear to contradict Conley's finding for the Whitcomb winglet that a small degree of toe-out improves performance. The Whitcomb winglet, however, is untwisted and needs to be toed out at the root to take advantage of the large inflow angles near the upper surface of the wing at the wingtip. In addition, the Whitcomb winglet is intended for near sonic flow speeds. The inflow angles are much lower for the tip tank because it works in incompressible flow and it increases the surface area of the wingtip. As a consequence, a toed-out fin cannot provide as much lift as an untoed fin because it is at a lower incidence relative to the tip flow. As well, the fin airfoil sections have a zero lift angle of -5^{o}, so the fins do not generate as much

lift when they are toed out by 5^{o} as they do when they are untoed. The marked difference in performance between configurations 020 2@-5 and 001 1@-5 may be explained in terms of the cant angle. Because the fin of configuration 020 2@-5 is canted outward, its incidence with respect to the tip flow increases with increasing wing incidence. The fin thus generates more lift and increases induced efficiency more than the uncanted fin of configuration 001 1@-5.

Both tip tank configurations experience a loss in effectiveness when their fins are toed from 0^{o} to 5^{o}. The losses, 2.5% and 0.3% for the 020 and 001 configurations respectively, are much less severe than these for toe-out apparently because a fin with toe-in is at a high incidence relative to the tip flow direction and can consequently generate a higher lift force. This lift would normally be expected to be greater than that for an untoed fin, which is at a lower incidence relative to the direction of flow round the wingtip. However, because the local flow rapidly turns toward the freestream direction with increasing radial distance from the wingtip, the outer portion of a toed-in fin is at a high incidence relative to the freestream direction. It has a larger projected area in a cross-stream plane than does an untoed fin, so it experiences a slight increase in parasite drag. Similarly, a toed-out fin also experiences a drag increase.

These results suggest that tip tank fins that are given an optimum or near optimum amount of cant must be untoed if they are to operate in incompressible flow. Unfortunately, there are not enough data to support a correlation between toe angle and cant angle.

d) **Fin Span**

Mangler [30] and Weber [31] conducted endplate studies that indicated spanwise loading in the region of the wingtip is heavily dependent on the endplate height. They calculated the effect of height on the induced drag factor κ, which is obtained from Equation 2-1 and relates induced drag to the total lift coefficient:

$$\kappa = \frac{C_{D_i}}{C_L^2/\pi A} .$$

Their results for an elliptical wing with vertical endplates on the upper surface are replotted in Figure 6-3. The induced drag factor follows a continuous decline with increasing endplate height.

Because a winglet is a form of endplate, its span is expected to be a dominant factor in induced drag reduction. This is because with increasing span, a winglet can generate more lift. Whitcomb [4] found induced drag to decrease slightly less than linearly with increasing winglet span. In addition, Spillman and Allen [12] showed the lift-dependent drag factor of a wing with a single horizontal fin to decrease steadily with increasing fin span. This result is reproduced in Figure 6-4. Unfortunately, the plots of Figures 6-3 and 6-4 cannot be superimposed because lift-dependent drag is only partly composed of induced drag. Nevertheless, both curves can be seen to exhibit similar trends.

The preceding results contrast with those given in Figure 6-5. Here, lift curves were measured for the 020 configuration with three different fin spans: 0.43 c_t , 0.65 c_t and 0.87 c_t . Although

induced drag reduction improves with increasing fin span, the curve is not continuous. Drag reduction appears to be roughly span-independent at about 8% for fin spans between 0.43 c_t and 0.65 c_t . A marked increase in effectiveness is shown for spans above 0.65 c_t , with induced drag reduction reaching 17.0% for the greatest span tested, 0.87 c_t .

A definite conclusion cannot be drawn from the data of Figure 6-5 because the curve is composed of only three widely-spaced points. Changes in fin span, however, will be seen in Section 6.2.1 to have pronounced effects on the vortex wake. Here, an explanation for the discontinuity in Figure 6-5 may lie in the redistribution of vorticity. The 020 configuration was observed to shed a strong secondary vortex no matter the fin length. Although the position and intensity of the vortex was found to vary with fin span, the pattern of variation was not continuous.

It is important to note that the endplates of Mangler and Weber were uncanted, whereas the fin of Spillman and Allen was oriented horizontally. One would expect, then, that the similar trends of Figures 6-3 and 6-4 should have little dependence on cant angle and should be evident in Figure 6-5. However, the differing geometries of the fins and endplates forbid a direct comparison.

The optimized spans of fins in a multiple-fin array must compromise induced drag reduction with increases in parasite drag and bending moment. The vertical foremost fin should probably have the greatest span as it must produce significant side forces. The horizontal aftmost fin should have the least span so that the wing root bending moments do not become too severe. An intricate test

program would be required to explore the full effects of span variation in a multiple-fin array.

e) Mutual Interference Between Fins

The lateral separation, Δj, of a wingtip configuration may be defined as the difference in cant angle between successive fins. It is the lateral separation which determines the extent of mutual inference between adjacent fins: with increasing separation, a trailing fin is placed further away from the downwash field of a leading fin and is less able to benefit from that downwash.

In order to test the role of mutual interference between fins in effecting induced drag reduction, lift curve measurements for several multiple-fin tip tank configurations with lateral separations ranging from 22.5^{o} to 90.0^{o} were conducted. The fins were always spiralled in a direction opposite to that of the wingtip flow so that the rearmost of a pair of fins was canted further outward than the foremost. The resulting induced drag reductions are compared against the lateral separations in Figure 6-6. A tip tank configuration code accompanies each data point on the plot. (Data for a lateral separation of zero degrees are not provided because they come from devices for which one fin lies within the wake of another.) The results as shown in the plot suggest no simple correlation between drag reduction and lateral separation. In fact, it would appear that lateral separation has little influence on induced drag at all.

f) Incremental Influence of an Additional Fin

The results of Figure 6-6 imply that these devices do not employ

mutual interference between fins as a drag reduction mechanism. Rather, the extent to which a given multiple-fin configuration reduces induced drag depends on how much each fin of the configuration performs when acting alone. For example, consider the single-fin configuration 020, which retains a fin canted 45^{o} at the middle chordwise position. This device reduced induced drag by 17.0%, more than any other single-fin configuration that was tested. It is seen in Figure 6-6 that multiple-fin configurations which retain this fin as a component (ie: devices 321, 021, 320, and 026 6@-5) have, on average, superior induced drag reduction compared to the other devices. When configuration 020 is combined with configuration 001, which also had high induced drag reduction (14.8%), the results are clearly superior: multiple-fin configurations 021 and 321 both reduced induced drag by over 25%, more than any other multiple-fin configuration.

These observations indicate that the influence of an additional fin in furthering induced drag reduction depends on the effectiveness of that fin. It will be shown here that the incremental influence of an additional fin also contributes a progressively less amount to induced drag reduction with increasing effectiveness of the original configuration. This effect was noted by Spillman and Allen [12] who found that three or four fins in an array was near optimum, and that little could be gained with the addition of more fins.

The preceding discussion implies that given two wingtip configurations A and B, which differ only in that configuration B retains an additional fin which is absent in A, the incremental change in lift curve slope between A and B should depend on the

magnitude of the lift curve slope for the original configuration A. That is,

$$m_B - m_A = f(m_A) ,$$

where f is some unknown functional dependence.

The dependent and independent variables of this equation may be normalized with respect to the lift curve slope of some reference configuration, m_R, and the two-dimensional lift curve slope, m_0, as follows:

$$\frac{m_B - m_A}{m_B - m_R} = g\left(\frac{m_A - m_R}{m_0 - m_R} \right) \qquad (6\text{-}1)$$

where g is another unknown function. The possible domains and ranges are

$$m_R \leq m_A \leq m_0 : \quad 0 \leq \frac{m_A - m_R}{m_0 - m_R} \leq 1 ,$$

$$m_R \leq m_A \leq m_B : \quad 1 \geq \frac{m_B - m_A}{m_B - m_R} \geq 0 .$$

That is, g takes on a value of 1 if the initial wingtip configuration is the reference configuration. The functional dependence tends to zero as the lift curve slope of the inital wingtip configuration approaches m_0.

The unfinned tip tank is used as a reference here, so that m_R is $1.358\,\pi$/radian. The variables of Equation 6-1 are tabulated for several sets of tip tank configurations A and B in Table 6-3. The

sets are categorized by fin support number: this is the fin support of configuration B into which an additional fin has been placed. Note the absence of any mention of fin support 4 in Table 6-3. The only case for which an additional fin could be placed into support 4 while keeping fins spiralled opposite to the tip flow direction is one where configuration 300 is transformed into configuration 340. However, the poor performance of the horizontal aftmost fin (configuration 300) was discovered early during testing so the lift curve of configuration 340 was never measured.

The data of Table 6-3 are plotted in Figure 6-7. The function of Equation 6-1 follows a steady decline with some increase in scatter as m_4 approaches m_3. Despite the scatter, which is apparently dependent on the placement and orientation of the additional fin, it can be seen that the influence of an additional fin in furthering induced drag reduction lessens with higher values of m_4. Logically, one can deduce that a wingtip configuration which reduces induced drag by a large amount is close to optimum, and little can be gained by adding more fins to the configuration.

6.2 WAKE ANALYSIS RESULTS

6.2.1 Rotational Velocity Distributions

Figures 6-8 to 6-18 contain the measured rotational velocity distributions for the round tip, the unfinned tip tank, and several tip tank configurations. The lift coefficients range from 0.33 to 0.90. The plot format was described in Section 4.2. Because the positions and internal characteristics of the vortices evolve with

downstream distance, the distributions were measured in the same cross-stream plane, 4.1 chord lengths behind the wing, in order to allow direct comparisons. Some plots contain closed data points within the vortex core: at these points either the flow angles exceeded 45^{o} and were thus beyond the measurement range of the probe, or else a suction had developed on the probe tip.

The wingtip vortices shed from the round tip and the unfinned tip tank are compared in Figures 6-8 and 6-9 respectively. Both configurations produce distributions with distinct cores and high peak rotational velocities for all tested lift coefficients. The effect of the tip tank is to widen the core slightly, with very little change in the shape of the distribution. Most notable are the increased flow angles in the core region.

A remarkable change in the wingtip vortex can be had with tip tank configuration 020. Figure 6-10, upon comparison with Figure 6-9, indicates a considerable reduction in both rotational velocity and core flow angles for all lift coefficients. The distribution shows a smooth transition between the core and the outer vortex so that the core limits are difficult to define. As well, the rotational velocity decreases with radial distance more gradually than it does for the unfinned tip tank. Thus, more vorticity is diffused into the outer regions of the vortex.

Device 020 shed a secondary vortex from its fin tip. The corresponding velocity distribution is presented in Figure 6-11. Note that the data from the horizontal and vertical traverses do not line up. In fact, data from the horizontal traverse on the downwash side of the vortex appear to mirror data from the vertical traverse on the

upwash side, and vice versa. Part of this result is due to the choice of a "downwash" side for the vortex when making a vertical traverse. This was taken to be the bottom side of the vortex. Had the top of the vortex been chosen instead, the peculiar symmetry of Figure 6-11 would not be apparent. There would still, however, be asymmetry, possibly due to one or both of the following:

1) The sheet of vorticity shed from the trailing edge of the fin is initially inclined 45^{o} with the test section walls. If this sheet is not completely rolled up, horizontal and vertical traverses through the inner wrappings of the sheet will produce velocities of differing magnitudes.

2) The weak secondary vortex convects in a counterclockwise direction around the stronger wingtip vortex as it travels downstream. (This phenomenon is analysed in Section 6.2.4.) The axis of the secondary vortex will thus point in the direction of motion: downstream and inboard. The flow angle probe, because it is inclined with the vortex axis, will thus measure flow angles that are too high on one side of the vortex and too low on the other side.

If the second of these conjectures is true, then the wingtip vortex should also exhibit some asymmetry due to its convection around the secondary vortex. This is shown to be the case at higher lift coefficients where the secondary vortex is stronger and thus more influential. Figures 6-10c and 6-10d show that the symmetry of the wingtip vortex behind configuration 020 is opposite in sense to that of the secondary vortex. That is, the wingtip vortex rotates

upward and outward as it travels downstream. The reader will note that the peak rotational velocity of the secondary vortex is less than that of the wingtip vortex for all lift coefficients, and that the core is more easily defined. Note also that the magnitudes of the rotational velocities approach those of the wingtip vortex with increasing lift. This indicates that the strengths of the two vortices become comparable.

A comparison of Figures 6-10 and 6-12 shows that the velocity distributions due to the 020 and 300 30-5 configurations are remarkably similar above a lift coefficient of 0.35. Yet, configuration 020 shed a measurable secondary vortex and provided superior induced drag reduction (17.0%) compared to configuration 300 30-5 (6.1%). Evidently the flow separation that was observed for configuration 300 30-5 prevents secondary vortex shedding by reducing the amount of lift generated on the fin. Also, a direct comparison of Figures 6-10 and 6-12 must be made with care because measurements were made only in the core regions and it is not known if the similarity of vorticity redistribution is continued beyond the cores.

If devices 020 and 300 30-5 are combined into configuration 320 30-5, the distribution shown in Figure 6-13 is obtained. The vortex here is the secondary vortex shed from the fin with 45^{o} cant. The lift coefficient is 0.90. One can see very little difference between this plot and that of Figure 6-11d for the 020 configuration. Induced drag reduction for configuration 320 30-5 is marginally better at 18.4%, compared to 17.0% for the 020 device. The horizontal fin may improve lift slightly on the outer regions of the wing, thus leading to a slight increase in induced drag reduction.

Another wingtip device which did not shed a measurable secondary vortex was configuration 001. Its wingtip vortex is examined in Figure 6-14. Upon comparison with Figure 6-9 for the unfinned tip tank, it is obvious that the auxiliary fin reduces rotational velocity and generates a thinner core. At higher lift coefficients rotational velocity reduction is not so pronounced but the core flow angles are reduced. Despite the absence of either a secondary vortex or extensive vorticity redistribution, this device still reduces induced drag by a respectable amount, 14.8%. This is probably because the fin acts like an endplate to increase lift near the wingtip.

When the fin of the 020 configuration is shortened to 0.65 c_t, both the rotational velocities and the core radius of the wingtip vortex are reduced. This may be seen by comparing Figures 6-15 and 6-10c, which were both measured for a lift coefficient of about 0.7. The secondary vortex, however, is reduced in strength. A comparison of Figure 6-16 with Figure 6-11c shows the rotational velocities to be reduced, and the core to be less well defined. When the fin is further shortened to 0.43 c_t, the wingtip vortex remains virtually unchanged as shown in Figure 6-17. This is possibly associated with the almost identical induced drag reductions for configurations 020 L1 and 020 L2, 8.0% and 7.5% respectively, and may explain the discontinuity of Figure 6-5. In contrast, the secondary vortex (Figure 6-18) is comparable in strength to that for the original configuration, which retains an unshortened fin. In fact, the peak rotational velocities exceed those of configuration 020, and the core is easily defined.

Results from the measured rotational velocity distributions are

summarized in Table 6-4. The main (wingtip) and secondary (fin) vortices of configurations that shed multiple-vortex wakes are analyzed individually. The main vortex for a given tip tank configuration is indicated with the label "A" following the code of that configuration. Secondary vortices are labeled with a "B".

Two sets of measured vortex core positions are provided in Table 6-4. The first of these lists the core positions in a cross-stream plane relative to the wind tunnel centerline, where the test section coordinate conventions of Figure 3-2 are used. The second set provides the core positions relative to either the wingtip, if a vortex is a main vortex, or the tip of a fin, if the vortex is a secondary vortex. Here the local coordinate conventions shown in Figure 6-19 are used. The local origin is always placed in the same cross-stream plane as the trailing edge of the wing, directly on or behind a tip. The x_l, y_l, z_l axes are parallel to and in the same direction as the X, Y, Z axes of the test section convention.

Unfortunately, not all secondary vortices could be measured, apparently because they were too weak to be detected with the five-hole probe. Extensive surveys were conducted within the wakes of many wingtip configurations for varying lift coefficients in an effort to locate a secondary vortex, but without success. These vortices, if they exist, are assumed to be weak enough that they may be neglected. Only a fin canted 45^{o} at the middle chordwise position on the tip tank shed a strong secondary vortex which could be measured.

6.2.2 Core Width and Peak Rotational Velocity

The structure of the wingtip vortex core depends heavily on the

load distribution near the tip and may be used to infer the lifting conditions on the wing. Grow [25] recognized that the boundary layer shed from the lower surface of the wing at the trailing edge rolls up into the core. Because the core width is determined by the boundary layer thickness, the core spreads out with increasing lift.

Figure 6-20 shows the measured core radii as a function of lift coefficient for the 001, 020, and 300 30-5 configurations, as well as for the unfinned tip tank and the round tip. Both the main and secondary vortices for the 020 configuration are represented. The varying core thicknesses indicate that an auxiliary fin can affect the load intensity in the region of the wingtip, with the degree of change dependent on the fin orientation.

The most striking results are those for configuration 020. Here, the wingtip vortex core thickness remains essentially unchanged for all lift coefficients. If the core width is an indication of the wing boundary layer thickness, then these results imply that this configuration provides the same amount of lift in the wingtip region regardless of wing incidence. The core of the secondary vortex shrinks as the wing incidence is increased, probably because the rate of roll-up increases with increasing lift, making the core tighter at higher lift coefficients.

The core widths of the main vortices shed by the 001 and 300 30-5 configurations are not nearly as impressive as those for the 020 configuration, possibly because neither one altered the wing vorticity distribution enough to shed a significant secondary vortex. Also, unlike the 020 configuration, the fins of the 001 and 300 30-5 configurations were not aligned with the wing trailing edge and were

consequently not in as good a position to affect the boundary layer shed from the wing trailing edge. Nevertheless, the induced drag reductions due to the 001 and 300 30-5 configurations (14.8% and 6.1% respectively) indicate that the auxiliary fins must still have a beneficial effect on the downwash distribution.

The effect of a wingtip device on the characteristics of the vortex wake may be understood by considering the manner in which the device affects the spanwise distribution of circulation on the wing. Figure 6-21a contains a sketch of the circulation distribution for the wing fitted with the unfinned tip tank. The corresponding distribution of vorticity, $d\Gamma_{\omega}/dx$, is provided as well. When an auxiliary fin is fitted to the tip tank, the circulation and vorticity distributions are conjectured to take a form similar to that shown in Figure 6-21b. The circulation must be continuous at the tip tank/fin juncture, even though the vorticity can have a discontinuity [29].

According to Bilanin et al [24], the number of trailing vortices that are shed on one side of a wing is equal to the number of local maxima of $d\Gamma_{\omega}/dx$. Further, the vorticity shed between local minima will roll up into a discrete vortex [32]. Therefore, the modified tip tank in Figure 6-21b will shed two vortices, where the trailing vortex sheet divides itself at the position, x_{min}, of the local minimum of $d\Gamma_{\omega}/dx$. The unfinned tip tank in Figure 6-21a will cause only a single wingtip vortex to be shed.

A wingtip vortex will become more intense as circulation is concentrated on the outer portions of the wing. Mason and Marchman [17] have noted this to be marked by an increase in rotational velocity. For constant loading at the wingtip, the value of the peak

rotational velocity is an indication of the magnitude of $d\Gamma_w/dx$ at a local maximum [33]. Figure 6-21 shows that with an added auxiliary fin, the circulation becomes nonzero at the wingtip. The magnitude of $d\Gamma_w/dx$ at the wingtip is consequently reduced, so the peak rotational velocities within the wingtip vortex are reduced as well.

The peak rotational velocities for the round tip, the unfinned tip tank, and the 001, 020, and 300 3@-5 configurations are presented as a function of lift coefficient in Figure 6-22. The peak rotational velocity of the main tip tank vortex is seen to always be reduced with the addition of a fin. The most significant reduction occurs for the 020 configuration.

The results for configurations 020 and 300 3@-5 are seen to exhibit similar trends. The low peak rotational velocities indicate that a fin draws some vorticity off the wing. The velocities also have low rates of change with lift coefficient. This indicates a low rate of change in the magnitude of $d\Gamma_w/dx$ in the region of the wingtip. On the other hand, the rotational velocities for the 001 configuration are comparable to those of the unfinned tip tank. This suggests that much of the loading remains on the outer portion of the wing and is not carried out onto the auxiliary fin. This is undoubtedly the reason a strong secondary vortex was not observed for the 001 configuration.

Accurate correlations between the lift curve slopes and the data in Figures 6-20 and 6-22 cannot be made because peak rotational velocity and core width depend on factors besides lift coefficient. For instance, Grow [25] noted that the peak rotational velocity increases with both aspect ratio and taper ratio of the wing, whereas

core width increases with taper ratio but is almost independent of aspect ratio. Core width may also be related to the point of transition between laminar and turbulent flow within the wing boundary layer: as the line of transition moves toward the leading edge, the core width necessarily increases because a turbulent boundary layer is thicker than a laminar boundary layer. This relation, however, is believed to have only a slight effect.

6.2.3 Vortex Intensity

The peak rotational velocity and core radius of a trailing vortex may be related through their product, the vortex intensity, which was defined in Section 2.3:

$$I = 2\pi(rv_t)_{max} \quad . \tag{2-9}$$

The intensity of a rolled-up, undecayed vortex must remain constant at successive points downstream of the wing [13], [25]. That is, reductions in peak rotational velocity as the vortex evolves must be associated with increases in core width and vice versa. This is a direct consequence of conservation of angular momentum, through which the total circulation of the vortex must be preserved. Therefore, even though the vortices shed behind different wingtip configurations may have slightly differing rates of evolution, they may all be compared in the same cross-stream plane on the basis of constant intensity. This is done in Figure 6-23 for the round tip and the 000,

001, 020 and 300 30-5 configurations.

The plots indicate that configurations which reduce induced drag also have wingtip vortices of reduced intensity, with the reduction being most pronounced for the 020 configuration. The results also show that the lower the intensity of a trailing vortex, the less this intensity increases with increasing lift coefficient. Once again, the main vortices of configurations 020 and 300 30-5 are shown to have similar results.

It was not possible to find a correlation between the rate of change of intensity with lift and the slope of the lift curve for any wingtip configuration. This is because the downwash distribution in the region of the wingtip and the induced drag depend not only on vortex intensity, but on vortex position and the distribution of circulation within the vortex as well.

6.2.4 Vortex Positions

Figures 6-24a through 6-24d depict the measured vortex core positions for the 000, 001, 020 and 300 30-5 configurations in a cross-stream plane 4.1 chord lengths behind the wing trailing edge. The plots are arranged in order of increasing lift coefficient, from 0.35 to 0.88. The plot for a lift coefficient of 0.71 includes core positions for the 020 configurations with shortened fins. The coordinate conventions of each plot follow those of Figure 3-2, with chain dashes marking the cross-stream axes of the test section and with flow out of the page. A wing contour enters from the left side and a plus symbol marks the tip tank centerline. A cross symbol indicates the cross-stream position of the fin tip for the 020

configuration.

The core positions for the 020 configuration are joined with a straight line; a closed-circle symbol on this line marks the centroid of these two vortices. The centroid here is based on vortex intensity, and its coordinates X_c, Y_c are calculated in the following manner, for a system of n vortices:

$$X_c = \frac{\sum_{i=1}^{n} I_i X_i}{\sum_{i=1}^{n} I_i} \qquad (6\text{-}2a)$$

$$Y_c = \frac{\sum_{i=1}^{n} I_i Y_i}{\sum_{i=1}^{n} I_i} \qquad (6\text{-}2b)$$

The measured vortex positions may not coincide with those to be found in free flight, due to constraints imposed by the wind tunnel walls. Nevertheless, the relative displacements of the vortices may be studied in order to gain an understanding of how a wingtip device affects flow on the wing.

The first thing to note about the vortex positions of Figure 6-24 is that the cores are displaced downward with increasing lift coefficient, as are the tip tank centerline and the fin tip. This occurs because the wing rotates about its quarter-chord axis as the incidence is increased, so the trailing edge moves downward with respect to the coordinate system.

Apart from this displacement mechanism, the position of a vortex core is affected by three things: convection, in which the trajectory of a wingtip vortex is affected by the presence of one or more weaker secondary vortices; redistribution of vorticity on the wing due to a

wingtip device; and constraints imposed by the experimental arrangement. A detailed exploration of these influences is provided in the following subsections.

a) Spanwise Displacement due to Mutual Convection

The phenomenon of mutual convection is best illustrated if one considers the main and secondary vortex positions for the 020 configuration. These are replotted in Figure 6-25a which is similar to Figure 6-24 except that the coordinate system originates at the tip tank centerline, in order to make the process of mutual convection between the vortices easier to see. Again, the cross-stream plane lies 4.1 chord lengths behind the wing trailing edge.

The results show that the rate of convection increases as the vortices become more intense with increasing lift. As well, the vortices convect in a direction dependent on their direction of rotation. Because rotary motion from one vortex forces convection of the other, and because both vortices rotate in a counterclockwise fashion, convection also proceeds in a counterclockwise direction with increasing lift. The secondary vortex is weaker than the wingtip vortex and is thus displaced further inboard than the wingtip vortex is displaced outboard. The center of rotation can be seen in Figure 6-25a to coincide roughly with the centroid location, especially at the higher lift coefficients. This implies that the intensities of both vortices remain proportional with changing lift.

Mutual rotation is also shown to proceed with increasing downstream distance as shown in Figure 6-25b. Here, the lift coefficient is held constant at 0.71 and the plot format once again

follows that of Figure 6-24. Measurements behind configuration 020 were conducted at 4.1, 9.3, and 12.0 chord lengths behind the wing. The positions of the vortex shed from the unfinned tip tank are included as well for reference. As rotational velocity distributions were not measured for all vortices, centroidal coordinates could not be obtained.

The outboard displacement of the wingtip vortex of the 020 configuration is thus seen to depend on the influence of a secondary vortex. If one refers again to Figure 6-24, one can see that the wingtip vortices of the 001 and 300 configurations are also displaced outward with increasing lift coefficient, albeit to a lesser extent. It seems evident that these displacements may be due to the influences of secondary vortices that are too weak to be measured with the flow angle probe.

Figure 6-26 compares the spanwise positions of the vortices of Figure 6-24 against lift coefficient. Displacements are measured horizontally from the wing root. The centroid of the 020 vortices is plotted as well. The round tip and the unfinned tip tank produce curves with negative slopes: the trailing vortices move inboard as the lift is increased. All other wingtip devices force the wingtip vortex outward with increasing lift. Note that mutual convection undoubtedly plays a role in the results of Figure 6-26. With increasing lift, the wingtip vortex of the 020 configuration travels outward to a greater extent than those of the others. The slope of the curve is higher as well. This attests to the presence of a strong secondary vortex. The motions of the wingtip vortices for the other tip tank configurations

are believed to be affected in a similar manner but to a lesser extent by weak secondary vortices. Because the unfinned tip tank and the round tip do not generate secondary vortices, the wingtip vortex is not convected outward but instead moves inward.

b) Spanwise Displacement due to Vorticity Redistribution

The possible influence of a secondary vortex is only partly responsible for the spanwise displacement of a wingtip vortex. A wingtip device increases the spanwise load distribution, particularly near the wingtip, and causes more vorticity to be shed from the tip region. The additional vorticity causes the centroid of the trailing vortex sheet to be shifted outward. Because the wingtip vortex rolls up about this centroid, its position is shifted as well.

The mechanism is illustrated schematically in Figure 6-27, which shows the circulation and vorticity distributions for a wing fitted in turn with the round tip, the unfinned tip tank, and a modified tip tank. The corresponding sites of vortex roll-up are indicated as well. As noted by Donaldson et al [33], roll-up sites occur at local maxima of $|d\Gamma_s/dx|$ and at abrupt changes in vortex sheet strength. The sheet divides itself at local minima of $|d\Gamma_s/dx|$. Betz [34] proposed that the circulation and the first and second moments of this circulation must be conserved at all stages of the roll-up process. The spanwise location, $\bar{x}$, of the centroid of vorticity on one half of the wing must therefore remain invariant. The magnitude of $\bar{x}$ increases as the wing and the load distribution are extended. A single auxiliary fin, when mounted on the tip tank, extends the vorticity distribution well beyond the wingtip. Vortex roll-up thus

centers on $\bar{x}$ and, so long as there is no influence due to a secondary vortex, remains at the same spanwise station for all points downstream. Hence, the measured value of x_v is equivalent to $\bar{x}$. However, once the convecting influence of a secondary vortex is introduced as in Figure 6-27c, the wingtip vortex is forced outward and x_v is no longer equivalent to $\bar{x}$.

The trends of Figure 6-26 may also be explained in terms of the effect a wingtip device has on the load distribution. A wingtip modification can cause more lift and vorticity to be generated on the outer portions of the wing as the incidence is increased. There is a consequent tendency for the centroid of the vorticity distribution to move outward and the trend in Figure 6-26 will exhibit a positive slope. This does not happen with a clean wing, where lift is generated on the inner portions of the wing with increasing incidence. The wingtip vortex moves inward, and the slope of the trend is negative.

An outward displacement of the wingtip vortex is expected to reduce downwash in the wingtip region and thus reduce induced drag. However, no correlation between $dC_l/d\alpha$ and dC_l/dx_v could be found for all the wingtip configurations. This is because the results of Figure 6-26 are due to a combination of both vorticity redistribution and vortex convection. Note in particular the results for the wingtip vortices shed from the 300 3@-5 and 001 configurations. The wingtip vortex for the 300 3@-5 configuration was displaced further outboard and moved outward at a greater rate with increasing lift. Yet, induced drag reduction for the 001 configuration was much higher (14.8%) than that for the 300 3@-5 device (6.1%). These results make

sense if each configuration sheds a secondary vortex which forces convection of the wingtip vortex. The magnitude of x_v and its rate of change with lift coefficient would consequently depend on both the shape of the vorticity distribution and the relative strengths of the main and secondary vortices.

c) Vortex Ascension due to the Experimental Setup

Flow visualization showed that for any tip tank configuration, the wingtip vortices originated directly behind the rearward point of the tip tank. An immediately obvious result from Figure 6-24, then, is that the wingtip vortices rise from the tip as they travel downstream whereas they should descend according to classical theory. However, Westwater [21] and Moore [22], in their numerical studies of the evolution of a trailing vortex sheet, have shown that the core of a wingtip vortex initially ascends slightly as the sheet rolls up. Ascension occurs within the first few chord lengths behind the wing trailing edge, after which the vortex descends.

The wingtip vortices are assumed to be essentially rolled up by the time they have travelled 4.1 chord lengths downstream, so the roll-up process described above is not believed to account for vortex ascension. Rather, ascension is likely due to one or more of the following:

1) a weak secondary vortex influences the motion of a wingtip vortex,
2) the traverse creates blockage in the test section and affects a vortex trajectory,

3) the roll-up process and subsequent vortex motion is constrained by the test section walls.

The first of these causes accounts for the results of Figure 6-25: the wingtip vortex shed from the 020 configuration ascends due to convection. However, this explanation is incomplete because the vortex shed from the unfinned tip tank also ascends (as shown in Figure 6-24), but without the influence of a secondary vortex. The second of the causes listed above is probable because the portable traverse creates a blockage of 7.2% (based on projected area) in the test section and forces the flow to accelerate up and over the traverse base, causing vortices to ascend in the process.

In order to illustrate the last of the possible causes listed above the physical situation must be replaced with a mathematical simulation. This is done with the vortex image system of Figure 6-28a. Here, the wing is replaced with a bound vortex along its span and a trailing vortex at its tip. Flow is out of the page. The test section walls are simulated by placing an image vortex, equal in strength and opposite in sense to the trailing vortex, behind each boundary to be represented. Each wall is thus replaced with a zero streamline. In order to provide a completely balanced system, the image vortices must be reflected as well so that an infinite grid of image vortices, alternating in sign, surrounds the trailing vortex. The system of Figure 6-28a is but a first-order representation: the higher order vortices are considered to be far enough removed from the test section that their cumulative influence on the trailing vortex is negligible. Therefore, they are not included in the simulation.

Suppose the image vortices are labelled A through H as shown in the figure and suppose the trailing vortex is centered on the test section centerline. Image vortex A and the trailing vortex mutually interact, with the downwash from one forcing the trajectory of the other downward. However, the trailing vortex also receives an equal amount of upwash from image vortex B, and its trajectory is forced upward an equal amount. The vertical influences from image vortices A and B thus cancel each other out. In like fashion, the induced velocities from image vortices C and D that would cause the trailing vortex to move laterally in a horizontal plane also cancel out. As well, the cumulative influence from image vortices E, F, G, and H is also zero, and the wingtip vortex trajectory is constrained to remain coincident with the test section centerline. The motion is in concordance with Theorem 3 of [34] which states that the motion of a vortex flanked by parallel walls is constrained to move parallel to the walls.

The mechanism described above may now be applied to the experimental results, where the wingtip vortex does not originate at the center of the test section. The arrangement is depicted in Figure 6-28b, where the image vortices are labelled as before and the trailing vortex originates on the horizontal axis of the test section, slightly to the right of the vertical axis. Now that the image system is asymmetric, the image vortices do not completely cancel each other out and a few simple calculations show that the cumulative effect of this first-order representation is to induce a slight amount of upwash on the trailing vortex. The interested reader may derive the calculations as an exercise; their introduction here would only serve

to complicate the discussion. Let it suffice to say that ascension of a vortex, as noted in the results, may be due in part to the action of image vortices. However, because the wingtip vortices of the experiments always originate at a point close to the test section centerline, image vortices are believed to have only a slight influence.

The philosophy of the preceding discussion may be applied to the image system of Figure 6-28c, which constrains the main and secondary vortices of the 020 configuration. Once again, however, the influence of image vortices is believed to be minimal; even though the secondary vortex is much farther from the test section centerline and should thus be influenced more by its image vortices, it is weak and its trajectory is dominated by the convecting influence of the wingtip vortex.

Of the image vortex system, traverse blockage, and secondary vortices, it is not known which affects the ascension of a wingtip vortex the most, although the role of image vortices is believed to be minor. One would suspect that these factors combine to affect the results of this investigation.

The trends of Figure 6-26 may also be explained in terms of the effect a wingtip device has on the load distribution. A wingtip modification can cause more lift and vorticity to be generated on the outer portions of the wing as the incidence is increased. There is a consequent tendency for the centroid of the vorticity distribution to move outward and the trend in Figure 6-26 will exhibit a positive slope. This does not happen with a clean wing, where lift is generated on the inner portions of the wing with increasing incidence.

The wingtip vortex moves inward, and the slope of the trend is negative.

An outward displacement of the wingtip vortex is expected to reduce downwash in the region of the wingtip and thus reduce induced drag. However, no correlation between lift curve slope and x_v could be found for the wingtip configurations. This may be due in part to the mutual rotation of the main and secondary vortices that was shown to happen for the 020 configuration and is believed to happen for the 001 and 300 configurations.

Appendix IV contains a detailed description of the assumptions, conservation laws and procedure due to Betz through which the circulation within a wingtip vortex may be related to the circulation on the wing.

6.3 FLOW VISUALIZATION

6.3.1 Observations of Surface Flow Patterns

Airfoil surfaces were painted with a coat of kaolin and varsol so that regions of flow separation could be revealed. Kaolin is a powder which, when combined with varsol, produces a mixture that turns white in regions of attached flow but remains clear in regions where flow separates.

This method of flow visualization revealed the presence of laminar separation bubbles on the upper surfaces of the wing and the tip tank fins. Laminar bubbles mark the point where a laminar boundary layer separates from an airfoil surface, becomes turbulent, and reattaches itself. They were located along the airfoil crests, approximately at the quarter chord.

One tip tank fin, mounted at the rearmost chordwise position and canted outward by 90^{o}, showed extensive regions of flow separation rather than a laminar bubble. This was alleviated somewhat by toeing the fin through -5^{o}. As was demonstrated in Section 6.1.1, the fin contributed very little to induced drag reduction, whether alone or in conjunction with other fins. Separation probably occurred because the fin is situated in a region where wake roll-up has already been initiated and where the flow angles are high.

6.3.2 Observations of the Trailing Vortices

A tuft of string, attached to a thin metal rod, was used to locate the position of a trailing vortex. The tuft spun rapidly when it was placed within the vortex core, otherwise it aligned itself with the freestream direction.

This very simple and direct method of flow visualization was used to show that main vortices originated directly behind the rearward point of the tip tank, or, if the tip tank was absent, directly behind the wingtip. A secondary vortex rolled up directly behind the tip of the fin from which it was shed.

The tip tank fins were all shown to shed secondary vortices, but only that of the 020 configuration could be followed downstream. All others were lost within a fraction of a chord length behind the wing. In addition, the secondary vortex of the 020 configuration caused the tuft to spin very rapidly and there was a noticeable decrease in the spin rate of the main vortex. On the other hand, the secondary vortices of the other configurations produced a low spin rate and

there was no noticeable change in the spin rates of the main vortices.

6.4 FINAL COMMENTS ON THE RESULTS

Although flow visualization had confirmed secondary vortices to be shed from all tip tank configurations, most of these were found to be weak and nonevident in the far vortex wake. They may have been dissipated by the strong rotary motion of the wingtip vortex.

The strength of a fin vortex indicates the intensity of loading on the fin. On the basis of the lift curve data, most of the more superior configurations retain an untoed fin, canted outward 45^{o}, with its trailing edge nearly in line with that of the wing. As this was the only fin placement which produced a strong secondary vortex, high loading on a fin is evidently a necessary factor in downwash redistribution. Here the fin is apparently at or near an optimum position and orientation relative to the local flow round the wingtip.

It should also be noted that a vertical fin mounted just behind the wing crest also contributes strongly to induced drag reduction, despite the absence of a strong secondary vortex. When this fin is combined with the one mentioned above, the results are excellent: induced drag reduction is 25.8% for the 021 configuration and 26.0% for configuration 321. The added lift in the wingtip region due to the vertical fin evidently combines with the vorticity-splitting action of the inclined fin to reduce induced drag considerably.

Because the rotational velocity distributions of configurations 020 and 300 30-5 are very similar, both configurations introduce similar rates of change of loading near the wingtip. However, because

separation occurs on the fin of configuration 300 30-5, this fin is unable to generate as much additional lift, and therefore cannot produce a strong secondary vortex. Induced drag reduction is, as a consequence, minimal.

7. CLOSING REMARKS

7.1 CONCLUSIONS

The technique of using lift curve slope to calculate induced drag reduction has been shown to be simple, effective, and repeatable. As well, studies of the vortex wake have proved to be invaluable in determining the mechanism through which a wingtip device accomplishes induced drag reduction.

The reduced downwash and subsequent induced drag reduction due to a wingtip device are caused by a reshaping of the vorticity distribution on the wing. The spanwise centroid of this distribution shifts outward in order to accommodate the added lift being generated in the wingtip region, with a consequent outboard displacement of the wingtip vortex. The vorticity distribution is also continued beyond the wingtip onto the wingtip device, with two consequences: the rate of change of loading at the wingtip is reduced, leading to a subsequent reduction in wingtip vortex intensity; and lift is generated on the device, sometimes enough to generate a secondary vortex. The wingtip vortex position is not necessarily indicative of the centroid position of the trailing vortex sheet because a strong secondary vortex will, through its rotary influence, convect the wingtip vortex outboard as both vortices travel downstream. As the rotation is mutual, the secondary vortex is convected inboard.

The loading intensity on an auxiliary fin is expected to increase with increasing fin span, with a consequent reduction in induced drag. Although the measured trend satisfies this expectation, it is still

inconclusive because it is supported by only three data points and it is discontinuous. As well, considerable changes in both the wingtip and secondary vortices due to changes in fin span were noted, but again there is not enough evidence to support a conclusion. An increased fin span must compromise reductions in induced drag with inevitable gains in weight and parasite drag.

The chordwise placement of an auxiliary fin on the wingtip must be chosen so as to avoid flow separation on either the fin or the wing rather than to minimize induced drag. The fin should not be placed behind the wing, where the flow angles are high, nor should it be located near the position of the wing pressure peak. The results of other researchers and this work appear to indicate that a fin placed with its trailing edge aligned with that of the wing will give superior results if it is given a fair amount (45^{o}) of outward cant.

The trends which relate induced drag reduction to variations in the toe angle and cant angle are somewhat inconclusive as only a few data points were measured. It appears, however, that an auxiliary fin on a low speed wingtip device should be untoed because it is otherwise oriented at too high or too low an incidence relative to the tip flow direction and thus cannot generate sufficient lift. As well, the fin may require a certain degree of outward cant in order to ensure smooth fairing between the wingtip and the fin. Best results for single-fin devices were obtained for cant angles of 45^{o} (configuration 020) and 0^{o} (configuration 001).

When a fin is added to a wingtip device, induced drag is reduced by an amount which depends on the effectiveness of the original device. Each additional fin contributes a progressively smaller

amount to effectiveness and a progressively increasing amount to overall weight and parasite drag. It would appear that two or three fins on a multiple-fin device are close to optimum.

An auxiliary fin which experiences high loading will tend to act as a wingtip sail, with its lift vector pointing in the direction of motion. At low speeds, however, this mechanism is believed to contribute a relatively minor amount to induced drag reduction compared to the action of vorticity redistribution. As well, on the basis of the results, the mechanism of mutual interference between adjacent fins is also believed to have a minimal influence on induced drag reduction.

7.2 RECOMMENDATIONS FOR FUTURE RESEARCH

Future research may be enriched through more detailed investigations of the spanwise loading on the wing and a wingtip configuration, with particular emphasis on the wingtip region. The loading could be determined either through wind tunnel measurements or through numerical calculations using a vortex lattice scheme to represent the wing geometry. As well, investigations of the wingtip vortices, including regions well outside the core, will aid in an understanding of the manner and extent to which a wingtip device redistributes vorticity. In particular, the method of Betz [34], which is outlined in Appendix V, may be used to calculate the wing circulation distribution by using the measured circulation distribution of the wingtip vortex. Finally, future studies must also consider the incremental gains in weight and parasite drag due to a

wingtip device in addition to the corresponding reductions in induced drag.

BIBLIOGRAPHY

[1] Snyder, M.H., Jr. and Zumwalt, G.W., "Effects of Wingtip-Mounted Propellers on Wing Lift and Induced Drag", AIAA Journal of Aircraft, Vol. 6, No. 5, Sept-Oct 1969, pp. 392-397.

[2] Dunham, R.E., Jr., "Unsuccessful Concepts for Aircraft Wake Vortex Minimization", NASA Symposium on Wake Vortex Minimization, NASA SP-409, Feb 25-26 1976, Washington, D.C., pp. 221-249.

[3] Schieman, J. and Shivers, J.P., " Exploratory Investigation of the Structure of the Tip Vortex of a Semispan Wing for Several Wing-Tip Modifications", NASA TN D-6101, Feb 1971.

[4] Whitcomb, R.T., "A Design Approach and Selected Wind Tunnel Results at High Subsonic Speeds for Wing-Tip Mounted Winglets", NASA TN D-8260, July 1976.

[5] Asai, K., "Theoretical Considerations in the Aerodynamic Effectiveness of Winglets", AIAA Journal of Aircraft, Vol. 22, No. 7, July 1985, pp. 635-637.

[6] Flechner, S.G., Jacobs, P.F. and Whitcomb, R.T., "A High Subsonic Speed Wind-Tunnel Investigation of Winglets on a Representative Second-Generation Jet Transport Wing", NASA TN D-8264, July 1976.

[7] Ishimitsu, K.K., "Aerodynamic Design and Analysis of Winglets" AIAA Preprint No. 76-940, AIAA Aircraft Systems and Technology Meeting, Dallas, TX, Sept 27-29 1976.

[8] Ishimitsu, K.K. and Zanton, D.F., "Design and Analysis of Winglets for Military Aircraft. Phase II.", Boeing Commercial Airplane Co., AFFDL TR-77-23, May 1977.

[9] Flechner, S.G. and Jacobs, P.F., "Experimental Results of Winglets on First, Second, and Third Generation Jet Transports", NASA TM 72674, May 1978.

[10] Conley, N., "Winglet Toe-Out Angle Optimization for the Gates Learjet Longhorn Wing", AIAA Journal of Aircraft, Vol. 17, No. 12, Dec 1980, pp. 851-855.

[11] Society of Automotive Engineers, Inc., "Winglets Introduced on Business Jets", Automotive Engineering, Vol. 87, No. 4, April 1979, pp. 44-47.

[12] Spillman, J.J. and Allen, J.E., "The Use of Wing Tip Sails to Reduce Vortex Drag", British A.R.C. 37190 Perf. 3550.

[13] Zimmer, H., "The Significance of Using End Configurations in Airfoil Design for Civil Aviation Aircraft", translated from "Die Bedentung der Flugelendformen Beim Tragflugelentwurf fur Flugzenge der Zivilen Luftfahrt", Jahrbuch Deutsch Ges Luft Raumfahrt, Vol. 1, 1977.

[14] Marsden, D.J., "Wind Tunnel Tests of a Slotted Flapped Wing Section", Canadian Aeronautics and Space Journal, Vol. 24, No. 2, March-April 1978, pp. 83-91.

[15] Wickens, R.H. and Williams, C.D., "Calibration and Use of Five-Hole Flow Direction Probes for Low Speed Wind Tunnel Application", Aeronautical Note NAE-AN-29, NRC No. 24468, National Research Council of Canada, National Aeronautical Establishment, July 1985.

[16] Uzel, J.N. and Marchman, J.F., III, "The Effect of Wing-Tip Modifications on Aircraft Wake Turbulence", College of Engineering, Virginia Polytechnic Institute and State University, VPI-E-72-8, July 1972.

[17] Mason, W.H. and Marchman, J.F., III, "Far-Field Structure of Aircraft Wake Turbulence", AIAA Journal of Aircraft, Vol. 10, No. 2, Feb 1973, pp 86-92. Also AIAA Paper No. 72-40, AIAA 10th Aerospace Sciences Meeting, San Diego, CA, Jan 17-19 1972.

[18] Spreiter, J.R. and Sacks, A.H., "The Rolling Up of the Trailing Vortex Sheet and its Effect on the Downwash Behind Wings", Journal of the Aeronautical Sciences, Vol. 18, No. 1, Jan 1951, pp. 21-32, 72.

[19] Corsiglia, V.R., Schwind, R.G. and Chigier, N.A.,"Rapid Scanning, Three-Dimensional Hot-Wire Anemometer Surveys of Wing-Tip Vortices", AIAA Journal of Aircraft, Vol. 10, No. 12, Dec 1973, pp. 752-757.

[20] Rossow, V.J., "Prediction of Span Loading from Measured Wake-Vortex Structure - An Inverse Betz Method", AIAA Journal of Aircraft, Vol. 12, No. 7, July 1975, pp. 626-628.

[21] Westwater, F.L. "Rolling Up of the Surface of Discontinuity Behind an Aerofoil of Finite Span", Reports and Memoranda No. 1692, British A.R.C., Aug 1935.

[22] Moore, D.W., "A Numerical Study of the Roll-Up of a Finite Vortex Sheet", Journal of Fluid Mechanics, Vol. 63, No. 2, April 1974, pp. 225-235.

[23] Bilanin, A.J., Snedeker, R.S. and Teske, M.E., "Interactions and Merging of Line Vortices", Aeronautical Research Associates of Princeton, Inc., Princeton, N.J., Tech. Memo. No. 76-5, June 1976.

[24] Bilanin, A.J., Teske, M.E. and Williamson, G.G., "Vortex Interactions and Decay in Aircraft Wakes", AIAA Journal, Vol. 15, No. 2, Feb 1977, pp. 250-260.

[25] Grow, T.L., "Effect of a Wing on Its Tip Vortex", AIAA Journal of Aircraft, Vol. 6, No. 1, Jan-Feb 1969, pp 37-41.

[26] Donaldson, C. duP. and Bilanin, A.J., "Vortex Wakes of Conventional Aircraft", AGARDograph No. 204, May 1975.

[27] Dosanjh, D.S., Gasparek, E.P. and Eskinazi, S., "Decay of a Viscous Trailing Vortex", The Aeronautical Quarterly, May 1962, pp. 167-188.

[28] Munk, M,M. "The Minimum Induced Drag of Aerofoils", NACA Report No. 121, 1921.

[29] Heyson, H.H., Riebe, G.D. and Fulton, C.L., "Theoretical Parametric Study of the Relative Advantages of Winglets and Wing-Tip Extensions", NASA TP 1020, Sept 1977.

[30] Mangler, W., "The Lift Distribution of Wings with End Plates", NACA TM 856, April 1938. (Translated by J. Vanier from "Die Auftriebsverteilung am Tragflugel mit Endschieben", Luftfahrtforschung, Vol. 14, No. 11, Nov 20 1937, pp. 564-569.)

[31] Weber, J., "Theoretical Load Distribution on a Wing with Vertical Plates", Reports and Memoranda No. 2960, British A.R.C., March 1954.

[32] Yates, J.E., "Calculation of Initial Vortex Roll-Up in Aircraft Wakes", AIAA Journal of Aircraft, Vol. 11, No. 7, July 1974, pp. 397-400.

[33] Donaldson, C. duP., Snedeker, R.S. and Sullivan, R.D., "Calculation of Aircraft Wake Velocity Profiles and Comparison with Experimental Measurements", AIAA Journal of Aircraft, Vol. 11, No. 9, Sept 1974, pp. 547-555.

[34] Betz, A., "Behaviour of Vortex Systems", NACA TM 713, June 1933. (Translated from "Verhalten von Wirbelsystemen", Zeitschrift fur Angewandte Mathematik und Mechanik, Bd. XII, Nr. 3, 1932, pp. 164-174.)

[35] Pope, A. and Harper, J.J., Low-Speed Wind Tunnel Testing, John Wiley and Sons Inc., 1966, Chapter 6.

[36] Squire, H.B., "The Growth of a Vortex in Turbulent Flow", The Aeronautical Quarterly, Aug 1965, pp. 302-306. Also British A.R.C. 16666, March 1954, Ministry of Supply, Aeronautical Research Council, London, England.

[37] Newman, B.G., "Flow in a Viscous Trailing Vortex", The Aeronautical Quarterly, May 1959, pp. 149-162.

[38] Bilanin, A.J., Teske, M.E., Dolnaldson, C. duP. and Snedeker, R.S., "Viscous Effects in Aircraft Trailing Vortices", NASA Symposium on Wake Vortex Minimization, NASA SP-409, Feb 25-26 1976, Washington, D.C., pp. 61-128.

[39] Hoffman, E.R. and Joubert, P.N., "Turbulent Line Vortices", Journal of Fluid Mechanics, Vol. 16, No. 3, July 1963, pp. 395-411.

[40] Brown, C.E., "Aerodynamics of Wake Vortices", AIAA Journal, Vol. 11, No. 4, April 1973, pp. 531-536.

TABLE 3-1 Wing surface coordinates of the static pressure taps

UPPER SURFACE		LOWER SURFACE	
σ/c_t	τ/c_t	σ/c_t	τ/c_t
0.0319	0.0359	0.0103	−0.0112
0.0535	0.0492	0.0602	−0.0283
0.0779	0.0604	0.1125	−0.0384
0.1040	0.0700	0.1673	−0.0461
0.1299	0.0783	0.2754	−0.0541
0.1819	0.0909	0.3839	−0.0549
0.2371	0.0995	0.4935	−0.0490
0.2898	0.1042	0.6009	−0.0338
0.3469	0.1051	0.6526	−0.0131
0.4002	0.1050	0.6617	−0.0192
0.4541	0.1008	0.7177	−0.0120
0.5089	0.0950	0.8275	0.0022
0.5616	0.0877	0.9227	0.0064
0.6157	0.0778	0.9841	0.0011
0.8299	0.0407		
0.8753	0.0312		
0.9250	0.0195		
0.9860	0.0045		

TABLE 3-2 Possible placements and orientations of a fin on the tip tank

CHORDWISE POSITION	FIN SUPPORT NUMBER	CANT ANGLE (degrees)	ALLOWABLE TOE ANGLES (degrees)
C	1	0	−5,0,+5
	6	22.5	−5
	7	45	−5
B	2	45	−5,0,+5
	4	0	−5,0,+5
	5	90	−5,0,+5
A	3	90	−5,0,+5

TABLE 6-1 Induced drag reductions and effective aspect ratio increases as determined from the lift curve slopes

WINGTIP CONFIGURATION	m $(\text{radian})^{-1}$	$-\Delta C_{D_i}$ (%)	ΔA_e (%)
ROUND TIP #1	1.337π	0.0	0.0
ROUND TIP #2	1.335π	0.0	0.0
000 #1	1.357π	5.5	5.8
000 #2	1.359π	6.0	6.4
001 #1	1.421π	16.3	19.5
001 #2	1.409π	13.3	15.3
001 1@-5	1.382π	6.4	6.8
001 1@+5	1.413π	14.5	16.9
006 6@-5	1.379π	5.7	6.0
007 7@-5	1.381π	6.1	6.5
020 #1	1.424π	17.0	20.5
020 #2	1.423π	16.9	20.3
020 2@-5	1.406π	12.6	14.4
020 2@+5	1.411π	14.0	16.2
020 L1	1.388π	8.0	8.7
020 L2	1.386π	7.5	8.2
021	1.460π	25.8	34.5
026 6@-5	1.428π	18.0	22.0
040	1.403π	11.9	13.6
050	1.401π	11.3	12.7
051	1.439π	20.7	26.0
056 6@-5	1.412π	14.1	16.4
057 7@-5	1.423π	16.8	20.1
300	1.381π	6.1	6.5
301	1.423π	16.9	20.4
320 #1	1.431π	18.8	23.2
320 #2	1.428π	18.0	21.9
321 #1	1.465π	26.9	36.7
321 #2	1.460π	25.1	33.4

TABLE 6-2 Influence of changes in the chordwise location of a fin on induced drag reduction

CANT ANGLE (°)	WINGTIP CONFIGURATION A	WINGTIP CONFIGURATION B	$(\Delta C_{D_i})_A$ (%)	$(\Delta C_{D_i})_B$ (%)	$(\Delta C_{D_i})_B - (\Delta C_{D_i})_A$ (%)
90	300	050	6.1	11.3	5.2
90	301	051	16.9	20.7	3.8
45	007 7@-5	020 2@-5	6.1	12.6	6.5
0	040	001	11.9	14.8	2.9

TABLE 6-3 The effect of an additional fin in furthering induced drag reduction

SUPPORT HOLDING ADDITIONAL FIN	WINGTIP CONFIGURATION A	WINGTIP CONFIGURATION B	$\frac{m_A - m_R}{m_0 - m_R}$	$\frac{m_B - m_A}{m_B - m_R}$
1	000	001	0	1
	020	021	0.129	0.357
	050	051	0.085	0.468
	300	301	0.045	0.651
	320	321	0.141	0.307
2	000	020	0	1
	001	021	0.112	0.441
	006 6@-5	026 6@-5	0.042	0.696
	300	320	0.045	0.680
	301	321	0.129	0.364
3	000	300	0	1
	001	301	0.112	0.132
	020	320	0.129	0.083
	021	321	0.201	0.012
5	000	050	0	1
	001	051	0.112	0.296
	006 6@-5	056 6@-5	0.042	0.606
	007 7@-5	057 7@-5	0.045	0.647
6	000	006 6@-5	0	1
	020	026 6@-5	0.129	0.064
	050	056 6@-5	0.085	0.204
7	000	007 7@-5	0	1
	050	057 7@-5	0.085	0.336

TABLE 6-4 Vortex core measurement results

WINGTIP DEVICE	$\left(\frac{z}{c}\right)_t$	C_t	CORE POSITION		r_{max}	$\frac{(v_\theta)_{max}}{U_\infty}$	$2\pi(rv_\theta)_{max}$
			X,Y (in.,in.)	x_t, y_t (in.,in.)	(in.)	(%)	(ft^2/sec)
ROUND TIP	1.5	0.16	-2.63,0.50	0.63,-1.19	0.200	25.4	3.7
	4.1	0.32	-1.74,0.09	1.51,-1.91	0.288	42.7	8.5
	4.1	0.50	-1.46,0.21	1.79,-2.17	0.363	57.4	14.4
	4.1	0.66	-1.16,0.65	2.09,-2.10	0.575	59.5	23.5
	4.1	0.82	-1.08,0.98	2.17,-2.21	0.675	63.1	29.7
	12.0	0.32	-0.56,-0.49	2.69,-2.49	0.300	39.6	8.2
000	4.1	0.34	-4.61,0.38	1.27,-1.19	0.313	47.1	10.2
	4.1	0.51	-4.36,0.65	1.52,-1.35	0.475	56.9	18.6
	4.1	0.68	-4.16,1.09	1.72,-1.54	0.625	63.6	27.4
	4.1	0.85	-3.98,1.50	1.90,-1.75	0.850	65.3	37.9
	9.3	0.68	-3.25,1.13	2.63,-1.50	N/M	N/M	N/M
	12.0	0.68	-2.81,0.81	3.06,-1.81	N/M	N/M	N/M
001 A	4.1	0.36	-5.34,0.44	0.54,-1.13	0.225	42.7	6.7
	4.1	0.54	-5.60,0.51	0.28,-1.49	0.375	50.9	13.2
	4.1	0.72	-5.61,0.68	0.27,-1.95	0.475	62.3	20.4
	4.1	0.89	-5.65,0.89	0.23,-2.36	0.638	63.3	27.9
020 A	4.1	0.35	-6.11,0.49	-0.24,-1.07	0.600	15.6	6.4
	4.1	0.54	-6.75,0.48	-0.88,-1.52	0.513	25.9	9.2
	4.1	0.72	-7.46,0.94	-1.59,-1.69	0.575	30.3	12.0
	4.1	0.89	-8.16,1.04	-2.29,-2.21	0.581	33.3	13.4
	9.3	0.72	-7.94,0.25	-2.06,-2.38	N/M	N/M	N/M
	12.0	0.72	-8.31,-0.38	-2.44,-3.00	N/M	N/M	N/M
020 B	4.1	0.35	-15.36,-11.45	2.70,-0.20	0.325	9.4	2.1
	4.1	0.54	-13.79,-11.53	5.52,-0.41	0.288	18.4	3.6
	4.1	0.72	-12.29,11.39	7.27,-0.52	0.250	26.7	4.6
	4.1	0.89	-10.85,11.19	8.71,-0.57	0.200	32.8	4.5
	9.3	0.72	-6.25,-11.81	13.31,-0.94	N/M	N/M	N/M
	12.0	0.72	-3.25,-11.50	16.06,-0.63	N/M	N/M	N/M
020 L1 A	4.1	0.70	-7.51,1.03	-1.64,-1.60	0.488	17.3	5.8
020 L1 B	4.1	0.70	-8.86,-8.01	7.89,0.05	0.425	14.2	4.1
020 L2 A	4.1	0.69	-8.16,0.58	-2.29,-2.05	0.463	18.5	5.9
020 L2 B	4.1	0.69	-5.38,-4.86	8.50,0.39	0.088	28.8	1.7
300 A	4.1	0.35	-5.94,0.31	-0.06,-1.25	0.338	26.5	6.2
	4.1	0.53	-6.20,0.90	-0.33,-1.10	0.538	26.4	9.8
	4.1	0.70	-6.71,1.68	-0.84,-0.95	0.625	29.9	13.0
	4.1	0.87	-7.58,2.68	-1.71,-0.57	0.575	34.4	13.8
320 C	4.1	0.90	-10.20,-10.25	9.36,0.38	0.225	34.3	5.3

N/M : NOT MEASURED

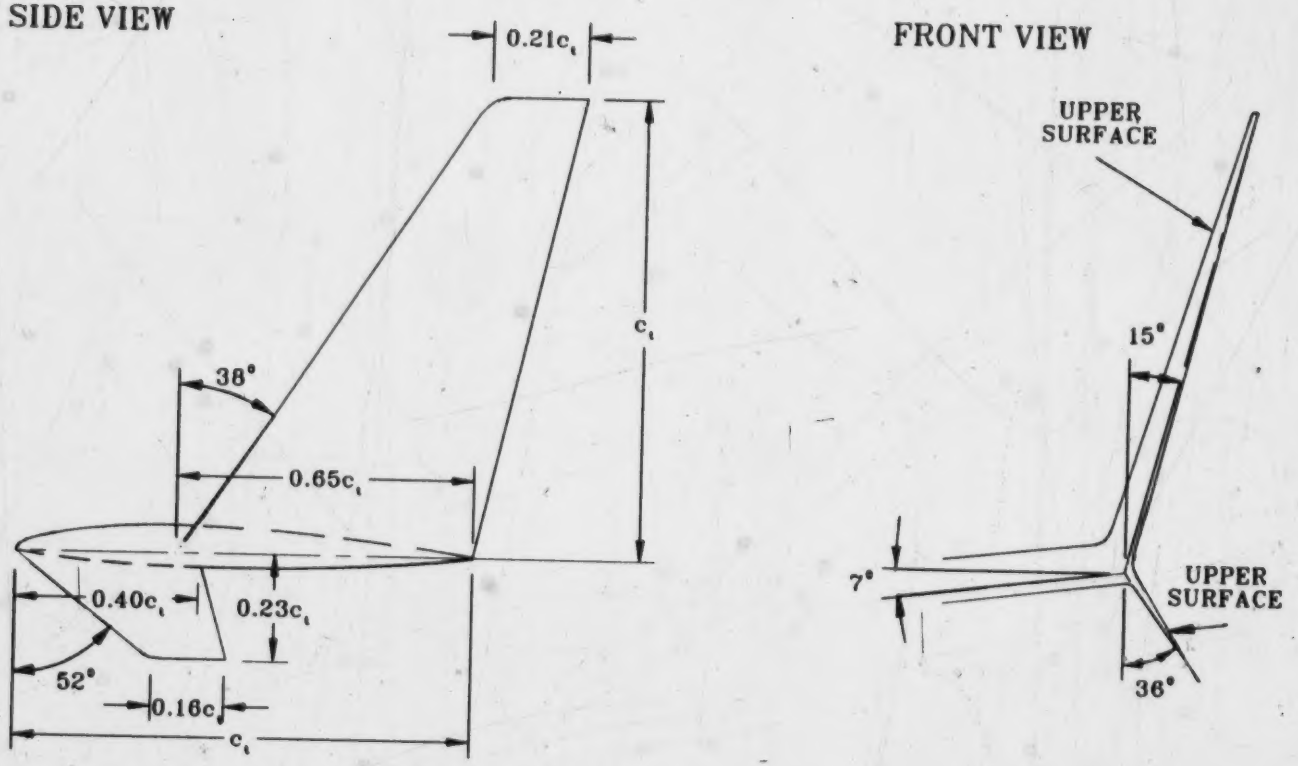

FIGURE 1-1 Specifications of the Whitcomb winglet (from [4])

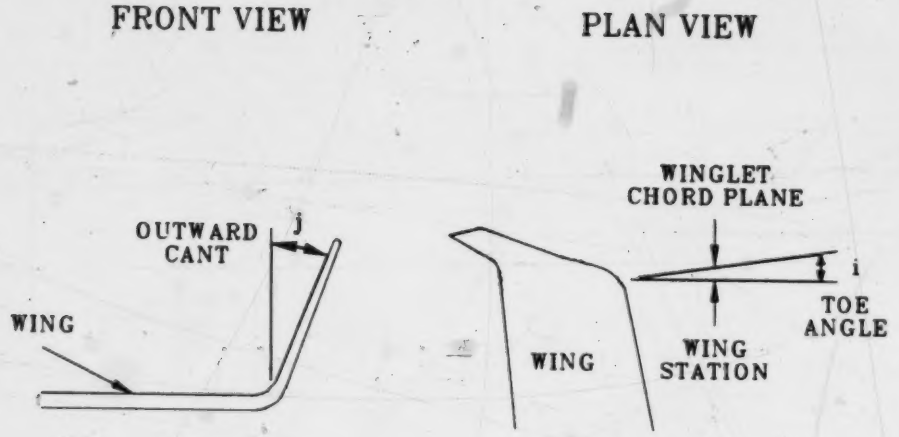

FIGURE 1-2 Definitions and conventions for the cant and toe angles of a winglet or fin

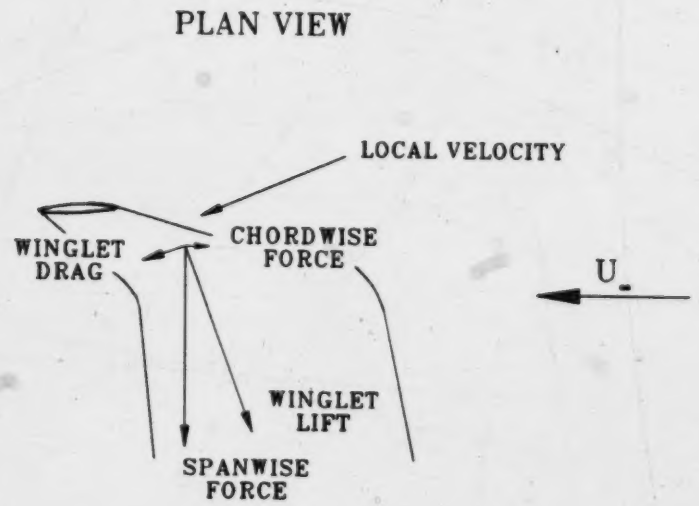

FIGURE 1-3 The mechanism through which a winglet behaves like a sail

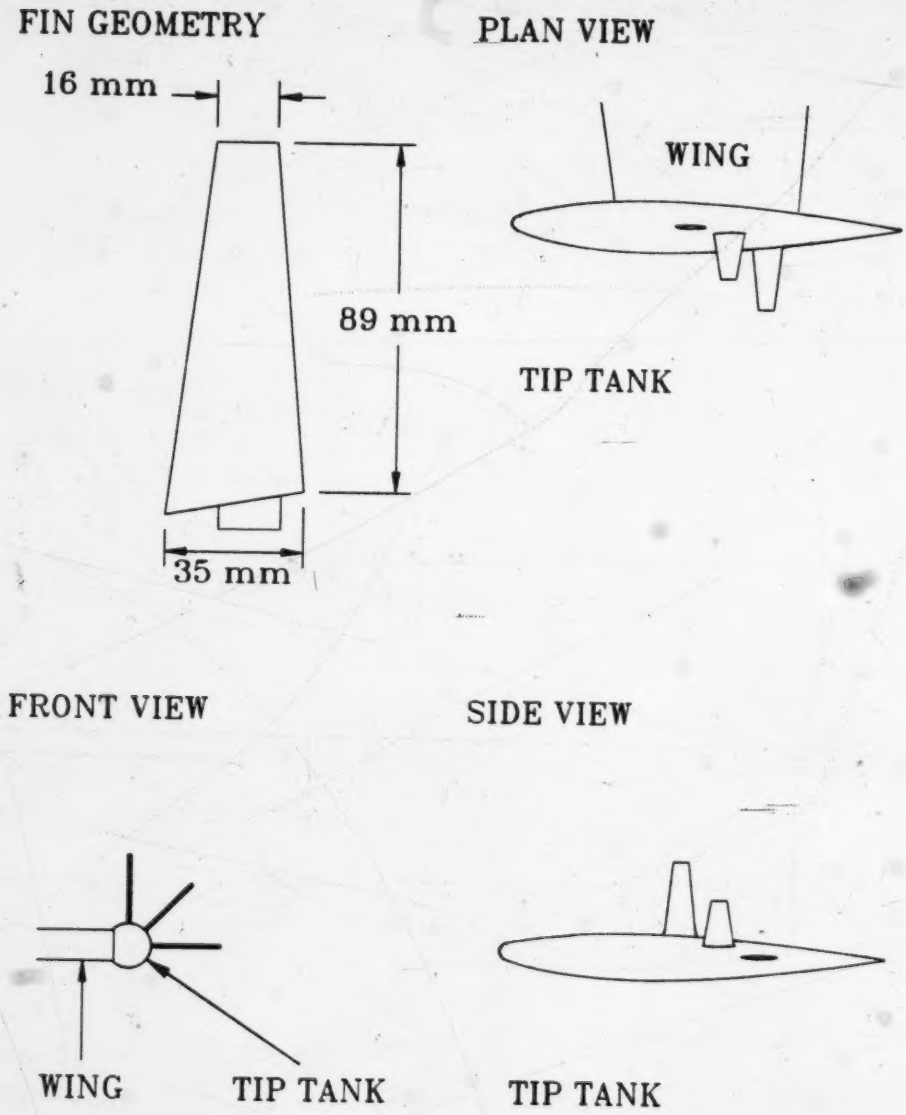

(a) Cascade arrangement

FIGURE 1-4 The wingtip configurations of Spillman and Allen [12]

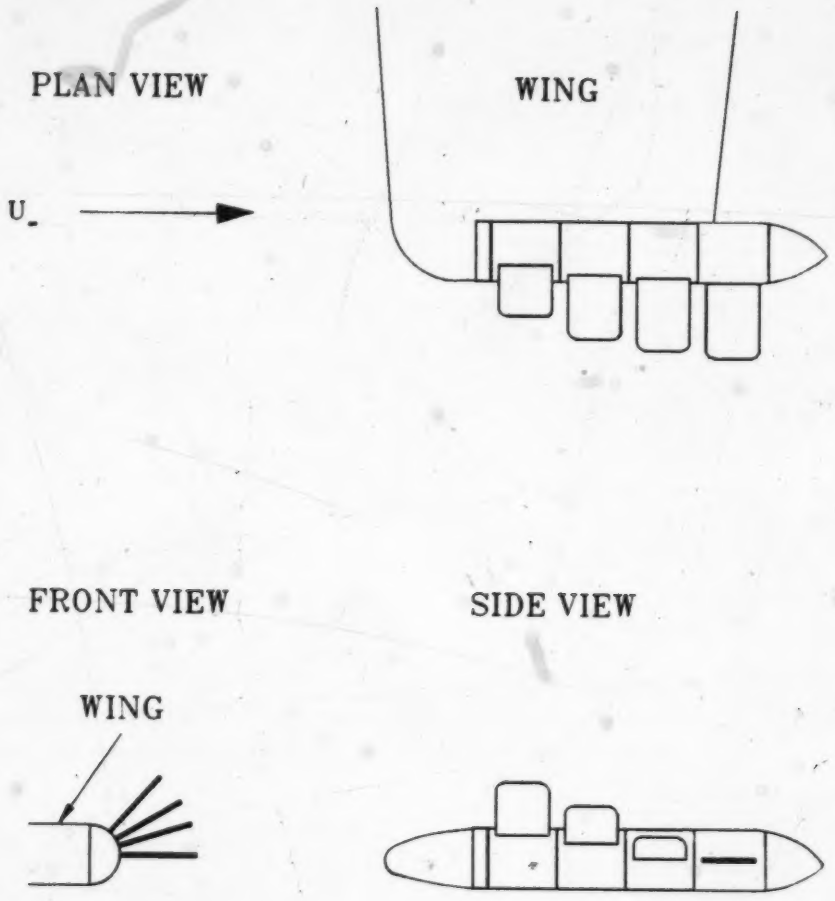

(b) Adjustable array of fins

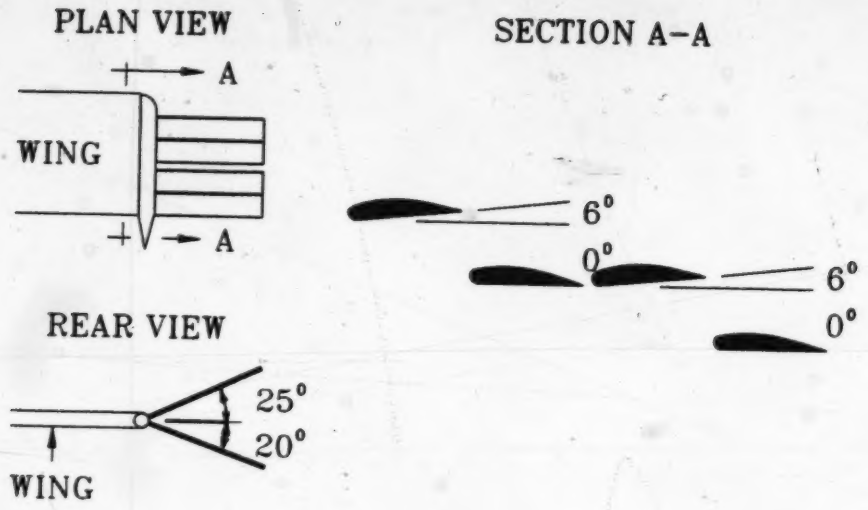

(a) The optimal biplane arrangement of a set of wingtip fins

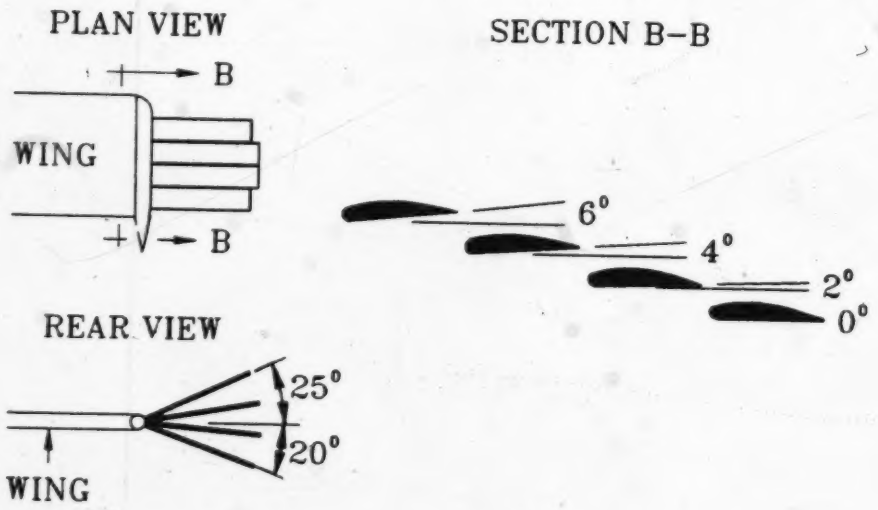

(b) Wingtip fins arranged with successively increasing incidences

FIGURE 1-5 The wingtip configurations of Zimmer [13]

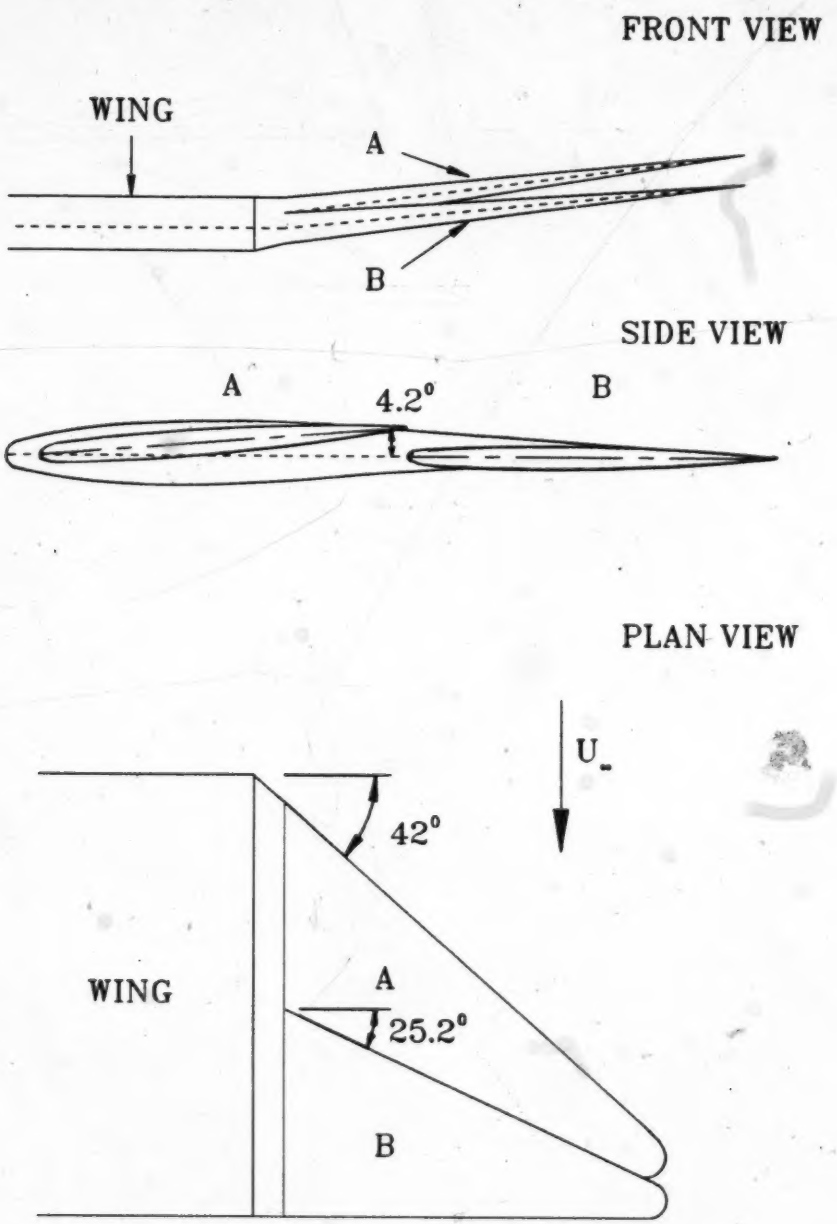

FIGURE 1-6 Wingtip fins which combine the optimal biplane arrangement with a triangular tip extension (from [13])

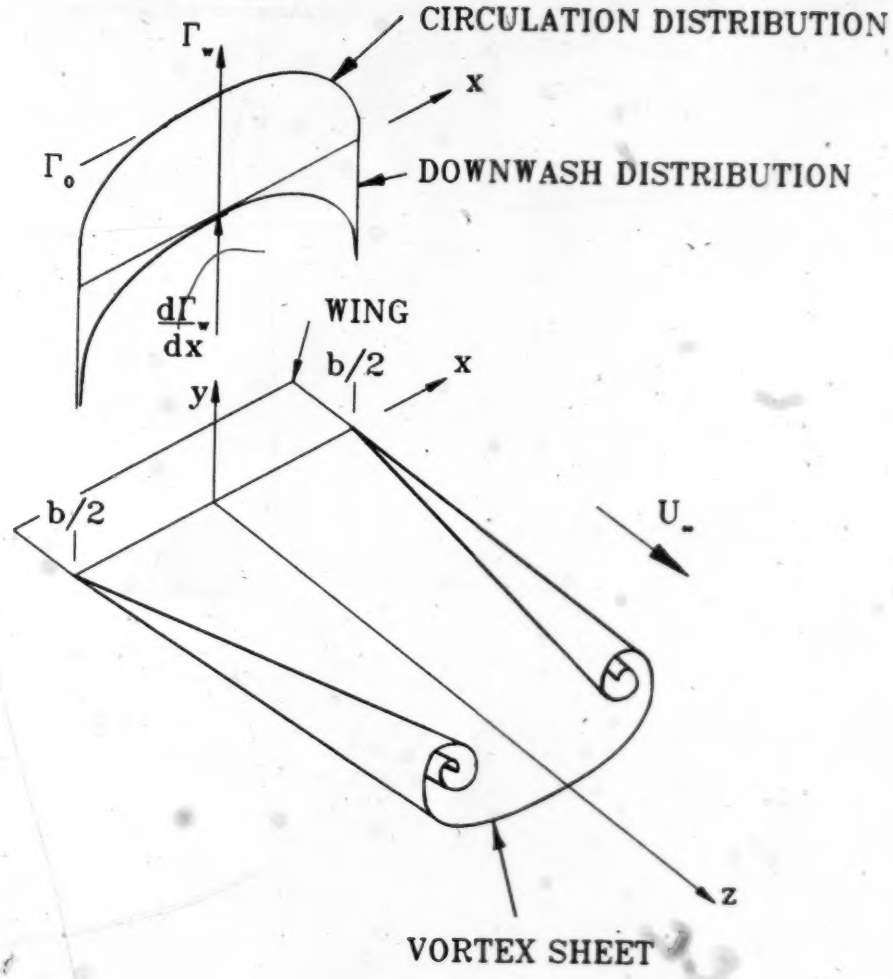

FIGURE 2-1 Roll-up of the trailing vortex sheet behind a lifting rectangular wing

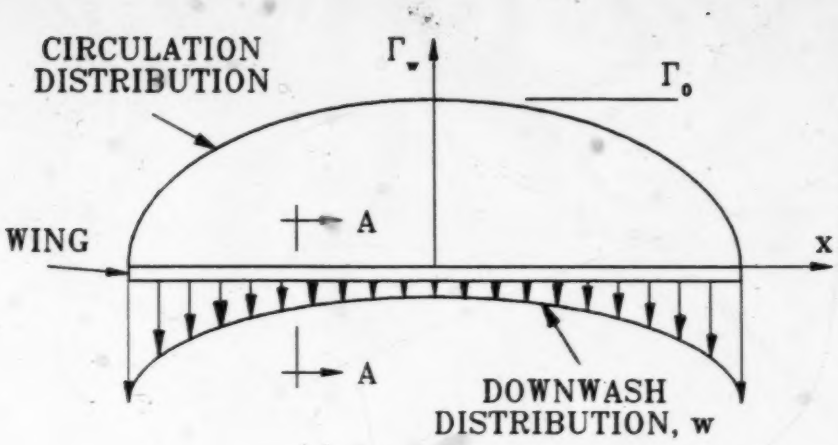

(a) Typical circulation and downwash distributions for a lifting wing, with flow out of the page

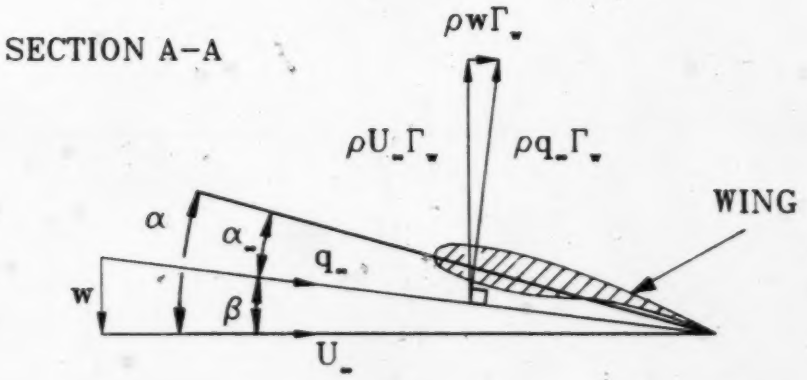

(b) Mechanism of induced drag

FIGURE 2-2 The relation between downwash and induced drag

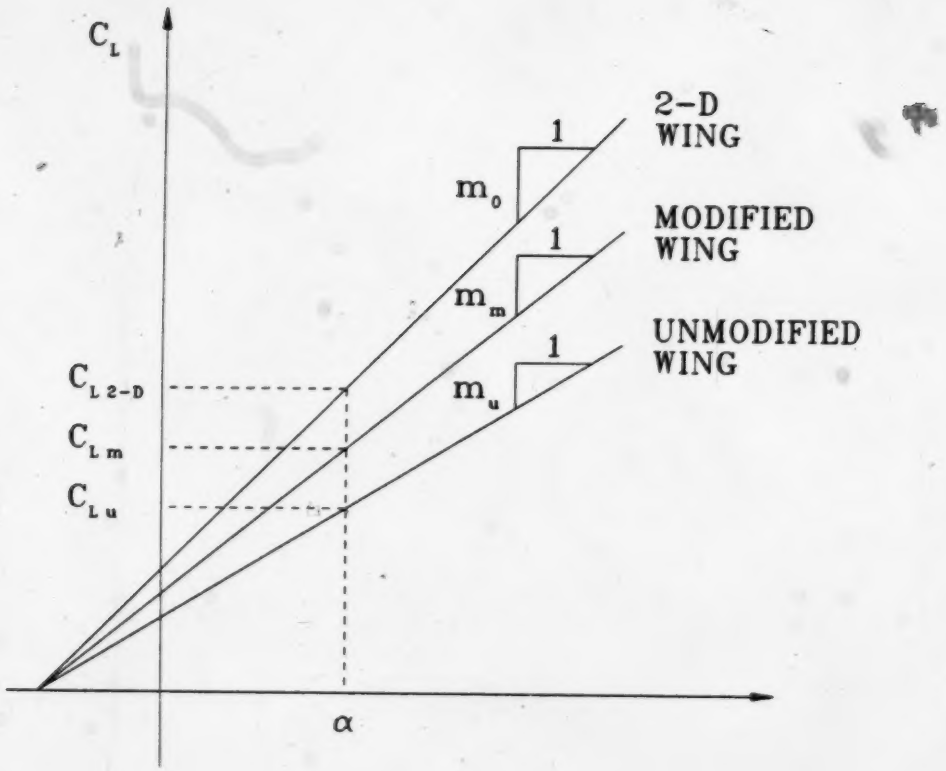

FIGURE 2-3 The influence of a wingtip modification on the lift curve

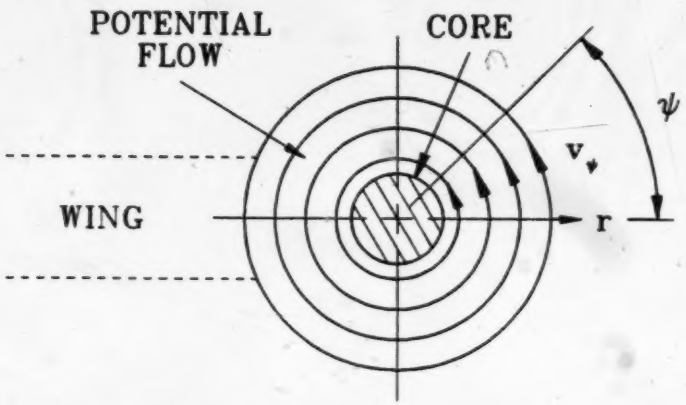

(a) A cross section of a tip vortex showing the direction of rotation, with flow out of the page

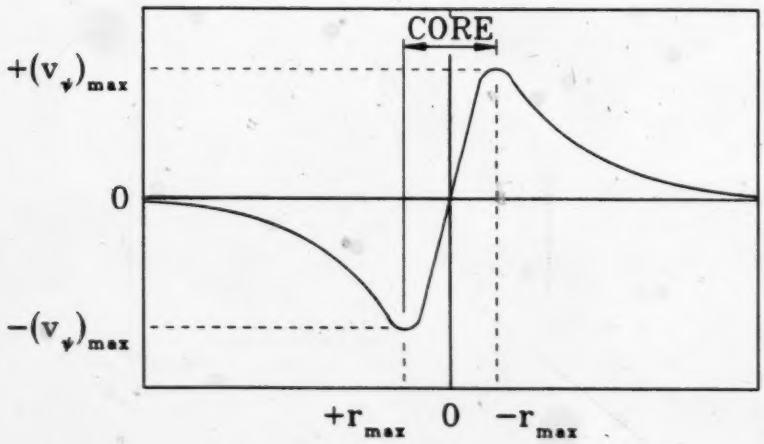

(b) The rotational velocity distribution of a wingtip vortex, showing the peak rotational velocities and the core limits

FIGURE 2-4 Definitions and conventions for the rotational velocity and core width of a trailing vortex

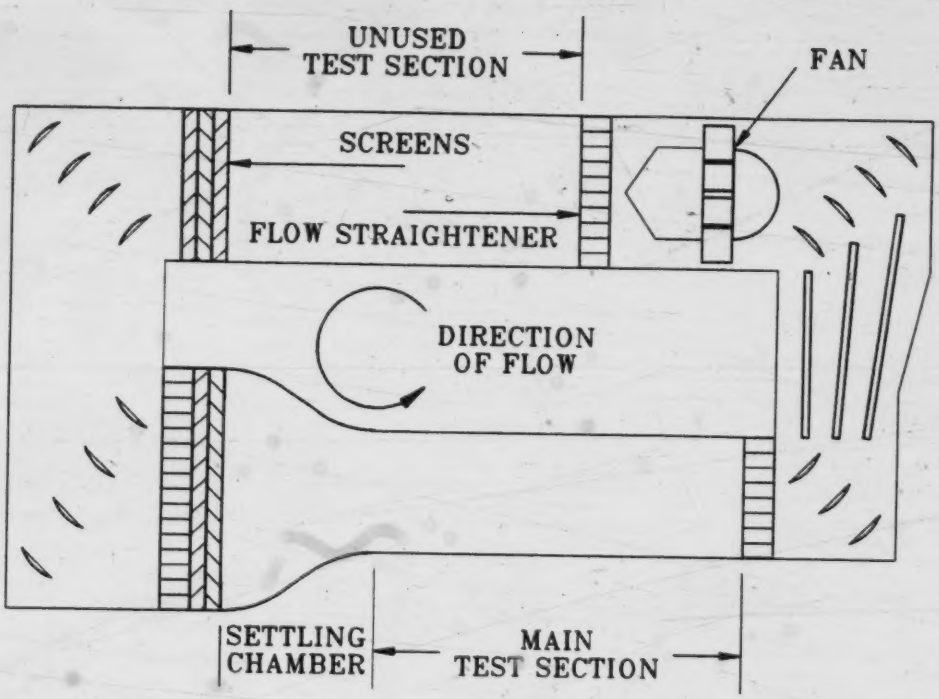

FIGURE 3-1 Schematic diagram of the low speed wind tunnel showing locations of the fan and the main test section (not to scale)

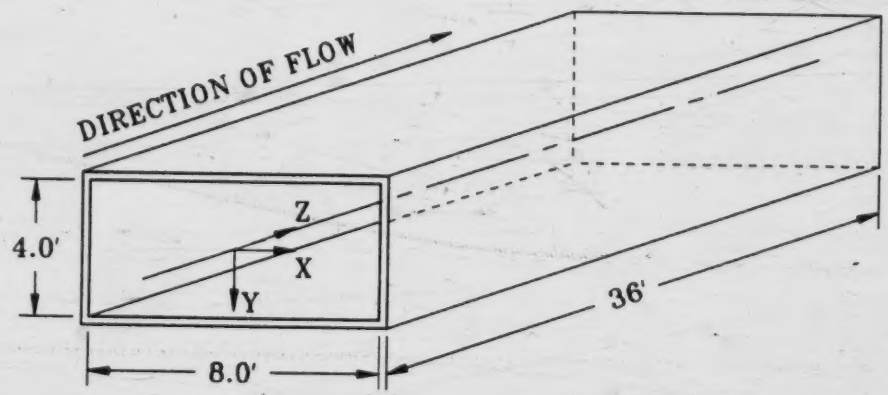

FIGURE 3-2 Main test section dimensions and Cartesian coordinate convention

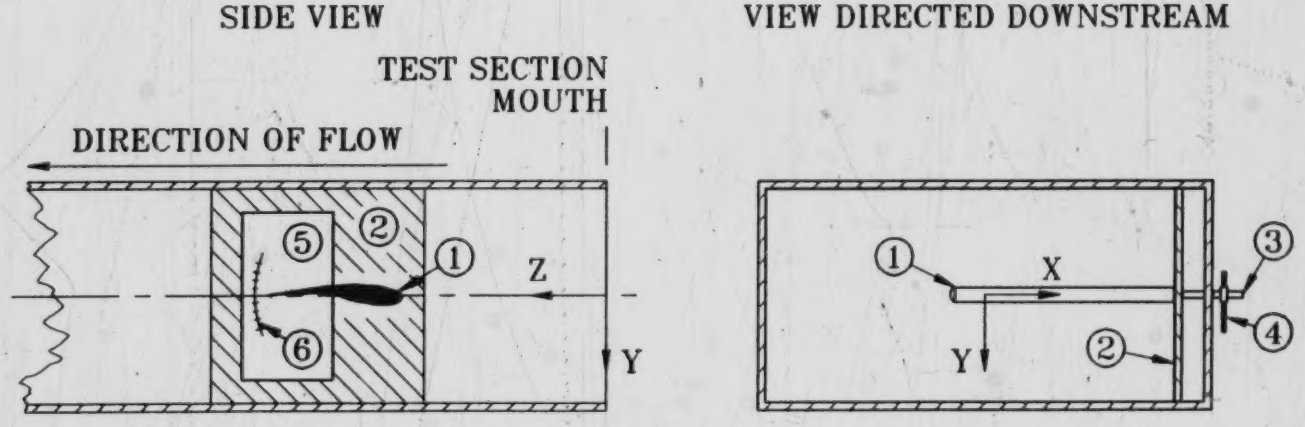

① WING SECTION (FX61-163/SF)

② SUPPORT PLATFORM

③ ROD

④ HANDLE

⑤ WINDOW

⑥ ANGLE OF ATTACK GRADUATIONS

FIGURE 3-3 Placement and orientation of the wing model in the main test section

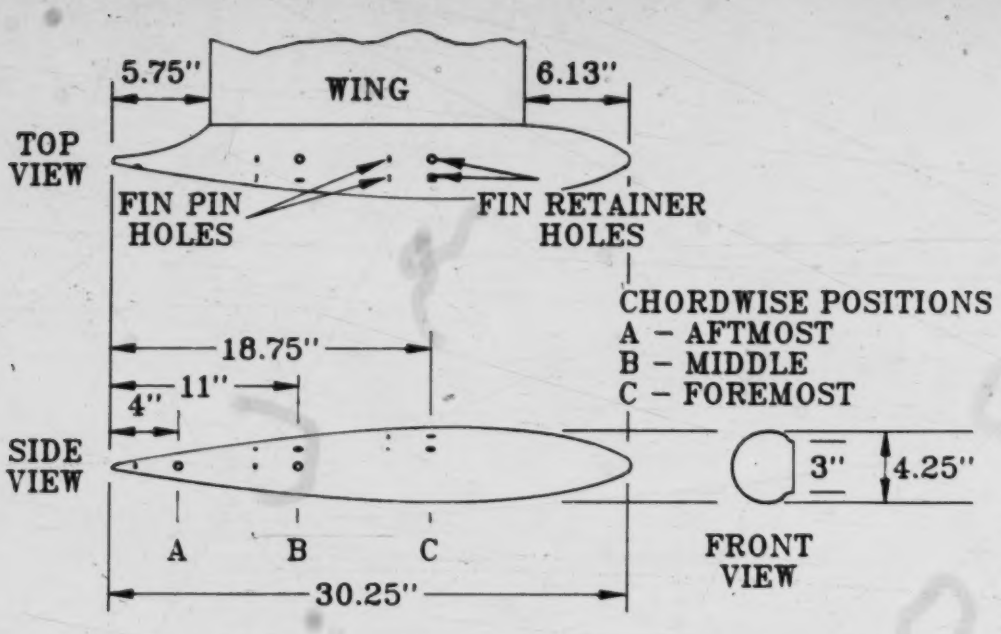

(a) Specifications of the tip tank, including locations of fin supports

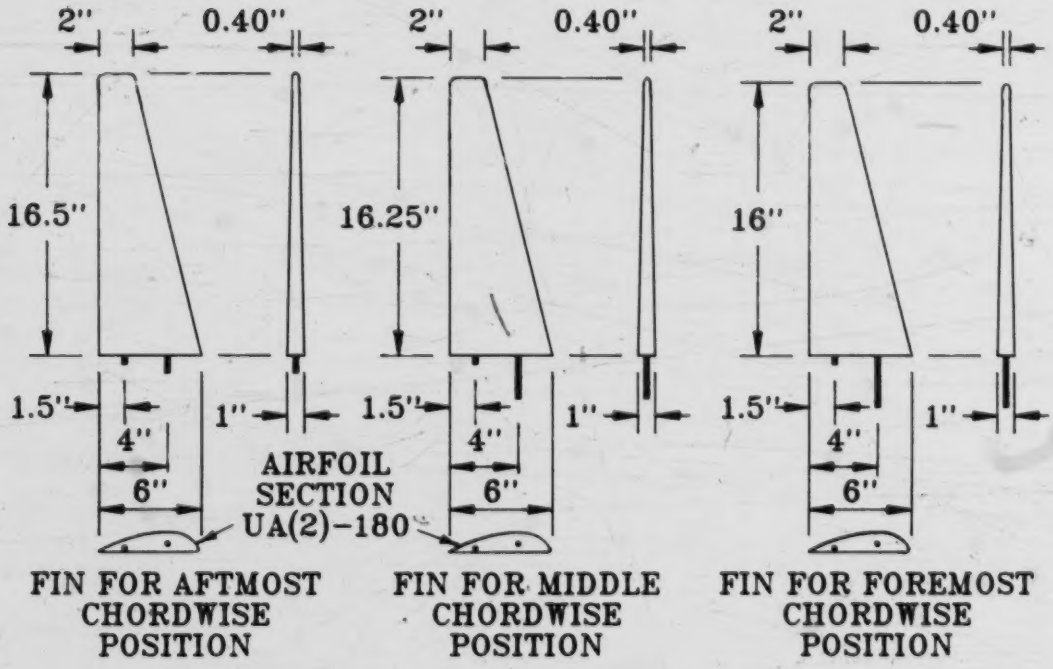

(b) Specifications of the tip tank fins

FIGURE 3-4 Dimensions and geometries of the wingtip modifications

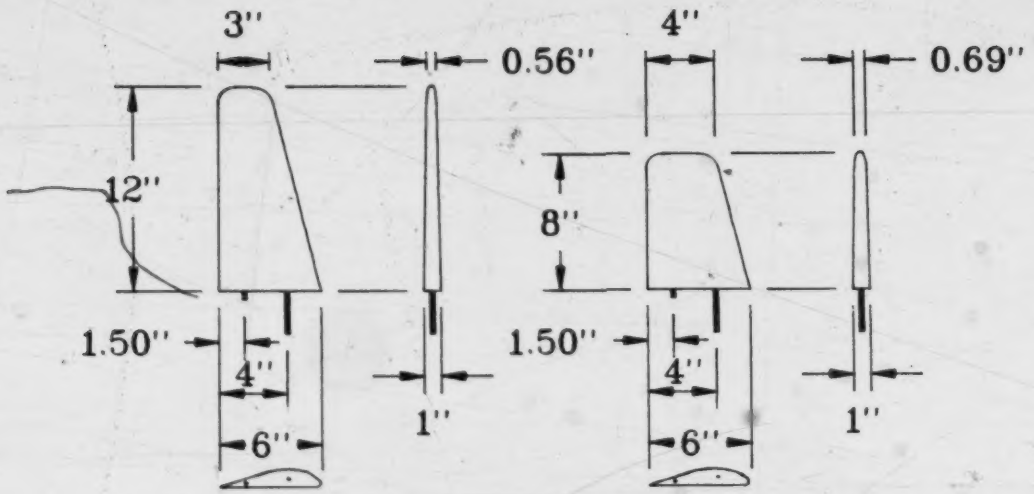

(c) Specifications of a truncated tip tank fin

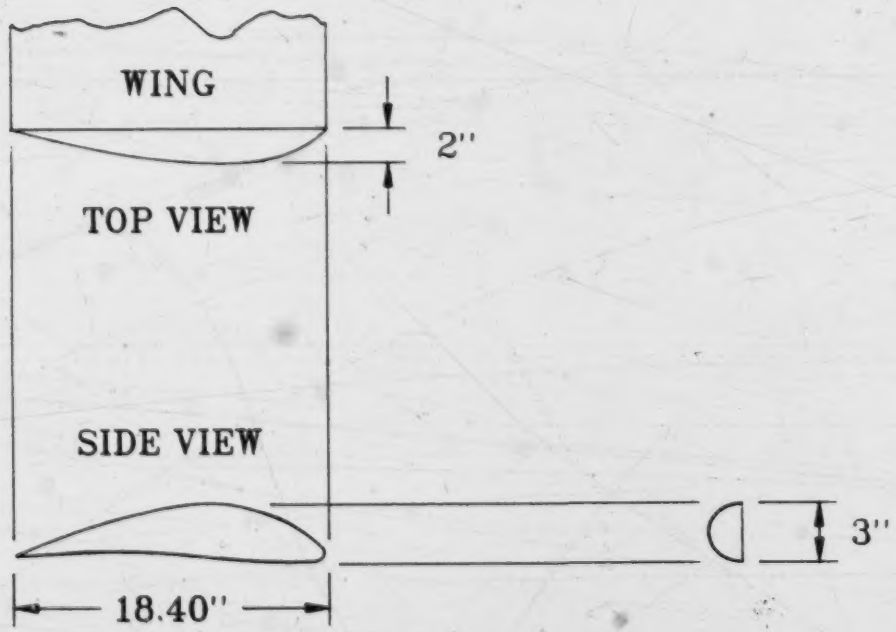

(d) Specifications of the round tip

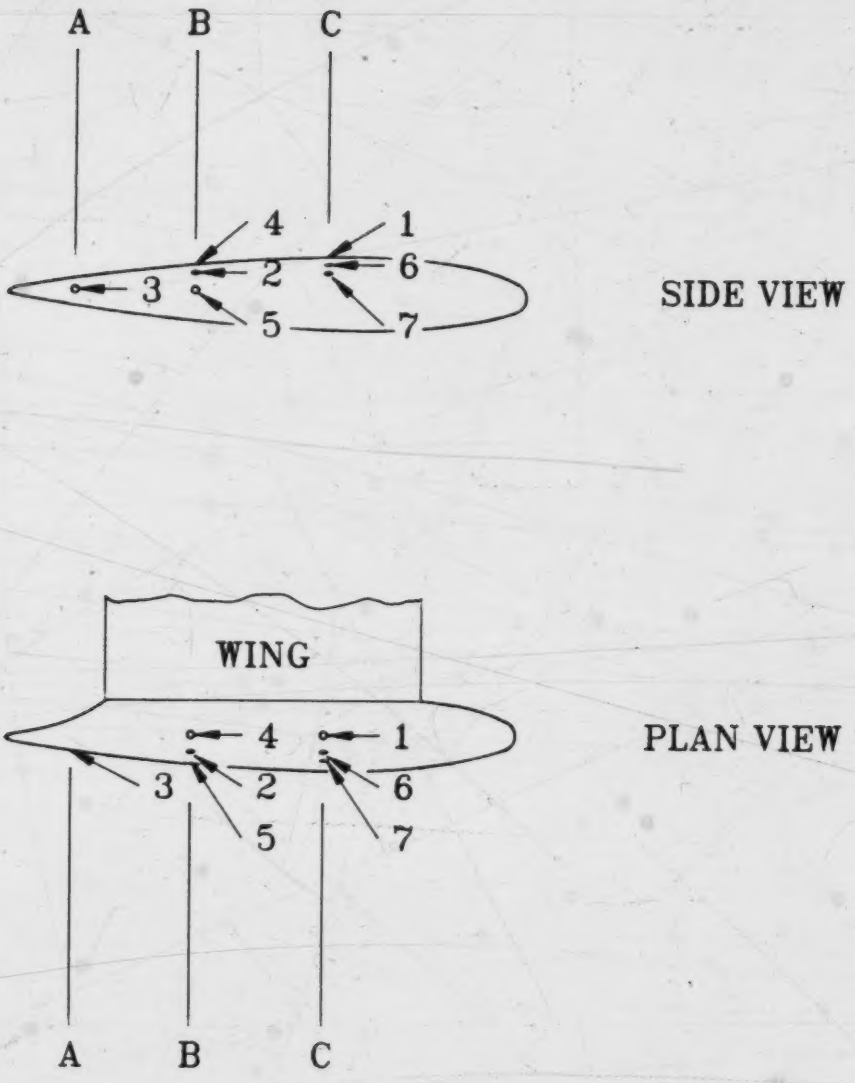

FIGURE 3-5 System of numbering tip tank fin supports

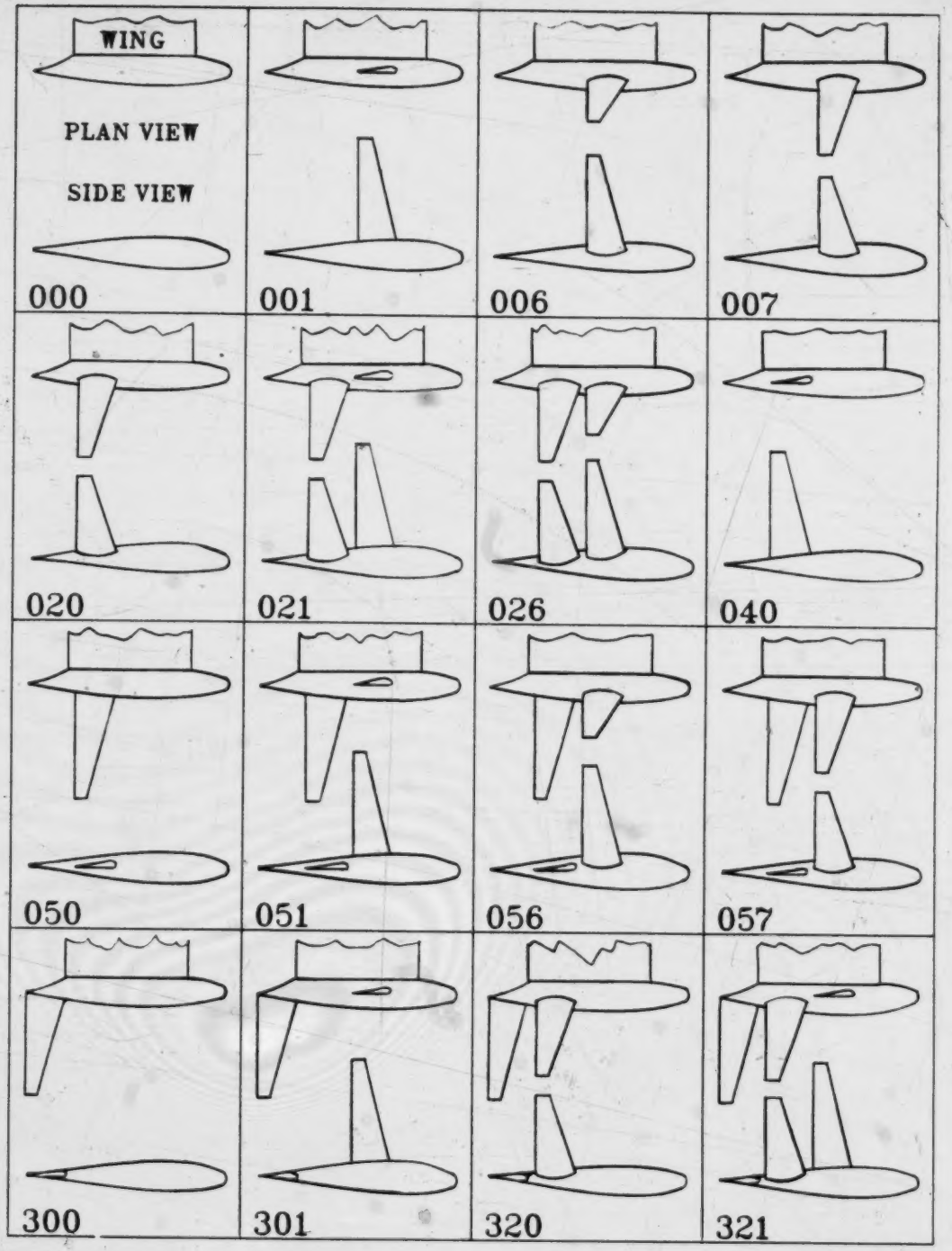

FIGURE 3-6 Tip tank fin combinations with their corresponding three-digit codes

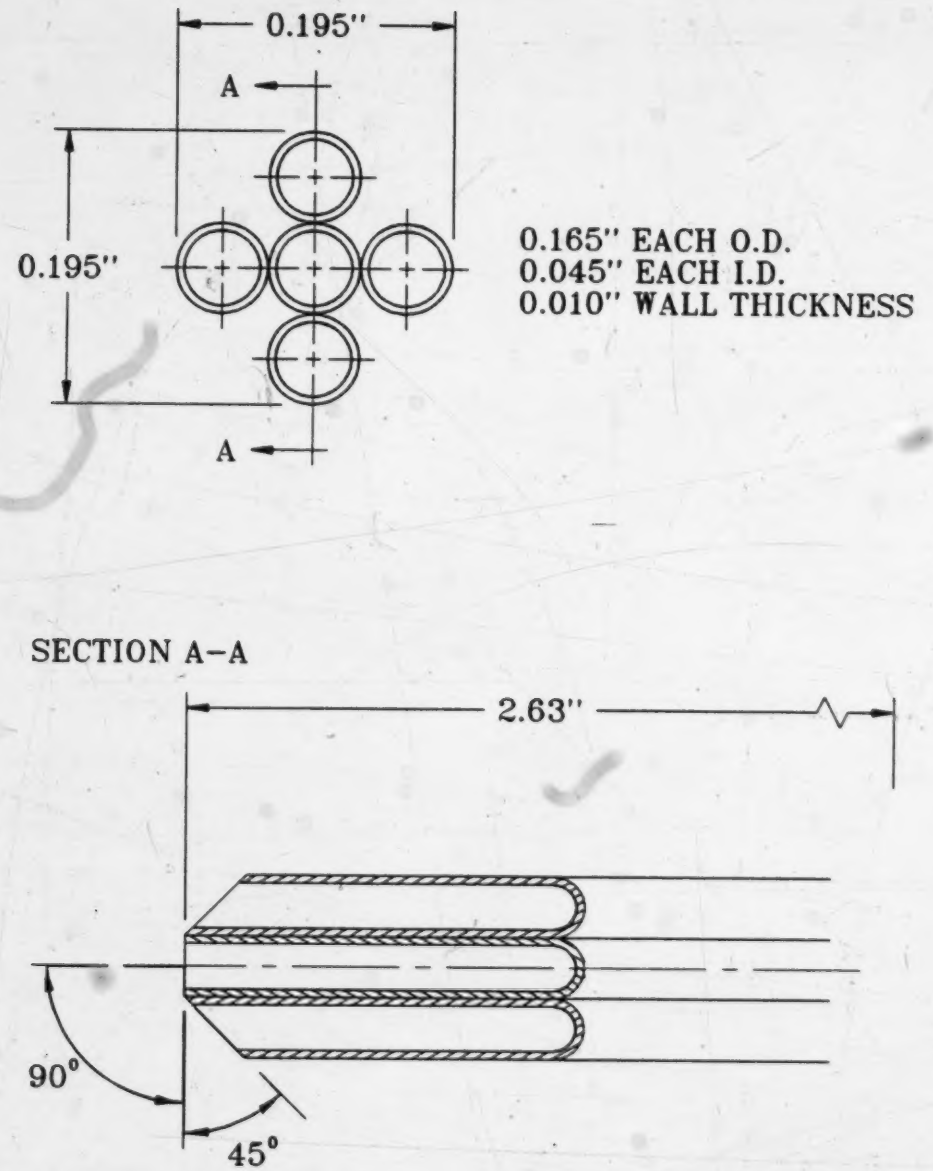

FIGURE 3-7 Arrangement and specifications of the five-hole flow angle probe

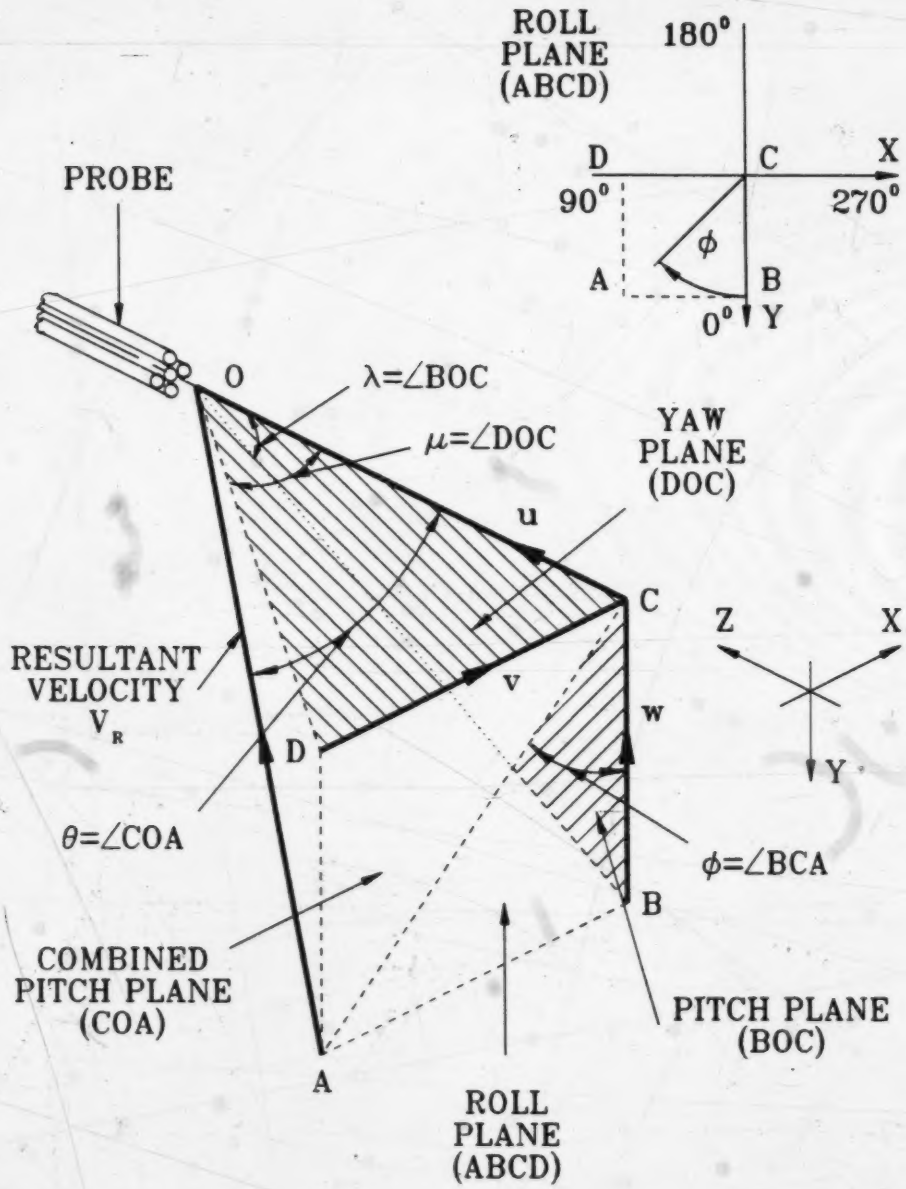

FIGURE 3-8 Local flow angle and velocity conventions for measurement with the five-hole flow angle probe

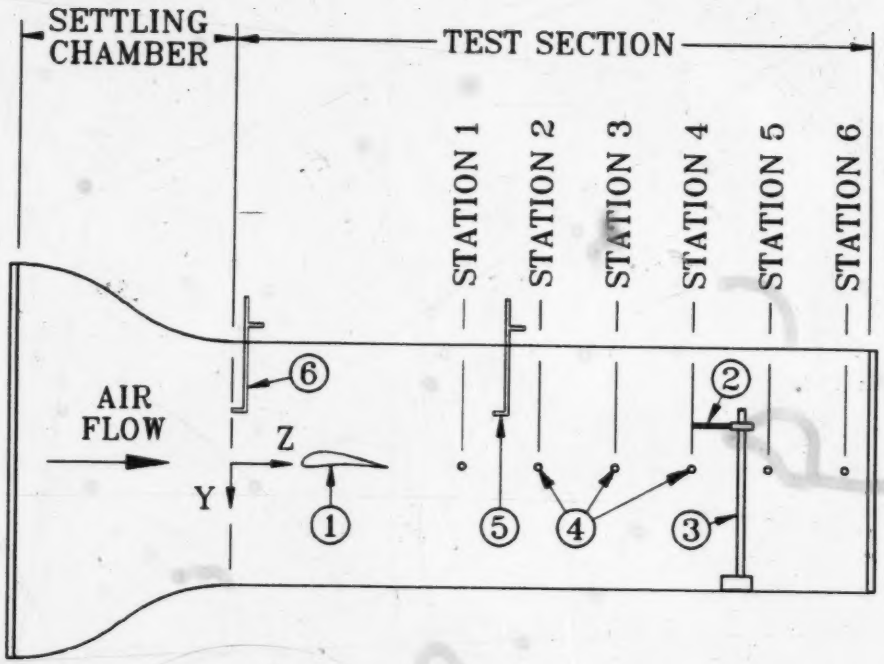

① WING SECTION (FX61-163/SF)

② FIVE-HOLE PROBE

③ PORTABLE XY TRAVERSE

④ TEST SECTION WALL TAP

⑤ PITOT-STATIC TUBE (TUNNEL)

⑥ PITOT-STATIC TUBE (MAIN)

FIGURE 3-9 Main test section showing arrangement of experimental apparatus

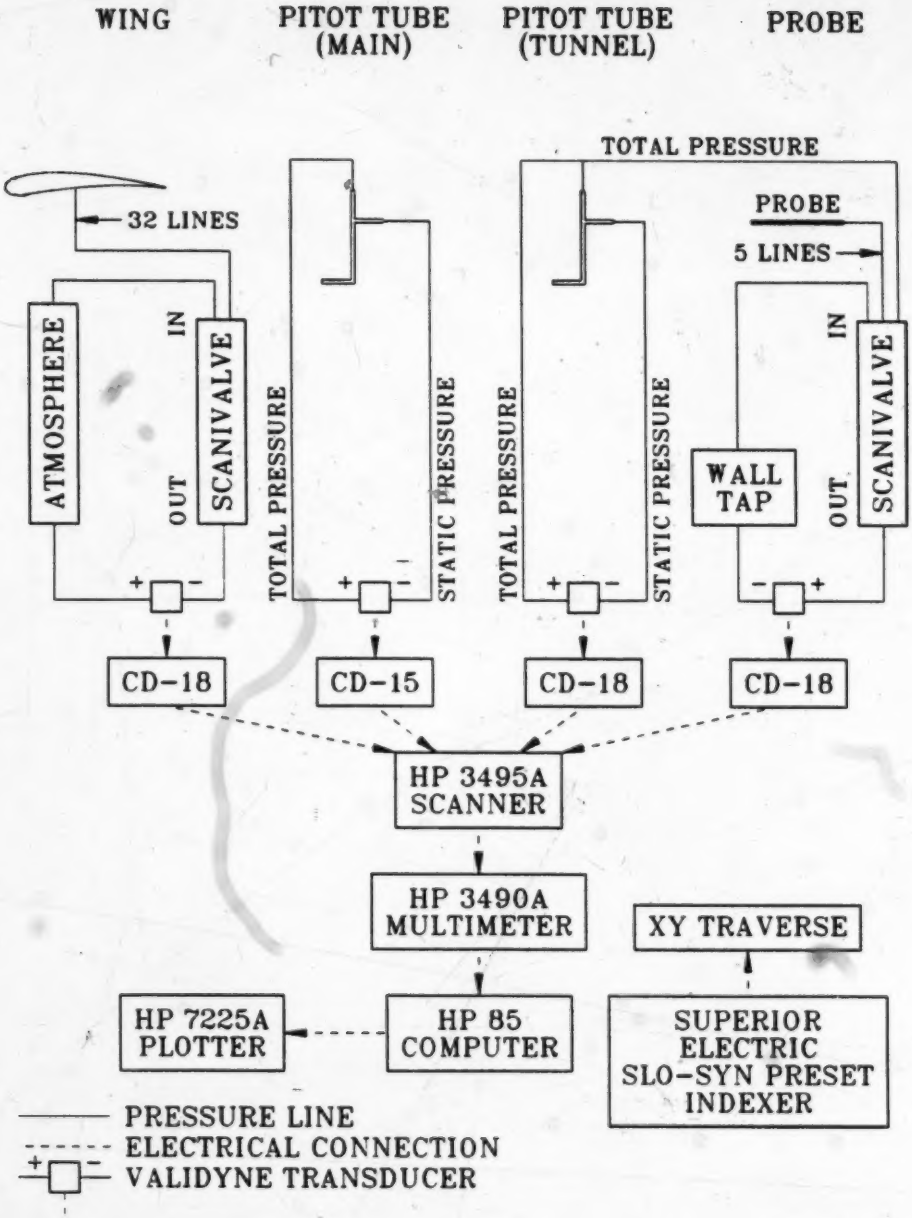

FIGURE 3-10 Transmission of data from the wing and wake measurements to the computer

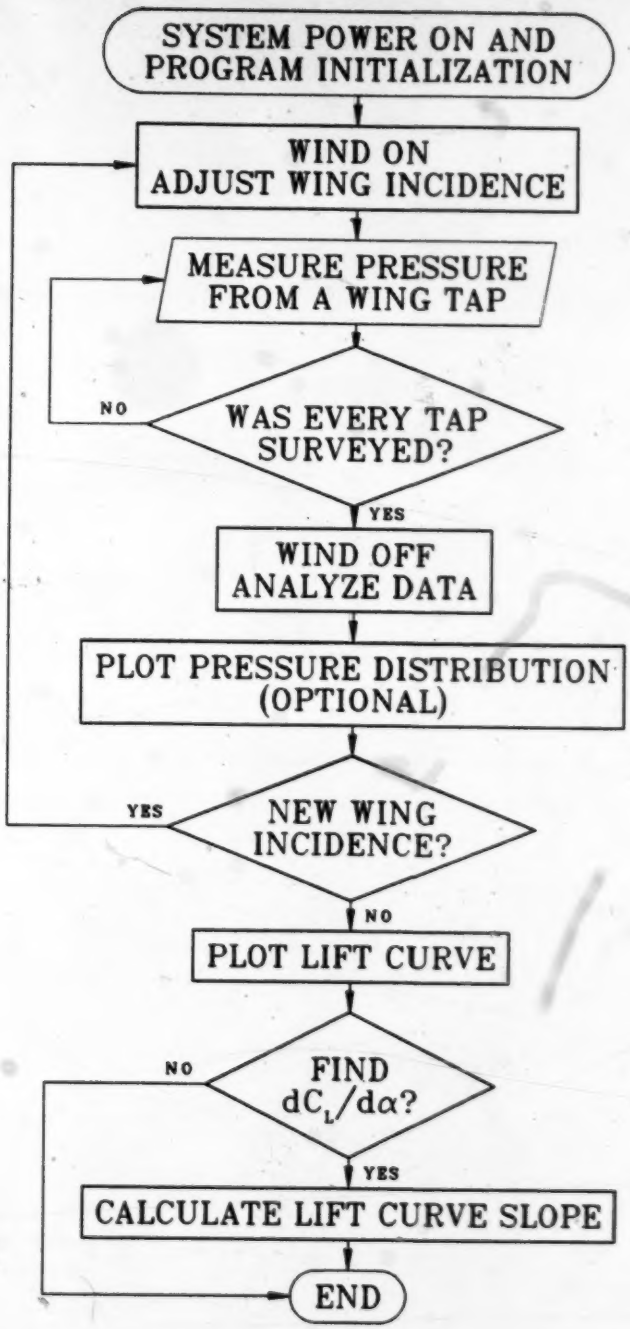

FIGURE 4-1 Flowchart showing summary of lift curve measurement procedure

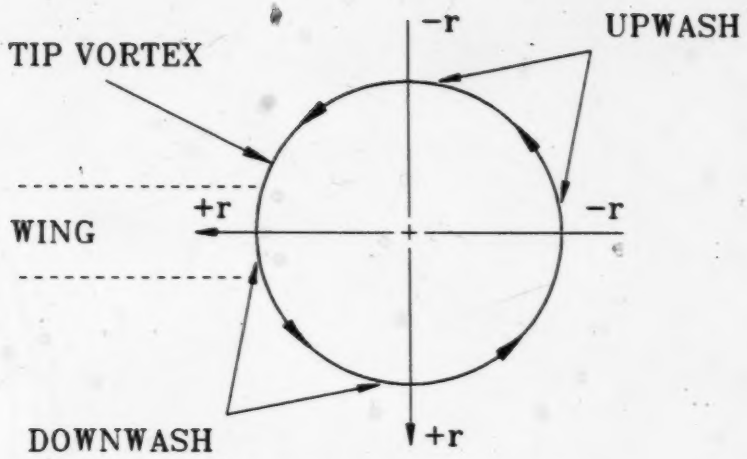

(a) The radial coordinates of a trailing vortex including downwash conventions (flow is out of the page)

FIGURE 4-2 Rotational velocity distribution measurement procedure

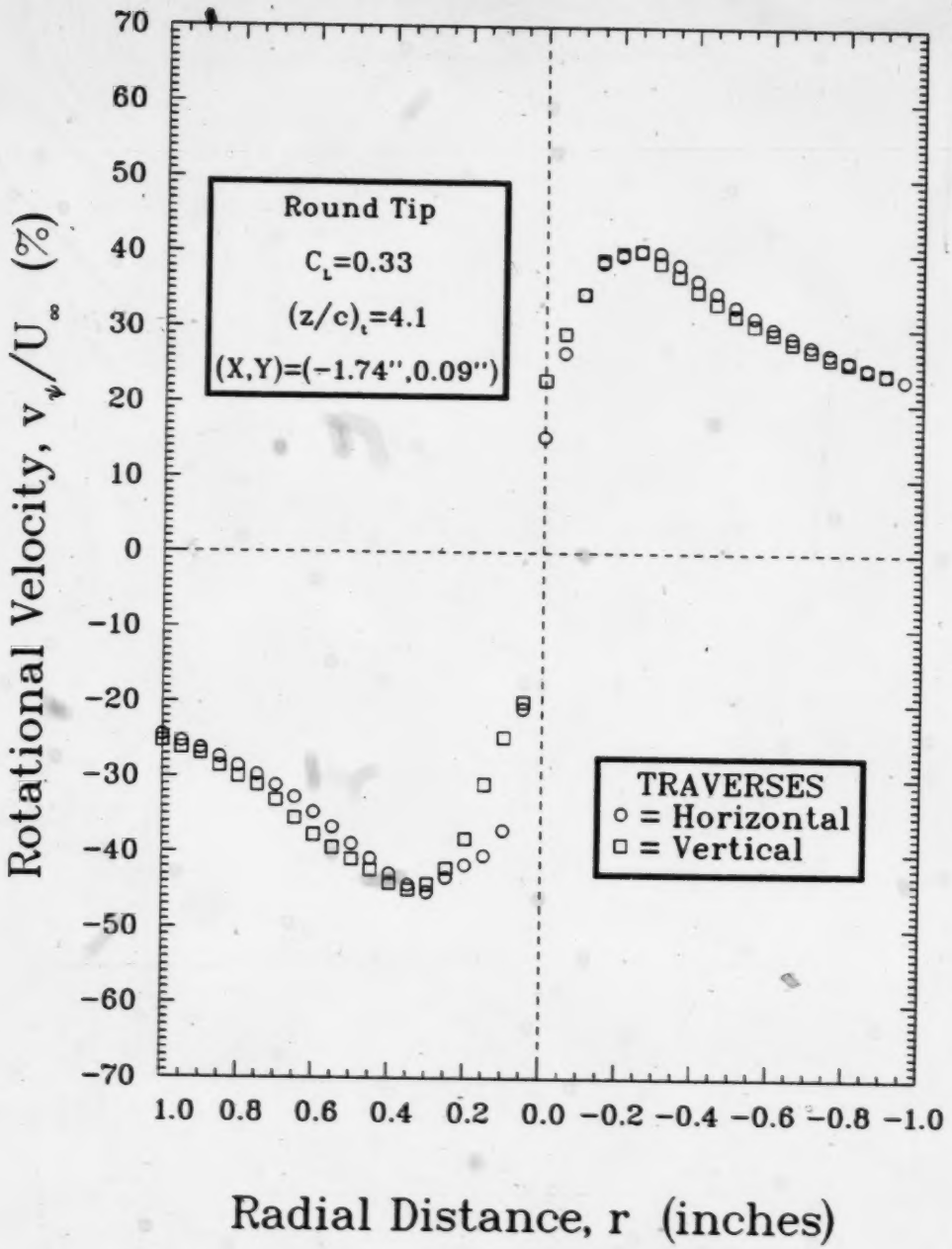

(b) Sample rotational velocity distribution of the vortex shed from the round tip with C_L = 0.33 and $(z/c)_t$ = 4.1

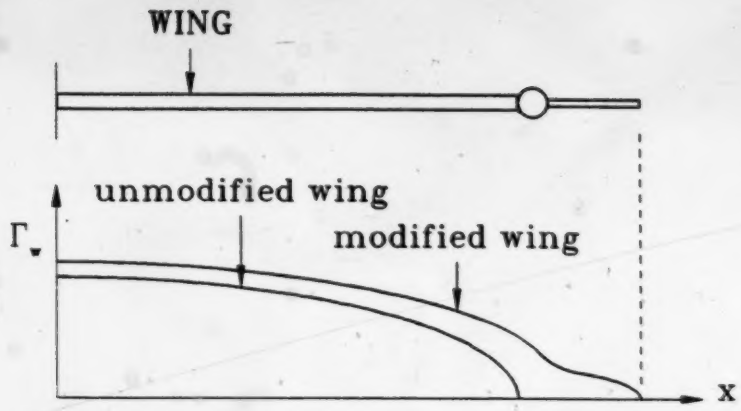

(a) Overall lift increase due to displaced wingtip vortex

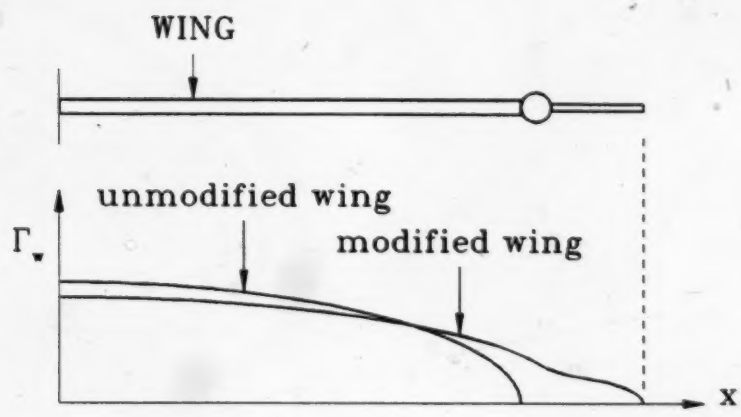

(b) Redistribution of lift due to a redistribution of the downwash pattern

FIGURE 5-1 Changes in the wing load distribution due to a wingtip device

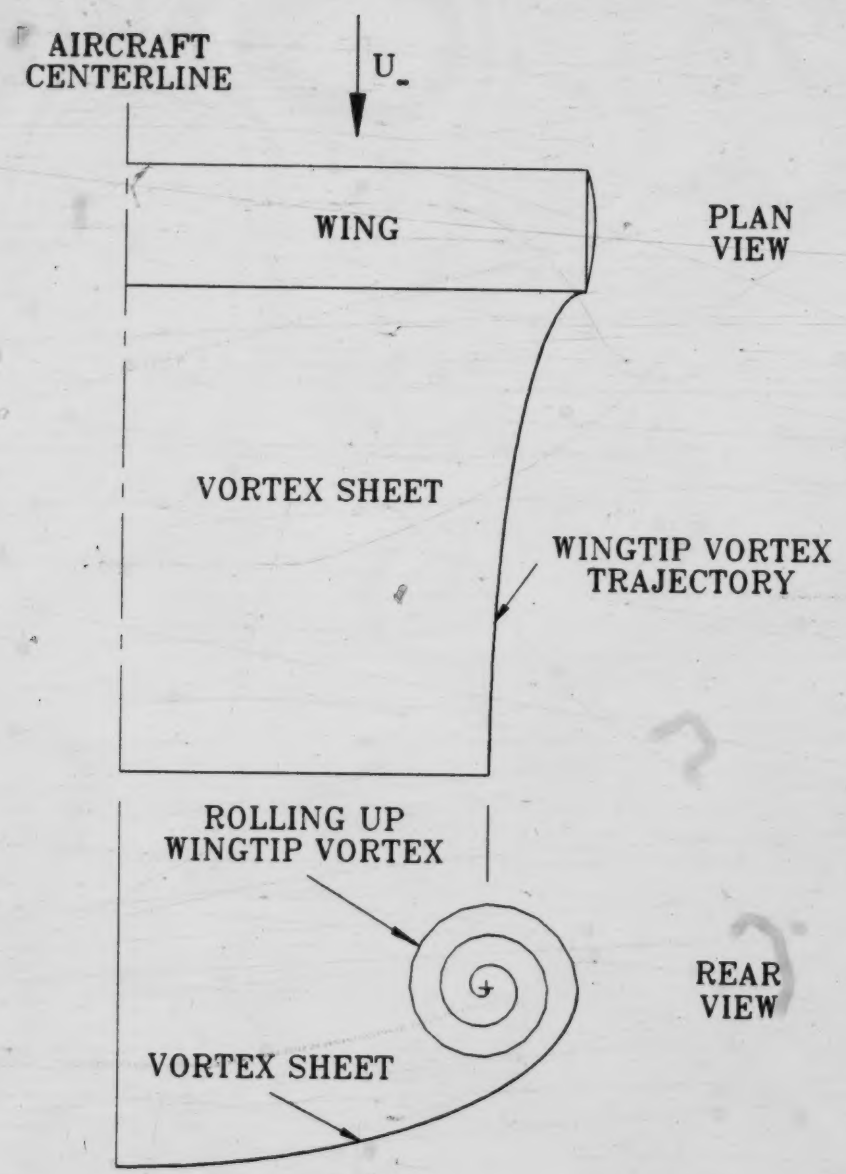

FIGURE 5-2 The trajectory of a wingtip vortex during completion of roll-up

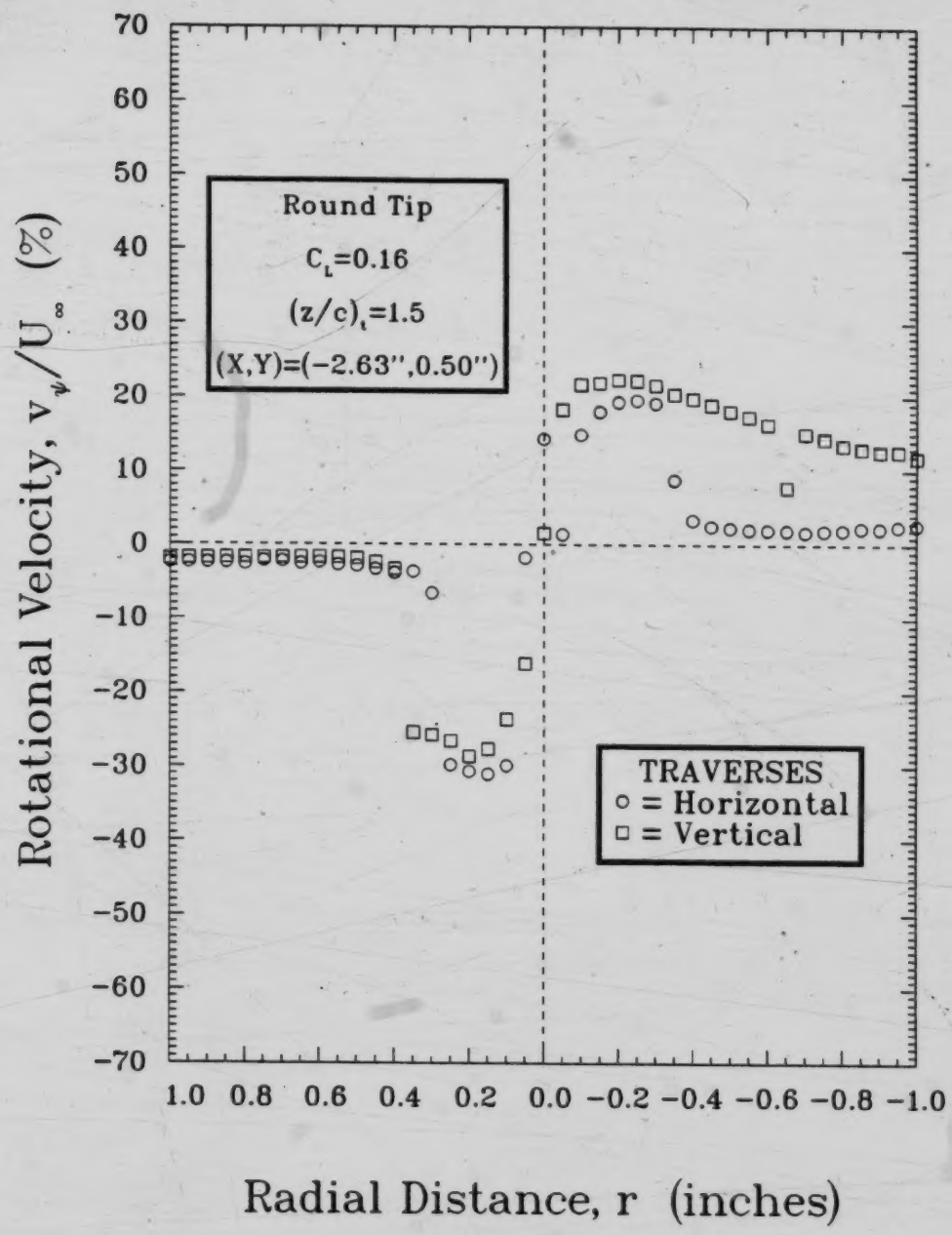

FIGURE 5-3 Rotational velocity distribution of the vortex shed from the round tip with C_L = 0.16 and $(z/c)_t$ = 1.5

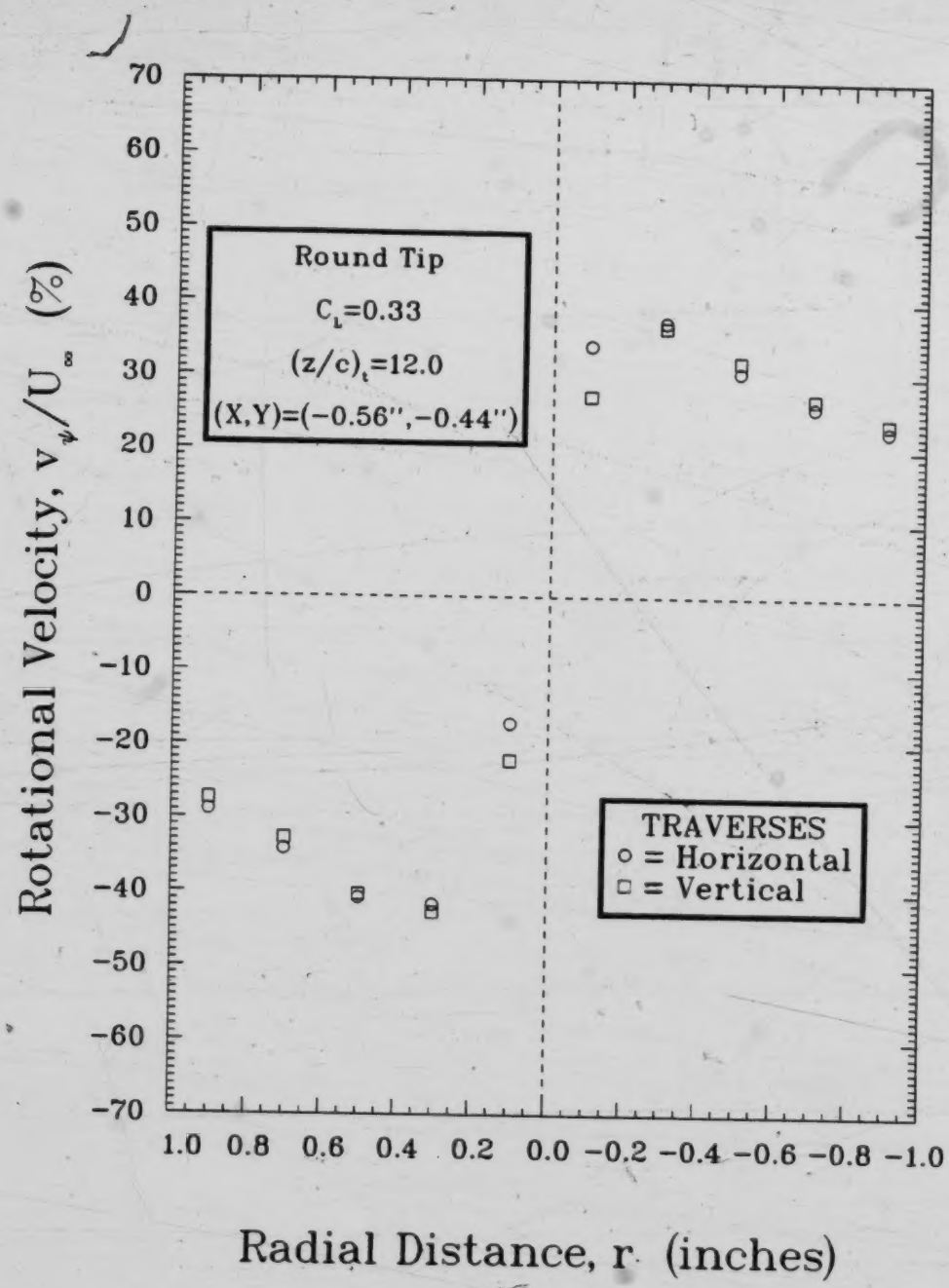

FIGURE 5-4 Rotational velocity distribution of the vortex shed from the round tip with C_L = 0.33 and $(z/c)_t$ = 12.0

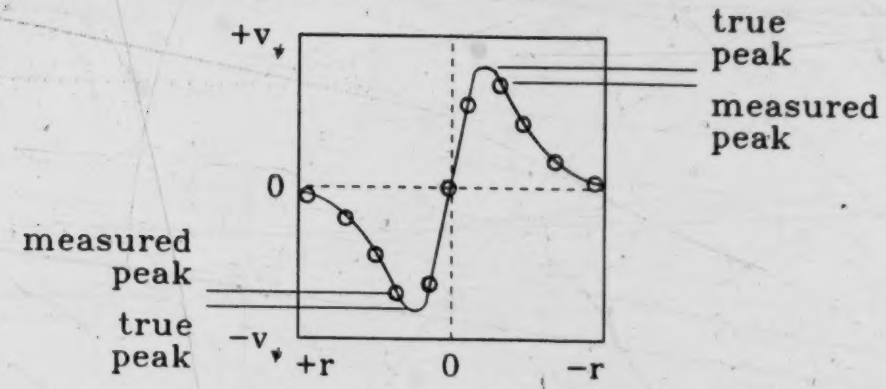

FIGURE 5-5 Resolution of the rotational velocity distribution due to the measurement procedure

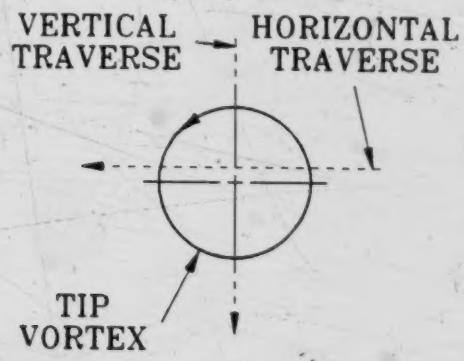

(a) An uncentered traverse. Here the vertical traverse is centered, and the horizontal traverse is slightly offset

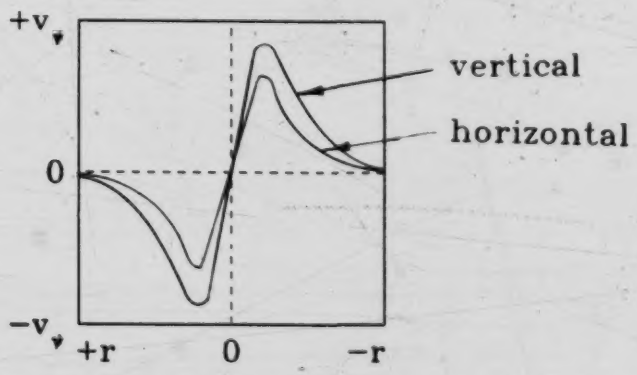

(b) The measured rotational velocity distribution from the traverse in (a)

FIGURE 5-6 The uncertainty in measured peak rotational velocity due to an uncentered traverse through a vortex

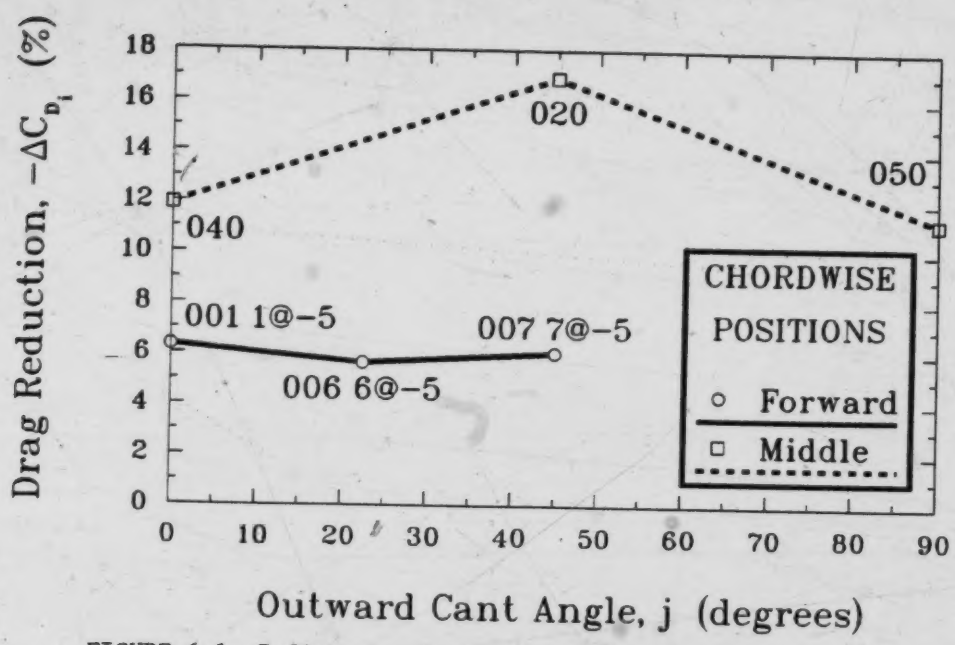

FIGURE 6-1 Influence of outward cant angle on induced drag reduction, measured at the foremost and middle chordwise positions

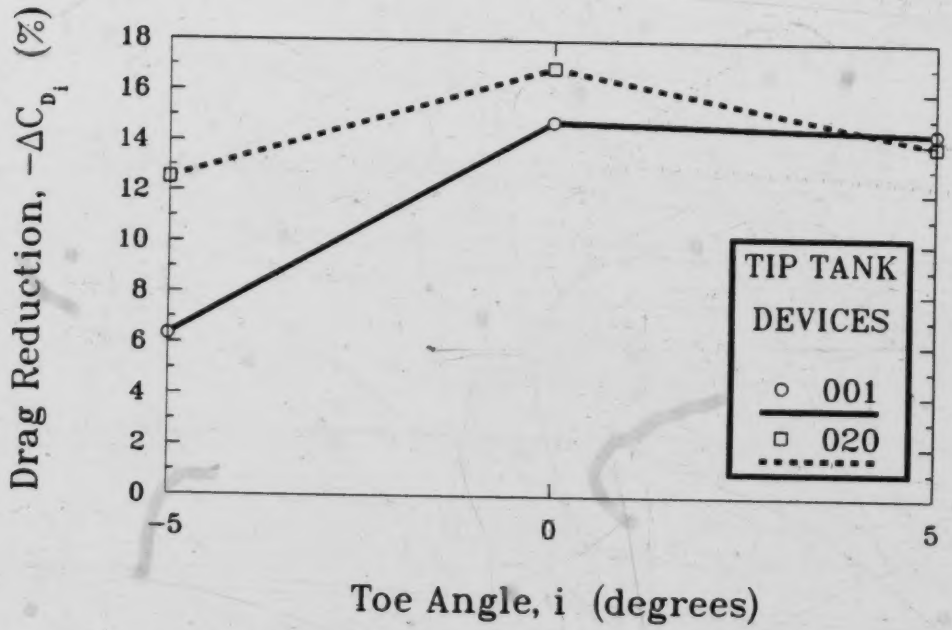

FIGURE 6-2 Influence of toe angle on induced drag reduction, measured for tip tank configurations 001 and 020

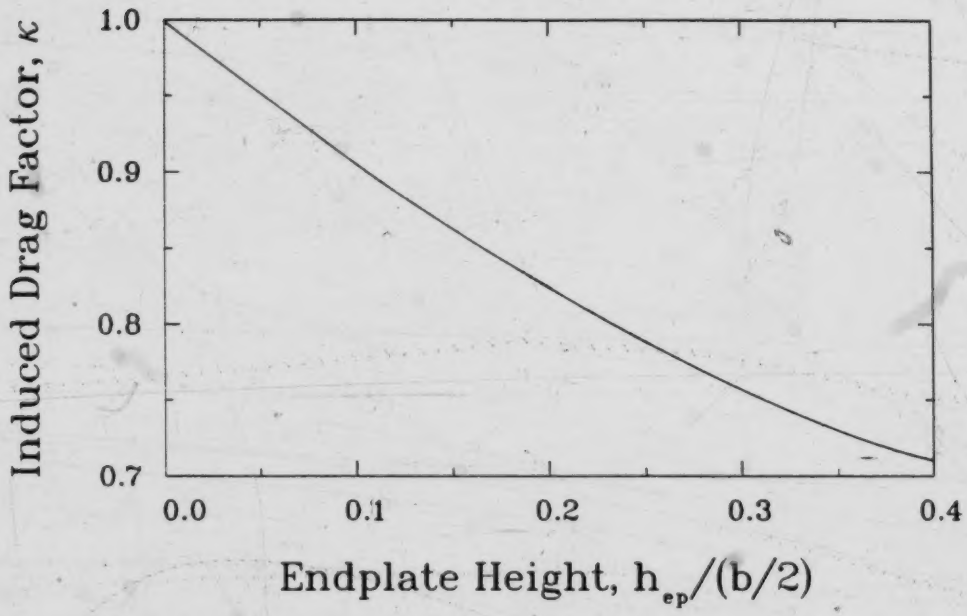

FIGURE 6-3 Results from Mangler [30] and Weber [31] for the theoretical induced drag factor of a wing with endplates on the upper surface at the wingtips

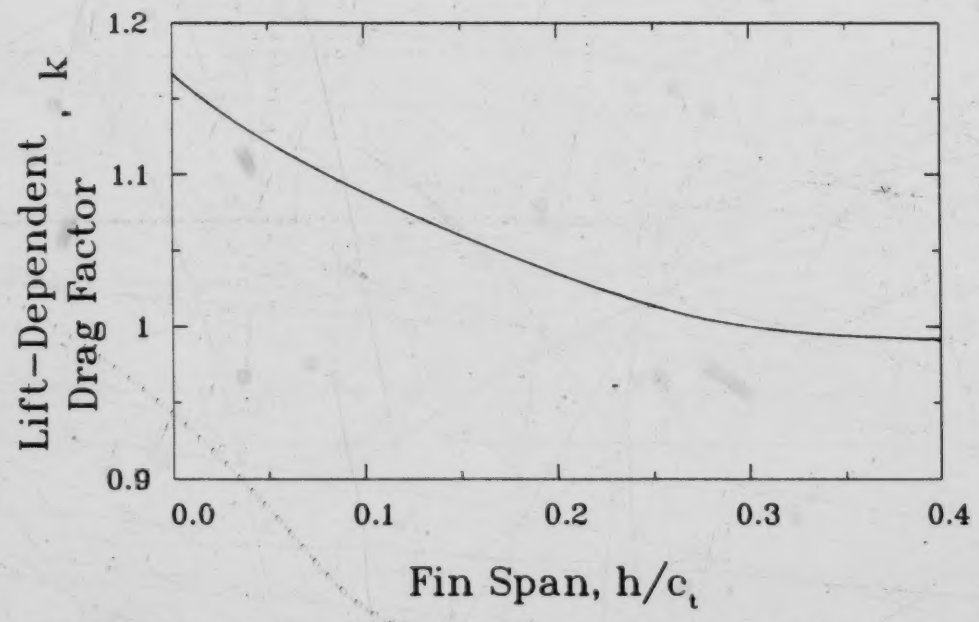

FIGURE 6-4 Experimental results from Spillman and Allen [12] for the influence of fin span on lift-dependent drag factor

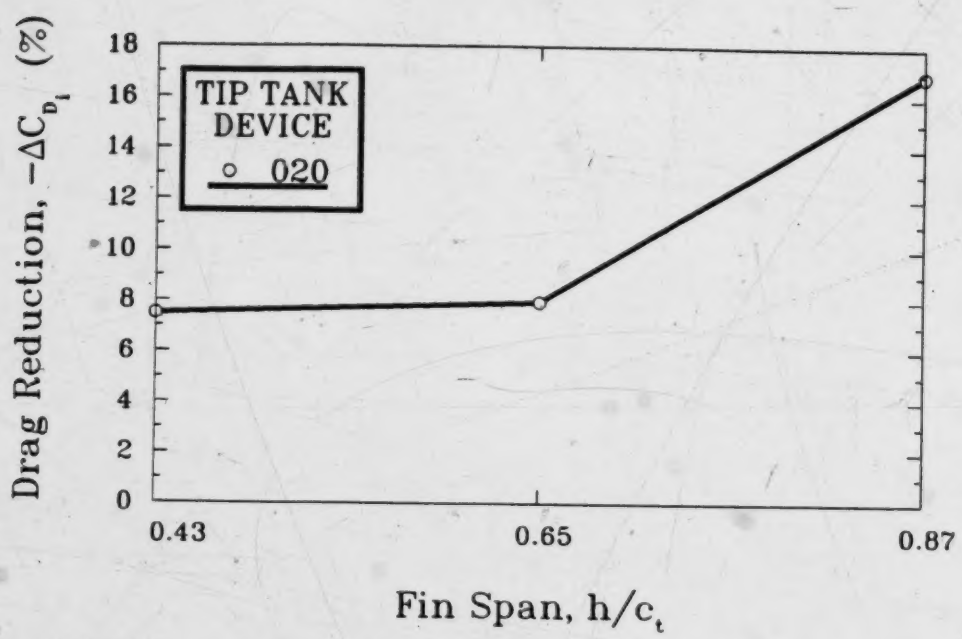

FIGURE 6-5 Influence of fin span on induced drag reduction for configuration 020

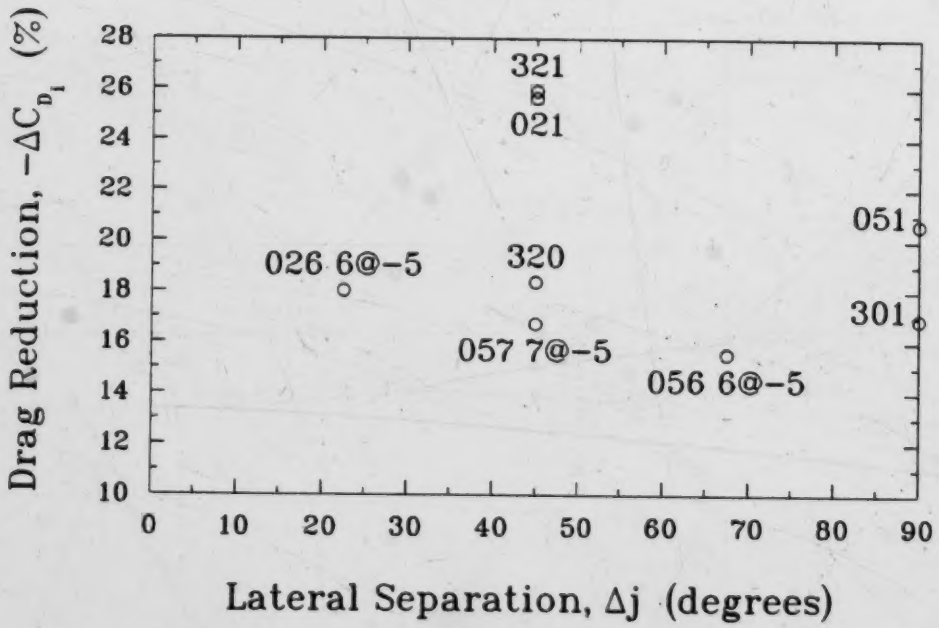

FIGURE 6-6 Influence of lateral separation between successive fins on induced drag reduction

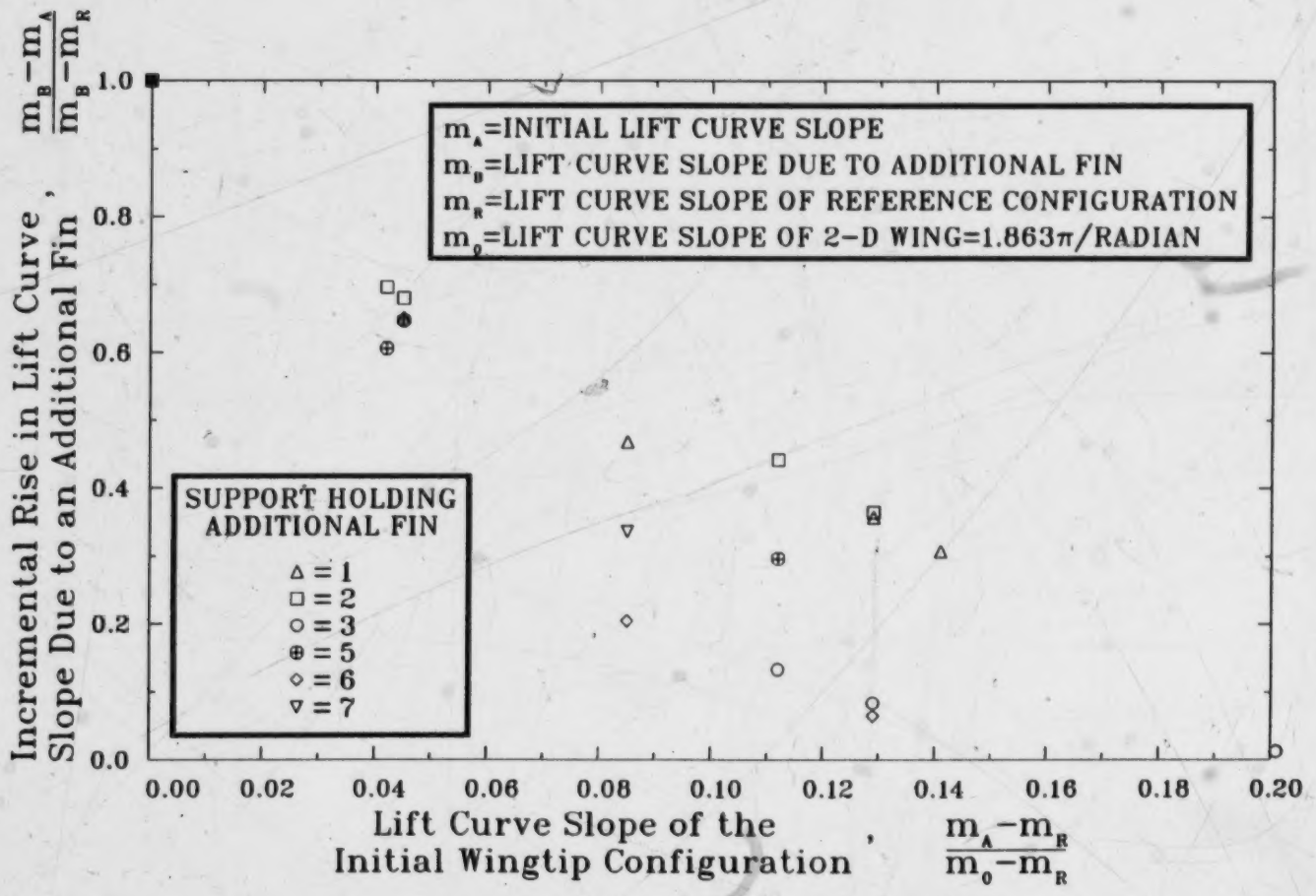

FIGURE 6-7 The effect an additional fin has in furthering induced drag reduction

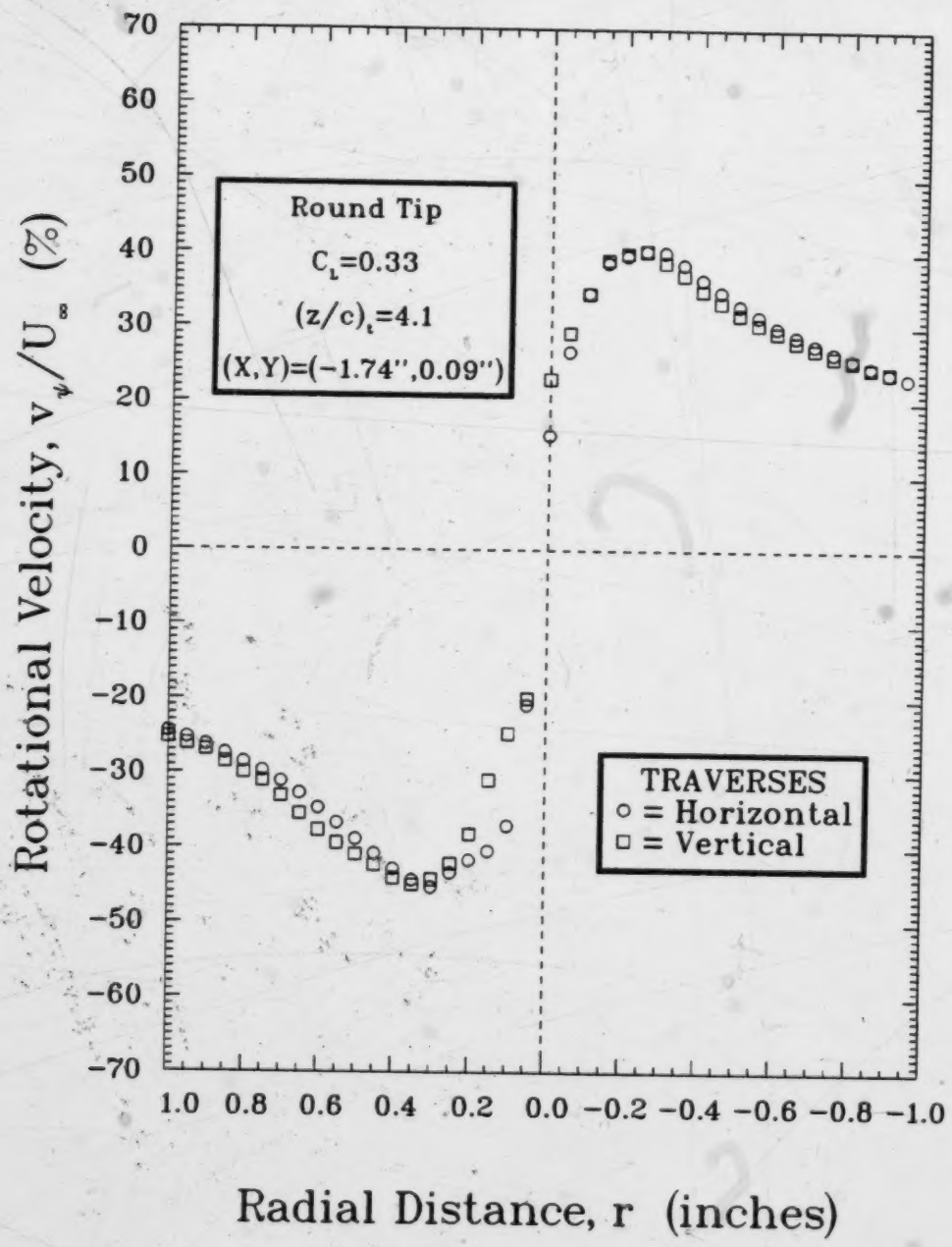

(a) C_L = 0.33

FIGURE 6-8 Rotational velocity distributions of the wingtip vortex due to the round tip with $(z/c)_t$ = 4.1

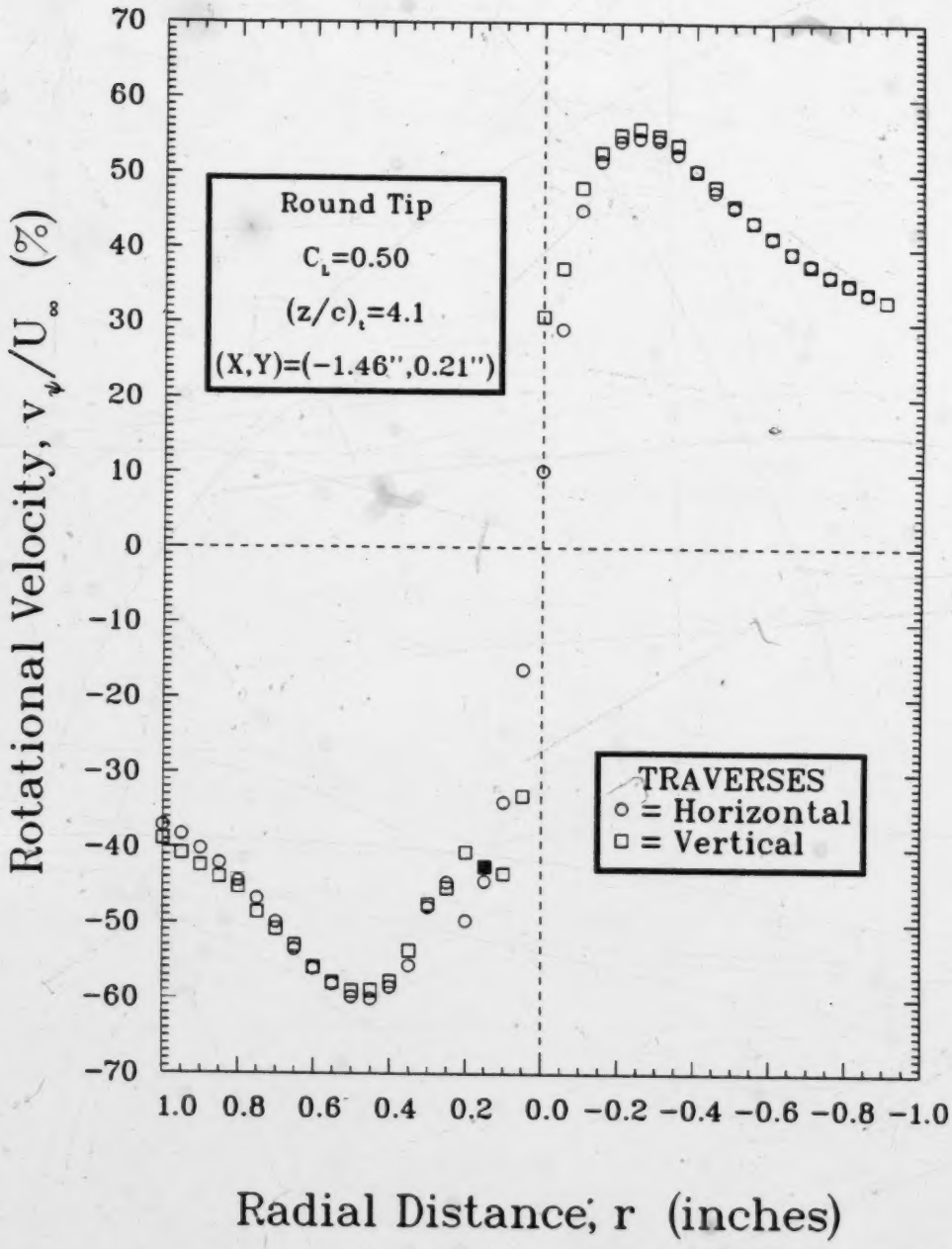
Round Tip
C_L=0.50
$(z/c)_t$=4.1
(X,Y)=(−1.46",0.21")
TRAVERSES
○ = Horizontal
□ = Vertical
Rotational Velocity, v_ψ/U_∞ (%)
Radial Distance, r (inches)
70
60
50
40
30
20
10
0
−10
−20
−30
−40
−50
−60
−70
1.0 0.8 0.6 0.4 0.2 0.0 −0.2 −0.4 −0.6 −0.8 −1.0

(b) C_L = 0.50

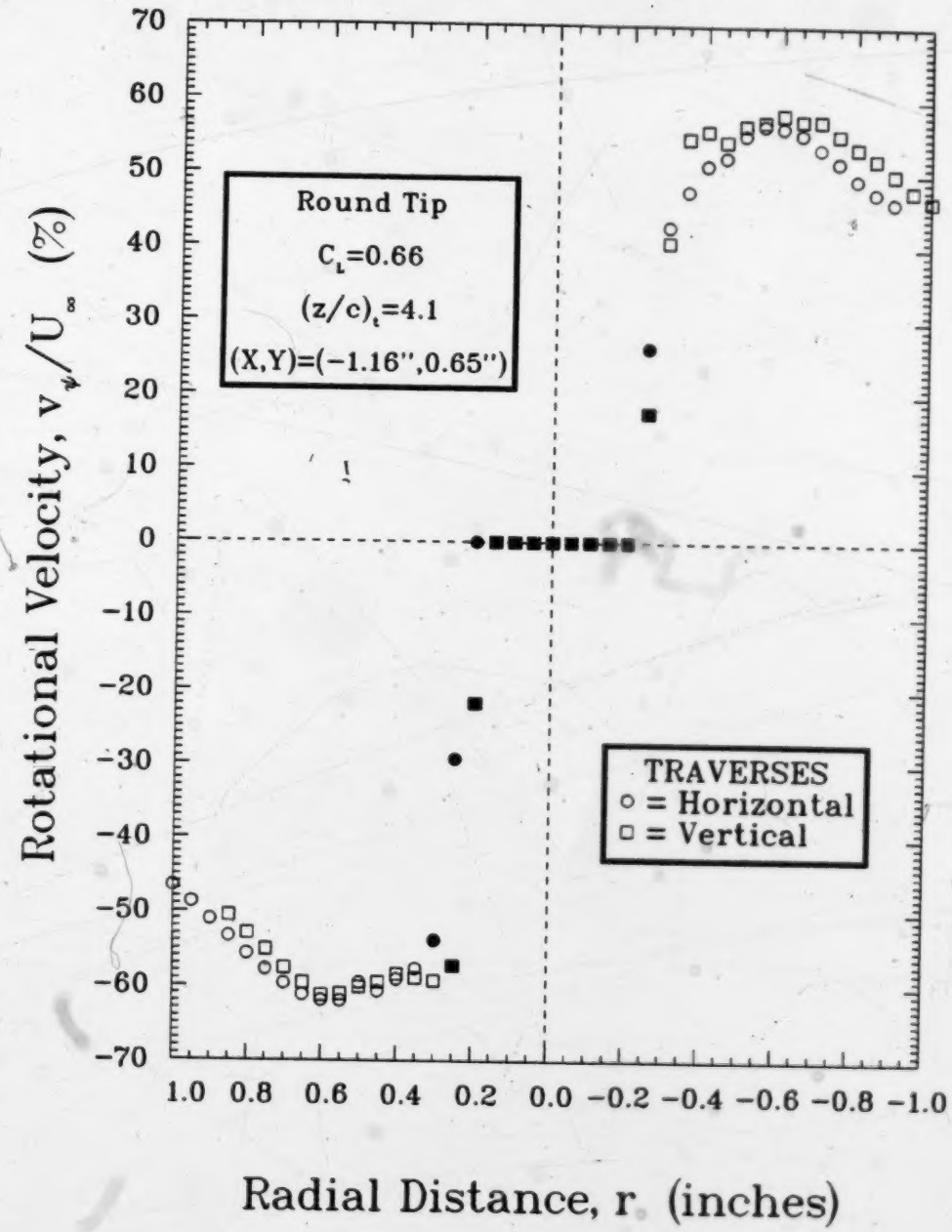
Round Tip
C_L=0.66
$(z/c)_t$=4.1
(X,Y)=(−1.16",0.65")
TRAVERSES
○ = Horizontal
□ = Vertical
Rotational Velocity, v_ψ/U_∞ (%)
70
60
50
40
30
20
10
0
−10
−20
−30
−40
−50
−60
−70
1.0 0.8 0.6 0.4 0.2 0.0 −0.2 −0.4 −0.6 −0.8 −1.0
Radial Distance, r (inches)

(c) C_L = 0.66

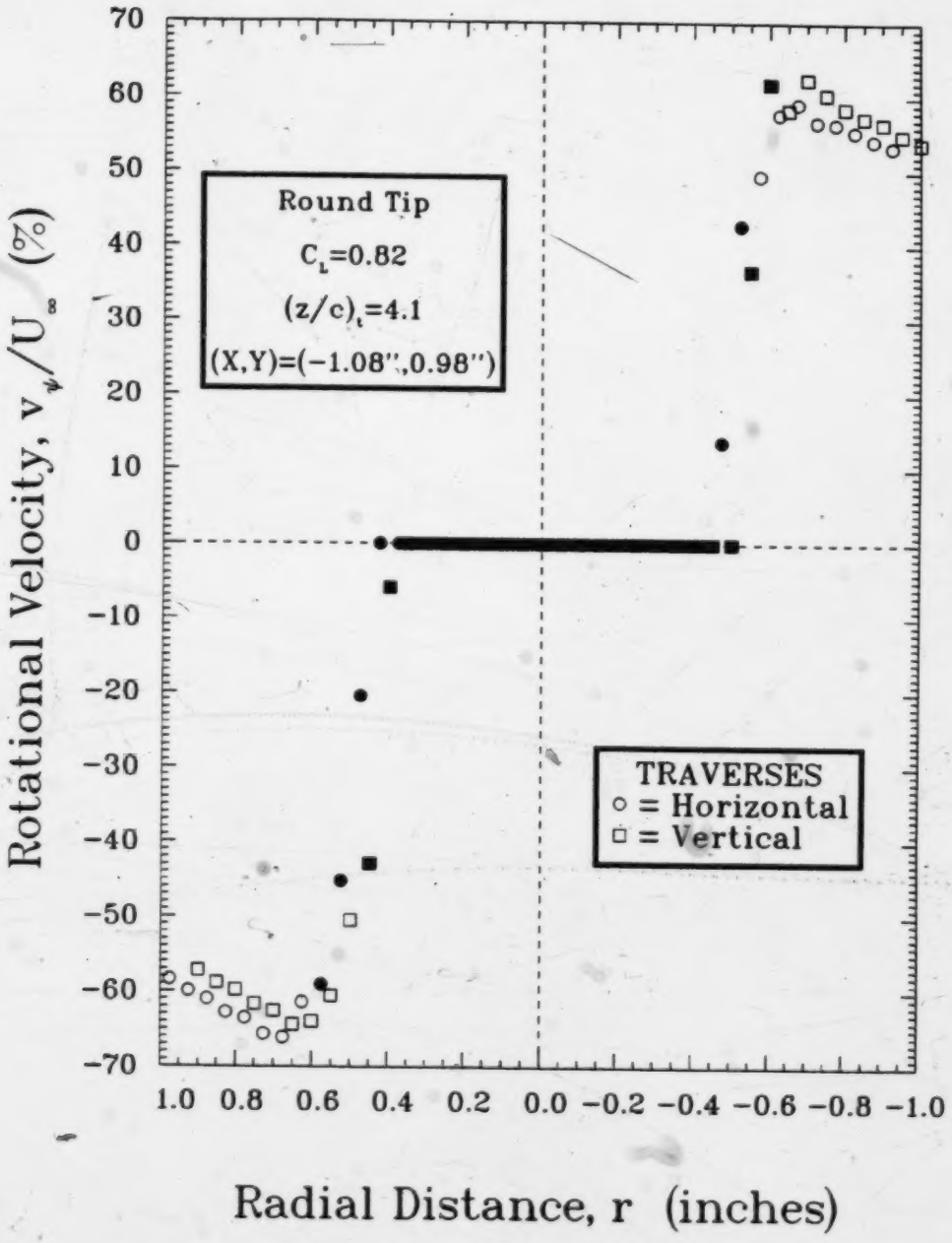
Round Tip
C_L=0.82
$(z/c)_t$=4.1
(X,Y)=(−1.08",0.98")
TRAVERSES
○ = Horizontal
□ = Vertical
Rotational Velocity, v_ψ/U_∞ (%)
70
60
50
40
30
20
10
0
−10
−20
−30
−40
−50
−60
−70
1.0 0.8 0.6 0.4 0.2 0.0 −0.2 −0.4 −0.6 −0.8 −1.0
Radial Distance, r (inches)

(d) C_L = 0.82

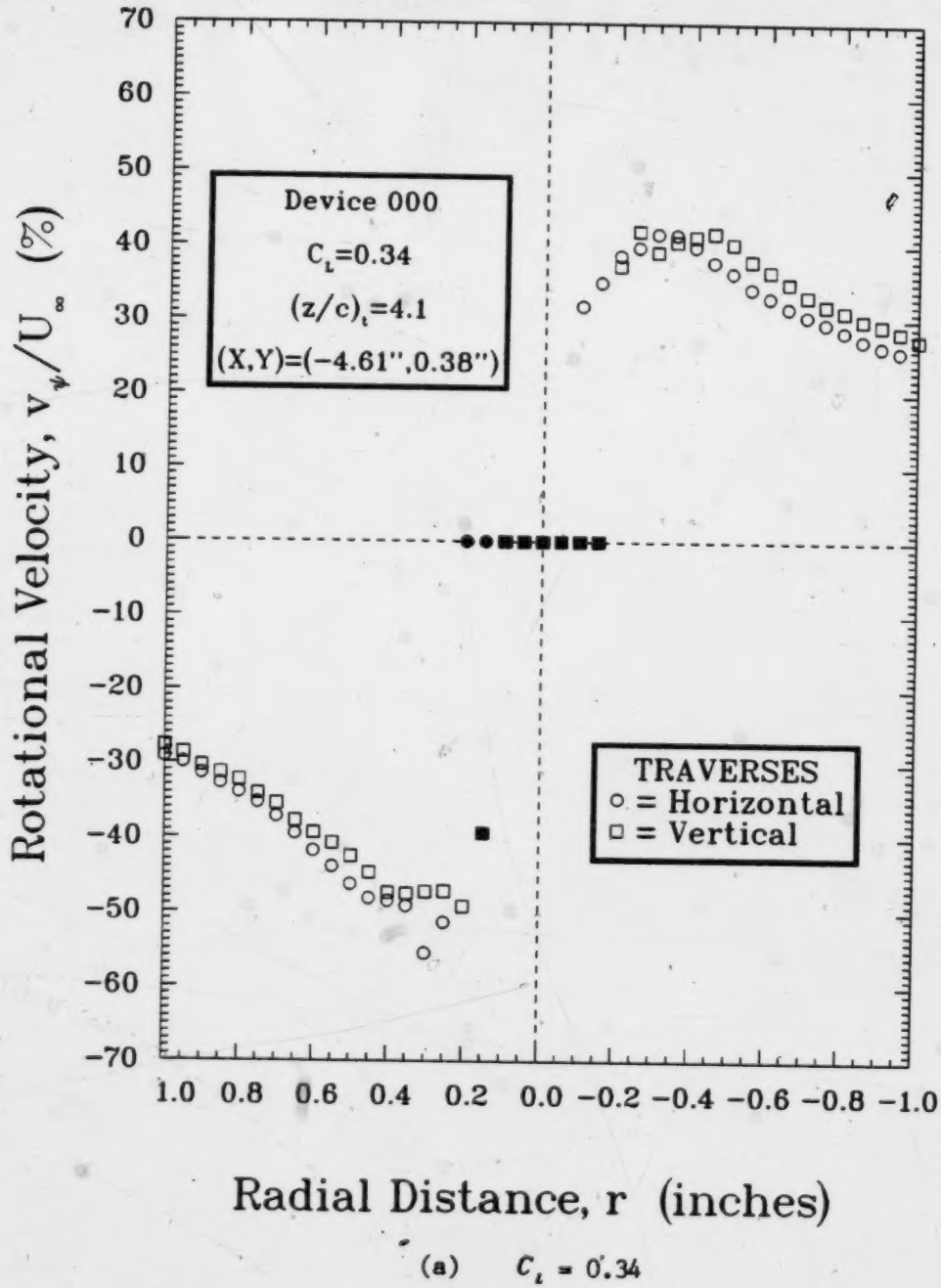

(a) C_L = 0.34

FIGURE 6-9 Rotational velocity distributions of the wingtip vortex due to the unfinned tip tank with $(z/c)_t$ = 4.1

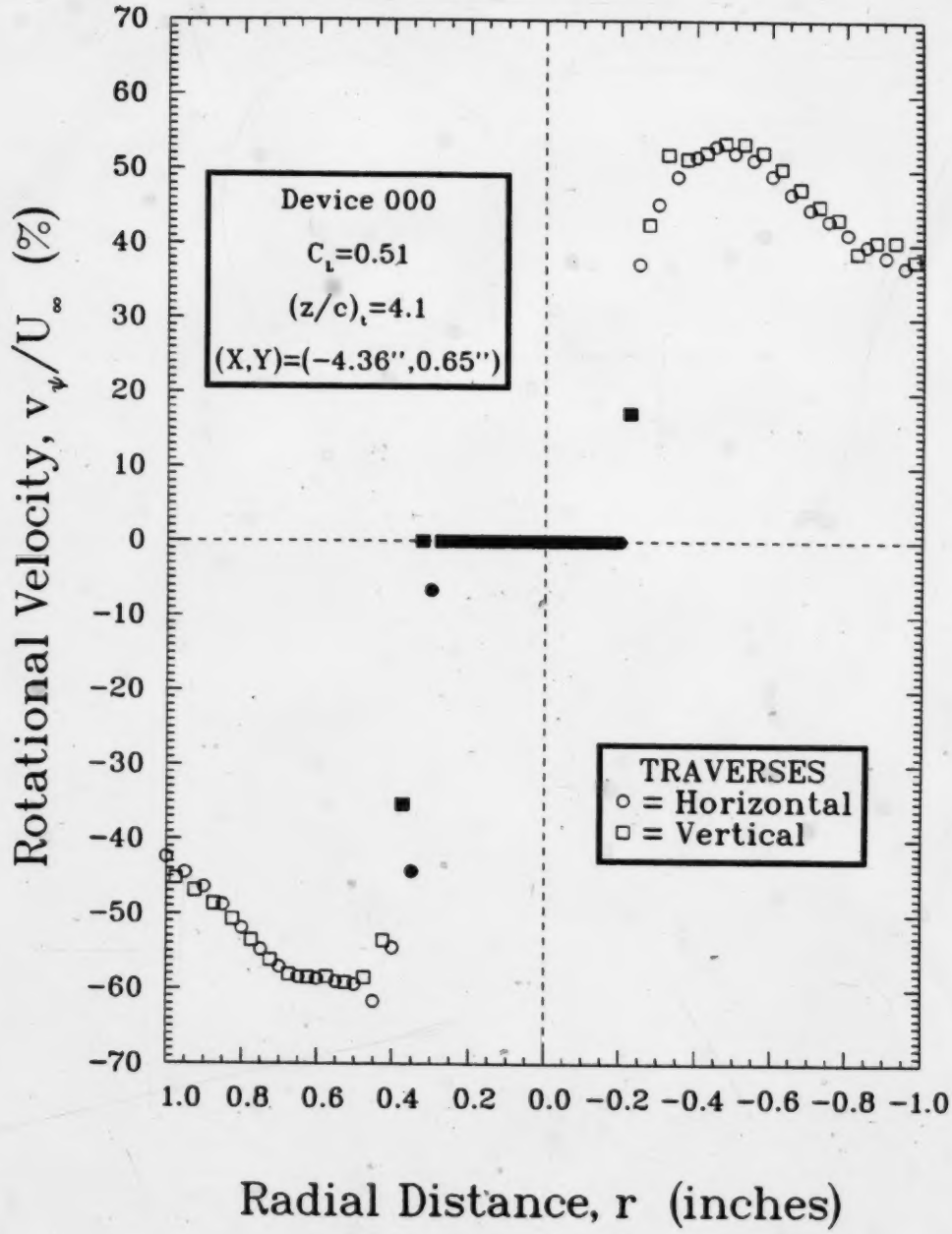
Device 000
C_L=0.51
$(z/c)_t$=4.1
(X,Y)=(−4.36",0.65")
TRAVERSES
○ = Horizontal
□ = Vertical
Rotational Velocity, v_ψ/U_∞ (%)
70
60
50
40
30
20
10
0
−10
−20
−30
−40
−50
−60
−70
1.0 0.8 0.6 0.4 0.2 0.0 −0.2 −0.4 −0.6 −0.8 −1.0
Radial Distance, r (inches)

(b) C_L = 0.51

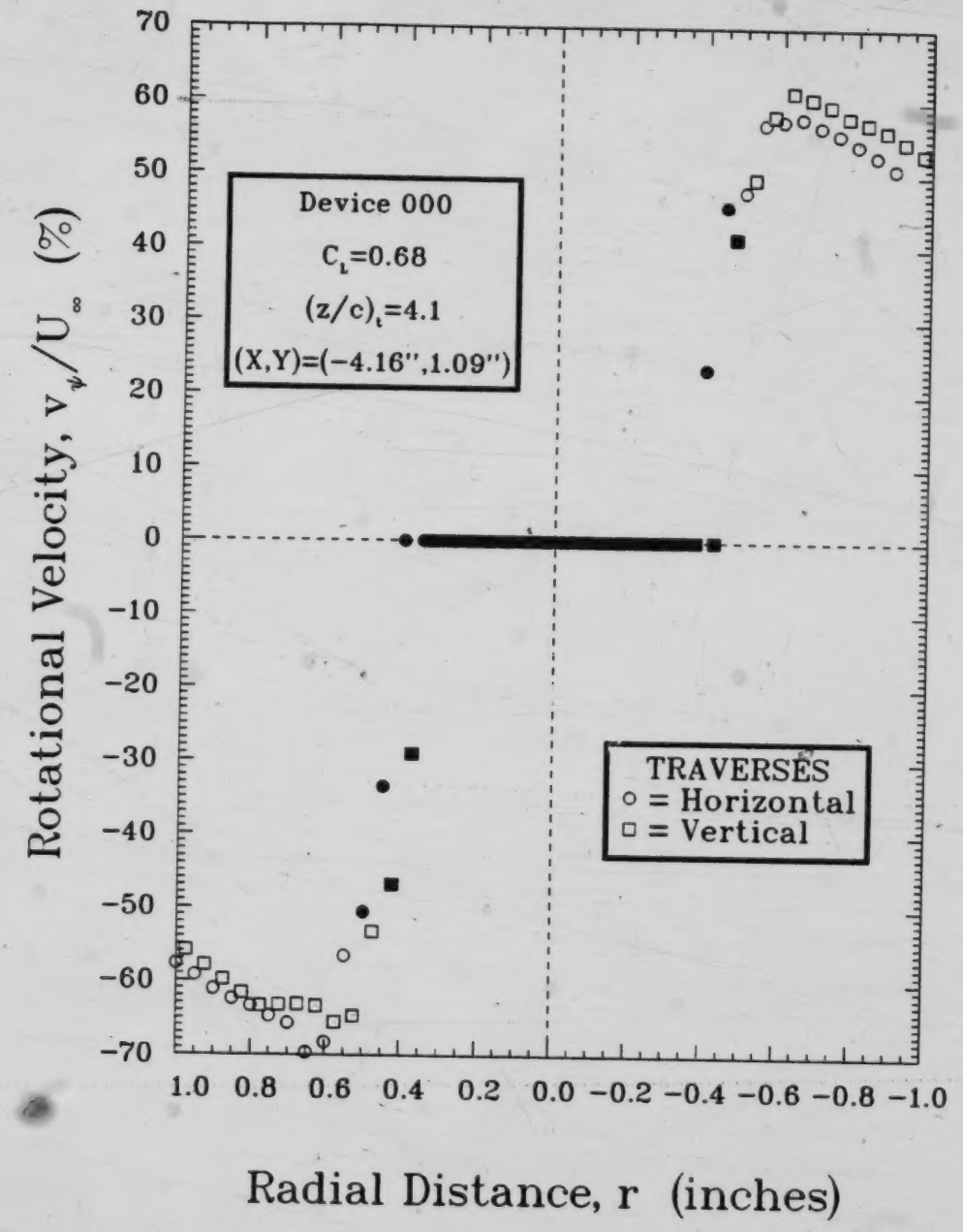
Device 000
C_L=0.68
$(z/c)_t$=4.1
(X,Y)=(−4.16",1.09")
TRAVERSES
○ = Horizontal
□ = Vertical
Rotational Velocity, v_ψ/U_∞ (%)
70
60
50
40
30
20
10
0
−10
−20
−30
−40
−50
−60
−70
1.0 0.8 0.6 0.4 0.2 0.0 −0.2 −0.4 −0.6 −0.8 −1.0
Radial Distance, r (inches)

(c) C_L = 0.68

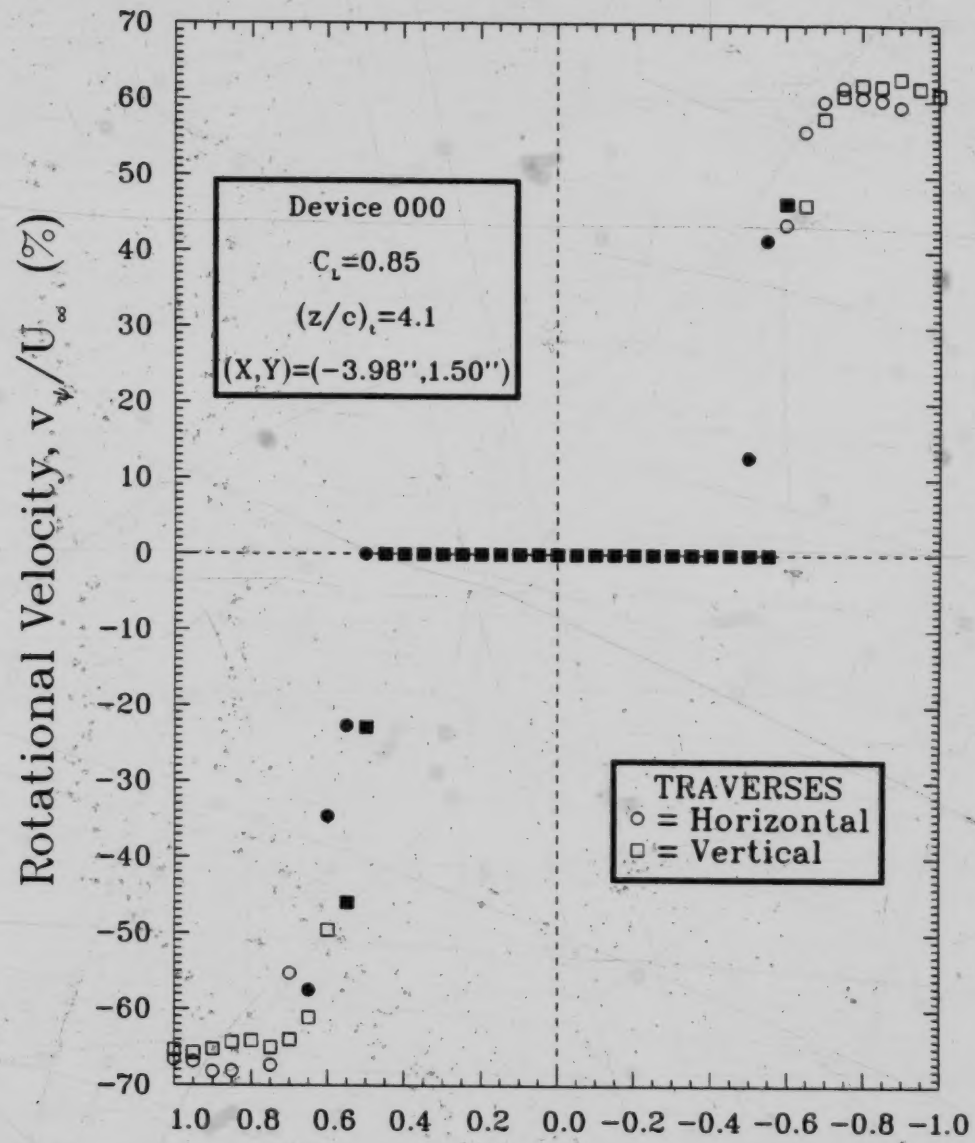
Device 000
C_L=0.85
$(z/c)_t$=4.1
(X,Y)=(−3.98",1.50")
TRAVERSES
○ = Horizontal
□ = Vertical
Rotational Velocity, v_ψ/U_∞ (%)
70
60
50
40
30
20
10
0
−10
−20
−30
−40
−50
−60
−70
1.0 0.8 0.6 0.4 0.2 0.0 −0.2 −0.4 −0.6 −0.8 −1.0
Radial Distance, r (inches)

(d) C_L = 0.85

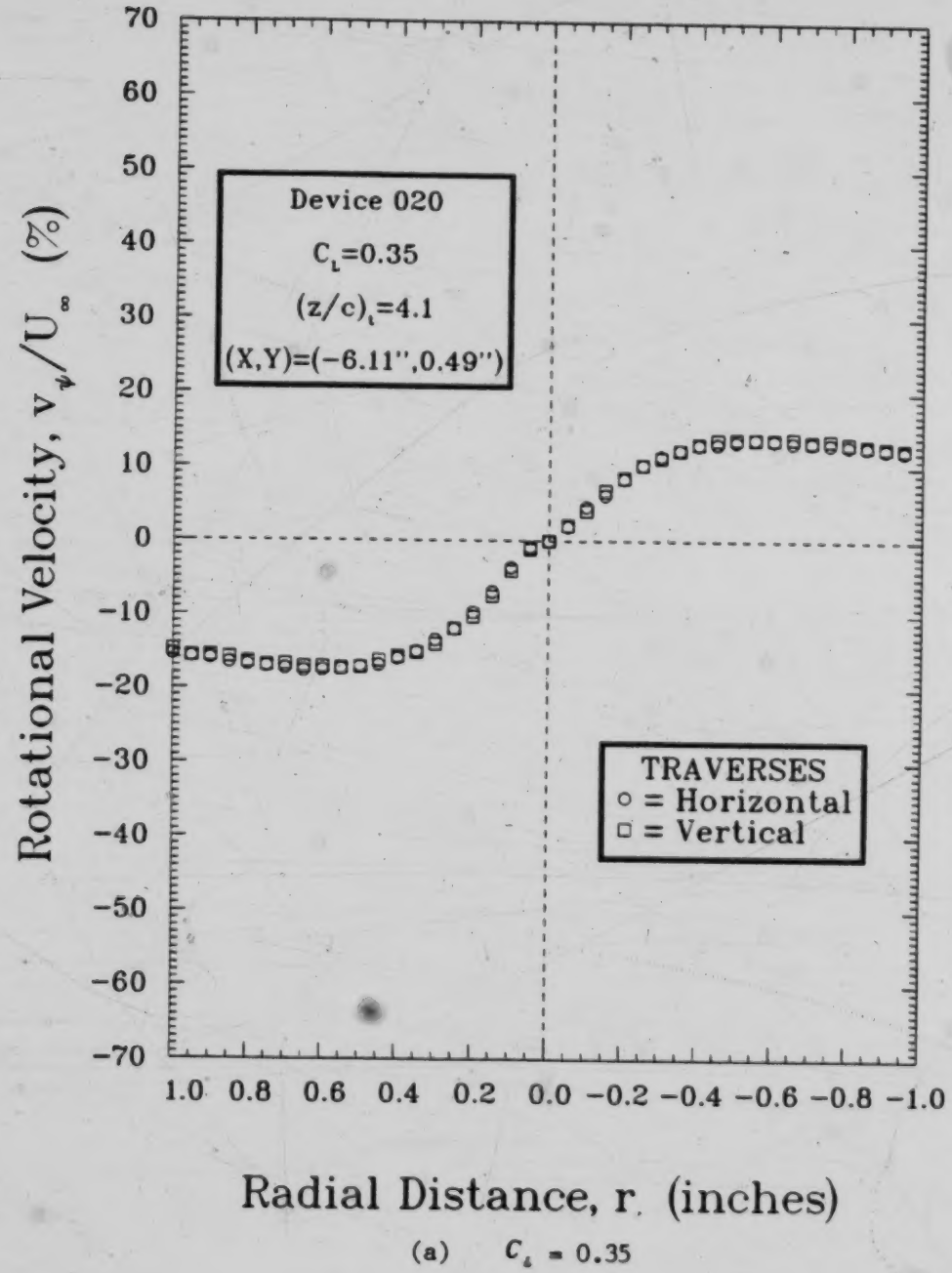

(a) C_L = 0.35

FIGURE 6-10 Rotational velocity distributions of the wingtip vortex due to device 020 with $(z/c)_t$ = 4.1

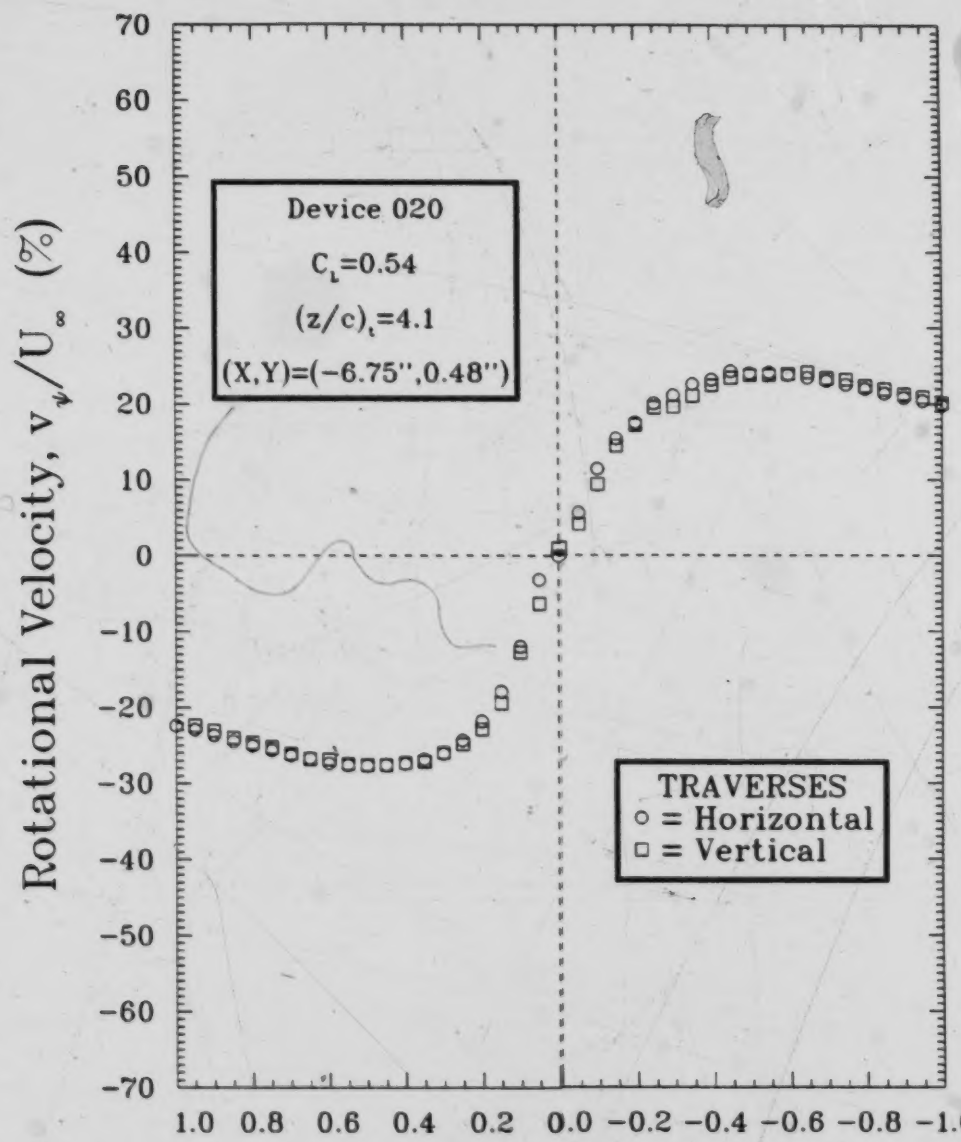
Device 020
C_L=0.54
$(z/c)_t$=4.1
(X,Y)=(−6.75",0.48")
TRAVERSES
○ = Horizontal
□ = Vertical
Rotational Velocity, v_ψ/U_∞ (%)
70
60
50
40
30
20
10
0
−10
−20
−30
−40
−50
−60
−70
1.0 0.8 0.6 0.4 0.2 0.0 −0.2 −0.4 −0.6 −0.8 −1.0
Radial Distance, r (inches)

(b) C_L = 0.54

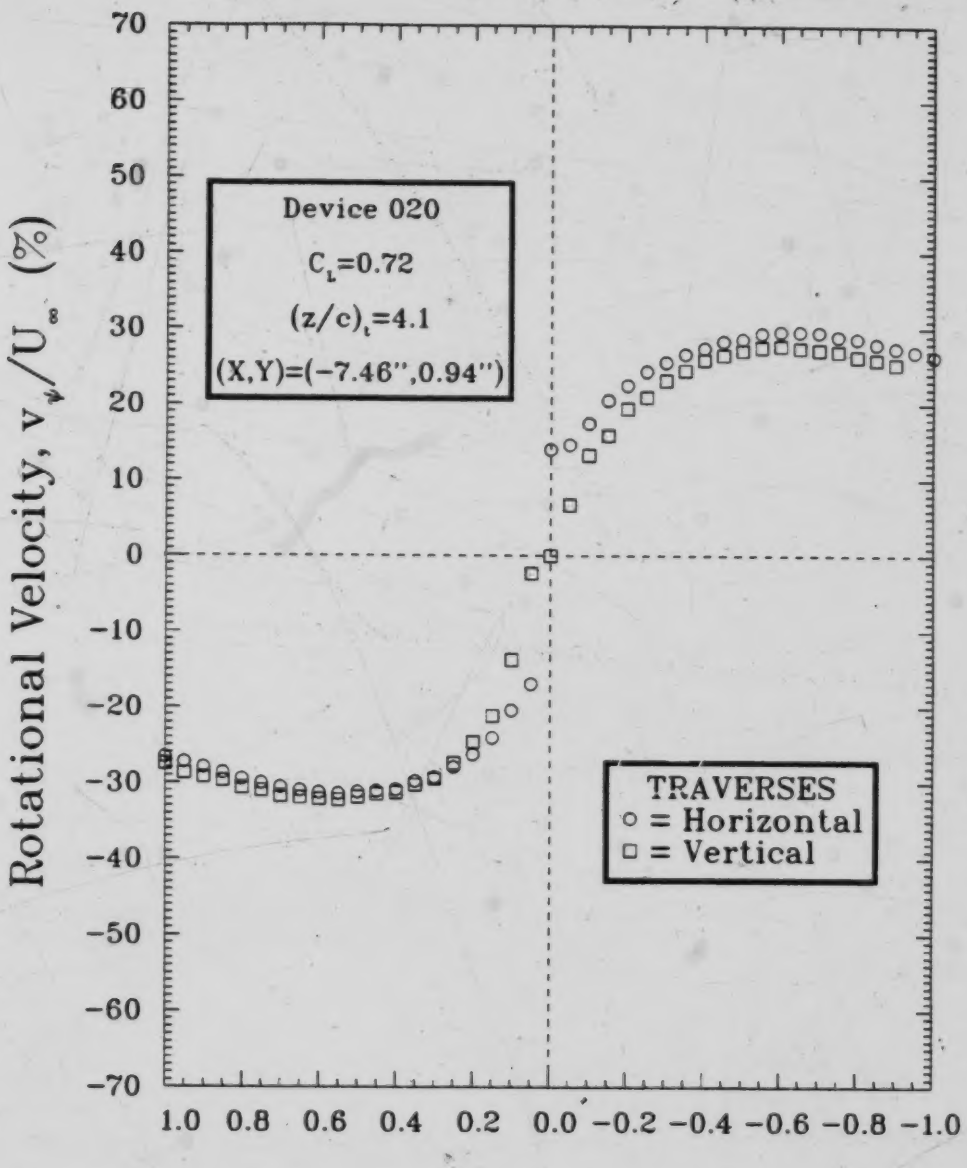
Device 020
C_L=0.72
$(z/c)_t$=4.1
(X,Y)=(−7.46",0.94")
TRAVERSES
○ = Horizontal
□ = Vertical
Rotational Velocity, v_ψ/U_∞ (%)
70
60
50
40
30
20
10
0
−10
−20
−30
−40
−50
−60
−70
1.0 0.8 0.6 0.4 0.2 0.0 −0.2 −0.4 −0.6 −0.8 −1.0
Radial Distance, r (inches)

(c) C_L = 0.72

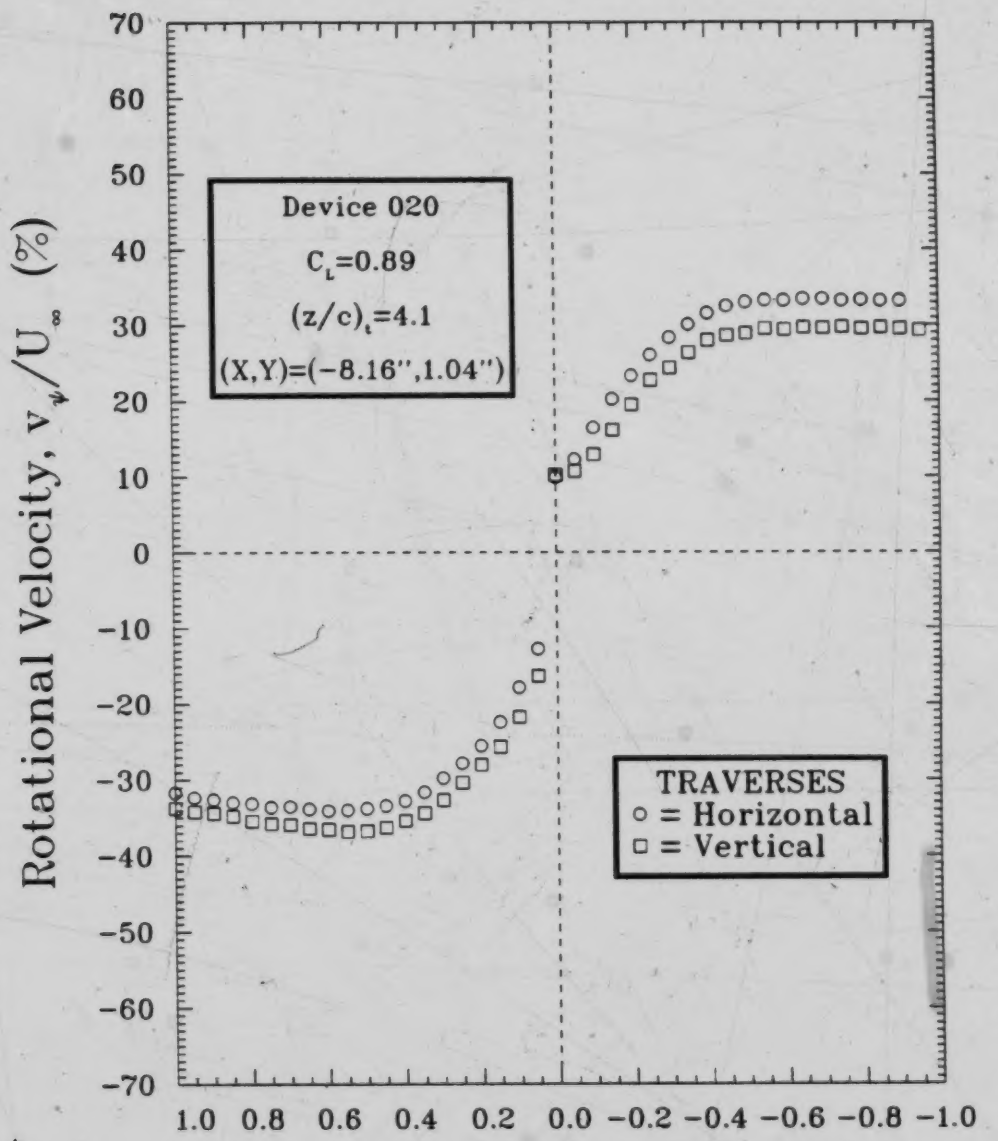
Device 020
C_L=0.89
$(z/c)_t$=4.1
(X,Y)=(−8.16",1.04")
TRAVERSES
○ = Horizontal
□ = Vertical
Rotational Velocity, v_ψ/U_∞ (%)
70
60
50
40
30
20
10
0
−10
−20
−30
−40
−50
−60
−70
1.0 0.8 0.6 0.4 0.2 0.0 −0.2 −0.4 −0.6 −0.8 −1.0
Radial Distance, r (inches)

(d) C_L = 0.89

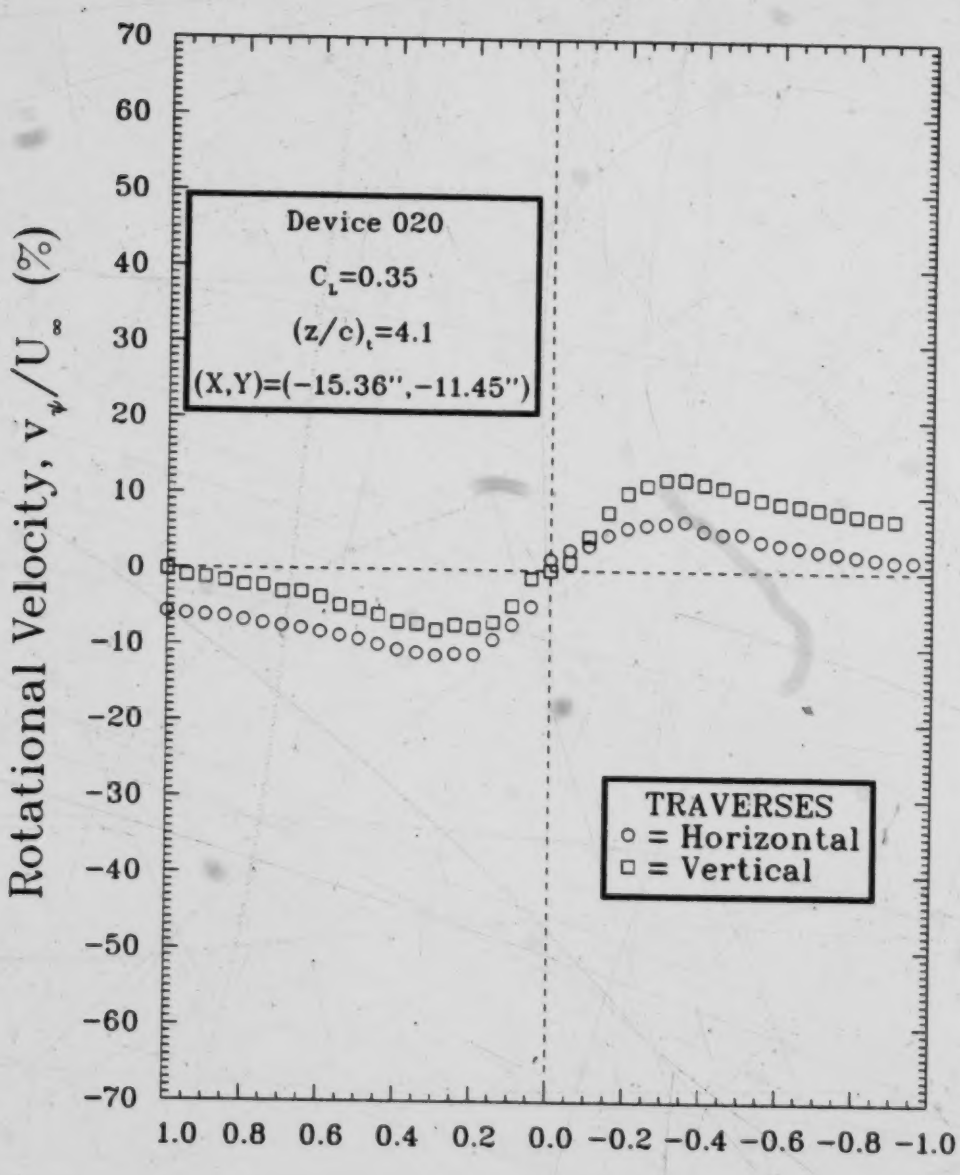

(a) C_L = 0.35

FIGURE 6-11 Rotational velocity distributions of the secondary vortex due to device 020 with $(z/c)_t$ = 4.1

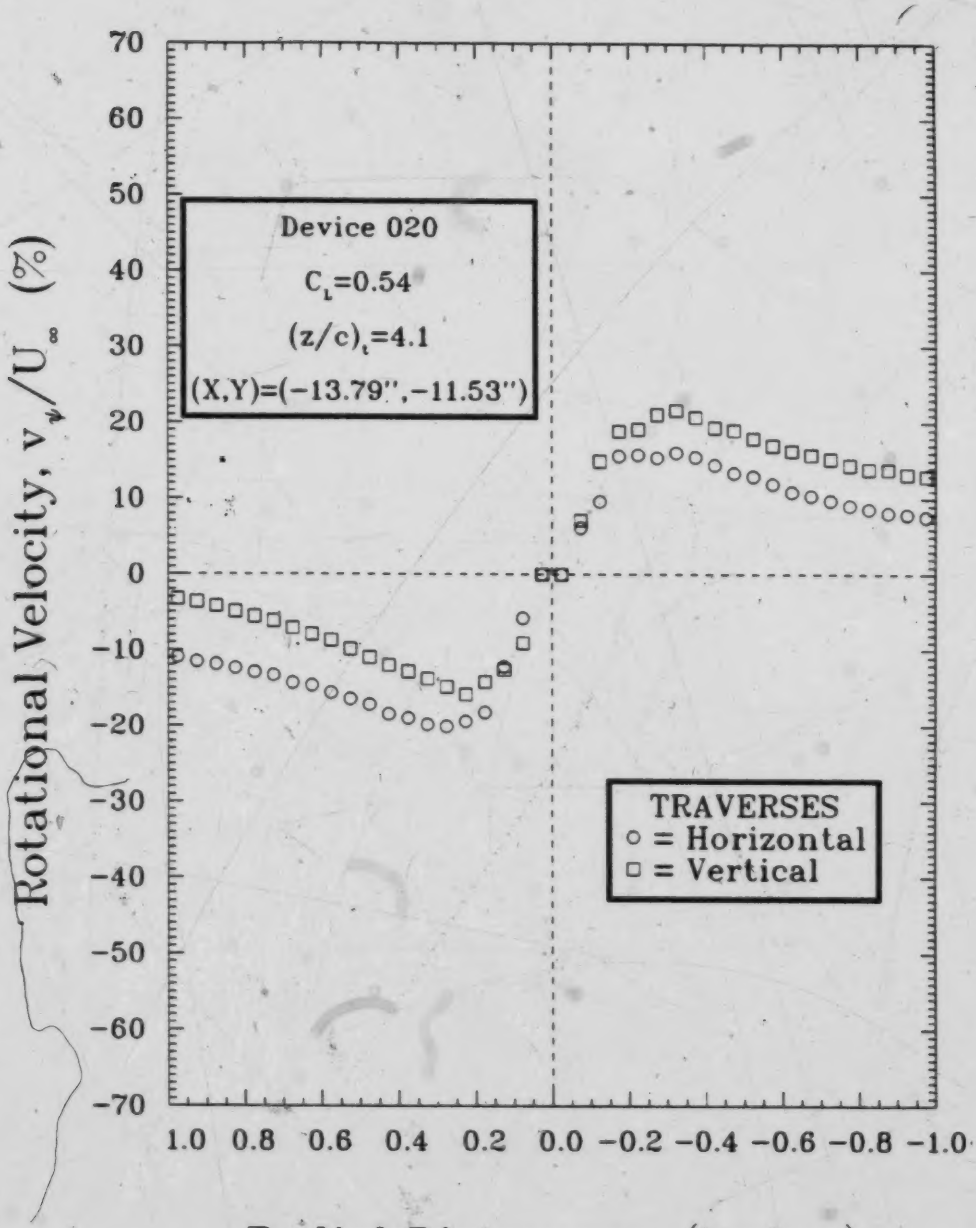
Device 020
C_L=0.54
$(z/c)_t$=4.1
(X,Y)=(−13.79",−11.53")
TRAVERSES
o = Horizontal
□ = Vertical
Rotational Velocity, v_ψ/U_∞ (%)
70
60
50
40
30
20
10
0
−10
−20
−30
−40
−50
−60
−70
1.0 0.8 0.6 0.4 0.2 0.0 −0.2 −0.4 −0.6 −0.8 −1.0
Radial Distance, r (inches)

(b) C_L = 0.54

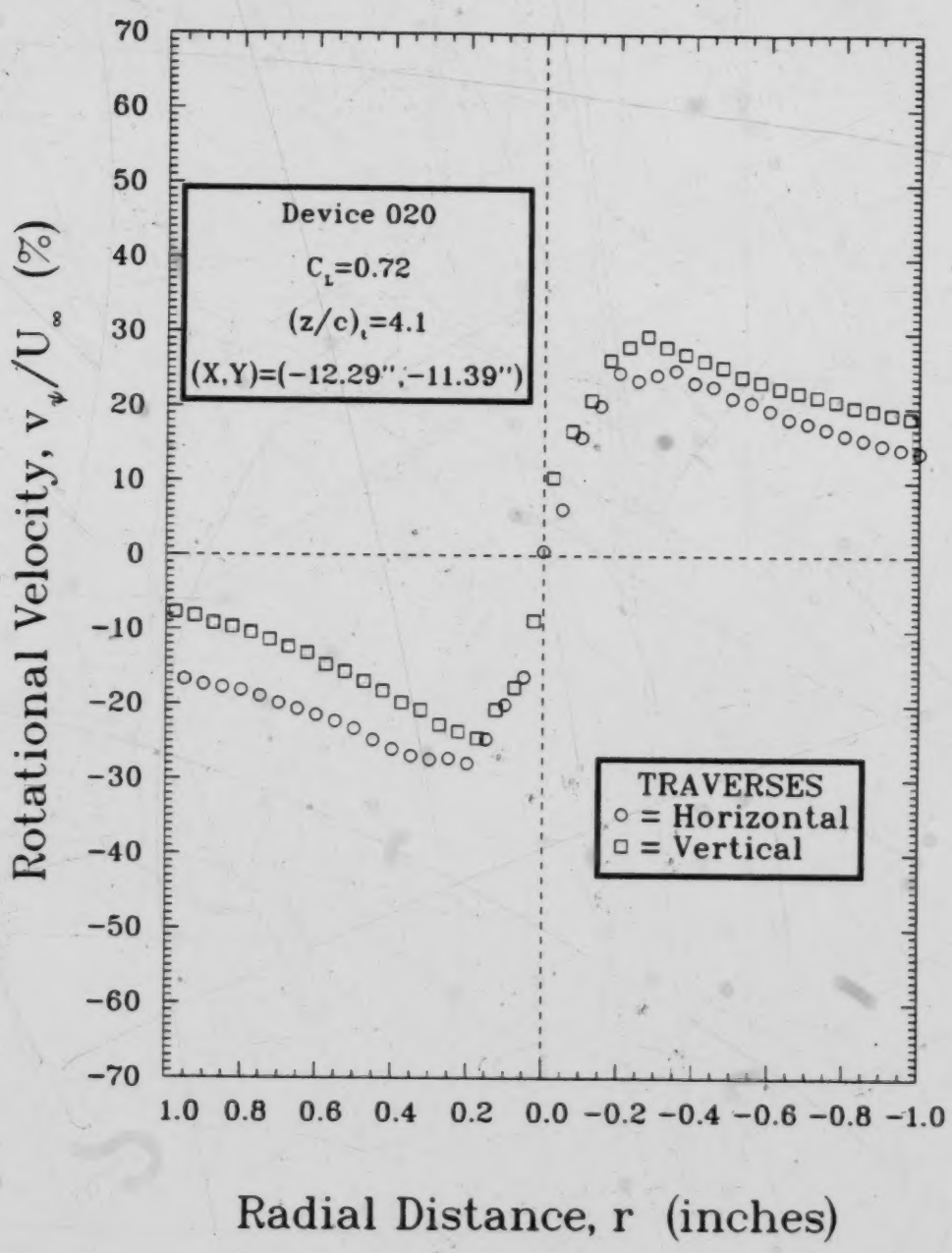
Device 020
C_L=0.72
$(z/c)_t$=4.1
(X,Y)=(−12.29",−11.39")
TRAVERSES
○ = Horizontal
□ = Vertical
Rotational Velocity, v_ψ/U_∞ (%)
70
60
50
40
30
20
10
0
−10
−20
−30
−40
−50
−60
−70
1.0 0.8 0.6 0.4 0.2 0.0 −0.2 −0.4 −0.6 −0.8 −1.0
Radial Distance, r (inches)

(c) C_L = 0.72

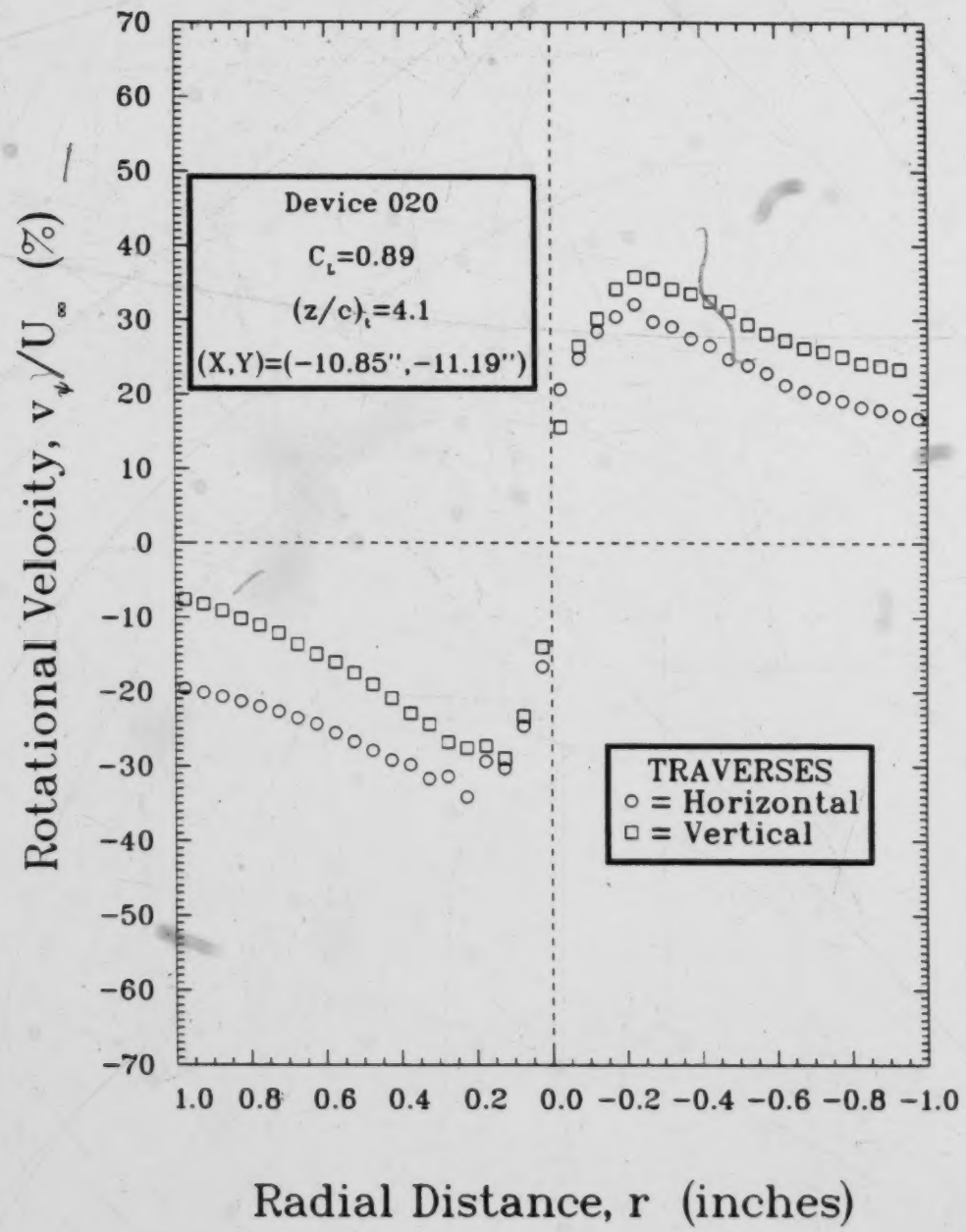
Device 020
C_L=0.89
$(z/c)_t$=4.1
(X,Y)=(−10.85", −11.19")
TRAVERSES
○ = Horizontal
□ = Vertical
Rotational Velocity, v_ψ/U_∞ (%)
Radial Distance, r (inches)
70
60
50
40
30
20
10
0
−10
−20
−30
−40
−50
−60
−70
1.0 0.8 0.6 0.4 0.2 0.0 −0.2 −0.4 −0.6 −0.8 −1.0

(d) C_L = 0.89

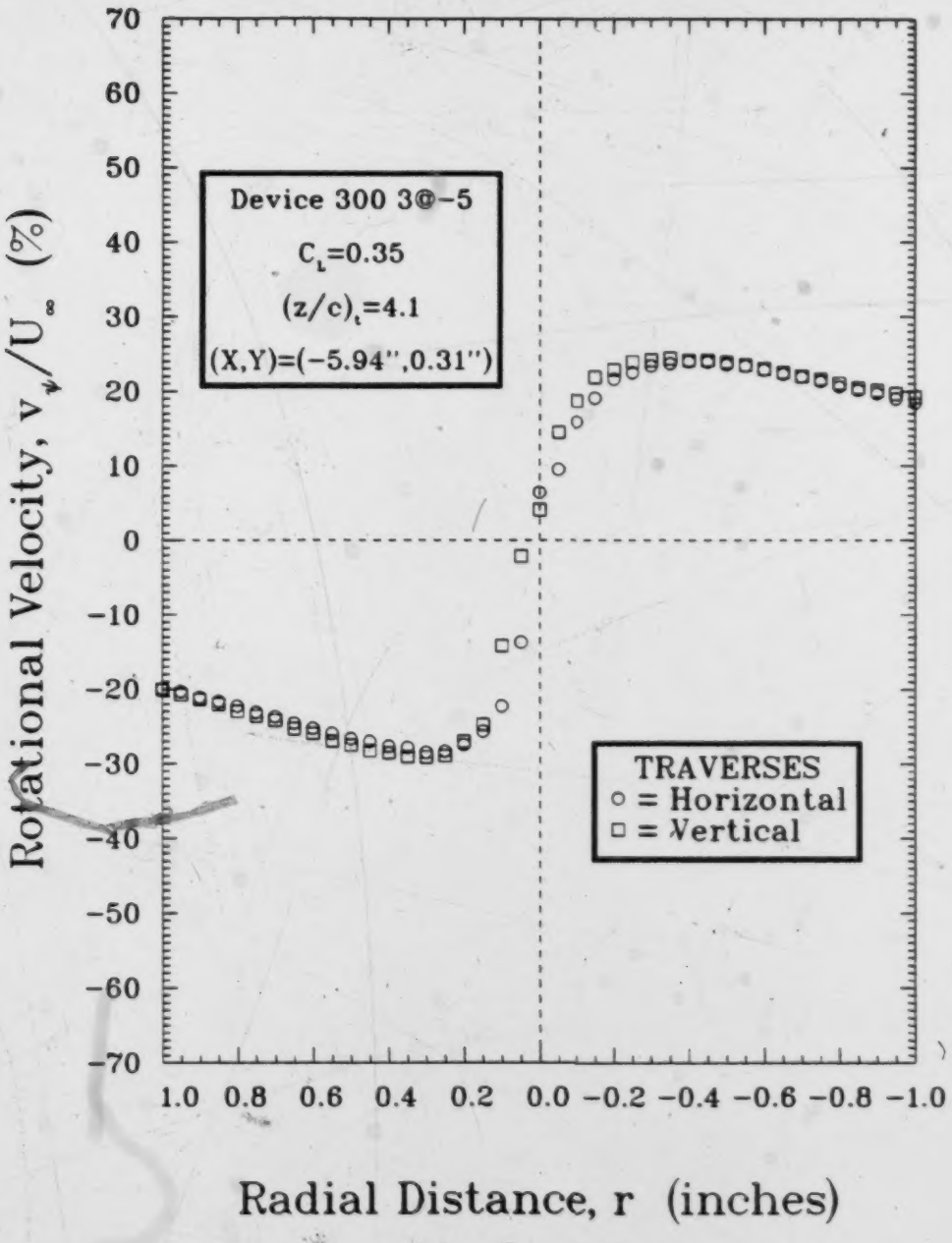

(a) C_L = 0.35

FIGURE 6-12 Rotational velocity distributions of the wingtip vortex due to device 300 3@ - 5 with $(z/c)_t$ = 4.1

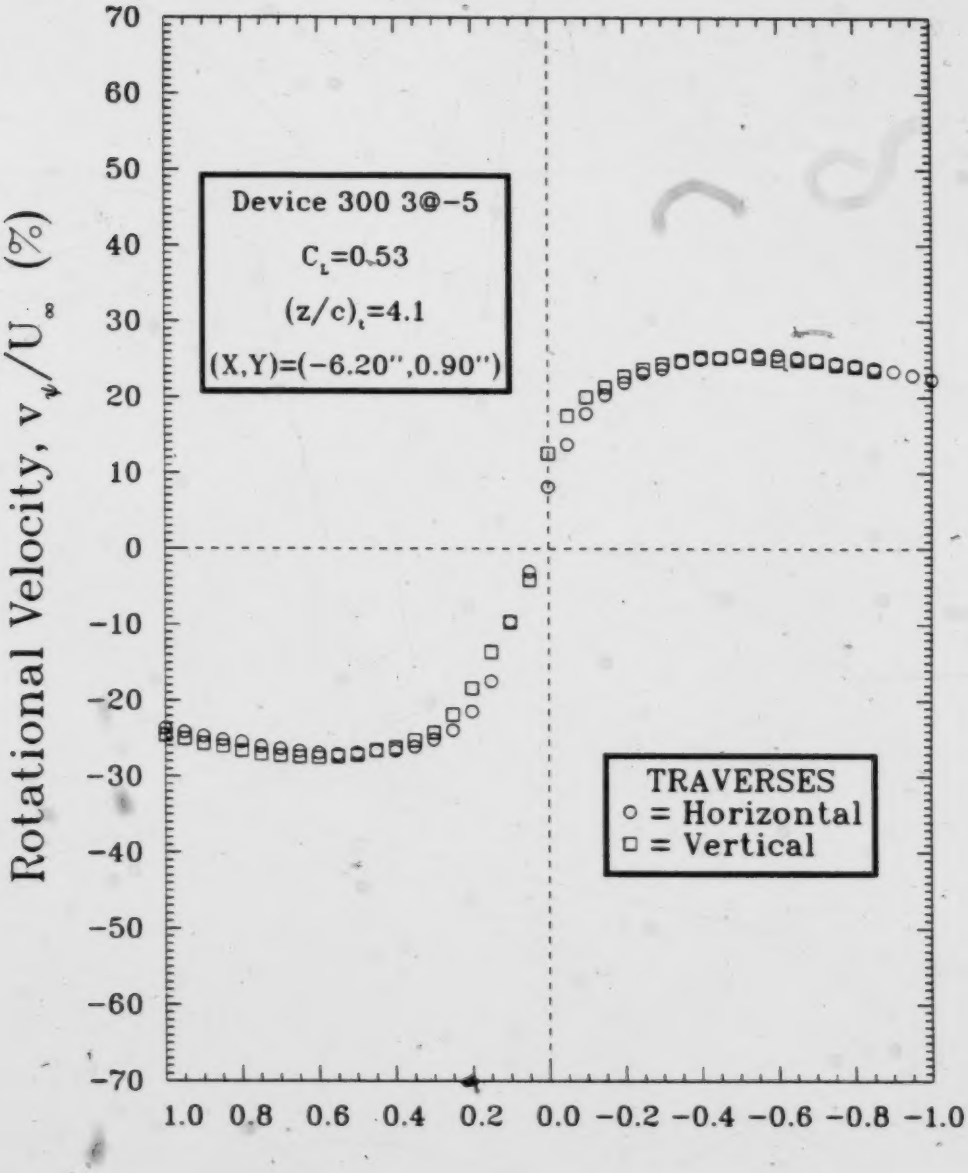
Device 300 3@-5
C_L=0.53
$(z/c)_t$=4.1
(X,Y)=(-6.20",0.90")
TRAVERSES
○ = Horizontal
□ = Vertical
Rotational Velocity, v_ψ/U_∞ (%)
70
60
50
40
30
20
10
0
-10
-20
-30
-40
-50
-60
-70
1.0 0.8 0.6 0.4 0.2 0.0 -0.2 -0.4 -0.6 -0.8 -1.0
Radial Distance, r (inches)

(b) C_L = 0.53

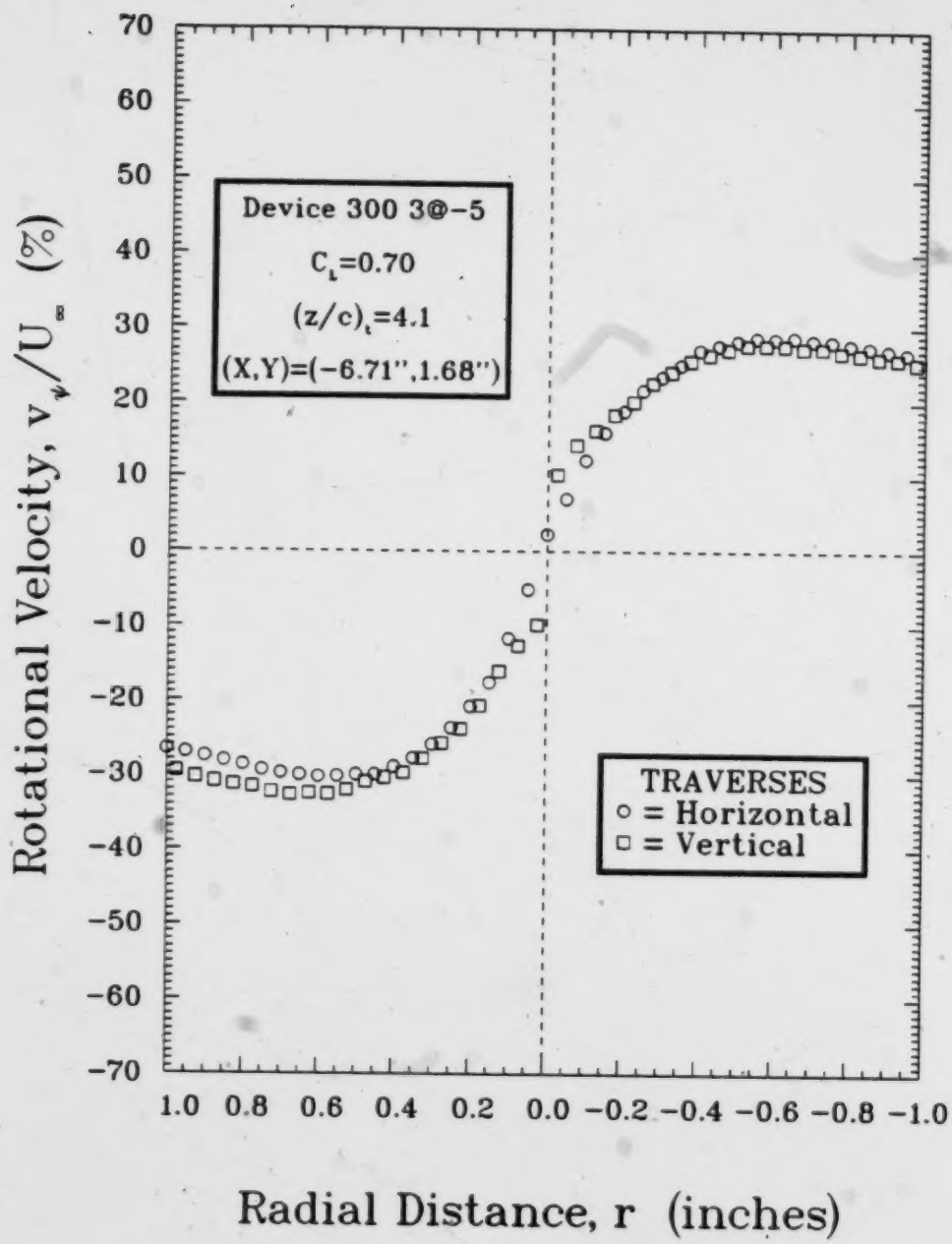
Device 300 3@-5
C_L=0.70
$(z/c)_t$=4.1
(X,Y)=(-6.71",1.68")
TRAVERSES
○ = Horizontal
□ = Vertical
Rotational Velocity, v_ψ/U_∞ (%)
70
60
50
40
30
20
10
0
-10
-20
-30
-40
-50
-60
-70
1.0 0.8 0.6 0.4 0.2 0.0 -0.2 -0.4 -0.6 -0.8 -1.0
Radial Distance, r (inches)

(c) C_L = 0.70

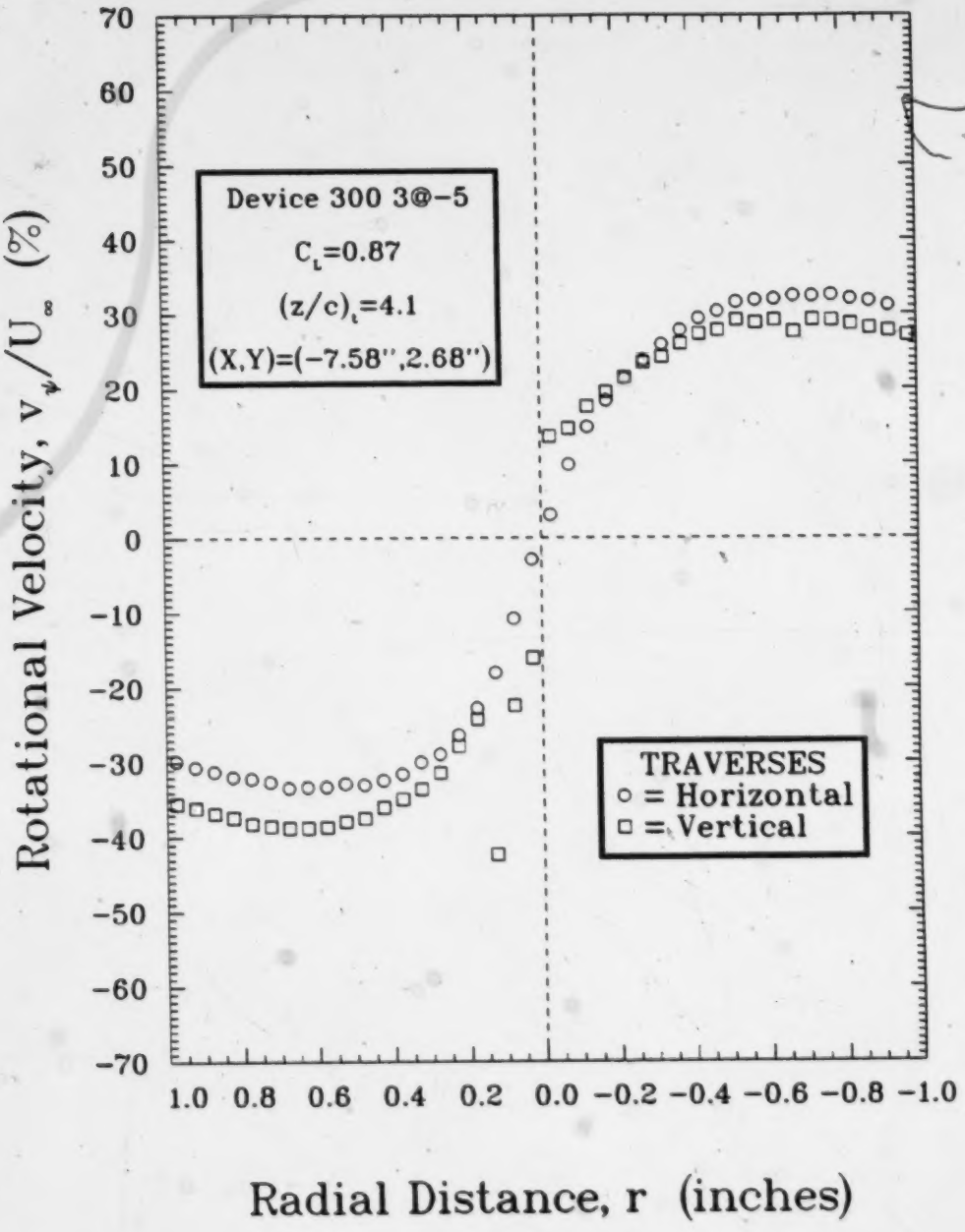
Device 300 3@-5
C_L=0.87
$(z/c)_t$=4.1
(X,Y)=(-7.58",2.68")
TRAVERSES
○ = Horizontal
□ = Vertical
Rotational Velocity, v_ψ/U_∞ (%)
70
60
50
40
30
20
10
0
-10
-20
-30
-40
-50
-60
-70
1.0 0.8 0.6 0.4 0.2 0.0 -0.2 -0.4 -0.6 -0.8 -1.0
Radial Distance, r (inches)

(d) C_L = 0.87

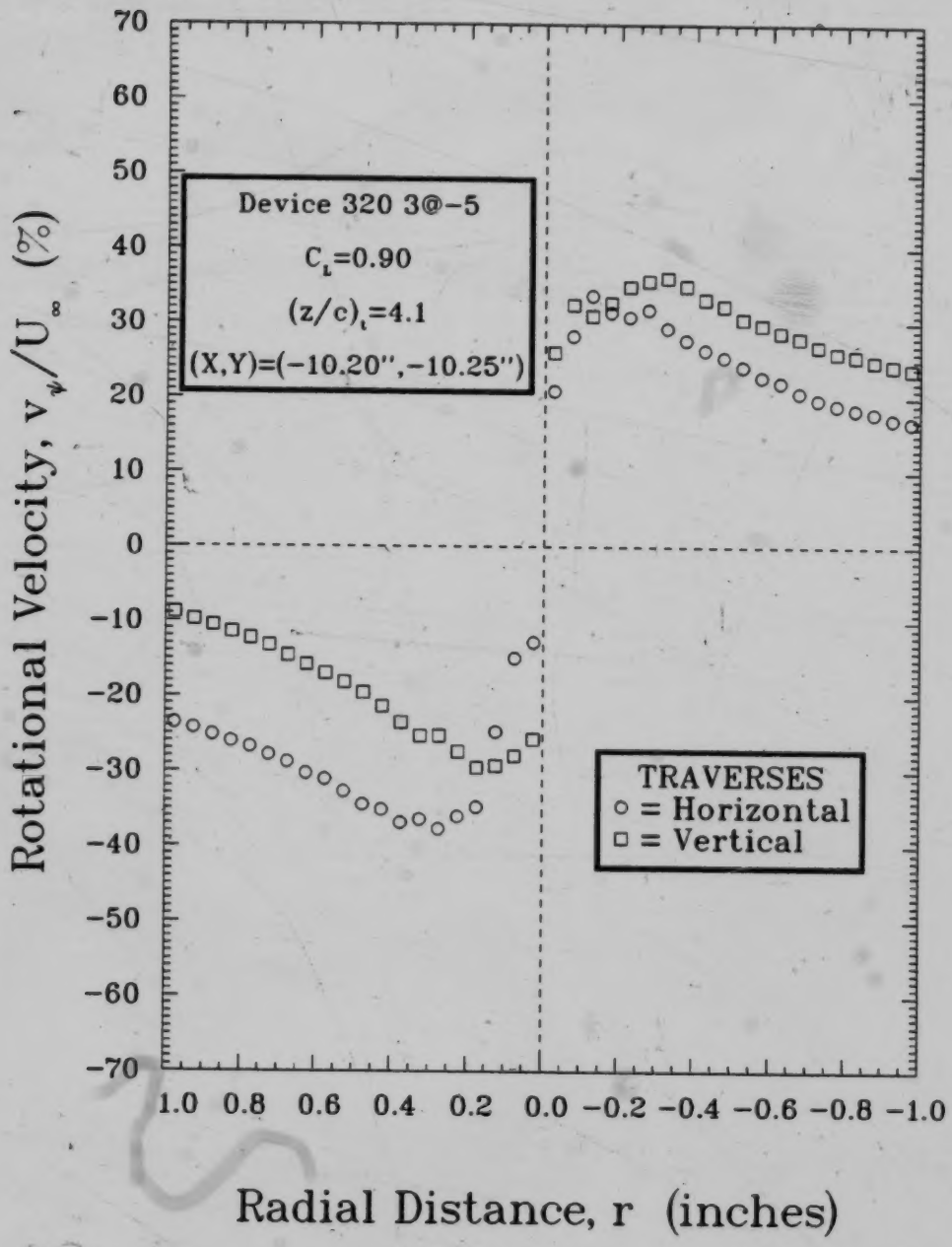

FIGURE 6-13 Rotational velocity distribution of the secondary vortex due to device 320 3@ - 5 with $(z/c)_t$ = 4.1 and C_L = 0.90

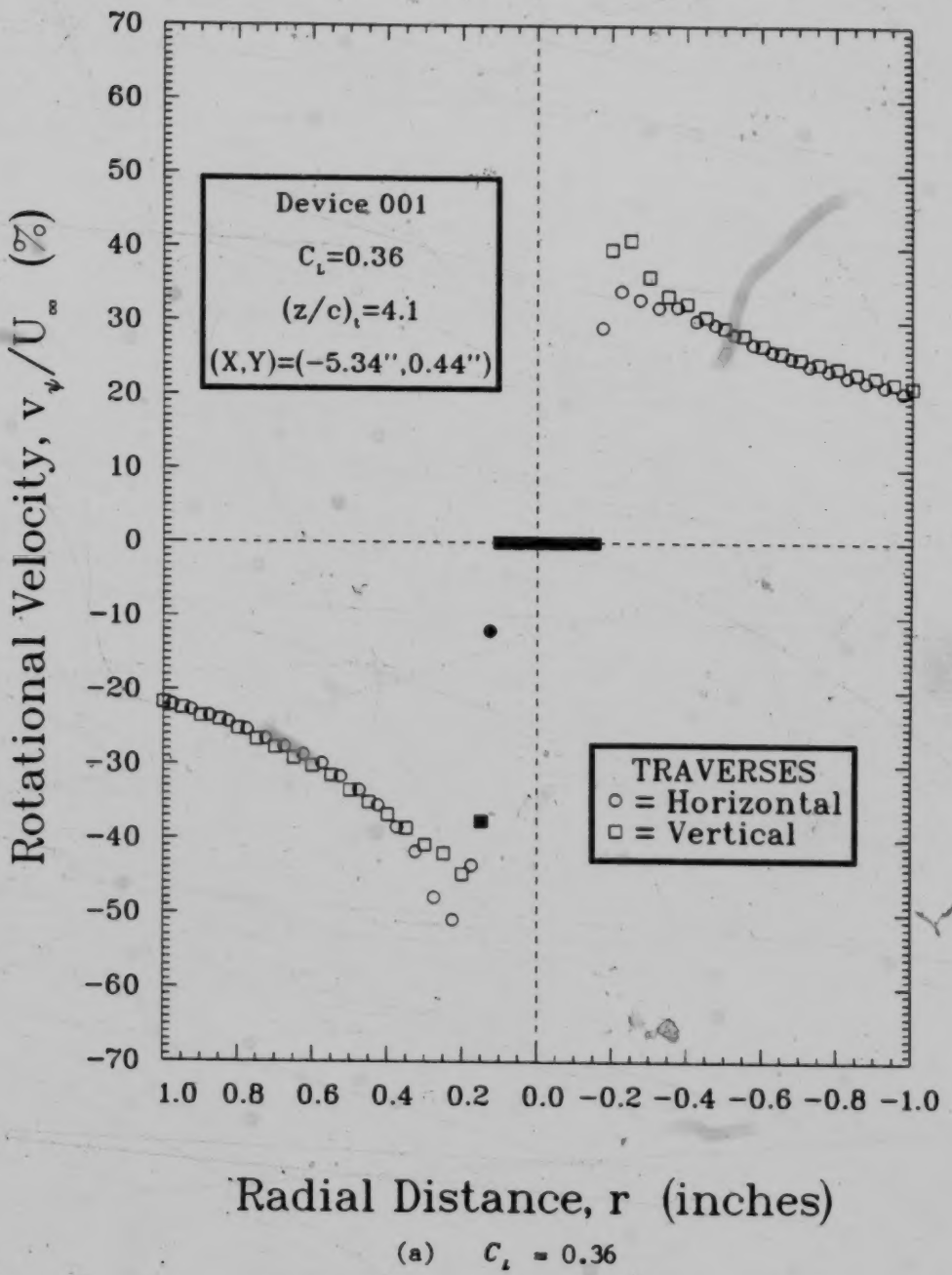

(a) C_L = 0.36

FIGURE 6-14 Rotational velocity distributions of the wingtip vortex due to device 001 with $(z/c)_t$ = 4.1

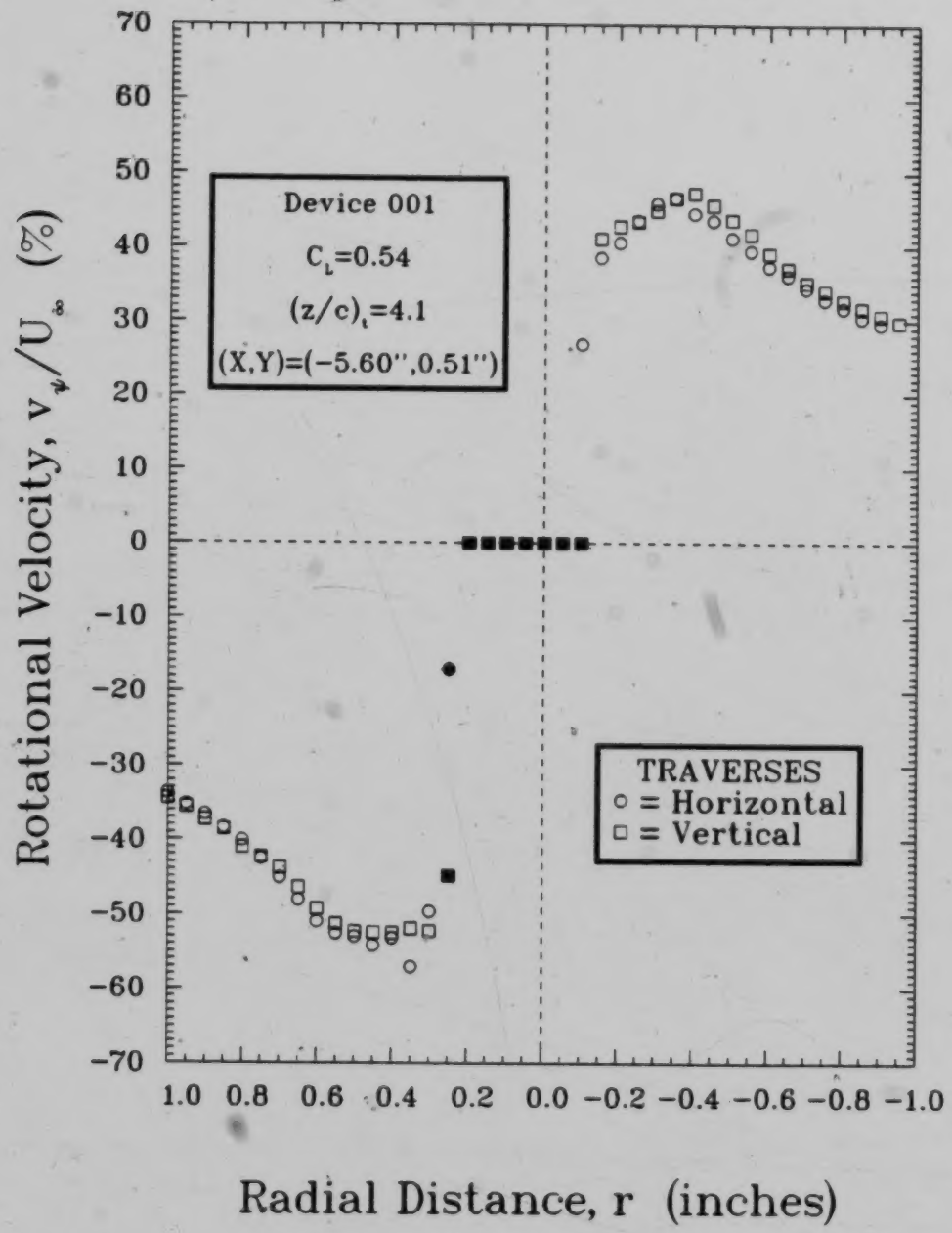
Device 001
C_L=0.54
$(z/c)_t$=4.1
(X,Y)=(−5.60",0.51")
TRAVERSES
○ = Horizontal
□ = Vertical
Rotational Velocity, v_ψ/U_∞ (%)
Radial Distance, r (inches)
70
60
50
40
30
20
10
0
−10
−20
−30
−40
−50
−60
−70
1.0 0.8 0.6 0.4 0.2 0.0 −0.2 −0.4 −0.6 −0.8 −1.0

(b) C_L = 0.54

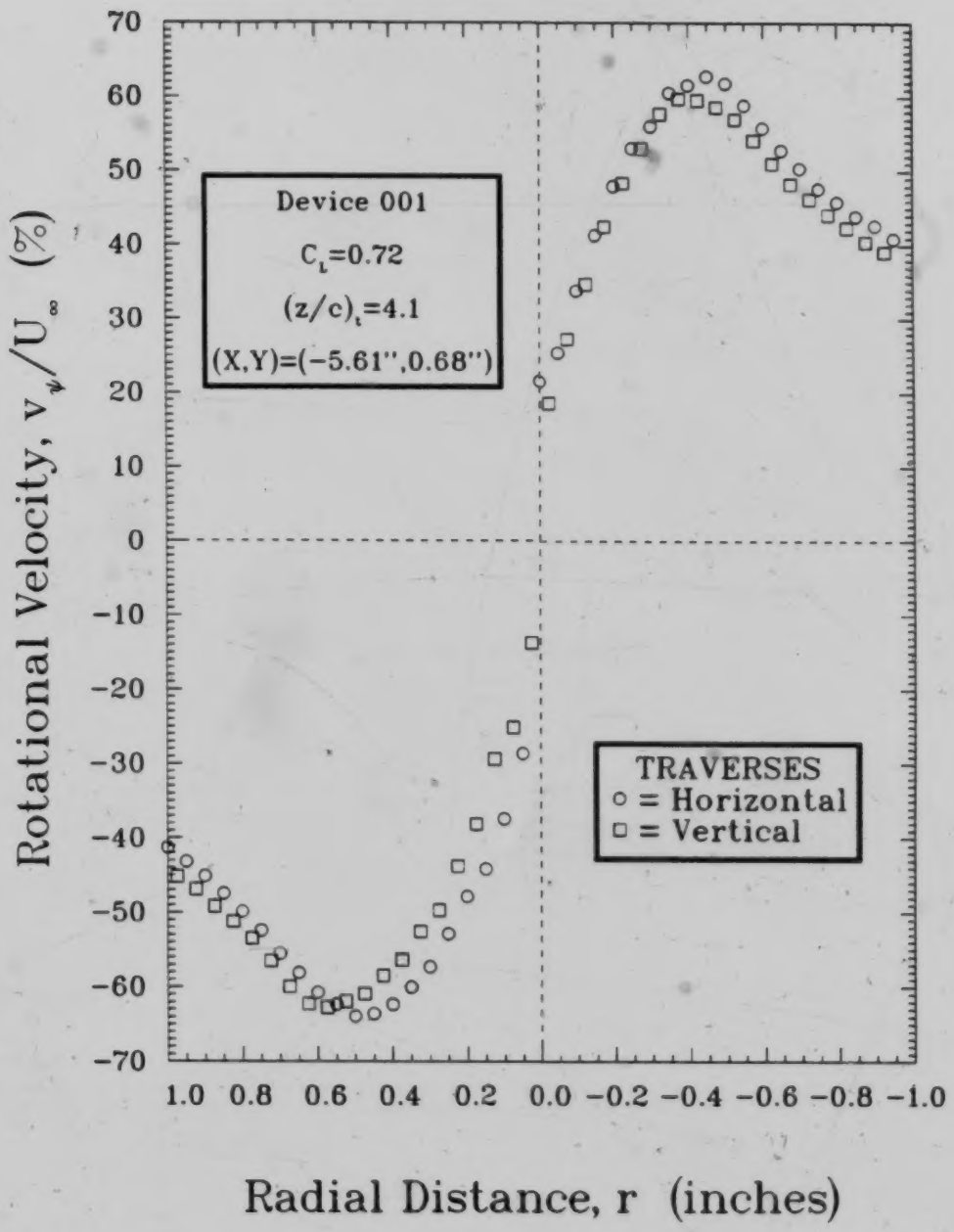
Device 001
C_L=0.72
$(z/c)_t$=4.1
(X,Y)=(−5.61",0.68")
TRAVERSES
○ = Horizontal
□ = Vertical
Rotational Velocity, v_ψ/U_∞ (%)
Radial Distance, r (inches)
70
60
50
40
30
20
10
0
−10
−20
−30
−40
−50
−60
−70
1.0 0.8 0.6 0.4 0.2 0.0 −0.2 −0.4 −0.6 −0.8 −1.0

(c) C_L = 0.72

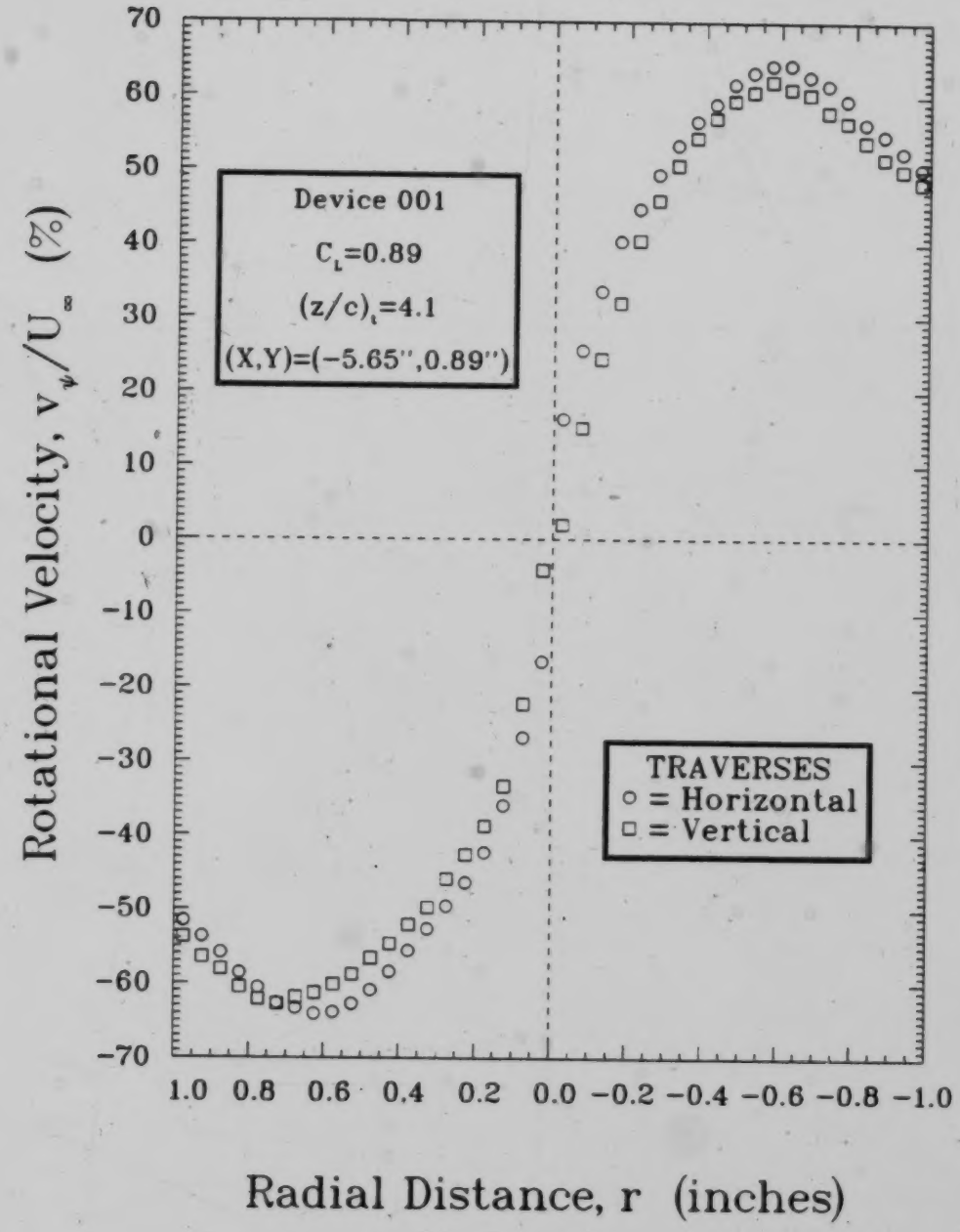
Device 001
C_L=0.89
$(z/c)_t$=4.1
(X,Y)=(−5.65",0.89")
TRAVERSES
○ = Horizontal
□ = Vertical
Rotational Velocity, v_ψ/U_∞ (%)
70
60
50
40
30
20
10
0
−10
−20
−30
−40
−50
−60
−70
1.0 0.8 0.6 0.4 0.2 0.0 −0.2 −0.4 −0.6 −0.8 −1.0
Radial Distance, r (inches)

(d) C_L = 0.89

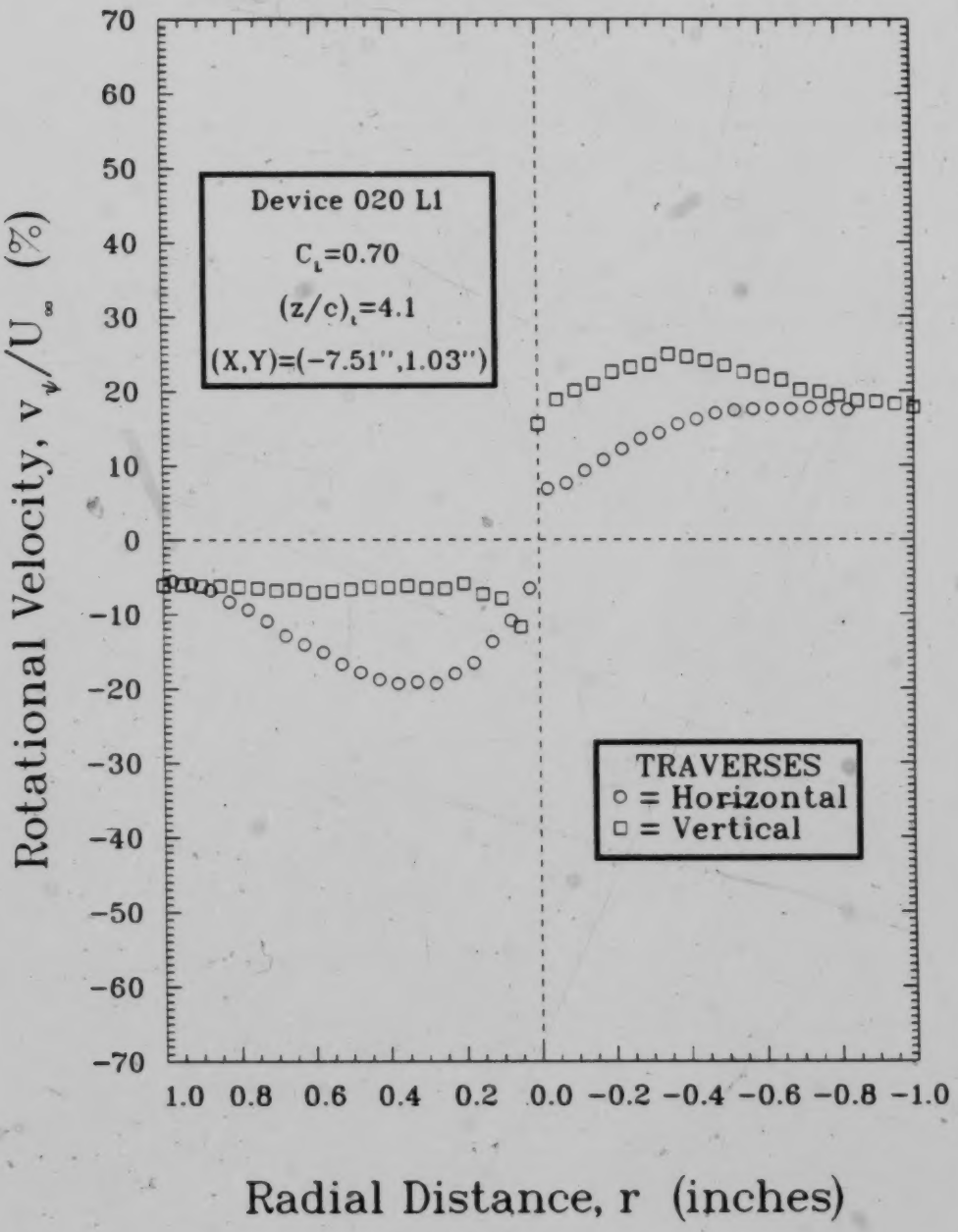

FIGURE 6-15 Rotational velocity distribution of the wingtip vortex due to device 020 with a fin span of 0.65 c_t, $(z/c)_t$ = 4.1, and C_L = 0.70

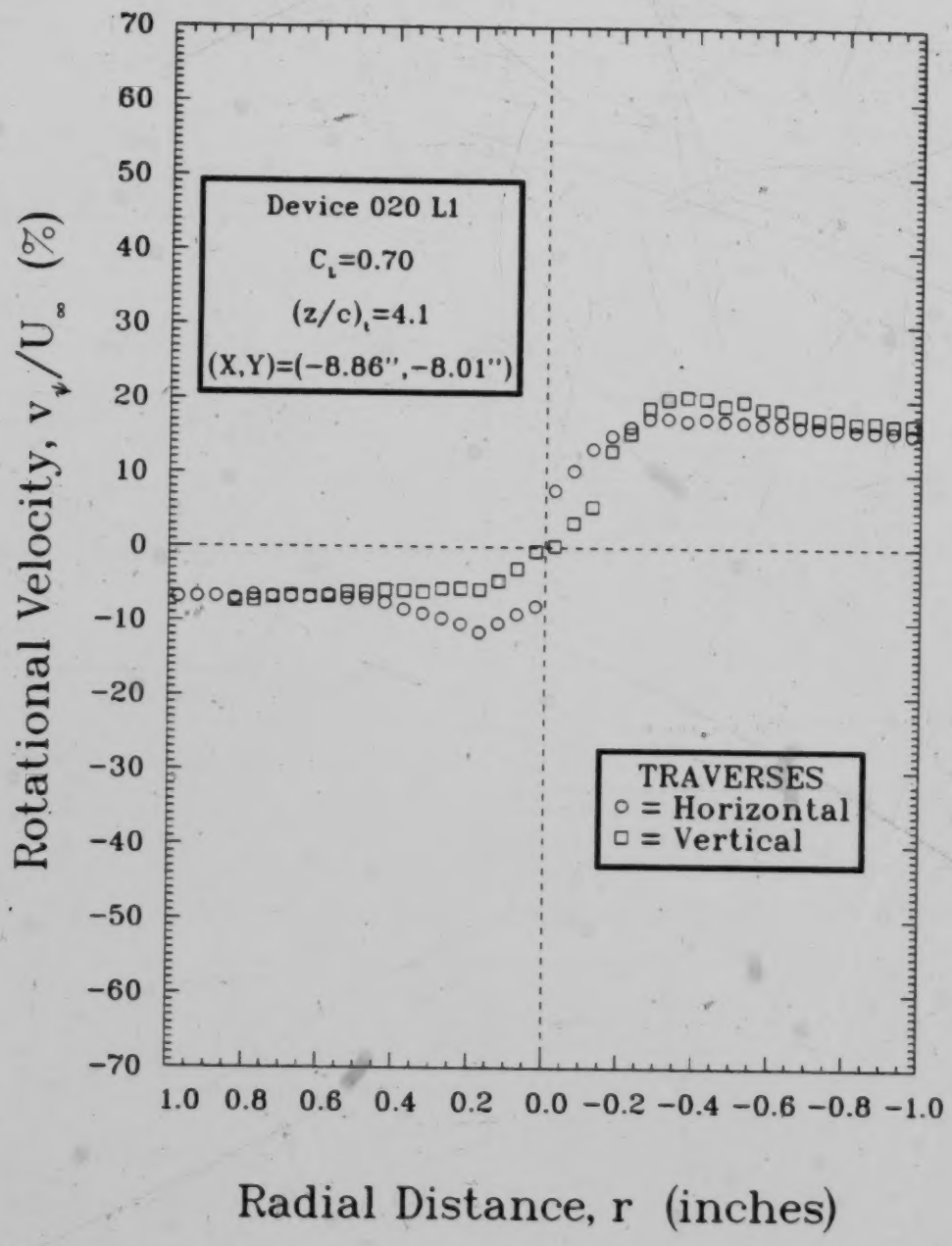

FIGURE 6-16 Rotational velocity distribution of the secondary vortex due to device 020 with a fin span of 0.65 c_t , $(z/c)_t$ = 4.1, and C_L = 0.70

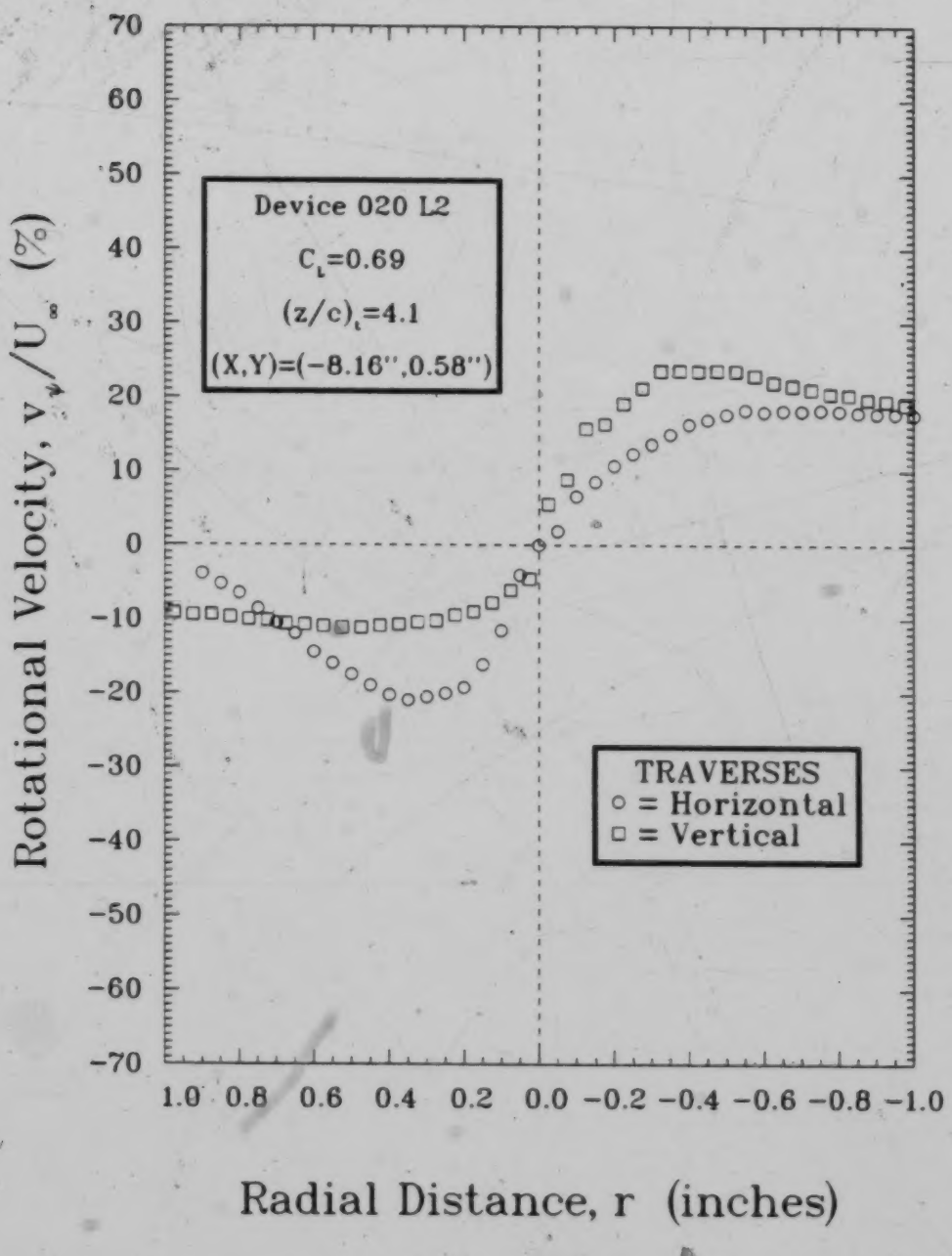

FIGURE 6-17 Rotational velocity distribution of the wingtip vortex due to device 020 with a fin span of 0.43 c_t, $(z/c)_t$ = 4.1, and C_l = 0.69

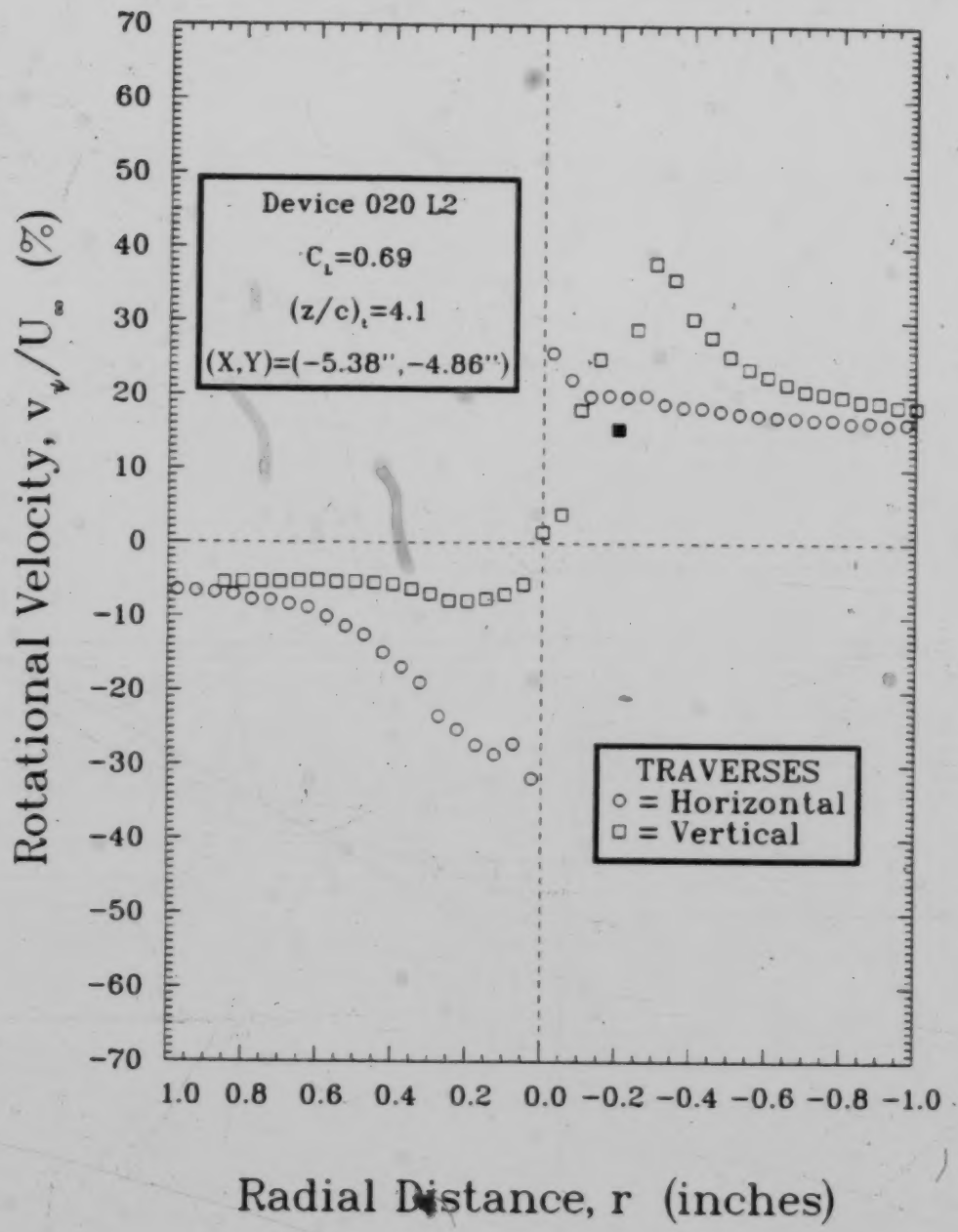

FIGURE 6-18 Rotational velocity distribution of the secondary vortex due to device 020 with a fin span of 0.43 c_t, $(z/c)_t$ = 4.1, and C_L = 0.69

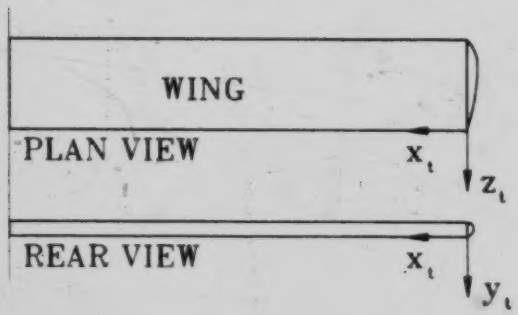

(a) Conventions for a vortex shed from the round tip

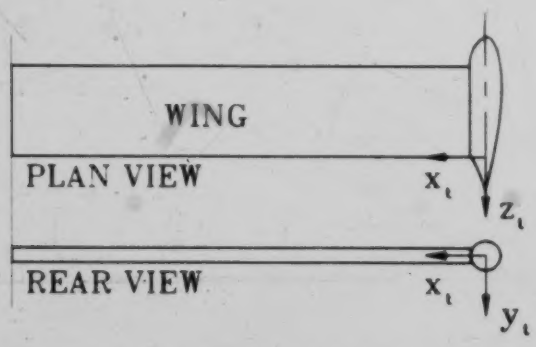

(b) Conventions for a wingtip vortex shed from a tip tank configuration

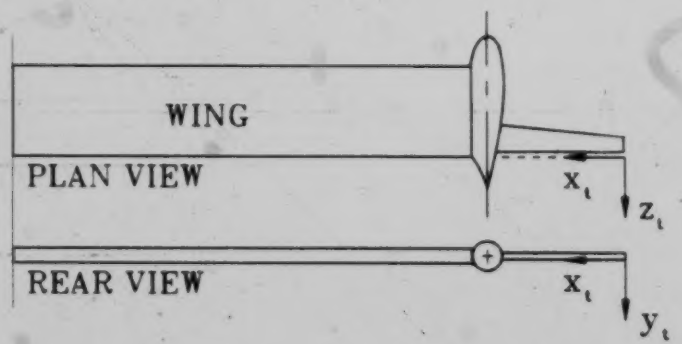

(c) Conventions for a secondary vortex shed from a tip tank configuration

FIGURE 6-19 Local Cartesian coordinates relative to a wingtip or a fin tip from which a vortex is shed

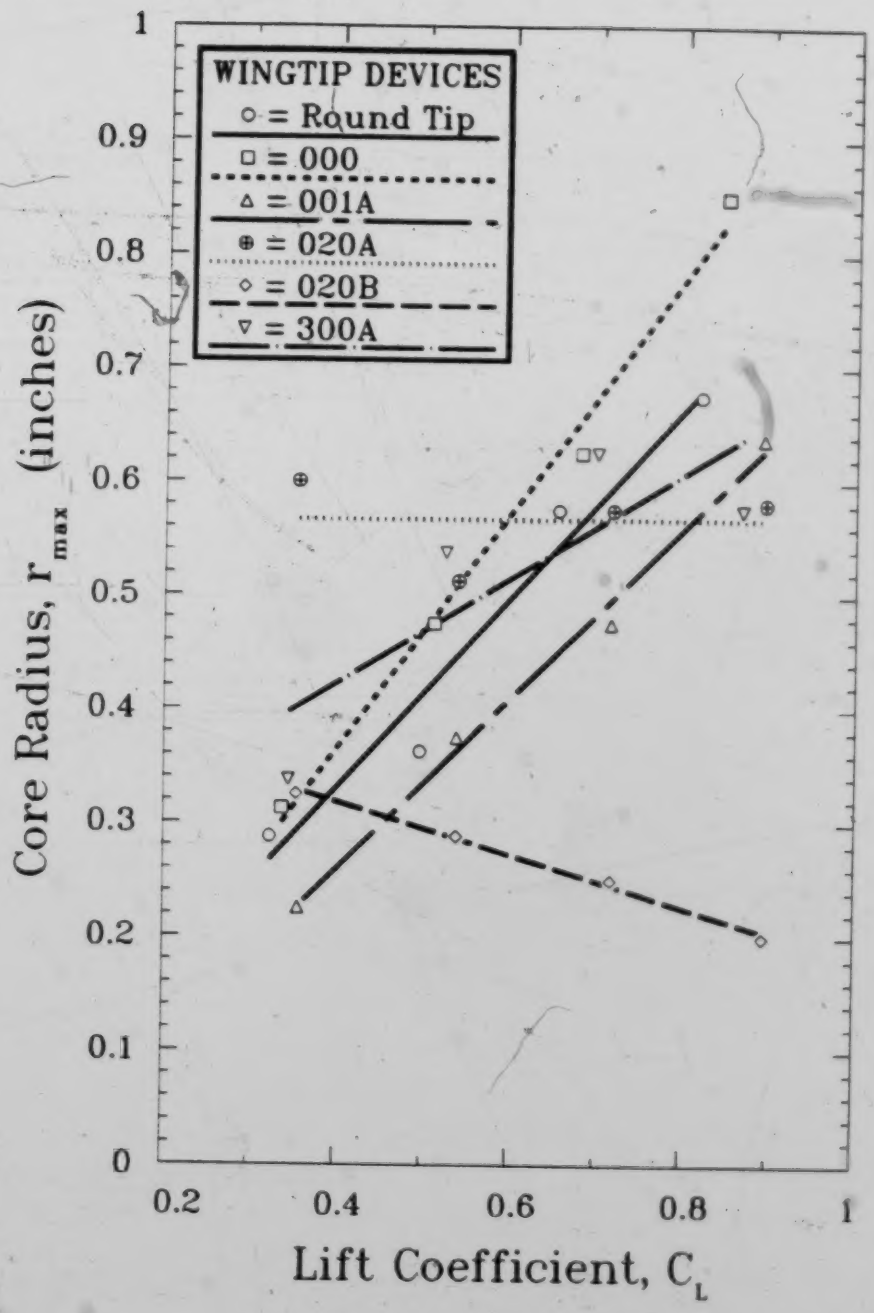

FIGURE 6-20 Core radii of various main and secondary vortices 4.1 chord lengths behind the wing trailing edge

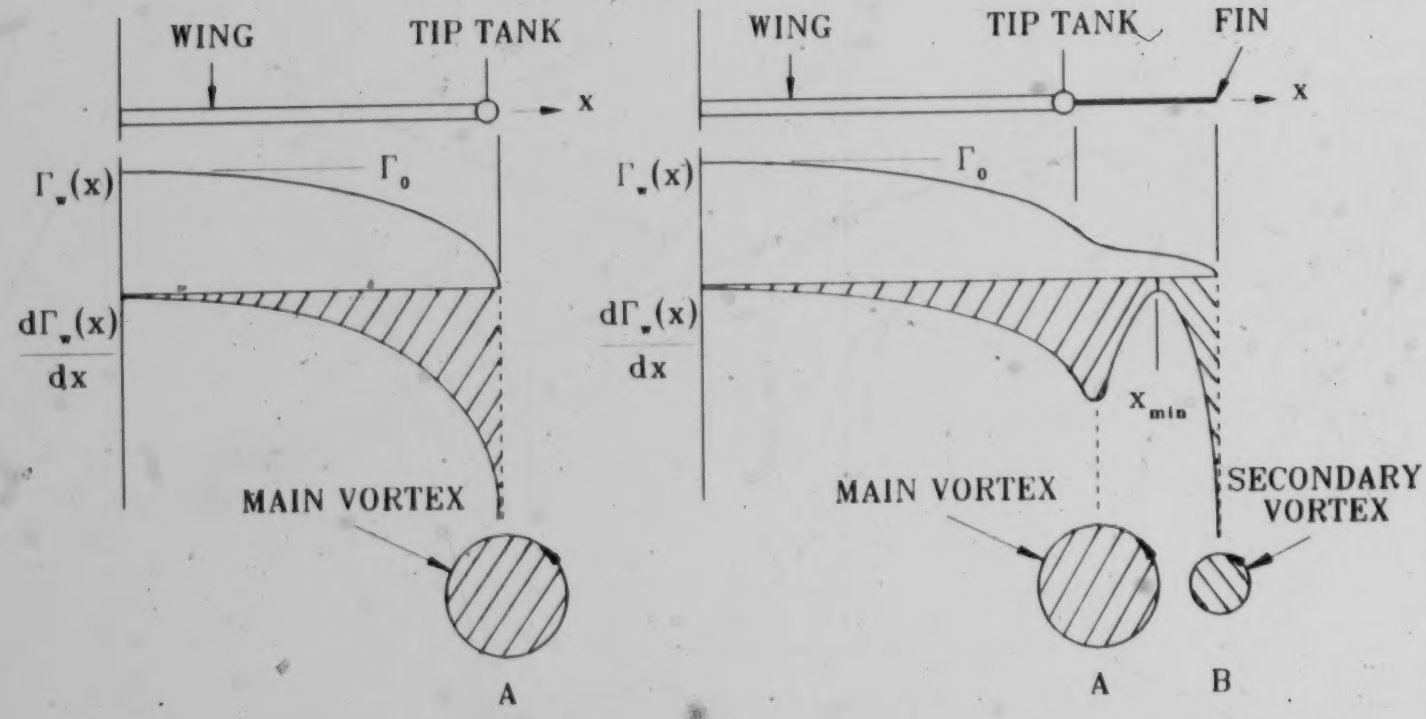

(a) Distributions due to the unfinned tip tank (b) Distributions due to the finned tip tank

FIGURE 6-21 The effect of a wingtip modification on the redistributions of circulation and vorticity, and on the shedding of secondary vortices

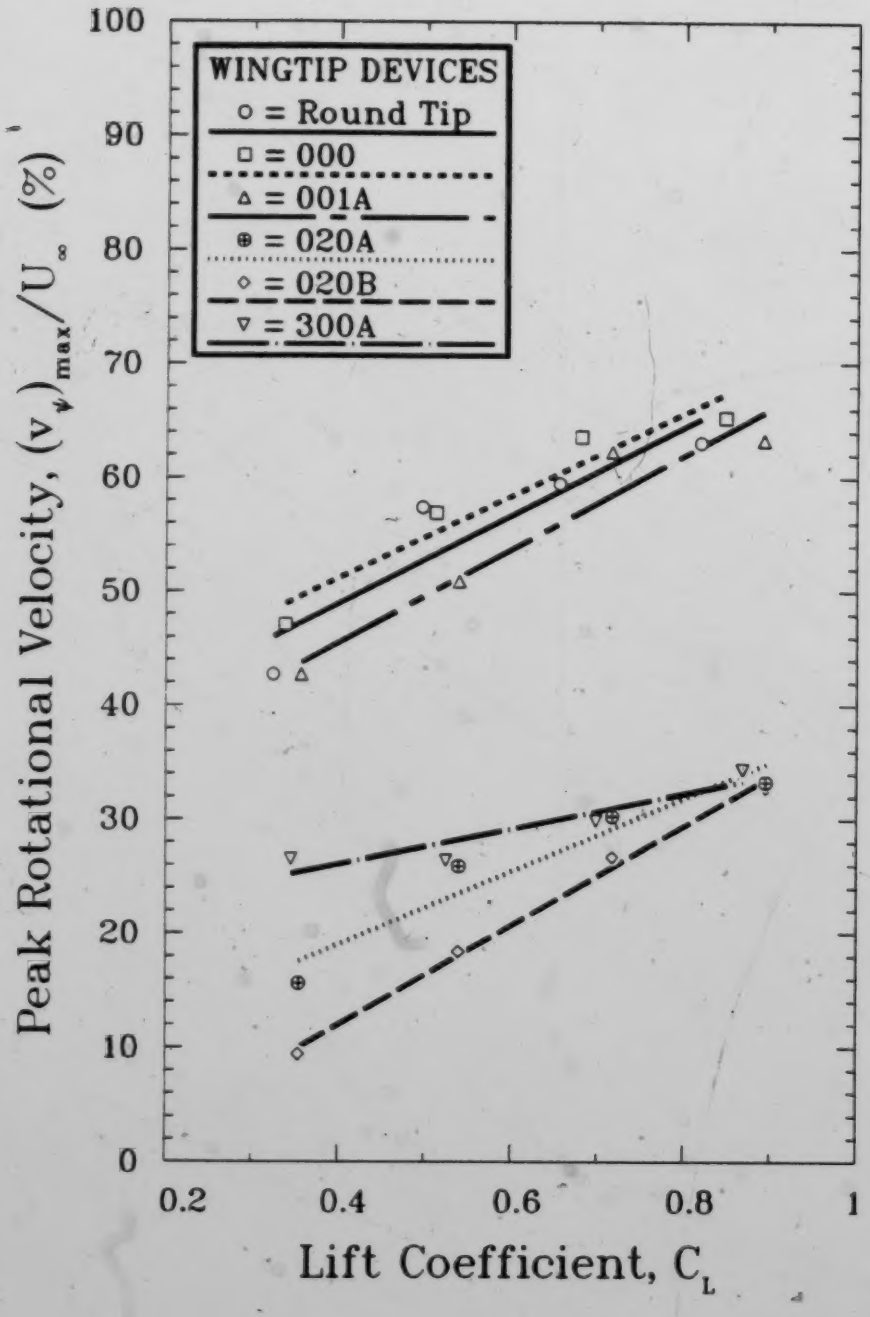

FIGURE 6-22 Peak rotational velocities of various main and secondary vortices 4.1 chord lengths behind the wing trailing edge

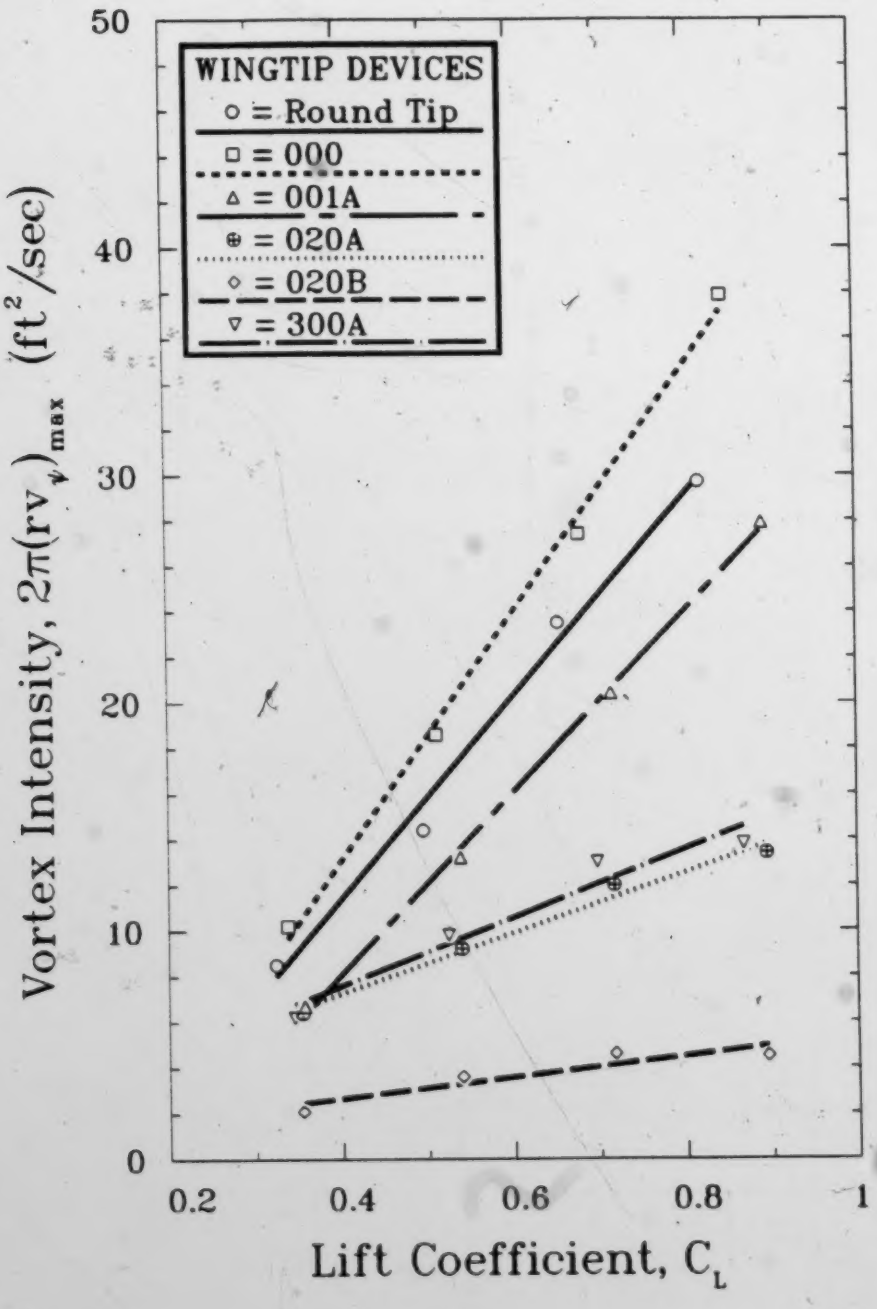

FIGURE 6-23 Intensities of various main and secondary vortices 4.1 chord lengths behind wing trailing edge

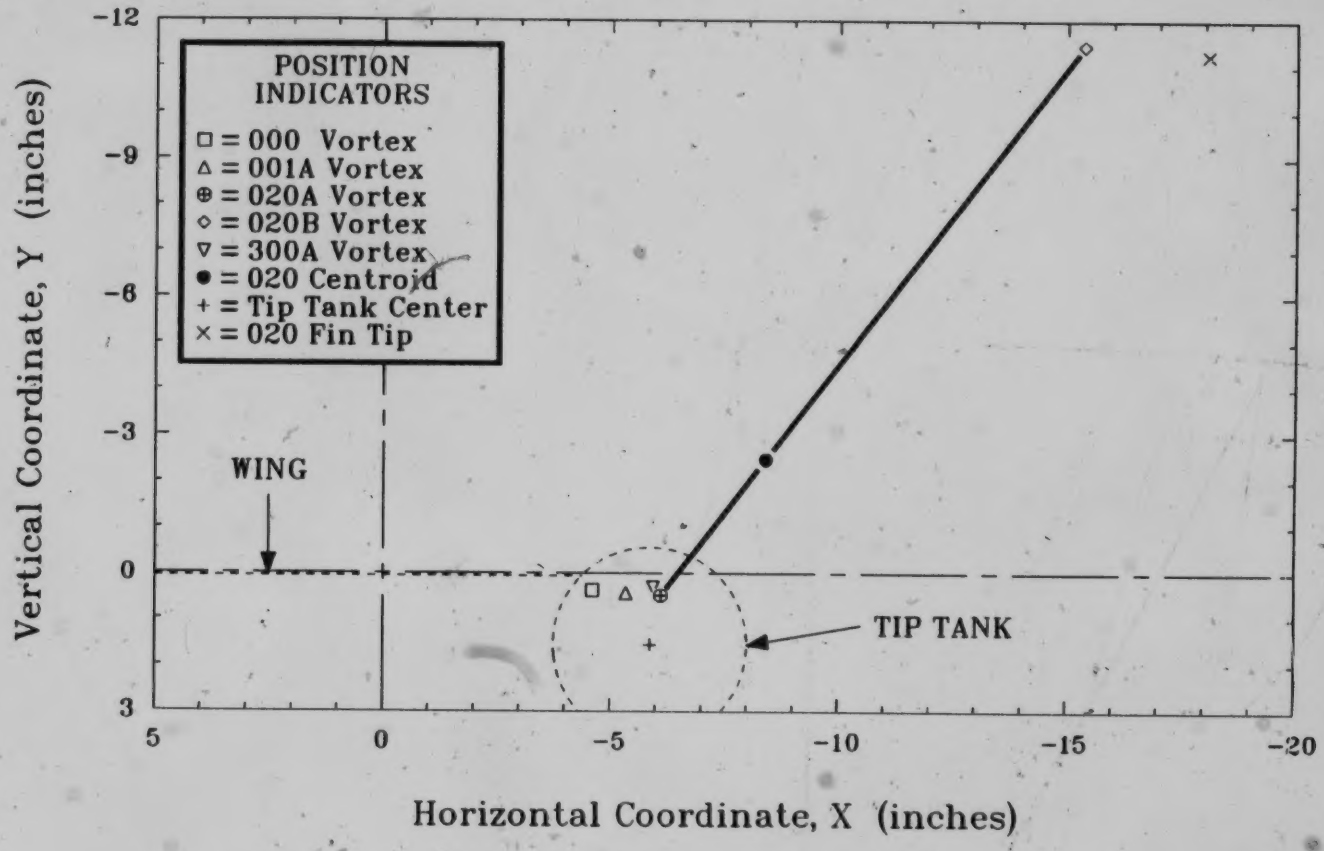

(a) $C_L = 0.35$

FIGURE 6-24 Vortex positions in a cross-stream plane 4.1 chord lengths behind the wing trailing edge

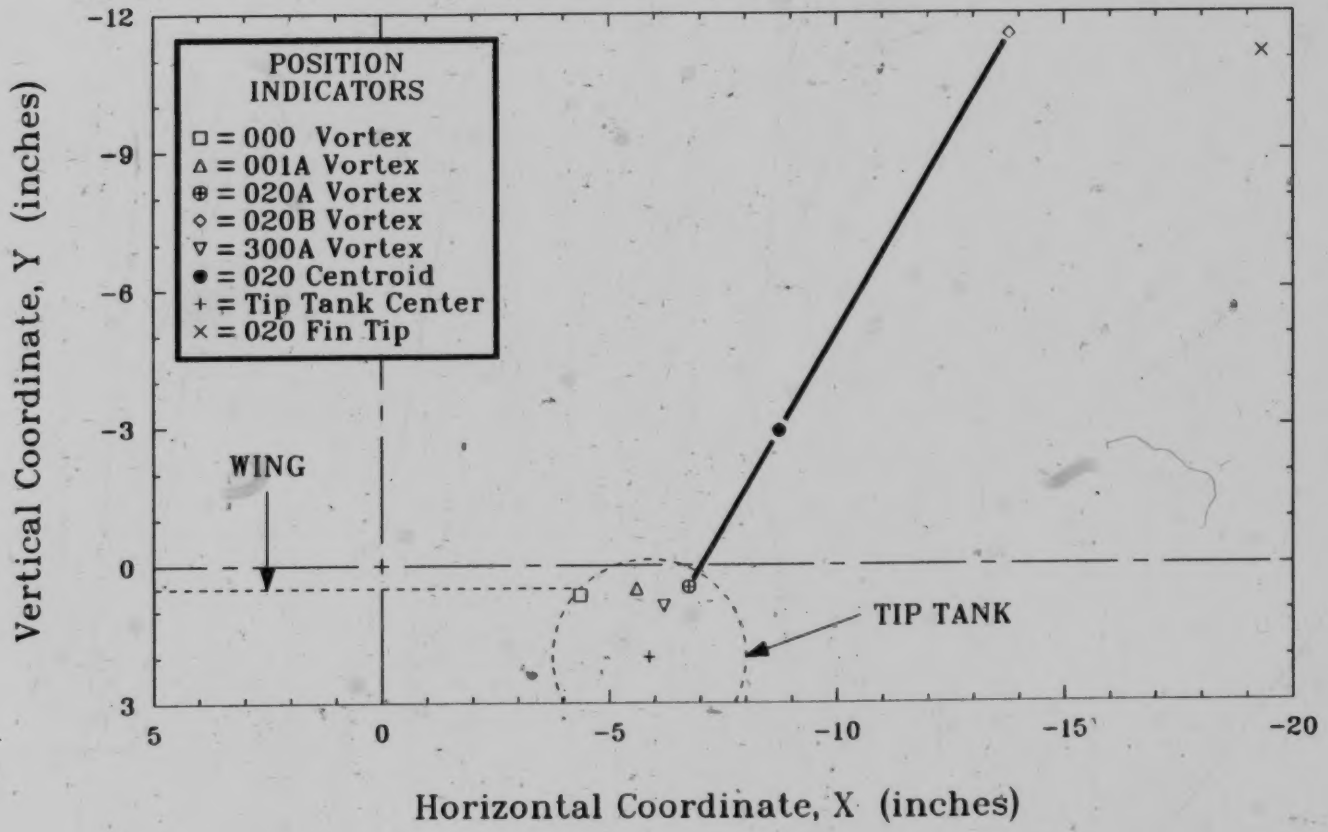
POSITION INDICATORS
□ = 000 Vortex
△ = 001A Vortex
⊕ = 020A Vortex
◇ = 020B Vortex
▽ = 300A Vortex
● = 020 Centroid
+ = Tip Tank Center
× = 020 Fin Tip
WING
TIP TANK
Vertical Coordinate, Y (inches)
Horizontal Coordinate, X (inches)
-12
-9
-6
-3
0
3
5
0
-5
-10
-15
-20

(b) $C_L = 0.53$

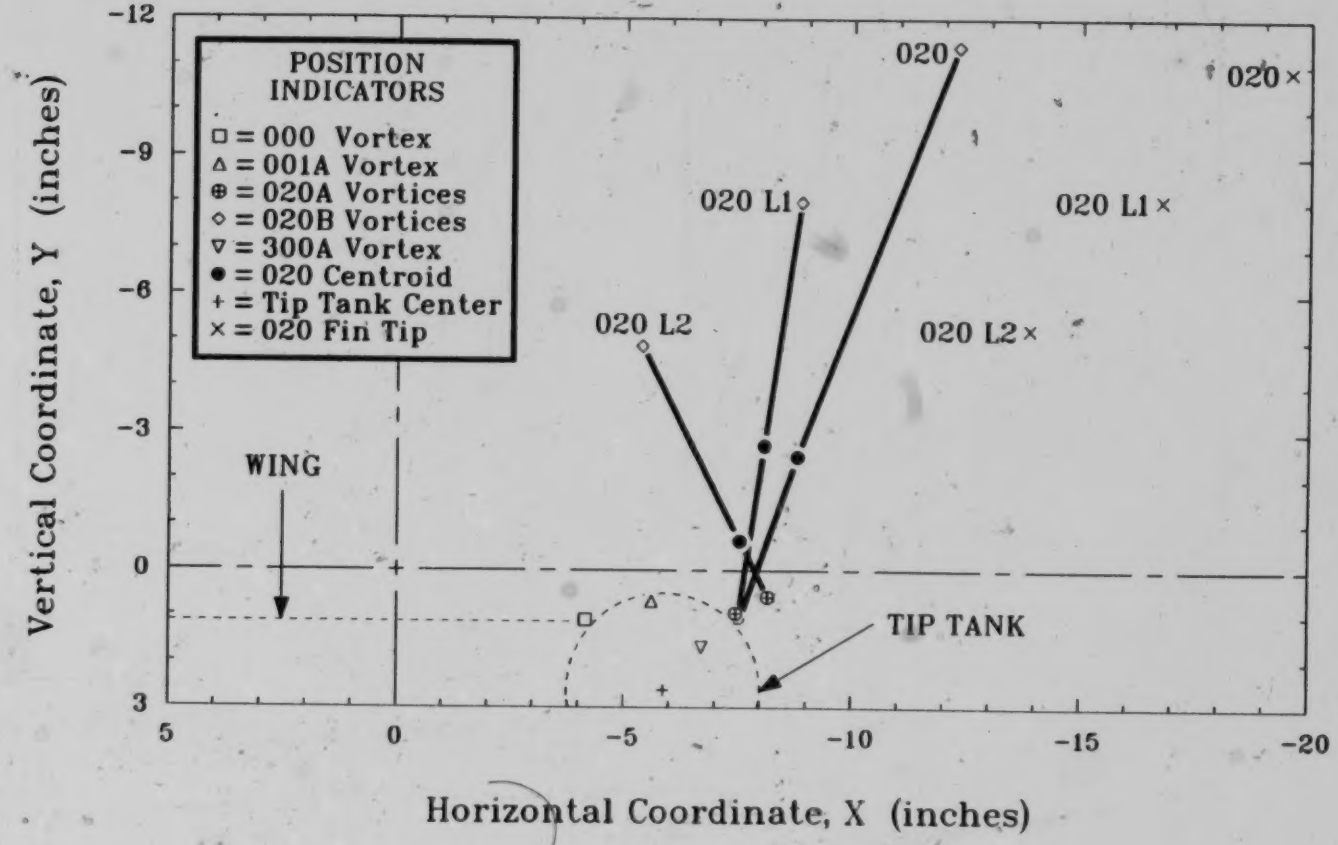

(c) Vortices due to shortened fins included, $C_L = 0.71$

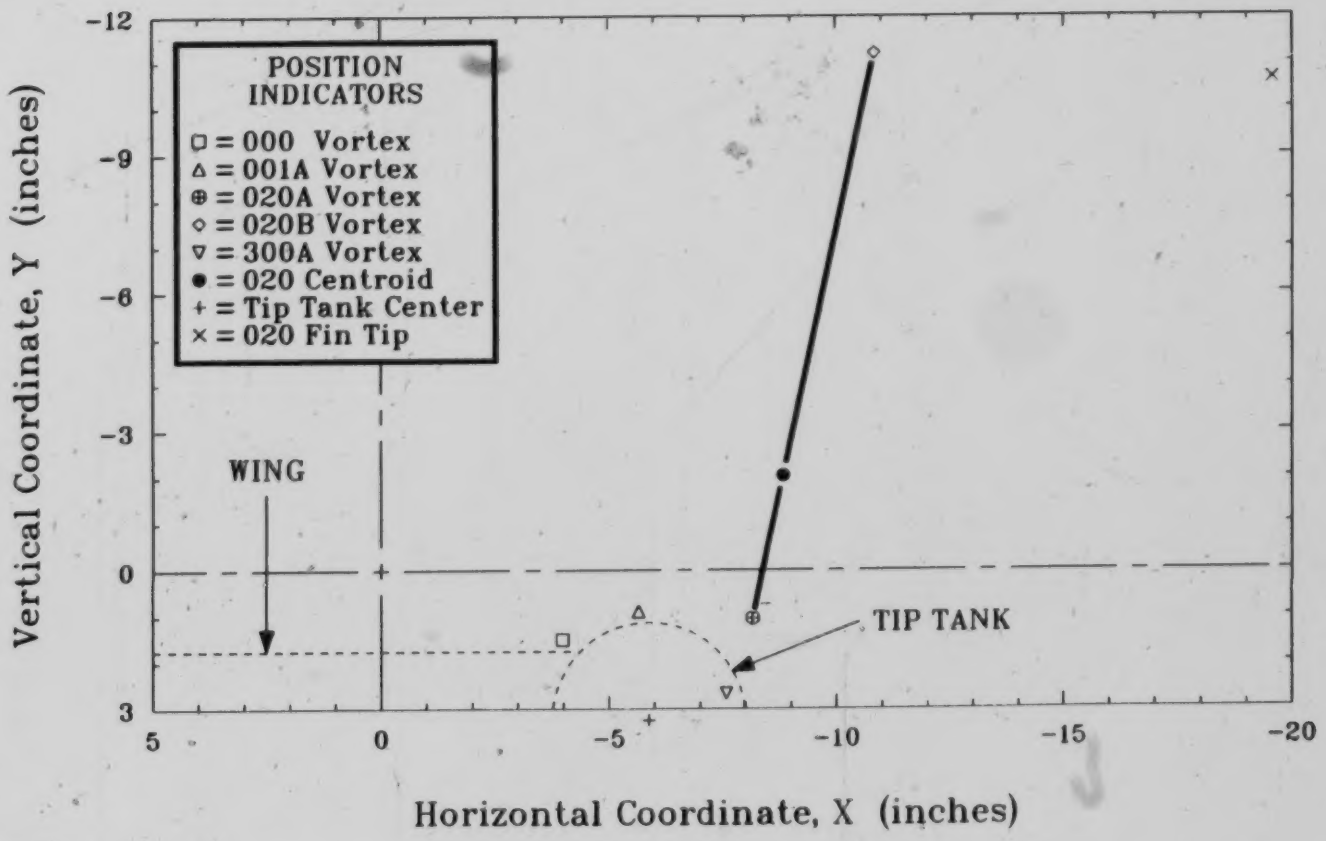
POSITION INDICATORS
□ = 000 Vortex
△ = 001A Vortex
⊕ = 020A Vortex
◇ = 020B Vortex
▽ = 300A Vortex
● = 020 Centroid
+ = Tip Tank Center
× = 020 Fin Tip
WING
TIP TANK
Vertical Coordinate, Y (inches)
-12
-9
-6
-3
0
3
5
0
-5
-10
-15
-20
Horizontal Coordinate, X (inches)

(d) $C_L = 0.88$

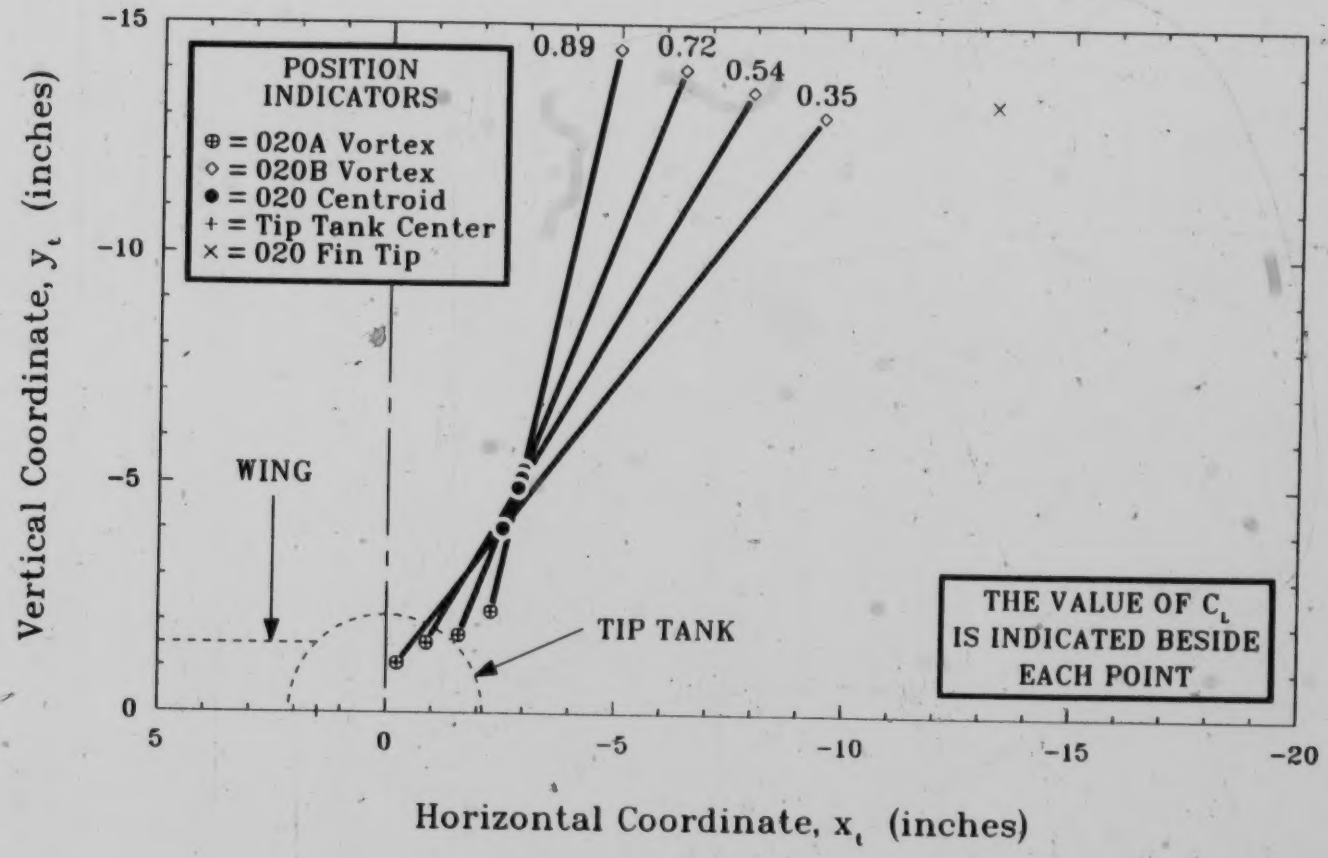

(a) Convection due to increasing lift, with $(z/c)_r$ 4.1

FIGURE 6-25 Mutual rotation of the main and secondary vortices due to configuration 020

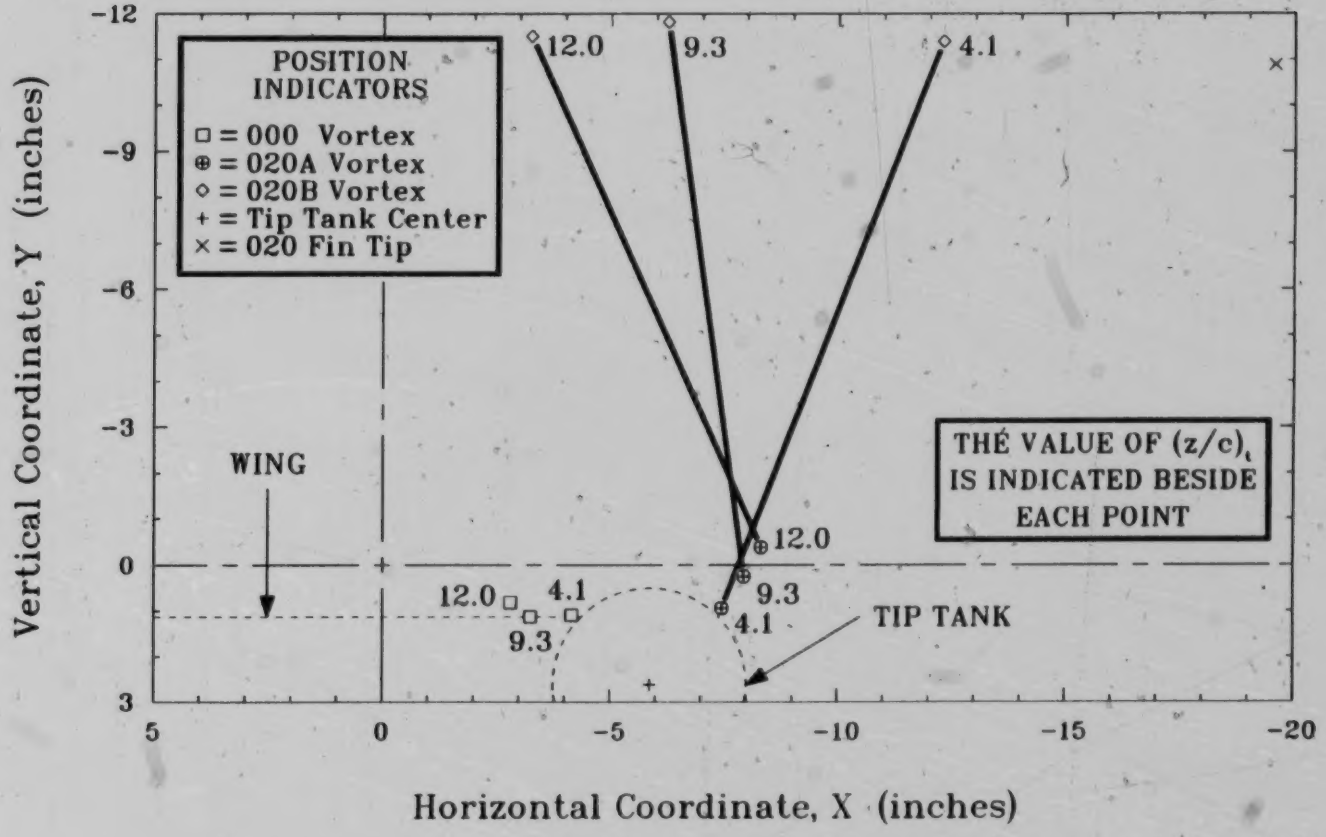

(b) Convection due to increasing downstream distance, with C_L = 0.71

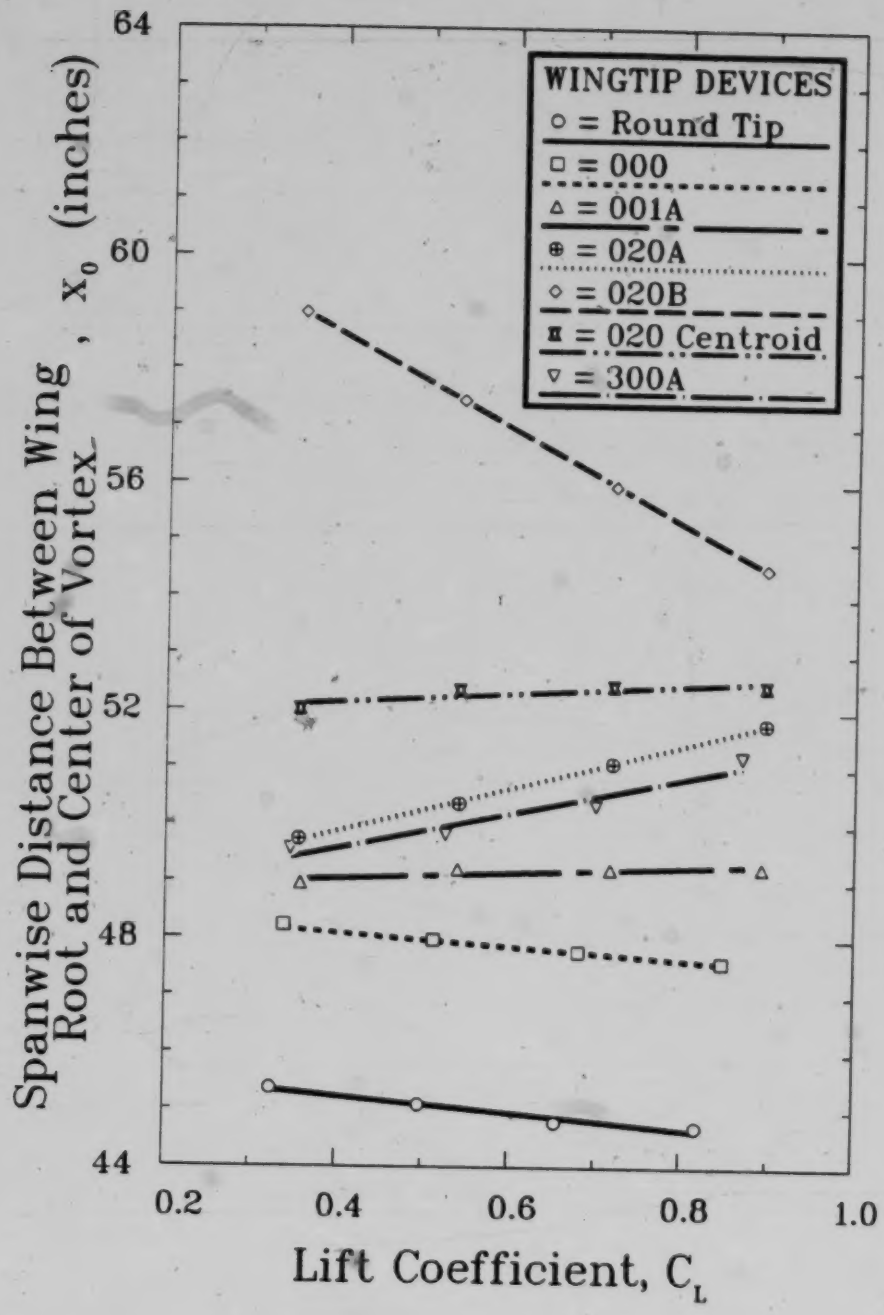

FIGURE 6-26 Spanwise displacements of various main and secondary vortices, including the centroid of the 020 vortices, 4.1 chord lengths behind wing trailing edge

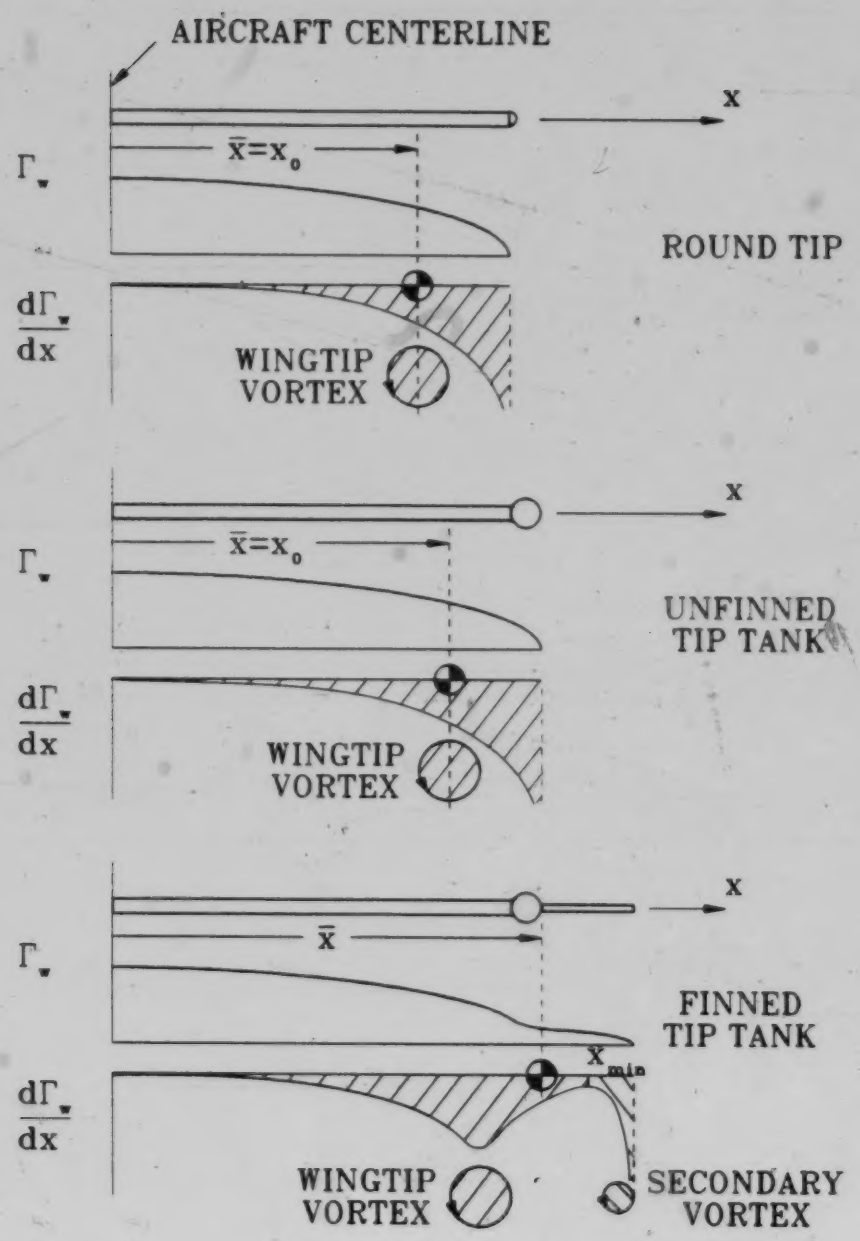

FIGURE 6-27 The outboard displacement of a wingtip vortex with increased loading near the tip.

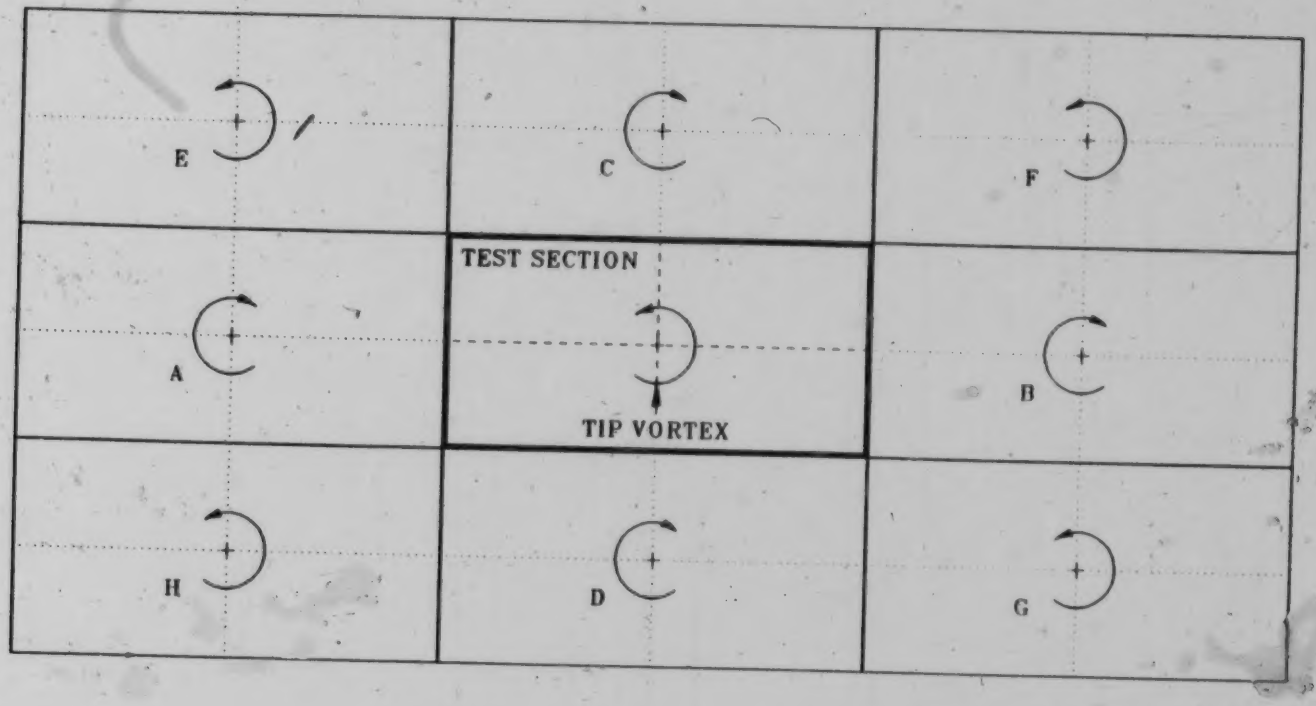

(a) Wingtip vortex centered on test section centerline

FIGURE 6-28 Vortex image for systems for a reflection plane model in a rectangular test section, with flow out of the page

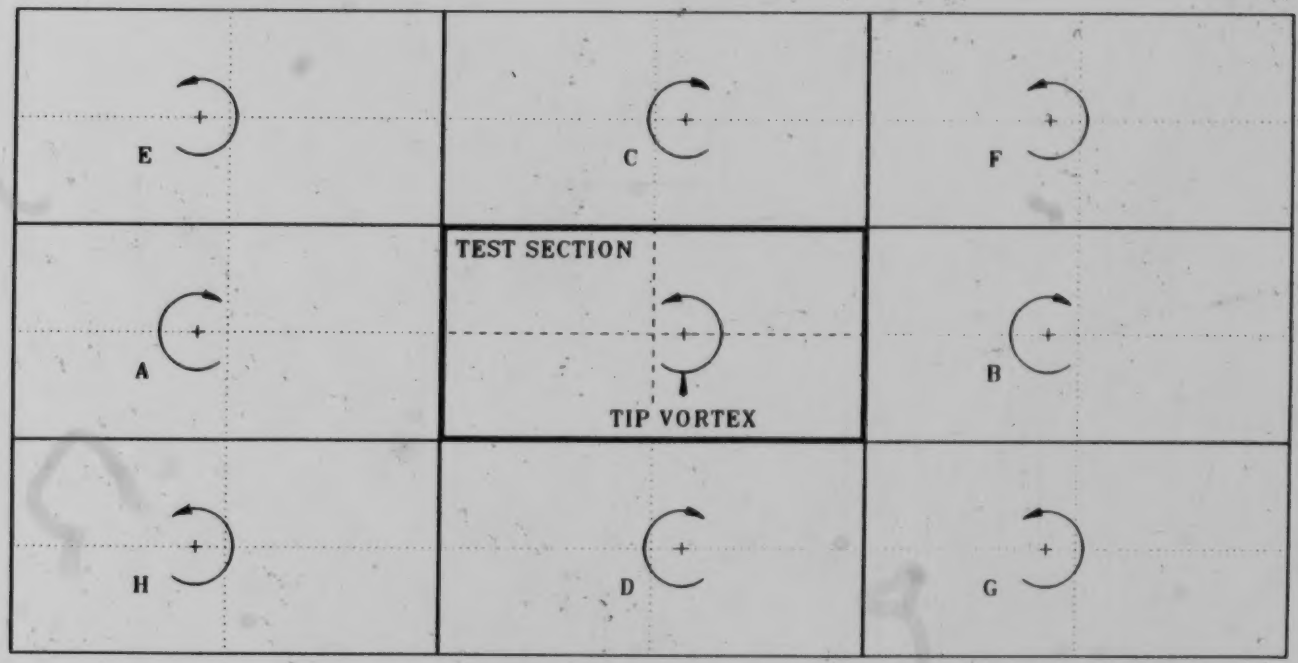

(b) Wingtip vortex displaced from test section centerline

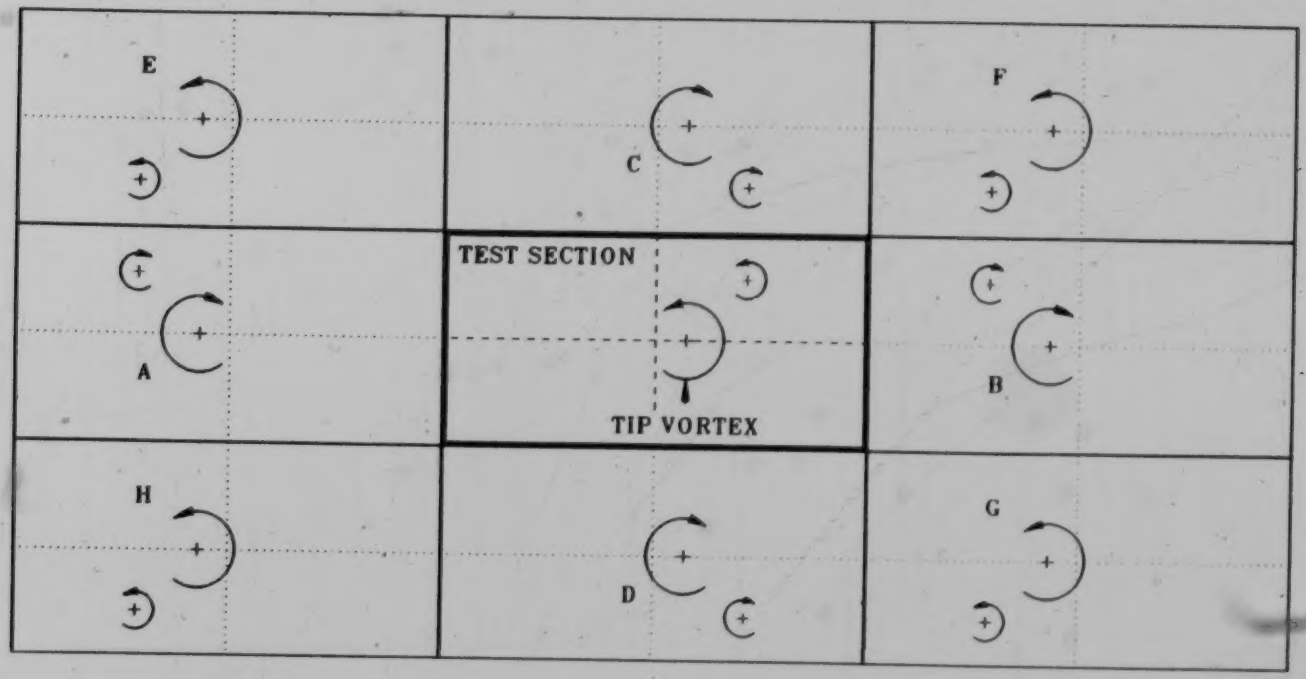

(c) Wingtip vortex displaced from test section centerline and accompanied by a secondary vortex

National Library
of Canada

Canadian Theses Service

Bibliothèque nationale
du Canada

Service des thèses canadiennes

NOTICE

AVIS

THE QUALITY OF THIS MICROFICHE IS HEAVILY DEPENDENT UPON THE QUALITY OF THE THESIS SUBMITTED FOR MICROFILMING.

UNFORTUNATELY THE COLOURED ILLUSTRATIONS OF THIS THESIS CAN ONLY YIELD DIFFERENT TONES OF GREY.

LA QUALITE DE CETTE MICROFICHE DEPEND GRANDEMENT DE LA QUALITE DE LA THESE SOUMISE AU MICROFILMAGE.

MALHEUREUSEMENT, LES DIFFERENTES ILLUSTRATIONS EN COULEURS DE CETTE THESE NE PEUVENT DONNER QUE DES TEINTES DE GRIS.

PLATE 3-1 Orientation of wing section FX61-163/SF in the main test section with the view directed downstream

PLATE 3-2 The wing fitted with the round wingtip

PLATE 3-3 One possible tip tank configuration showing fins placed at all three chordwise positions

PLATE 3-4 XY portable traversing mechanism with the five-hole flow angle probe, viewed downstream

PLATE 3-5 Close-up view of the five-hole flow angle probe with its calibration mount

APPENDIX I: CALIBRATION AND USE OF THE FIVE-HOLE FLOW ANGLE PROBE

The methods for calculating flow pressure parameters and for using the probe in an unknown flow field are obtained directly from [15].

I.1 PROBE COEFFICIENTS

The probe orifices are identified with the numbering system specified in Figure I-1, where the view is directed downstream into the probe. A set of pressure coefficients may be defined as follows, where the pressure p_i sensed by the i^{th} orifice is referenced to the wall tap static pressure p_0:

$$C_{p_i} = \frac{(p_i - p_0)}{(p_T - p_0)}, \quad i = 1, 2, 3, 4, 5.$$

The coefficients are normalized to the test section total pressure p_T. Another pressure coefficient represents the average of the pressures sensed by the peripheral orifices and is defined as

$$\bar{C}_p = \frac{(C_{p_1} + C_{p_2} + C_{p_3} + C_{p_4})}{4}.$$

A set of flow parameters may now be defined. These are:

dynamic parameter $$P = C_{p_5} - \bar{C}_p, \qquad \text{(I-1a)}$$

sidewash parameter $$Q = \frac{C_{p_2} - C_{p_4}}{P}, \qquad \text{(I-1b)}$$

upwash parameter $$R = \frac{C_{p_3} - C_{p_1}}{P}, \qquad \text{(I-1c)}$$

static parameter $$S = \frac{1 - C_{p_5}}{P}. \qquad \text{(I-1d)}$$

I.2 PROBE CALIBRATION PROCEDURE

A static pressure gradient along the test section length necessitated probe calibration at several stations, each corresponding to a wall tap. At each station, the probe was faced upstream and aligned with the test section centerline. Except for the probe, the portable XY traverse, and a pitot-static tube, the test section was empty.

The calibration setup allowed the probe angles to be ranged as follows:

roll angle $0^\circ \leq \phi \leq 360^\circ$, increments of 10°,

pitch angle $0^\circ \leq \theta \leq 45^\circ$, increments of 5°.

These angles are illustrated in Figure 3-8 of the main report. A stepping motor incremented the roll angle by rotating the probe about is longitudinal axis. The pitch angle was set by fixing the probe at an inclination with its mount. Any flow interference effects that may have been caused by the presence of the probe mount were nullified by leaving the mount in place during experiments.

The flowchart in Figure I-2 outlines the calibration procedure. For each fixed pitch angle, the roll angle was stepped in 5° increments with data gathered by the computer at each step. Upon completion of measurements, a set of calibration curves were calculated and plotted. This procedure was repeated at every station.

Correlations between the flow angles and the flow parameters P,

Q, R, and S were retained within a set of four calibration plots. The crossflow parameters measure sidewash and upwash respectively, so the ratio Q/R reflects the magnitude of the roll angle. The relation is pictured in Figure I-3 and is fairly independent of pitch angle. In turn, $(Q^2+R^2)^{1/2}$ indicates the magnitude of the velocity vector and is largely independent of roll angle. Its variation with pitch is shown in Figure I-4. Although the polynomial fit follows a rather haphazard trend for pitch angles higher than about 35^{o}, the probe is less accurate in this region anyway as is shown by the wide spread of data points. The pitch angle and the measured dynamic parameter $P_{\alpha\beta}$ are correlated in Figure I-5. The correlation is largely independent of roll for small pitch angles. This restriction holds true as well for Figure I-6, which relates the measured static flow parameter $S_{\alpha\beta}$ to the square of the pitch angle. The curves diverge remarkably for large pitch angles.

Empirical relations were obtained by fitting polynomials to the data. The polynomial coefficients were retained in a data file for later analysis of experimental data.

The calibration furnished a side-hole sensitivity of

$$\frac{\Delta p}{(\rho U_\infty^2/2)\Delta\theta} = 0.0552 \text{ per degree},$$

where Δp is the pressure difference between opposing peripheral orifices of the probe. This result compares well with the value (0.0583 per degree) obtained by Wickens and Williams [15] for their probe.

I.3 USE OF THE PROBE IN AN UNKNOWN FLOW

An automated method for using the probe to determine the characteristics of an unknown flow field may be summarized as follows:

1) Calculate the flow parameters P, Q, R, and S from the experimental data.

2) Determine the local roll and pitch angles from the polynomial fits to Figures I-3 and I-4:

$$\phi = f_1(\tan^{-1}(|Q/R|)), \quad \theta = f_2((Q^2+R^2)^{1/2}).$$

3) Compute the local dynamic pressure from

$$\frac{q}{q_T} = \frac{P}{P_{cal}},$$

where the subscript T refers to the freestream value and P_{cal} is obtained from Figure I-5 using the computed values of θ and ϕ.

4) Determine the local resultant velocity

$$\frac{V_R}{U_\infty} = \left(\frac{q}{q_T}\right)^{1/2},$$

and its components:

longitudinal $$\frac{u}{U_\infty} = \left(\frac{V_R}{U_\infty}\right)\cos\theta,$$

sidewash $$\frac{v}{U_\infty} = \left(\frac{V_R}{U_\infty}\right)\sin\theta\sin\phi,$$

upwash $$\frac{w}{U_\infty} = \left(\frac{V_R}{U_\infty}\right)\sin\theta\cos\phi.$$

The signs of the components are assigned according to the signs of Q and R.

5) Compute the local total pressure coefficient

$$C_{p_T} = C_{p_s} + PS_{est} \,, \tag{I-2}$$

where S_{est} is obtained from Figure I-6 using the computed values of θ and ϕ.

6) Compute the local static pressure coefficient

$$C_{p_s} = C_{p_T} - \frac{q}{q_T} \,. \tag{I-3}$$

7) Determine the local induced velocity at a point in a vortex wake:

$$\frac{v_\phi}{U_\infty} = \left[\left(\frac{v}{U_\infty}\right)^2 + \left(\frac{w}{U_\infty}\right)^2\right]^{1/2} = \left(\frac{V_R}{U_\infty}\right) \sin\theta \,.$$

The reader may find it more convenient to express the local flow angles θ and ϕ as λ, the pitch in a vertical plane, and μ, the yaw in a horizontal plane. These angles are shown in Figure 3-8 of the main report and are defined as follows:

$$\lambda = \tan^{-1}(\tan\theta \cos\phi) \,, \quad \mu = \tan^{-1}(\tan\theta \sin\phi) \,.$$

Inverse relations are

$$\theta = \sin^{-1}\left((\sin^2\mu + \cos^2\mu \sin^2\lambda)^{1/2}\right) \,, \qquad \phi = \tan^{-1}\left(\frac{\tan\mu}{\tan\lambda}\right) \,.$$

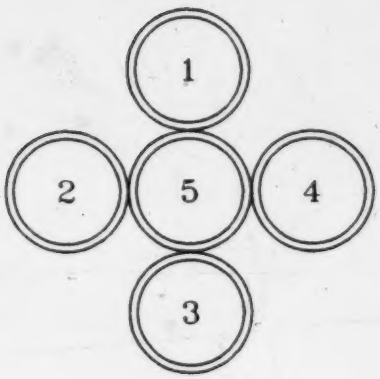

FIGURE I-1 Numbering of probe orifices, with view directed downstream into the probe

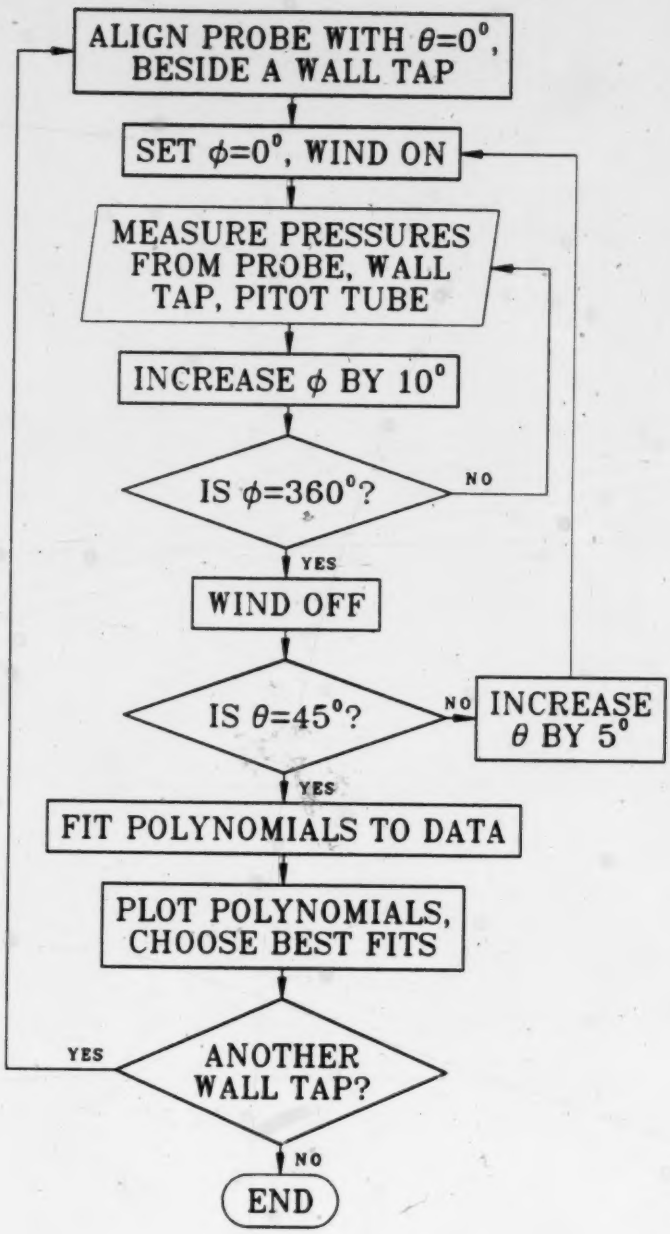

FIGURE I-2 Flowchart showing summary of five-hole flow angle probe calibration procedure

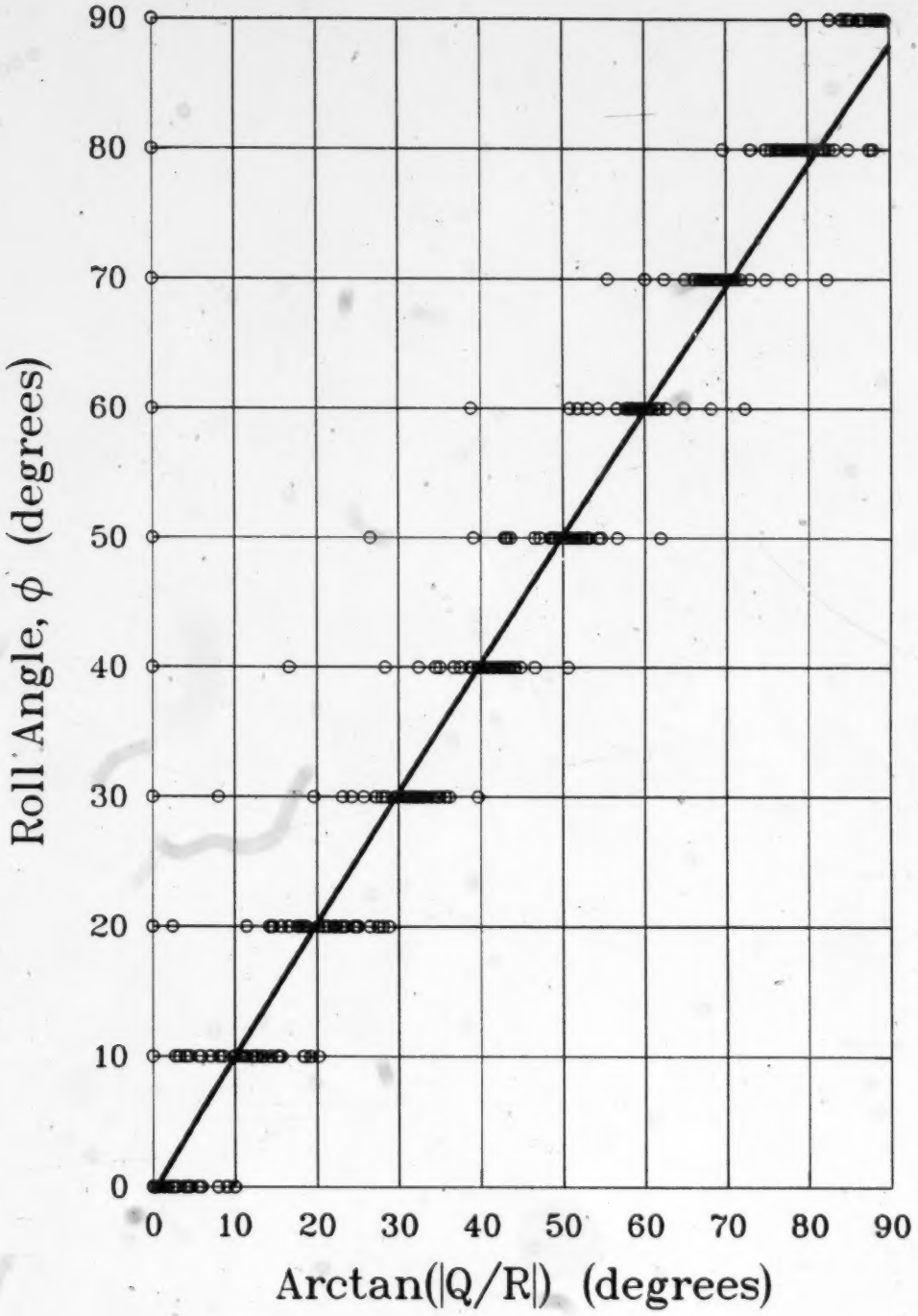

FIGURE I-3 Local roll angle as determined from the calibration data

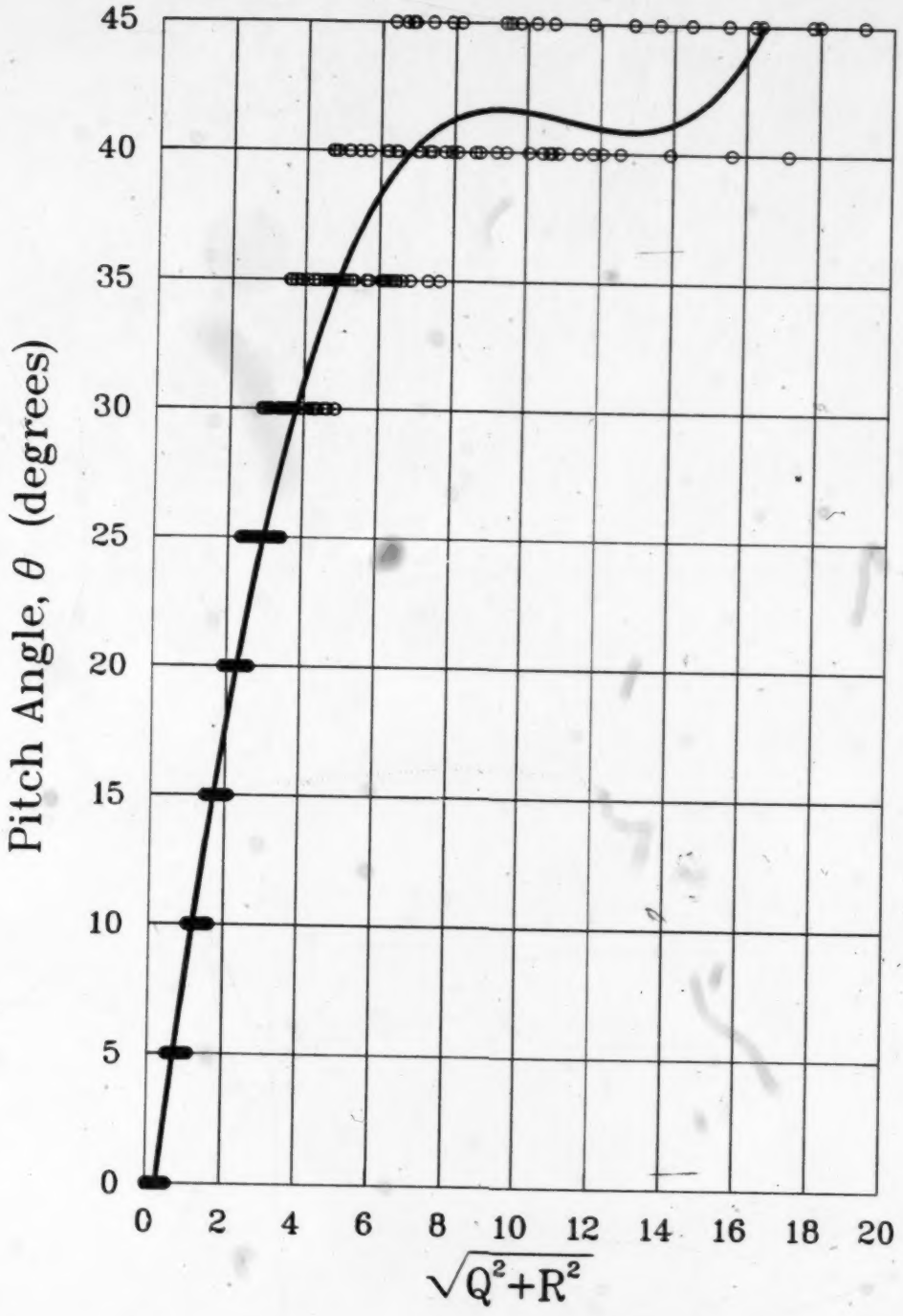

FIGURE I-4 Local pitch angle as determined from the calibration data

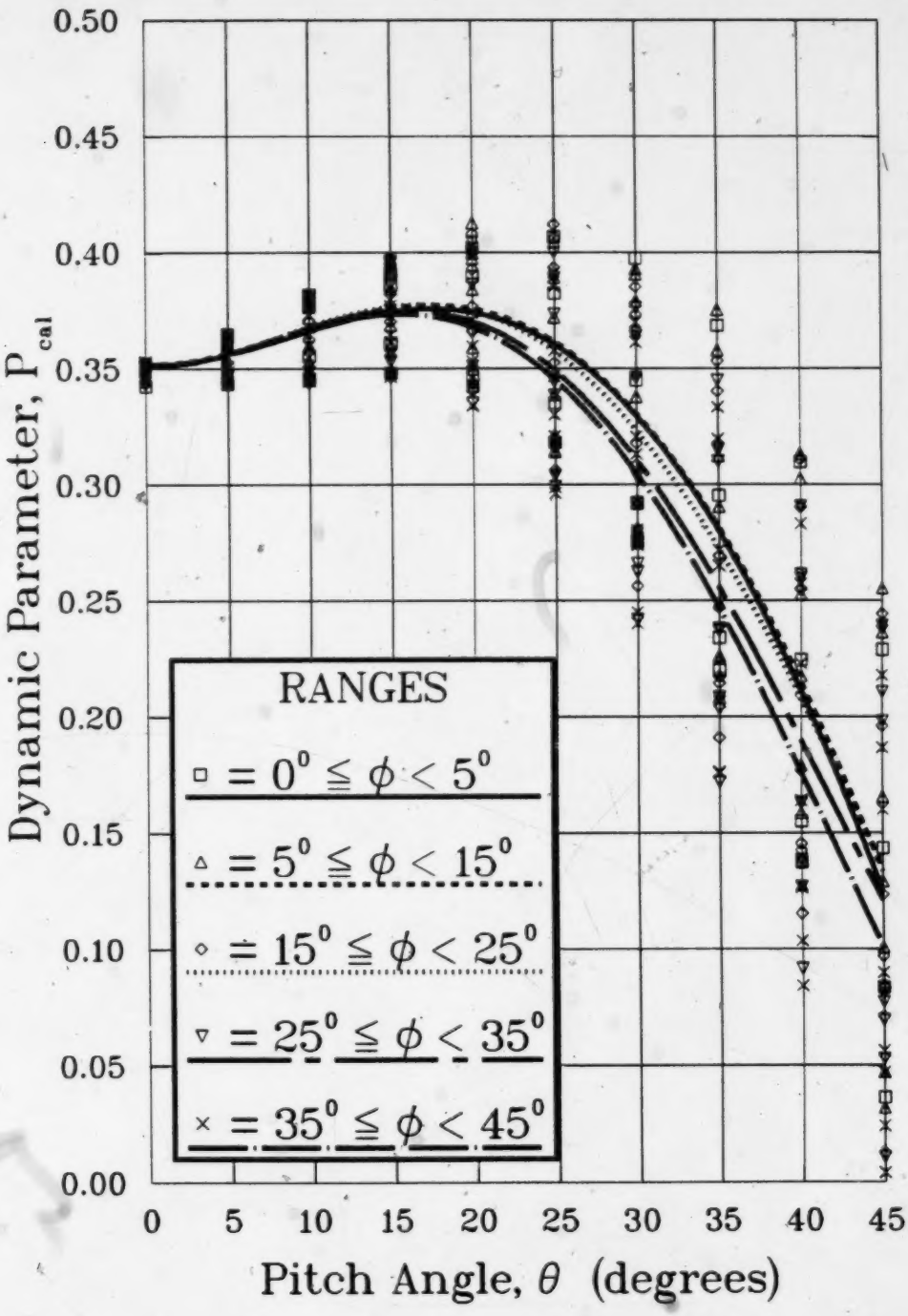

FIGURE I-5 Influence of pitch and roll angles on the dynamic pressure parameter

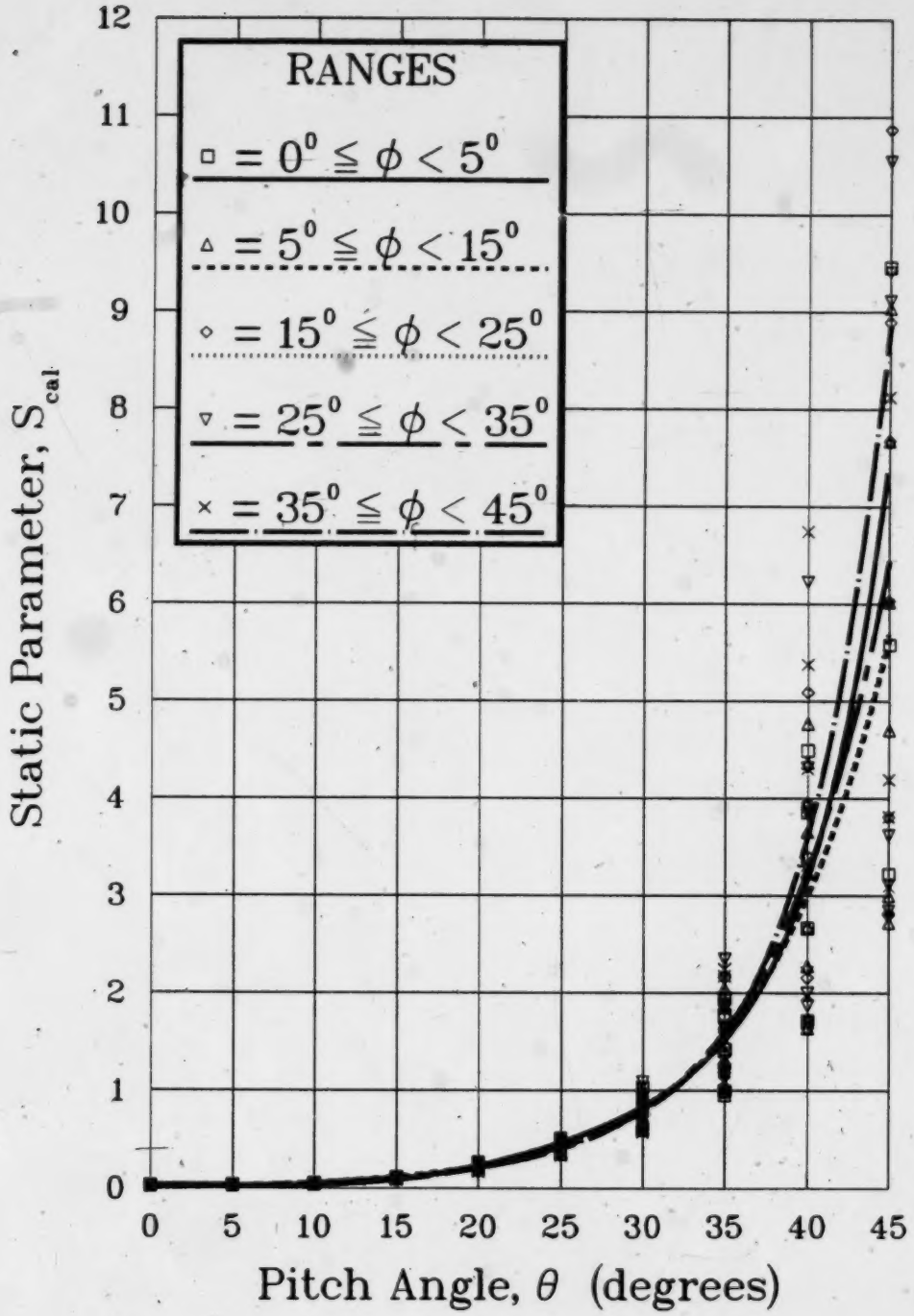

FIGURE I-6 Influence of pitch and roll angles on the static pressure parameter

APPENDIX II: CALIBRATION OF VALIDYNE TRANSDUCERS

The Validyne pressure transducers were each calibrated in turn against a U-tube water manometer. A dial gauge was used to measure pressure differences to an accuracy of 0.0001 inches of water. The Validynes were calibrated over their entire operating range and a regression analysis of the pressure-voltage curve for each transducer indicated an extremely linear response - the correlation coefficient was always greater than 0.99992. A sample calibration curve for the tunnel airspeed Validyne is provided in Figure II-1.

The responses have an inherent tendency to drift slightly with time so calibrations had to be conducted directly before a test run. During a test run, equal pressures were periodically applied to both sides of the wing Validyne in order to update the y-intercept of the pressure-voltage response.

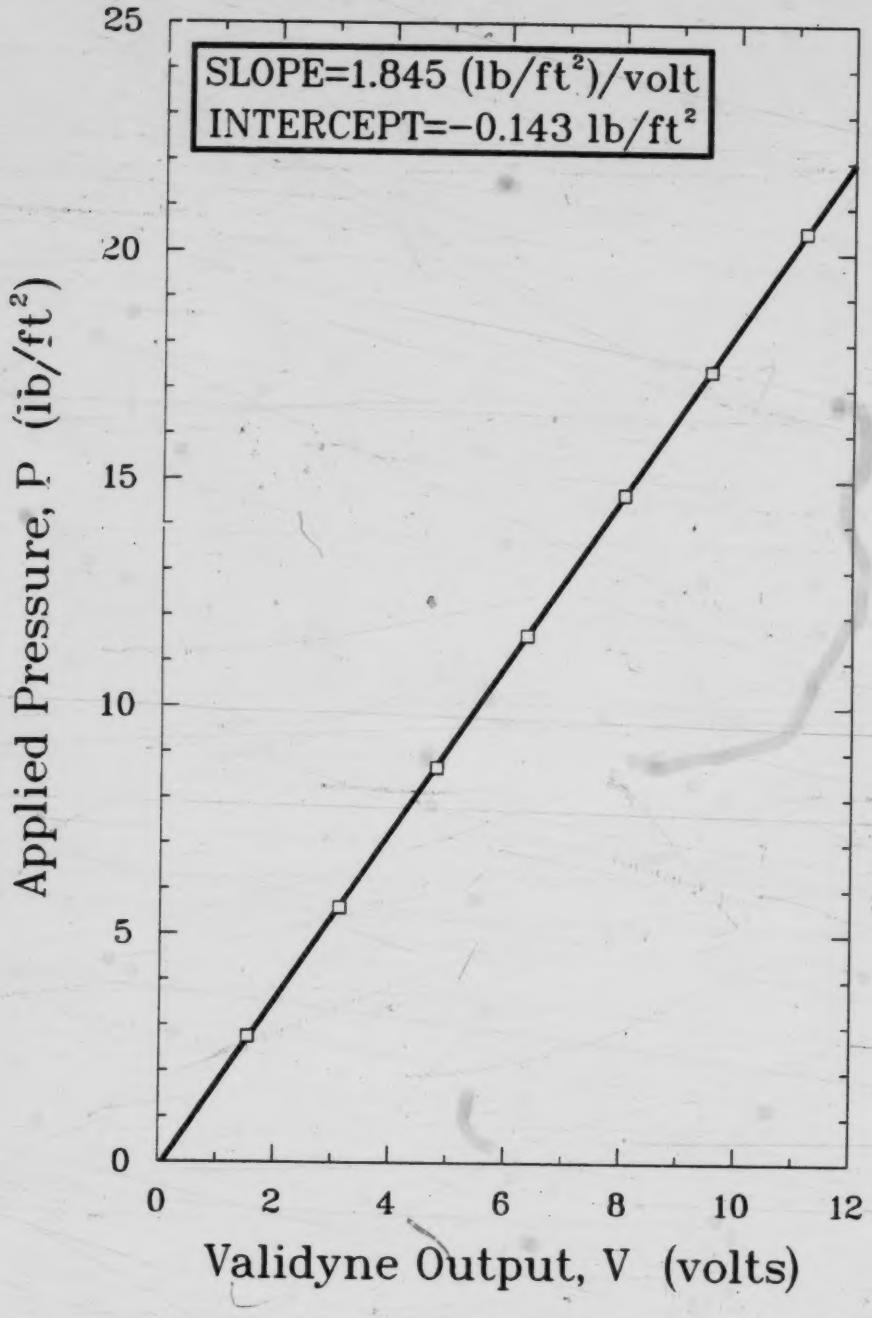

FIGURE II-1 Sample plot for calibration of a Validyne transducer

APPENDIX III: WIND TUNNEL BOUNDARY CORRECTIONS

The wing model in the test section does not experience precisely the same flow conditions as it would in free flight. The flow streamlines and the vortex system behind the model are constrained by the test section walls, and the model creates some blockage as well. In order to gain realistic and interpretable test results, the experimental data must necessarily be corrected for the test section boundaries.

Wind tunnel boundary corrections for a three-dimensional wall-mounted wing model are derived in Pope and Harper [35]. The derivation begins with a mathematical simulation of the test section boundaries by introducing the vortex image system of Figure 6-28, which was explained in Section 6.2.4 of the report. Although it contains an infinite distribution of image vortices, the first order representation of Figure 6-28 will suffice. Corrections must be made for the following factors:

1) Solid blocking: The model obstructs part of the test section, so the flow velocity must increase in the region of the model. The airflow is simulated by replacing the model with a doublet, which is constrained to remain stationary in the test section by introducing an infinite series of image doublets.

2) Wake blocking: The test section walls prevent the model wake from expanding laterally. This action is simulated by representating the wake with a source, and a sink of equal strength is introduced (for continuity) far downstream.

3) Streamline curvature: The boundary-induced upwash at the model is found by superimposing the upwash contributions from the image vortices.

4) Downwash: The upwash induced by the image vortices reduces the downwash of the model, giving too low a value for the measured induced drag. With the upwash accounted for, the induced angle of flow and induced drag increment due to the walls may be found.

Boundary corrections for the model FX61-163/SF are summarized below. Uncorrected parameters are indicated with the subscript u. The planform area, S_t, and volume, V_t, of a wingtip device partly determine the magnitudes of the corrections and are summarized in Table III-1. The wing section area and volume have already been incorporated into the equations. An uncorrected total drag coefficient, C_{D_u}, of 0.01 is estimated for the corrections. The planform area and volume of a wingtip device must be given respectively in units of square inches and cubic inches for the corrections that follow.

Freestream velocity:

$$U_\infty = U_{\infty_u}\left[1.00634+4.049(10^{-4})V_t+\frac{(862.3+S_t)\,C_{D_u}}{15752}\right].$$

Dynamic pressure:

$$q = q_u\left[1.01268+8.098(10^{-4})V_t+\frac{(862.3+S_t)\,C_{D_u}}{7876}\right].$$

Reynolds number based on wingtip chord:

$$Re_{c_t} = Re_{c_{t_u}}\left[\frac{U_\infty}{U_{\infty_u}}\right].$$

Total lift coefficient:

$$C_L = C_{L_w}\left[0.98732 - 8.098(10^{-6})V_t - \frac{(862.3+S_t)\,C_{D_w}}{7876}\right] \ldots$$

$$\ldots - 8.970(10^{-6}) - 1.041(10^{-7})S_t \,.$$

Angle of attack:

$$\alpha = \alpha_w + C_L\left(1.5482 + 1.795(10^{-5})S_t\right) \,. \quad (degrees)$$

Pitching moment about the wing quarter chord:

$$C_{M1/4} = C_{M1/4_w}\left[0.98732 - 8.098(10^{-6})V_t - \frac{(862.3+S_t)\,C_{D_w}}{7876}\right] \ldots$$

$$\ldots + 2.242(10^{-6}) + 2.602(10^{-8})S_t \,.$$

TABLE III-1 Planform areas and volumes of the wingtip devices

WINGTIP CONFIGURATION	PLANFORM AREA S_t ($in.^2$)	VOLUME V_t ($in.^3$)
ROUND TIP	25	53
000	89	340
001	89	385
006	113	385
007	134	385
020	134	385
020 L1	127	382
020 L2	117	374
021	134	430
026	158	430
040	89	385
050	153	385
051	153	430
056	177	430
057	198	430
300	153	385
301	153	430
320	198	430
321	198	475

APPENDIX IV: SOME COMMENTS ON VORTEX WAKE ANALYSIS

IV.1 LAMINAR VORTEX EQUATIONS

Detailed derivations of the equations for a laminar vortex may be found in [27], [36], and [37]. The equations may be obtained by first linearizing the Navier-Stokes equations for incompressible flow through the following assumptions:

1) The axial velocity deficit and the rotational velocity at any point within the vortex are small compared to the freestream velocity,
2) The radial velocity is much smaller than the freestream velocity,
3) The Reynolds number (based on freestream velocity and downstream distance) is large.

The linearized equations are, with these assumptions,

$$\frac{v_\theta^2}{r} = \frac{1}{\rho}\frac{\partial p}{\partial r},$$

$$U_\infty \frac{\partial v_\theta}{\partial z} = \nu\left[\frac{\partial^2 v_\theta}{\partial r^2} + \frac{1}{r}\frac{\partial v_\theta}{\partial r} - \frac{v_\theta}{r^2}\right],$$

$$U_\infty \frac{\partial v_z}{\partial z} = \nu\left[\frac{\partial^2 v_z}{\partial r^2} + \frac{1}{r}\frac{\partial v_z}{\partial r}\right].$$

The boundary conditions and initial conditions are

1) For $z>0$, $v_\theta, v_z \to 0$ as $r\to\infty$,
2) For $z\to\infty$, $v_\theta, v_z \to 0$ for all r,
3) When $z=0$, $v_\theta = \Gamma_\infty/2\pi r$ and $v_z = 0$.

With these, some vortex parameters are

$$v_\phi = \frac{\Gamma_0}{2\pi r}\left[1-exp\left(\frac{-U_\infty r^2}{4\nu z}\right)\right],$$

$$\Gamma_v = \Gamma_0\left[1-exp\left(\frac{-U_\infty r^2}{4\nu z}\right)\right],$$

$$(v_\phi)_{max} = 0.638\frac{\Gamma_0}{2\pi}\left(\frac{U_\infty}{4\nu z}\right)^{1/2},$$

$$r_{max} = \left[\frac{1.26\,(4\nu z)}{U_\infty}\right]^{1/2},$$

$$I = 2\pi(rv_\phi)_{max} = 0.716\Gamma_0.$$

No attempt was made to correlate these parameters with the experimental data partly because it is not known if the vortices are laminar or turbulent and partly because of the first assumption through which the Navier-Stokes equations were linearized: the peak rotational velocities were found to be as much as 70% of the freestream velocity and are thus too large to allow a correlation with the laminar vortex equations.

IV.2 TURBULENCE

The core width, peak rotational velocity, and distribution of circulation within a vortex depend on whether the vortex is laminar or turbulent. Some ways in which a laminar vortex may be distinguished from a turbulent vortex are discussed in the following subsections.

IV 2.1 Causes and Mechanisms of Turbulence

A vortex is classically modelled as a viscous core surrounded by potential flow. Stresses and strains between the rotational and irrotational fields can generate turbulent eddies. Turbulence can also be created from variations in the axial velocity distribution. However, turbulent eddy diffusivity tends to be reduced in a stable rotating wake and turbulent eddies tend to be gathered into the core and damped out. Although the cores from simply loaded wings tend to be laminar [38], the loading of a wing with a modified tip is more complex and may lead to a turbulent core.

IV 2.2 Rate of Core Growth

The presence of turbulence in a vortex may be verified or ruled out by studying the core width as the vortex evolves. The core of a laminar vortex grows parabolically with distance downstream; this result may be derived from the linearized Navier-Stokes equations of Section IV.1. The core of a turbulent vortex was determined to grow linearly by Hoffman and Joubert [39], but this result was derived from mixing length theory. Perhaps a more accurate result is that of Brown [40], where an analysis of the wing vorticity distribution was used to show that core growth proceeds as the two-thirds power of time.

The experimental results of Figures 4-2b and 5-4 of the main report show little change in core width over the length of the test section, so it cannot be determined on the basis of core width if a wingtip vortex is laminar or turbulent.

IV 2.3 Decay of Peak Rotational Velocities

The peak rotational velocity of a vortex at any point downstream can vary slightly, depending on the point within the wing boundary layer at which laminar flow becomes turbulent flow. Brown [40] predicts the peak rotational velocity of a turbulent vortex to decay with the inverse one-third power of time. According to the results of the linearized Navier-Stokes equations, the peak rotational velocity of a laminar vortex should decay as the inverse one-half power of time.

It cannot be determined on the basis of peak rotational velocity if the vortices of this work are laminar or turbulent because again, Figures 4-2b and 5-4 show very little change in velocity for the same vortex over the length of the test section.

IV 2.4 Vortex Circulation Distribution

Corsiglia et al [19] divided the circulation distribution of a turbulent vortex into three regions based on comparision with turbulent boundary layers: an inner or core region, a region in the vicinity of the rotational velocity peak where the distribution is logarithmic, and an outer region. The distribution differs from that of a laminar vortex, where the distribution is exponential.

A simple and direct way to find out if a vortex is turbulent is to look for a circulation overshoot, which occurs only in turbulent vortices. The overshoot is a localized excess of circulation which occurs at the core edge because conservation of momentum requires the core edge velocities to increase so as to compensate for axial

velocity defects.

For most of the vortices that were analysed, no discontinuities in rotational velocity that would indicate a circulation overshoot were noted, except near the core center. For others, the flow angles near the core edge were so high that they were outside the measurement range of the five-hole probe. In all likelihood the vortices are laminar, but this proposal can be neither vigorously defended nor denied.

IV 2.5 Effective Eddy Viscosity

The effect of turbulence may be incorporated into the equations for a laminar vortex simply through the use of an effective eddy viscosity [36]. The kinematic viscosity ν in the equations is replaced with an effective eddy viscosity $\nu+\alpha\Gamma_v$, where α is an empirically determined constant. It turns out, though, that this method does not fully account for shears and strains within the vortex. Mason and Marchman [17], for instance, report substantial inconsistencies in the laminar vortex equations when this method is used.

APPENDIX V: RELATION BETWEEN WING AND VORTEX CIRCULATION DISTRIBUTIONS

V.1 THE METHOD OF BETZ

The circulation distribution within a tip vortex may be correlated directly with that on the wing by implementing the conservation laws of Betz [34]. Although the Betz model of the vortex is inviscid and unconcerned with the inner core, it has been found to be very reliable for regions outside of the core.

The method of Betz is founded on five assumptions:

1) The vortex is axially symmetric,
2) The vortex sheet rolls up in an orderly fashion,
3) There is negligible interaction from the opposite wingtip vortex,
4) The opposite vortices just touch each other on completion of roll-up,
5) Plane flow and straight parallel vortex filaments exist in the initial stages of roll-up.

The model is applied to the early rolled-up vortex before decay is initiated and before turbulence mechanisms have had time to act.

Donaldson and Bilanin [26] provide an extensive summary of the Betz method. It is founded on the four integral invariants of a two-dimensional incompressible rotational fluid motion. These are: the total circulation, which must remain conserved during roll-up; the spanwise location of the centroid of the circulation distribution; the dispersion of vorticity about this centroid; and the kinetic energy of the fluid motion. Of special interest here are the circulation and the spanwise centroid of vorticity on one half of the wing. Consider

the centroid of the vorticity contained between the wingtip and an inboard station, x, as illustrated in Figure V-1 for a simply loaded wing. As the vortex sheet rolls up, the centroidal position remains at a constant spanwise station, $\bar{x}(x)$, with distance downstream.

The conservation laws of Betz are those due to the circulation and the first and second moments of this circulation:

$$-\int_0^x \frac{d\Gamma_w(\xi)}{d\xi}\,d\xi = \int_0^r \frac{d\Gamma_v(\rho)}{d\rho}\,d\rho$$

$$\int_x^{b/2} \xi \frac{d\Gamma_w(\xi)}{d\xi}\,d\xi = \bar{x}(x)\int_x^{b/2} \frac{d\Gamma_w(\xi)}{d\xi}\,d\xi$$

$$-\int_x^{b/2} [\xi-\bar{x}(x)]^2 \frac{d\Gamma_w(\xi)}{d\xi}\,d\xi = \int_0^r \rho^2 \frac{d\Gamma_v(\rho)}{d\rho}\,d\rho$$

These may be used to calculate the circulation distribution within a wingtip vortex given the distribution on the wing.

Rossow [20] proposed an inverse Betz method through which the circulation distribution in the vortex out to a radius r_1 may be used to reproduce the distribution on the wing between the tip and an inboard station x_1. The relevant equations are

$$\frac{b}{2} - x_1 = r_1 + \int_0^{r_1} \frac{1}{v_v(\rho)}\,d[\rho v_v(\rho)]$$

$$r_1 = -\frac{1}{\Gamma_w(x_1)}\int_{b/2}^{x_1} \Gamma_w(\xi)\,d\xi$$

There is, however, a serious drawback with this method in that the tip loading cannot always be accurately reproduced due to viscous and turbulent shears that are generated in the wing boundary layer and

that wind up in the core. For this reason, the method was not used for this work.

The method of Betz may be extended to multiple-vortex wakes so long as each vortex rolls up independently and does not interact significantly with any other. The method is beyond the scope of this work but the interested reader may consult Donaldson et al [33].

V.2 CENTRAL ROTATIONAL VELOCITY

The conservation laws of Betz may be used to relate the singular rotational velocity at the center of a wingtip vortex to the rate of change of loading at the wingtip. From Donaldson et al [33], this velocity is

$$v_\phi)_{r=0} = -\frac{1}{\pi}\frac{d\Gamma_w}{dx}\Big)_{x=b/2}$$

An extensive derivation is provided by Donaldson and Bilanin [26], who incorporated the contribution of the central axial velocity:

$$v_\phi)_{r=0} = -\frac{1}{\pi}\left(\frac{u)_{r=0}}{U_\infty}\right)^{1/2}\frac{d\Gamma_w}{dx}\Big)_{x=b/2} \qquad \text{(V-1)}$$

Axial velocity deficits reduce the central rotational velocity for an inviscid vortex. Axial velocity variations are a consequence of axial momentum variations which arise from the speed defect in the wing boundary layer. The axial and rotational velocities are linked through the radial static pressure gradient which balances the centrifugal force generated by the rotary motion. A reduction in this

pressure gradient is associated with a reduction in both the axial and rotational velocities.

Equation V-1 was used to calculate the value of $d\Gamma_w/dx)_{max}$ for some selected vortices and the results are presented in Figure V-2. The substantial amount of scatter may be attributed to three things: as was the case for the inverse Betz method, the wingtip loading cannot be reproduced accurately because of viscous actions and turbulent shears in a vortex core; the five-hole probe does not perform well in regions with high flow angles; and the exact position of the vortex core is known only to a fraction of an inch so the true value of the central rotational velocity may not have been measured.

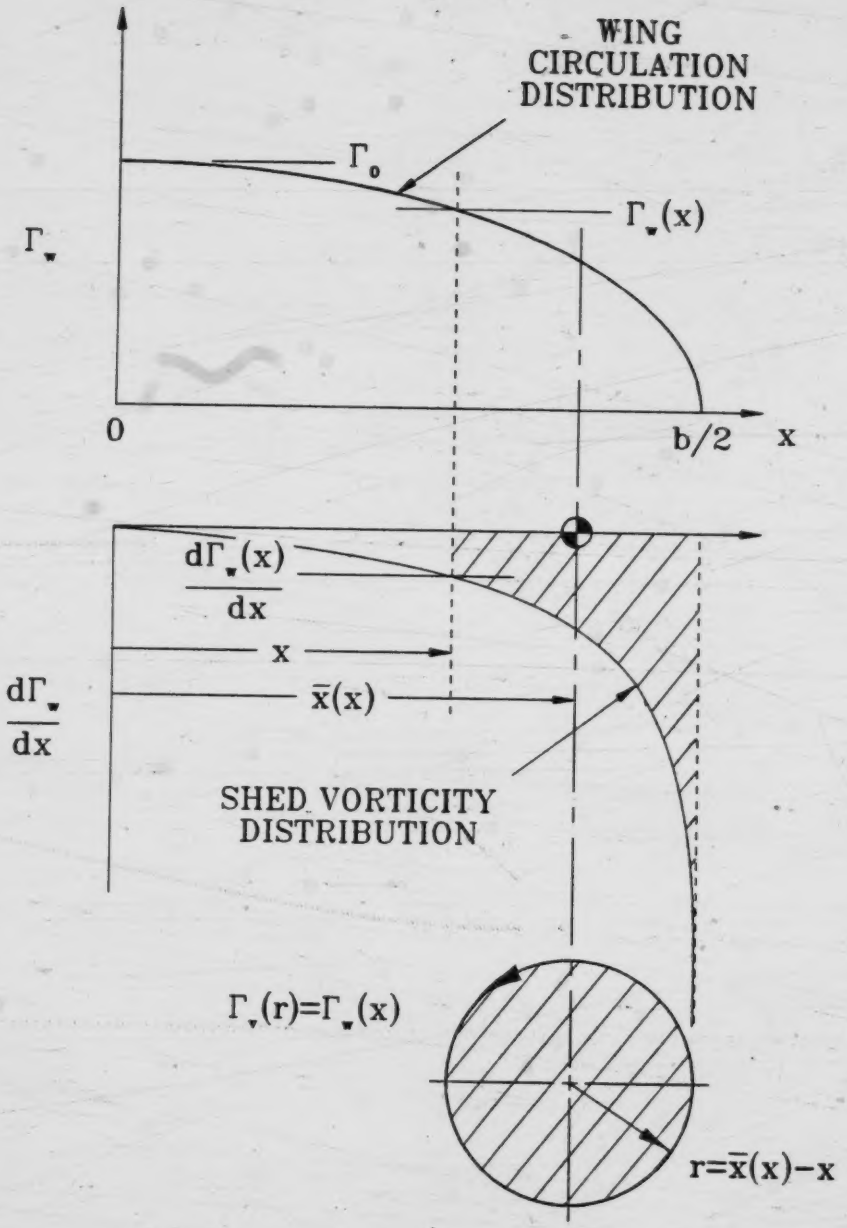

FIGURE V-1 The Betz [34] roll-up model for a simply loaded wing

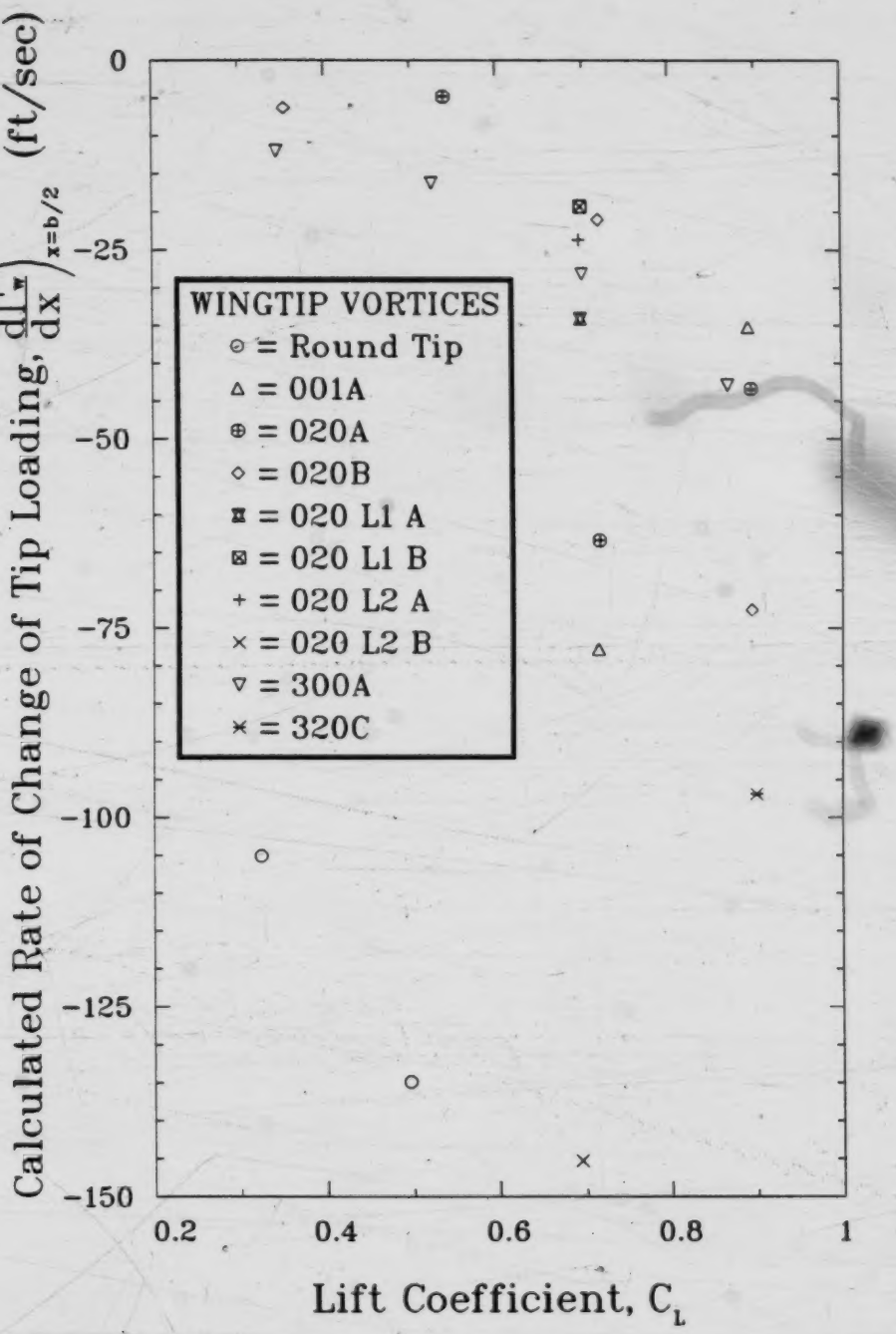

FIGURE V-2 Rate of change of wingtip loading as determined from the central rotational velocities of various main and secondary vortices 4.1 chord lengths behind the wing trailing edge